Universitat Autònoma de Barcelona

# FUNCTIONALIZATION OF CARBON NANOMATERIALS WITH NITROGEN, HALIDES AND OXIDES

**Stefania Sandoval Rojano**

Universitat Autònoma de Barcelona

# FUNCTIONALIZATION OF CARBON NANOMATERIALS WITH NITROGEN, HALIDES AND OXIDES.

**Stefania Sandoval Rojano**

**Tesis Doctoral**

**Programa de Doctorado en Ciencia de Materiales**

Directores: **Gerard Tobias Rossell**
**Amparo Fuertes Miquel**

Tutor: **Lluis Escriche Martínez**

**Departamento de Química**
**Facultad de Ciencias**

**2016**

Instituto de Ciencia de Materiales de Barcelona
Consejo Superior de Investigaciones Científicas
Campus de la UAB
08193 Bellaterra (Barcelona)

Universidad Autónoma de Barcelona
Departamento de Química
08193 Bellaterra (Barcelona)

Memoria presentada para aspirar al Grado de Doctor por

**Stefania Sandoval Rojano**

Visto bueno de

**Gerard Tobias Rossell**

**Amparo Fuertes Miquel**

Bellaterra, Junio 20 de 2016

La Dra. **Amparo Fuertes Miquel**, profesora de investigación y el Dr. **Gerard Tobias Rossell,** científico titular del Consejo Superior de Investigaciones Científicas en el Instituto de Ciencia de Materiales de Barcelona, y el Dr. **Lluis Escriche Martínez,** titular de universidad en la Universidad Autónoma de Barcelona,

CERTIFICAN:

Que Stefania Sandoval Rojano, licenciada en Química, ha realizado bajo su dirección el trabajo que lleva por título "*Functionalization of carbon nanomaterials with nitrogen, halides and oxides*", el cual es presentado en esta memoria para optar al grado de Doctor por la Universidad Autónoma de Barcelona.

Y para que así conste, firman el presente certificado,

Prof. Amparo Fuertes Miquel

Dr. Gerard Tobias Rossell

Dr. Lluis Escriche Martínez

Bellaterra, Junio 20 de 2016.

*"All my life through, the new sights on Nature made me rejoice like a child"*

*Marie Curie*

# Acknowledgements.

Me gustaría agradecer especialmente a Amparo y a Gerard por haberme dado la oportunidad de comenzar la tesis con ustedes. Estos años han sido incalculablemente enriquecedores para mí, no sólo en el ámbito profesional sino también en el personal. Gracias Gerard, por tu dedicación y motivación continuas. Es un placer trabajar contigo. Gracias por tu confianza y paciencia y por permitirme seguir haciendo lo que me gusta; es algo que para mí no tiene precio. También a los miembros del Tribunal por haber aceptado hacer parte de ésta tesis.

I would like to thank to Prof. C. N. R. Rao, Dr. A. Sundaresan and their entire group for their kindly welcome and support during my stay at the Jawaharlal Nehru Centre for Advanced Scientific Research in Bangalore, India. I specially would like to thank to Nitesh and Urmi. I felt like home. Time with you was extraordinarily enriching. It is amazing how much you can learn from simple things.

Esta tesis doctoral ha sido financiada por el Ministerio de Economía y Competitividad mediante los proyectos MAT2011-24757 y MAT2014-53500-R y en colaboración con el Departamento de Ciencia y Tecnología (DST, India) por el proyecto ACI2009-0861. Los datos de XPS fueron adquiridos en el Laboratorio de Microscopías Avanzadas (LMA)-Instituto de Nanociencia de Aragón (INA), las medidas de Análisis Elemental se llevaron a cabo en los Centres Científics I Tecnòlogics de la Universidad de Barcelona y las imágenes de TEM de alta resolución se adquirieron en el Instituto Catalán de Nanociencia y Nanotecnología (ICN2). Gracias a la Dra. Belén Ballesteros por su colaboración en la adquisición de las imágenes de TEM de alta resolución y en particular a Ela. Sé que has pasado muchas horas en el microscopio para encontrar la imagen “perfecta”, que no siempre llega. Muchas gracias por tu tiempo.

Por otro lado, me gustaría agradecer a las personas que han estado directa o indirectamente relacionadas con el desarrollo de ésta tesis doctoral.

A los integrantes del grupo de investigación “Nanoengineering of Carbon and Inorganic Materials”, Magdalena, Marcus, Jorge y en especial a ti Laura, mi *nanotubes mate*, por acogerme y aguantarme tanto.

A las personas pertenecientes al Departamento de Estado Sólido del ICMAB y en particular a los que han pasado por el despacho *On Fire*. Javi, Alex, Sebastian, Ashley, Manu y Pedro, por las conversaciones y risas entre líneas y experimentos. A los compañeros del laboratorio en general; por su paciencia ante mi “cantaleta” constante durante el trabajo. A Ana López, Jessica N, Angelita, Ana Milena y Jullieth. Han sido tantas charlas y risas… Cada una me ha aportado momentos invaluables. Soy muy afortunada de haberlas conocido. Nina, eres extraordinaria. Pocas veces se tiene la suerte de conocer personas como tú. Te voy a extrañar mucho Antonia-*Magali*! Nerea, muchas gracias por estar allí en tantos momentos.

A mis vecinas de despacho, Marta y Cris; perdí la cuenta de cuantos cafés/tés nos tomamos. Siempre un aire fresco ante el estrés del día a día. A uds. las extraño ya. Laura López, espero que haya más viajes y cerves, para seguir “quejándonos” del poco “material” disponible ;). A la gente del ICMAB en general, Arantxa, David, Romen, Jessy, Marta V, Regina, Carlos, Berta, Justo, es difícil no dejarse a alguien… Todos siempre con una cara amable. Me han hecho sentir como en casa. Al Dr Ángel Pérez y a la Dra Eniko Gyorgy, por su colaboración con las reacciones asistidas por laser, que aunque no hacen parte de ésta tesis me han ayudado a entender un poco más los procesos de funcionalización tanto de nanotubos como de grafeno.

Gracias al personal de los Servicios Científico técnicos del ICMAB. Al servicio de Microscopía: Judith, eres un sol! Las largas horas en el microscopio se hacen leves contigo. Gracias por tu buena disposición y entusiasmo siempre, tanto fuera como en el trabajo y por enseñarme a hacer fotos medio decentes con el SEM y el TEM (Espero que algún día me queden como las tuyas). A las chicas del servicio de análisis térmico, Marixa Arnedillo y Roberta Ceravola, por su colaboración y eficiencia en las medidas de

TGA (a pesar de las inclemencias del tiempo). Roberta, gracias por escuchar mis conversaciones con y sin importancia, y por calmar a veces mi mal humor. A Anna Crespi, Joan B Esquius y Francisco Javier Campos por las medidas de difracción de rayos X y al personal técnico de la plataforma de nanoestructuración, Neus y Luigi por su colaboración en la Sala Blanca.

Al personal de administración del Instituto, Rebeca, María, y en especial a Trini, Vicente y Pietat por su entrega y disposición, y por ayudarme a lidiar con los interminables trámites de extranjería.

A la "tribu" colombiana (los nativos y adoptados), Roque, Maria, Andresito, Diego y Mari, a mi profe de baile James, Raquel y Sol! Con ustedes las distancias se hacen más cortas. A ti Jackeline, que puedo decir, no sabes cuánto te admiro. Eres un ejemplo de fortaleza y ganas de salir adelante.

A mis "nenuchis" del alma. Mari y Lina. Hace 7 años empezamos éste viaje juntas y no puedo imaginar mejores compañeras, cómplices, amigas… hermanas. Gracias por estar siempre allí para mí. Con ustedes nunca me siento sola. Las quiero. También a Alejo y a Fran, por su eterna sonrisa y recibirme siempre.

Y por último, a mi familia. Los amo. Ustedes son mi motivación, mi fuerza, mi todo. A mi papá Edwin; me has dado una de las cosas que más valoro: la inquietud constante. No tienes idea de cuánto te admiro. Mami, eres un ejemplo de amor y sacrificio. A mis hermanos. Jennifer, Cindy, Wendy, Edwin y Hansel. No puedo imaginar mi vida sin ustedes. Los extraño cada momento de mi vida. Al pequeño Isaac. Le has dado una nueva alegría a mi vida. Gracias a Moisés también por hacerme tía.

A mis tias, Amira, Denis, Marbel y Magali, ustedes le dan significado a la palabra familia. Las amo.

A todos, Muchas gracias!

# Abstract.

Graphene and carbon nanotubes (CNTs) are of wide interest in materials science due to their outstanding properties. Several approaches allow modulating their properties further expanding their potential applications in many fields.

This thesis reports on the functionalization of carbon nanomaterials with nitrogen, halides and oxides. The modification of the structure of multiwalled carbon nanotubes (MWCNTs) and graphene derivatives has been carried out through solid-gas and solid-liquid reactions. Different methods of functionalization, which include oxidation, nitrogen functionalization and doping, as well as endohedral and exohedral modifications have been employed for tuning the properties of the prepared nanostructures. A systematic study of the conditions of treatment and an extensive characterization has allowed the determination of the structural characteristics of the samples and the evaluation of some of their physical and chemical properties.

In this thesis we propose a simple, efficient and reproducible method for the synthesis of nitrogen-containing reduced graphene oxide (RGO). The nature of the nitrogen atoms within the RGO lattice has been tuned by ammonolysis treatments of graphene oxide (GO) in the range of 25 ˚C-800 ˚C. The reported protocol allows the introduction of aliphatic moieties (N-functionalization) and structural nitrogen (N-doping). Additionally, the structural composition of the N-containing RGO has been modified by post-annealing the material under non-oxidizing atmospheres. High temperature treatments induce internal rearrangements, leading to samples with an enhanced thermal stability.

On the other hand, endohedral and exohedral functionalization of MWCNTs with inorganic materials have been carried out. We report on the formation of single-layered inorganic nanotubes within the cavities of MWCNTs through a molten phase capillary

wetting technique. We have optimized the conditions of the synthesis to enhance the growth of the single-layered nanotubes, while decreasing the formation of other nanostructures (nanoparticles, nanorods and nanosnakes). A new technique for the confinement and/or release of the filled substances within the hollow cavity of the CNTs has also been developed. We have explored the potential of fullerenes as corking agents and as promoting species for the release of guest structures.

Finally, we have prepared MWCNTs decorated with reduced titanium oxides employing high temperature treatments. By oxidation of MWCNTs self-standing titania "nano-necklaces" are formed. The photocatalytic performance of the carbon supported materials overpasses that of the reference material titania P25.

# Resumen.

Los materiales compuestos por grafeno y nanotubos de carbono han despertado un amplio interés debido a sus propiedades excepcionales. La variación de éstas, empleando diversas técnicas de modificación aumentan sus aplicaciones potenciales en muchos campos.

Ésta tesis describe la funcionalización de nanomateriales de carbono con nitrógeno y diversos haluros y óxidos. La modificación de la estructura de nanotubos de carbono multicapa (MWCNTs) y derivados de grafeno se llevó a cabo mediante reacciones sólido-gas y sólido-líquido. Hemos empleado diferentes métodos de funcionalización, que incluyen oxidación, funcionalización con nitrógeno y dopaje, así como modificaciones de las cavidades internas y superficies externas de los nanotubos de carbono, para modular las propiedades de las nanoestructuras preparadas. Mediante un estudio sistemático de las condiciones de tratamiento y una exhaustiva caracterización se determinaron las características estructurales de las muestras y se evaluaron algunas de sus propiedades fisicoquímicas.

En ésta tesis proponemos un método simple, eficiente y reproducible para la síntesis de óxido de grafeno reducido (RGO) modificado con nitrógeno. La naturaleza de los átomos de nitrógeno dentro de la red del RGO se ha modulado mediante tratamientos de amonolísis de óxido de grafeno (GO) a temperaturas comprendidas entre 25 ˚C y 800 ˚C. El protocolo propuesto permite tanto la introducción de grupos funcionales alifáticos (funcionalización con N) como la de nitrógeno estructural (dopaje con N). Adicionalmente, la composición estructural de las muestras funcionalizadas y dopadas con nitrógeno se modificó mediante tratamientos posteriores empleando altas temperaturas y atmosferas no oxidantes. Éstos tratamientos provocan rearreglos internos que confieren mayor estabilidad térmica a los materiales.

Por otro lado, se llevó a cabo el llenado de las cavidades y la decoración de las superficies externas de los MWCNTs con compuestos inorgánicos. Reportamos la formación de nanotubos inorgánicos monocapa dentro de los nanotubos de carbon empleando una técnica de capilaridad del material laminar en su fase fundida. Además, mediante la optimización de los parámetros experimentales conseguimos favorecer el crecimiento de éstos sistemas inorgánicos monocapa con respecto la formación de otras nanoestructuras, tales como, nanopartículas, nanobarras y nanoserpientes de los halogenuros empleados. Hemos descrito una nueva técnica para el aislamiento ó liberación de las sustancias previamente introducidas en las cavidades de los MWCNTs. Así, exploramos el uso potencial de los fulerenos como agentes aisladores o promotores de la liberación de estructuras huéspedes.

Finalmente, hemos preparado MWCNTs decorados con óxidos de titanio reducidos empleando tratamientos a altas temperaturas. Mediante la oxidación de los nanotubos se obtuvieron “nanocollares” de titania libres de carbono. Los materiales soportados presentan una actividad fotocatalítica superior a la del material de referencia titania P25.

# Table of contents.

**Acknowledgements** ..... **I**

**Abstract** ..... **V**

**Resumen** ..... **VII**

**Table of contents** ..... **IX**

**Index of figures and schemes** ..... **XIII**

**Index of tables** ..... **XXIII**

**List of symbols, abbreviations and acronyms** ..... **XXVI**

**Chapter 1. INTRODUCTION. GENERAL OBJECTIVES AND MOTIVATION** ..... **1**

1.1. Graphene. General aspects. ..... 4

1.1.1. Chemical Modification of graphene. ..... 8

1.1.1.1. Functionalization of graphene. ..... 8

1.1.1.2. Doping of graphene. ..... 12

1.2. Carbon nanotubes. General aspects. ..... 14

1.2.1. Synthesis and purification of carbon nanotubes. ..... 17

1.2.2. Modification of carbon nanotubes. ..... 22

1.2.2.1. Functionalization of carbon nanotubes. ..... 22

1.2.2.2. Endohedral functionalization: Encapsulation of materials inside CNTs. ..... 24

1.2.2.3. External decoration with inorganic materials. ..... 26

1.2.2.3. External decoration with inorganic materials. 26

1.3. General objectives. 28

**Chapter 2. EXPERIMENTAL METHODS. 29**

2.1. Synthetic procedures. 31

2.1.1. Graphene-based materials. 31

2.1.2. Ammonolysis and high temperature treatments under inert atmospheres. 31

2.1.3. Purification of multiwalled carbon nanotubes. 32

2.1.4. Synthesis of carbon nanotubes-inorganic nanostructures. 33

2.1.4.1. Filling and decoration of multiwalled carbon nanotubes. 33

2.1.5. Washing and removal of the inorganic material after synthesis. 34

2.1.6. Photochemical activity of titanium oxide-multiwalled carbon nanotube derivatives. 34

2.2. Characterization techniques. 35

2.2.1. Electron microscopy. 35

2.2.2. Elemental analysis. 36

2.2.3. Thermogravimetric analysis. 36

2.2.4. X-Ray Diffraction. 37

2.2.5. Contact angle measurements. 37

2.2.6. Fourier transform-infrared spectroscopy. 37

2.2.7. Ultraviolet-visible spectroscopy. 38

2.2.8. X-ray photoelectron spectroscopy. 38

2.2.9. Raman spectroscopy. ..... 38

**RESULTS I**
**SYNTHESIS, CHARACTERIZATION AND THERMAL PROPERTIES OF N-CONTAINING REDUCED GRAPHENE OXIDE. ..... 39**

**Chapter 3. TUNING THE NATURE OF NITROGEN ATOMS IN N-CONTAINING REDUCED GRAPHENE OXIDE ..... 41**

3.1. Introduction. ..... 43

3.2. Objectives. ..... 45

3.3. Synthesis of N-containing reduced graphene oxide. ..... 46

3.3.1. Synthesis and Characterization of graphene oxide. ..... 46

3.3.2. Ammonolysis treatments. Influence of the conditions of reaction. ..... 50

3.4. Thermal stability of N-doped reduced graphene oxide. ..... 73

3.5. High temperature post-synthesis treatments ..... 78

3.5.1. Role of the atmosphere used in the treatments. ..... 79

3.5.2. Role of the functionalities present in the starting material. ..... 86

3.5.3. Role of temperature. ..... 92

3.6. Conclusions. ..... 98

**RESULTS II**
**SYNTHESIS OF CARBON NANOTUBE-INORGANIC NANOSTRUCTURES ..... 101**

**Chapter 4. FILLING OF CARBON NANOTUBES WITH INORGANIC MATERIALS. ..... 103**

4.1. Introduction. ..... 105

4.2. Objectives. ..... 109

4.3. Purification of multiwalled carbon nanotubes. 110

4.4. Synthesis of single-layered inorganic nanotubes encapsulated within multiwalled carbon nanotubes. 111

4.5. Encapsulation of fullerenes: A versatile procedure for the confinement and release of materials within open-ended multiwalled carbon nanotubes. 124

4.5.1. End corking of multiwalled carbon nanotubes with fullerenes. 124

4.5.2. Release of crystalline structures from multiwalled carbon nanotubes assisted by fullerenes. 131

4.6. Conclusions. 137

**Chapter 5. DECORATION OF MULTIWALLED CARBON NANOTUBES WITH TITANIUM OXIDES. 139**

5.1. Introduction. 141

5.2. Objectives. 144

5.3. Synthesis of multiwalled carbon nanotubes decorated with titanium oxide nanoparticles. 145

5.4. Post-synthesis oxidation of TiO-MWCNTs hybrids: Preparation of $TiO_2$-based catalysts. 156

5.5. Applications in UV-catalysis. Degradation of methyl orange by titanium oxide nanostructures. 162

5.6. Conclusions. 166

**Chapter 6. GENERAL CONCLUSIONS 169**

I. SYNTHESIS, CHARACTERIZATION AND THERMAL PROPERTIES OF N-CONTAINING REDUCED GRAPHENE OXIDE. 171

II. SYNTHESIS OF CARBON NANOTUBE-INORGANIC NANOSTRUCTURES. 172

**BIBLIOGRAPHY 175**

# Index of figures and schemes.

Figure 1.1. Graphitic forms of carbon nanomaterials. Graphene can be wrapped up into 0D buckyballs, rolled into 1D nanotube or stacked into 3D graphite. ..... 4

Figure 1.2. (a) Band structure of graphene. The energy band (zoom) of graphene is represented like an "intermediate" between the conductive character of metals and the semiconductor materials with a small difference between the valence and conductive bands. Reprinted with permission from ref. [10] (b) Substitutional doping types. ..... 6

Scheme 1.1. Chemical functionalization of graphene. Different moieties can be linked to the sheet by (a) non-covalent interactions and covalent bonds on (b) the edges and (c) the basal plane. ..... 8

Figure 1.3. A 2D graphene sheet (left) showing the chiral vector $C_h$, chiral angle ($\theta$), and possible rolling directions, which origins (a) zigzag, (b) chiral and (c) armchair nanotubes (right). ..... 15

Figure 1.4. Representation of non–covalent interactions of CNTs with (a) surfactant species, (b) polymers and (c) aromatic moieties. Some possible strategies for covalent functionalization; [100] (d) Filled SWCNTs, (e) $C_{60}$@SWCNT ("Nanopeapod") and (f) external decoration of CNTs. ..... 23

Figure 2.1. (a) Ammonolysis system employed for the preparation of nitrogen-modified materials. (b) Purification system employed for the elimination of amorphous carbon and graphitic particles from CNT samples. ..... 32

Figure 3.1. Synthetic procedure employed to prepare graphene oxide by chemical oxidation of graphite powder. ..... 46

Figure 3.2. Thermogravimetric analysis of GO prepared from graphite powder <20 μm (S, continuous line) and GO prepared from graphite flakes <150 μm (L, dashed line). Analyses were performed under flowing air at a heating rate of 10 °C.min$^{-1}$..... 47

Figure 3.3. SEM images of GO samples prepared from (a) graphite powder (S) and (b) graphite flakes (L). The distribution of sizes of both (c) S and (d) L was determined by measuring the acquired images. ..... 48

Figure 3.4. (a) TEM image of GO (S) with the corresponding (b) SAED pattern and (c) line profile. ..... 49

Figure 3.5. (a) C1s and (b) O1s high resolution XPS of GO (S) prepared by a modified Hummer's method. ..... 50

Figure 3.6. Nitrogen content in N-containing RGO samples prepared by annealing GO in $NH_3$ atmosphere. The rhombus corresponds to a sample of RGO-treated in $NH_3$ (sample name: SR1050). (a) Effect of temperature (flow rate$_{NH3}$= 300 mL.min$^{-1}$; time = 60 min), (b) role of the time (T = 500 °C; flow$_{NH3}$ = 300 mL.min$^{-1}$) and flow rate (T = 800 °C; time = 60 min). (c) Nitrogen content of the ammonia-treated GO prepared from 20 μm graphite powder (black line, SNR) and 150 μm graphite flakes (red line, LNR). ..... 51

Figure 3.7. (a) SEM, (b), TEM, (c) HR-TEM and (d) AFM of nitrogen-containing samples prepared from S at 500 °C (SNR500). The inset in (a) shows the size distribution of the obtained sheets. ..... 53

Figure 3.8. FT-IR of GO (S) and ammonia-treated GO (SNR samples) at temperatures ranged between 100 °C and 800 °C. ..... 55

Figure 3.9. TG analyses of S and the N-containing RGO samples (SNR) prepared by annealing S under ammonia at temperatures ranged between (a) 25 °C- 400°C and (b) 500 °C- 800°C. Thermal analyses were performed under flowing air at a heating rate of 10 °C.min$^{-1}$..... 56

Figure 3.10. Effect of the temperature of treatment in the wettability of thin layers of the N-containing RGO samples (SNR, black solid rhombus), prepared after ammonolysis reactions. Both, GO (S, blue empty rhombus) and graphite (blue empty square) are include as benchmarks. The dashed line separates the N-functionalized RGO (100-400 °C) from the N-doped RGO samples (500-800 °C). Error bars are included for all the samples (some of them are almost not visible due to the low error of the measurement). ..... 59

Figure 3.11. UV-Vis spectra of S and $NH_3$ treated S samples after (a) dispersion-partial centrifugation and (b) dispersion-exhaustive centrifugation in water:ethanol (1:1). ..... 60

Scheme 3.1. Internal electrostatic interaction (H-bond) between hydroxylic and carbonylic groups present in GO sheets. The hydroxy-ketone form turns to be the most abundant resonant structure (85 %). ..... 61

Figure 3.12. General survey scan of S and 100 °C, 220 °C, 500 °C and 800 °C $NH_3$ treated S samples (SNR). ..... 63

Figure 3.13. High resolution N1s XPS spectra of (a-e) N-functionalized RGO (25 °C- 400 °C) and (f-i) N-doped RGO (500 °C- 800 °C ) samples prepared by ammonolysis of GO (S). ..... 64

Scheme 3.2. Synthesis of some N-containing moieties via $NH_3$ nucleophilic addition to hydroxylic, carbonylic groups and derivatives. Higher temperature treatments favor reduction and formation of cyclic moieties. ..... 65

Figure 3.14. High-resolution O1s spectra of (a) S, (b-j) $NH_3$ treated S (100 °C to 800 °C) and (k-l) Ar treated S (500 °C and 800 °C). ..... 67

Figure 3.15. High-resolution C1s spectra of (a-e) N-containing RGO samples prepared by ammonolysis treatment at temperatures ranged between 25 °C and 800 °C and (f) Ar treated S at 500 °C. ..... 69

Scheme 3.3. Graphical representation of both, N-bearing functionalities and structural nitrogen introduced into the graphene oxide structure after ammonolysis treatments at low (left) and high (right) temperatures. ..... 70

Figure 3.16. (a) Raman spectra of N-containing RGO (100 °C-800 °C, SNR) and RGO (800 °C, SArR800). (b) Comparison of the G-band position of two samples treated at 800 °C under Ar and $NH_3$. (c) Effect of temperature on the D-band to G-band intensity ratio ($I_D/I_G$) of N-containing RGO (black squares). A sample of GO (S) and GO reduced under Ar (SArR800, blue rhombus) are also included for comparison. ..... 71

Figure 3.17. (a) TG analyses and (b) DSC curves of undoped RGO (SArR) and N-doped RGO ($NH_3$ treated S, SNR) prepared at 500 °C and 800 °C. TGA and DSC analyses were performed under flowing air at a heating rate of 10 °C.min$^{-1}$. ..... 73

Scheme 3.4. Combustion reactions for the different types of nitrogen and carbon present in N-doped RGO (1-3) and RGO (4). ..... 77

Figure 3.18. High resolution (a, c) C1s and (b, d) O1s spectra of LNR500 and LNR500-1050Ar/$H_2$ samples respectively. ..... 82

Figure 3.19. TGA of N-doped RGO sample prepared under $NH_3$ at 500 °C before (dashed line) and after (continuous lines) annealing treatment under $N_2$ (orange), Ar (blue) and Ar/$H_2$ (green) at 1050 °C. TGA were performed under flowing air at a heating rate of 10 °C.min$^{-1}$. ..... 83

Figure 3.20. High-resolution N1s spectra of (a) LNR500, (b) LNR500-1050Ar/$H_2$, (c) LNR500-1050$N_2$ and (d) LNR500-1050Ar samples. ..... 85

Figure 3.21. Thermogravimetric analyses of nitrogen containing RGO samples (220 °C, 500 °C and 800 °C) after thermal treatment at 1050 °C under Ar atmosphere. Thermal analyses of the starting materials are included for comparison. Analyses were performed under flowing air at a heating rate of 10 °C.min$^{-1}$. ..... 88

Figure 3.22. High Resolution O1s XPS of the 220 ˚C N-containing RGO (LNR220) and the 800 ˚C N-doped RGO (LNR800) (a-b) before and (c-d) after the 1050 ˚C treatment under Ar respectively. 90

Figure 3.23. Thermogravimetric analyses of the 220 °C nitrogen functionalized RGO sample before (LNR220) and after thermal treatment at 500 °C (LNR220-500Ar), 800 °C (LNR220-800Ar) and 1050 °C (LNR220-1050Ar) under argon. Analyses were performed under flowing air at a heating rate of 10 °C.min$^{-1}$. 92

Figure 3.24. High- resolution N1s spectra of LNR220 after treatment at (a) 500 ˚C, (b) 800 ˚C and (c) 1050 ˚C under argon. 94

Figure 3.25. Thermal stabilities of the N-containing RGO materials (LNR220 and LNR500) after treatment at 800 °C under argon. The TG curves of the 500 °C and the 800 °C N-doped samples (LNR500 and LNR800 ) are included for comparison. Analyses were performed under flowing air at a heating rate of 10 °C.min$^{-1}$ 96

Figure 4.1. HRTEM image of a $CeI_3$ inorganic single-layered nanotube confined within a MWCNT. 111

Figure 4.2. High-resolution transmission electron microscopy (HRTEM) images of (a) a $CeI_3$ nanorod, (b) a $CeI_3$ nanosnake and (d) $CeCl_3$ nanoparticles contained within purified multiwalled carbon nanotubes after molten phase capillary wetting. (d) The presence of different inner nanostructures can be clearly differentiated from empty areas inside the CNT 112

Figure 4.3. HAADF STEM images of (a) both $CeI_3$ tubular nanostructures and nanorods grown within a MWCNT. The inset shows a magnified area containing the $CeI_3$ SLINT. (b) Comparison of the intensity profiles of an empty and a $CeI_3$ SLINT-containing area of a MWCNT. 114

Figure 4.4. Intensity profiles of two segments of a MWCNT containing a nanotube (red line) and a nanorod (green line) of $CeI_3$. ..... 114

Figure 4.5. Bar diagram showing the distribution (frequency, %) of the different $CeCl_3$ and $CeI_3$ inner structures grown within multiwalled carbon nanotubes after annealing treatments. ..... 116

Figure 4.6. TEM images of (a) long $CeI_3$ single-layered nanotube, (b) short $CeCl_3$ nanotubes and (c) $ZnI_2$ short nanotubes grown within MWCNTs. ..... 117

Figure 4.7. (a) Low magnification STEM image of $ZnI_2$@MWCNTs prepared at 475 °C, (b) crystalline patterns of $ZnI_2$ inside a MWCNT, (c) HAADF STEM images of two adjacent MWCNT containing both, an inner nanotube as well as a nanorod (A and B arrowed sections respectively). ..... 119

Figure 4.8. (a) HAADF-STEM image of $ZnI_2$@MWCNTs with its respective intensity profile along the red line (b). (c) EDX analysis confirming the presence of C, both Zn and I in the sample along with C (from the CNTs); Al and Cu signal arise from the support employed for the analysis, whereas the Si peak comes from the silica ampoule employed for the synthesis. (d) Schematic representation of a single-layered $ZnI_2$ nanotube with the diameter observed in the experimental image, projected along the main axis and cross section. ..... 120

Figure 4.9. (a) Low magnification TEM image of $ZnI_2$@MWCNTs prepared at 700 °C. (b) TEM of a $ZnI_2$ nanorod and (c) HRTEM of an inner $ZnI_2$ nanotube inside MWCNTs. (b) and (c) have been grown at 1000 °C. ..... 121

Figure 4.10. Bar diagram showing the distribution (frequency, %) of $ZnI_2$ inner nanostructures grown within MWCNTs after annealing treatments. ..... 122

Figure 4.11. (a)Detailed analysis on the effect of temperature towards the formation of $ZnI_2$ nanotubes, differentiating between long and short. (b) Role of temperature in the

formation of other $ZnI_2$ nanostructures, different from inorganic nanotubes, namely nanorods and “nanosnakes”. ..... 124

Figure 4.12. (a) $PbI_2$ filled MWCNTs after molten phase capillary wetting synthesis. (b) HRTEM image of a polycrystalline $PbI_2$ nanorod grown within a MWCNT. (c) Detail of an open ended $PbI_2$@MWCNT. ..... 125

Figure 4.13.(a) $C_{60}PbI_2$@MWCNTs sample. The inset shows a magnified area of an open ended CNT containing fullerenes. (b)$PbI_2$ filled nanotube with fullerenes (white arrows) isolating the inorganic nanostructure. ..... 127

Figure 4.14. (a) Low magnification image of the $PbI_2$@MWCNTs after washing with water. (b) A-C show individual nanotubes containing both fullerenes (white arrows) and $PbI_2$ nanostructures (black arrows) which have not been removed after washing. A low magnification image (right) shows that most of the corked nanotubes maintained its filling after washing. ..... 128

Figure 4.15. (a) $C_{60}ZnI_2$ @MWCNTs sample. (b) $C_{60}CeI_3$ @MWCNTs sample and (c) Open ended MWCNT covered by fullerenes after the $C_{60}$ corking of filled MWCNTs ..... 130

Figure 4.16. (a) $PbI_2$@MWCNTs and (b) $C_{60}PbI_2$@MWCNTs after washing with anhydrous ethanol at 80 ˚C during 16 h. ..... 132

Scheme 4.1. Schematic representation of the fullerene assisted release of $PbI_2$ from MWCNTs employing ethanol as promoting solvent. ..... 134

Figure 4.17. (a) $PbI_2$@MWCNTs after washing at 80 ˚C during 16 h with a dispersion of fullerenes in absolute ethanol. ..... 135

Scheme 4.2. Schematic representation of the mechanisms of corking of MWCNTs and release of the guest material from the hosting nanotubes promoted by fullerenes..... 136

Figure 5.1. (a) Low magnification TEM image of the MWCNT/$TiCl_2$ mixture, after annealing at 1060 °C. (b) Nanoparticles filing a nanotube and (c-d) MWCNTs partially decorated with Ti-based nanoparticles. ..... 146

Figure 5.2. XRD analysis of the purple crystals obtained as secondary products in the synthesis of the MWCNTs decorated with Ti-based nanoparticles. The XRD pattern was acquired by protecting the sample with a Kapton® film (broad background within 10-30 degrees). ..... 147

Figure 5.3. EDX analysis confirming the presence of Ti, Cl and C in thee sample. Al and Cu signals arise from the support employed for the analysis, and the Si peak comes from the silica ampoule employed for the synthesis. ..... 148

Figure 5.4. Scheme of oxygen point defects present in the silica structure. ..... 149

Figure 5.5. (a) Low magnification TEM image of the MWCNT/$TiCl_2$ mixture, after annealing at 1060 °C in presence of the titanium film. The inset shows a high magnification of a selected area of the main image. (b) Histogram showing the distribution (frequency, %) of diameters of the synthesized nanoparticles and (c) SAED pattern corresponding to the TiO decorating nanoparticles. ..... 150

Figure 5.6. (a) Low magnification SEM image of MWCNTs decorated with Ti-based nanoparticles prepared by annealing a $TiCl_2$/MWCNTs mixture in presence of metallic titanium. (b) EDX analysis confirms the presence of Ti, Cl and C in the sample. (c) X-ray Diffraction pattern of the obtained powder. ..... 151

Figure 5.7. (a) XPS general survey scan of the TiO decorated MWCNTs prepared after annealing a $TiCl_2$/MWCNTs mixture in presence of metallic Ti (under vacuum). High resolution spectra of the (b) Ti2p and (c) C1s regions. ..... 152

Figure 5.8. (a) Thermal analysis of the TiO decorated MWCNTs (TiONPs-MWCNTs) prepared by the 1060 ˚C annealing the $TiCl_2$/MWCNTs mixture in presence of metallic

Ti. The analysis was performed under flowing $O_2$ at a heating rate of 10 ˚C.min$^{-1}$. XRD patterns of the residue obtained after annealing the sample at (b) 470 ˚C and (c) 1400 ˚C. ..... 155

Figure 5.9. (a) TG and (b) DSC analyses of the TiONPs-MWCNTs sample after annealing at 250 ˚C (black line), 275 ˚C (violet line), 370 ˚C (blue line) and 450 ˚C (green line) under oxygen for 6 h. TGA and DSC analyses were performed under flowing $O_2$ at a heating rate of 10 °C.min$^{-1}$. ..... 157

Figure 5.10. XRD patterns of the TiONPs-MWCNTs (a) before and after annealing at (b) 350 ˚C, (c) 370 ˚C, (d) 380 ˚C, (e) 400 ˚C and (f) 450 ˚C during 6h under oxygen flowing at 165 mL.min$^{-1}$. ..... 158

Figure 5.11. XRD patterns of the TiONPs-MWCNTs after annealing at (a) 350 ˚C and (b) 370 ˚C during 12 h under flowing oxygen at 165 mL.min$^{-1}$..... 160

Figure 5.12. (a-b) TEM images of the $TiO_2$ structures obtained after annealing the TiONPs-MWCNTs at 370 ˚C, during 6 h under flowing $O_2$ (165 mL.min$^{-1}$) and (c) anatase $TiO_2$ particles resulting from the oxidizing process at 350 ˚C during 12 h..... 162

Figure 5.13. (a) Absorbance spectrum of a 2.5 ppm methyl orange (MO) solution, having a maximum at 464 nm, (b) calibration curve employed to calculate the MO concentration in the irradiated solutions. (c) Photodegradation rate calculated after UV irradiation of the MO solutions in the presence of TiONPs-MWCNTs prepared by annealing $TiCl_2$ and MWCNTs at 1060 ˚C (blue line), and $TiO_2$ necklace-like nanostructures prepared after oxidation of the TiONPs-MWCNTs at 370 ˚C, during 6h, under flowing $O_2$ (green line). The photocatalytic activity of the P25 $TiO_2$ (black line) is included for comparison. ..... 165

# Index of tables.

Table 1.1. Operational details and characteristics of the most usually employed CNTs synthetic procedures. ..... 18

Table 3.1. Composition of C, N and H present in GO and ammonia-treated samples determined by elemental analysis. ..... 52

Table 3.2. Onset of combustion temperature in air of S annealed in ammonia at temperatures ranged between 500 °C and 800 °C. ..... 57

Table 3.3. Nitrogen, oxygen and carbon content of S, $NH_3$ treated S (25 °C-800 °C) and Ar treated S (500 °C, 800 °C) determined by XPS analysis. (*) These energies could be contributed either by aliphatic functionalities ($CONH_2$/$CNH_2$) or by structural pyridinic ($C_5N$:) and pyrrolic ($C_4N$:) groups ..... 62

Table 3.4. Ratio between N, O and C species present in S, $NH_3$ treated S (100 °C-800 °C) and Ar treated S (500 °C, 800 °C) determined by XPS analysis. (*) These energies could be contributed either by aliphatic functionalities ($CONH_2$/$CNH_2$) or by structural pyridinic ($C_5N$:) and pyrrolic ($C_4N$:) groups ..... 68

Table 3.5. Toolbox of characterization techniques for the assessment of N-containing species in graphene-based materials. ..... 72

Table 3.6. Onset of combustion temperature in air of GO annealed in $NH_3$ (N-RGO) and Ar (RGO) at 500 °C and 800 °C. ..... 74

Table 3.7. Nitrogen content determined by elemental analysis (total content) and XPS (ratio of nitrogen types) in samples of N-doped RGO prepared at 500 ˚C and 800 ˚C in $NH_3$. ..... 75

Table 3.8. Mean bond enthalpies (Δ*H*) involved in the combustion reaction of SArR and SNR samples.[196] ..... 76

Table 3.9. Changes in the Gibbs Energy (Δ*G*) for the combustion reactions of RGO and N-doped RGO ..... 78

Table 3.10. Nitrogen, oxygen and carbon atomic content (at. %, determined by XPS) present in LNR500 (500 °C $NH_3$ treated L sample) before and after annealing at 1050 °C under Ar, $N_2$ and Ar/$H_2$ ..... 79

Table 3.11. Composition of carbon, nitrogen and hydrogen (wt. % determined by elemental analysis) present in L and LNR500 (500 °C $NH_3$ treated L samples) annealed at 1050 °C under different inert atmospheres. ..... 80

Table 3.12. Carbon, nitrogen and oxygen atomic content (at. %, determined by XPS) present in LNR500 (500 °C $NH_3$ treated L sample) before and after annealing at 1050 °C under Ar, $N_2$ and Ar/$H_2$. In all cases the contribution of the specific functionalities is registered ..... 81

Table 3.13. Onset of combustion temperature in air of the 500 °C ammonia treated L sample (LNR500) after annealing at 1050 °C under Ar (LNR500-1050Ar), $N_2$ (LNR500-1050$N_2$) and Ar/$H_2$ (LNR500-1050Ar/$H_2$ ). ..... 84

Table 3.14. Composition of carbon, nitrogen and hydrogen (wt. %, determined by elemental analysis) present in LNR220 and LNR800 before and after annealing at 1050 °C under Ar ..... 87

Table 3.15. Onset of combustion temperature in air of the nitrogen containing materials (LNR) before and after treatments under argon at 1050 °C. ..... 89

Table 3.16. Carbon, oxygen and nitrogen content (at. % determined by XPS) of $NH_3$ treated L (220-800 °C) before and after 1050 °C treatment under argon, determined by XPS analysis. (*) These values could correspond to aliphatic functionalities ($CONH_2$/$CNH_2$) or to structural pyridinic ($C_5N$:) and pyrrolic ($C_4N$:) groups. ..... 91

Table 3.17. Onset of combustion temperature in air of the nitrogen-containing materials (LNR) before and after treatments under argon at 500 °C, 800 °C and 1050 °C..... 93

Table 3.18. Carbon, nitrogen and oxygen content (at. % determined by XPS) of the 220 ˚C $NH_3$ treated L (LNR220) before and after annealing at 500 ˚C, 800 ˚C, and 1050a ˚C under argon. The concentration of the species was determined by XPS analysis. (*) These energies could be contributed either by aliphatic functionalities ($CONH_2$/$CNH_2$) or by structural pyridinic ($C_5N$:) and pyrrolic ($C_4N$:) groups. ..... 94

Table 3.19. Composition of carbon, nitrogen and oxygen present in $NH_3$ treated L samples (220 ˚C and 500 ˚C) before and after annealing at 800 °C under argon. The atomic content was determined by XPS analyses. (*) These values could correspond to aliphatic functionalities ($CONH_2$/$CNH_2$) or by structural pyridinic ($C_5N$:) and pyrrolic ($C_4N$:) groups. ..... 95

Table 3.20. Onset of combustion temperature in air of the nitrogen-containing materials (LNR220 and LNR500) before and after 500 ˚C and 800 ˚C treatments under argon. The data of the 800 ˚C N-doped RGO (LNR800) is included for comparison. ..... 96

Table 4.1. Numerical data collected after counting the number of the different types of inner nanostructures present in the samples of purified MWCNTs mixed with either $CeI_3$ or $CeCl_3$ after annealing at different temperatures. ..... 115

Table 4.2. Effect of the treatment temperature in the distribution of nanotubes and other nanostructures confined within MWCNTs.....121

Table 5.1. $TiO_2$ phase obtained after annealing the TiONPs-MWCNTs sample in $O_2$ at temperatures ranged between 350 ˚C and 450 ˚C. .....159

# List of symbols, abbreviations and acronyms.

| | |
|---|---|
| 1D | One dimensional |
| 2D | Two dimensional |
| 3D | Three dimensional |
| AFM | Atomic force microscopy |
| at | Atomic |
| BE | Binding energy |
| $C_{60}$ | Fullerene |
| CA | Contact angle |
| $C_h$ | *Chiral vector* |
| CNT(s) | Carbon nanotube(s) |
| $C_p$ | Heat capacity |
| CVD | Chemical vapor deposition |
| DSC | Differential scanning calorimetry |
| DWCNT(s) | Double walled carbon nanotube (s) |
| EA | Elemental analysis |
| EDX | Energy dispersive X-ray analysis |
| EtOH | Ethanol |
| FT-IR | Fourier transform infrared spectroscopy |
| GPa | Gigapascal |
| $G$ | Gibbs energy |
| GO | Graphene oxide |
| $H$ | Enthalpy |
| HAADF | High angle annular dark field |
| HiPCO | High pressure disproportionation process |

| | |
|---|---|
| HOMO | Highest occupied molecular orbital |
| HRTEM | High resolution transmission electron microscopy |
| L | Graphene oxide prepared from large graphite particles (<150 μm) |
| LNR | Nitrogen containing reduced graphene oxide (flakes) |
| LUMO | Lowest unoccupied molecular orbital |
| MO | Methyl orange |
| MWCNT(s) | Multiwalled carbon nanotube(s) |
| NPPs | Nanopeapods |
| NPs | Nanoparticles |
| ppm | Part(s) per million |
| PECVD | Plasma enhanced chemical vapor deposition |
| Ph | Phenol |
| PLV | Pulsed laser vaporization |
| RGO | Reduced graphene oxide |
| *S* | Entropy |
| S | Graphene oxide prepared from small graphite particles (<20 μm) |
| SAED | Selected area electron diffraction |
| SEM | Scanning transmission electron microscopy |
| SLINT(s) | Single-layered inorganic nanotube (s) |
| SNR | Nitrogen containing reduced graphene oxide (from small GO) |
| STD | Surface transfer doping |
| STEM | Scanning transmission electron microscopy |
| SUD | Substitutional modification |
| SWCNT(s) | Single walled carbon nanotube(s) |
| TEM | Transmission electron microscopy |
| TGA | Thermogravimetric analysis |
| TiONPs | Nanoparticles of titanium oxide |
| X@MWCNTs | Multiwalled carbon nanotubes filled with X |
| XPS | X-ray photoelectron spectroscopy |

| | |
|---|---|
| XRD | X-ray diffraction |
| UV | Ultraviolet |
| UV-Vis | Ultraviolet-visible |
| λ | Wavelength |
| wt | Weight |
| Ø | Diameter |
| Δ° | Increment |
| ν | Wavenumber |

# Chapter 1.

# Introduction. General Objectives and motivation.

This chapter introduces the general aspects of the main carbon-based nanomaterials: Graphene, carbon nanotubes and fullerenes. Its structural characteristics, physicochemical properties and potential applications are briefly described. Finally the general objectives in this thesis are presented.

Carbon is one of the most abundant elements on earth. It has the ability to form a large variety of structures, being the main component of the organic compounds and interacting with a large amount of inorganic species. Furthermore, it has the possibility to interconnect with other carbon atoms through single or multiple bonds (different hybridization states), leading to the formation of stable frameworks with varying dimensionalities and properties.

Carbon derivatives are known since prehistoric times. Diamond and graphite, the most popular and frequently employed among the known carbon allotropes, have been widely studied, its structure solved and its properties exploited. Graphite is known by its usefulness in drawing; writing and printing, while the strong covalent bonds present in diamond confer it the highest known hardness. Carbon based-materials have played a main role in the development of the human society. For this reason, a continuous search to obtain them through synthetic routes has been carried out. Additionally, the exploration of post-synthesis treatments to improve their properties is of a wide interest. First synthetic graphite was produced in 1896[1] and the development of a commercial synthetic procedure for obtaining diamonds was registered in 1955.[2] Since then, further advances in the discovery and production of new carbon derivatives have been carried out.

In 1985 Kroto and Smalley discovered the particularly stable and symmetric buckminsterfullerene structure,[3] opening a door for the production of carbon nanostructures. The structure of carbon nanotubes was described in 1991 by Iijima[4] and the subsequent isolation and measurement of graphene properties was reported in 2004 by Geim and Novoselov.[5] Fascinating physical and chemical properties have been attributed to these new allotropic forms of carbon and applications in diverse fields of the materials science and nanotechnology are constantly reported.[6, 7]

## 1.1. Graphene. General aspects.

Graphene is the basic structural parent of all graphitic forms of carbon, being the essential building block for a family of nanomaterials strictly composed by carbon atoms, which include 1D carbon nanotubes (CNTs) and 0D buckyballs. Besides, the 3D structure of graphite results from the stacking of multiple graphene layers linked by Van der Waals forces and interactions of the $\pi$ orbitals of the carbon atoms present in adjacent layers (**Figure 1.1**).[8] Despite that graphene was already theoretically described by P. R. Wallace in 1947 (in order to understand the electronic properties of graphite),[9] its isolation and experimental properties were not described until 2004 by Novoselov, Geim et al.[5] Since then it has become one of the most studied solids in materials science.

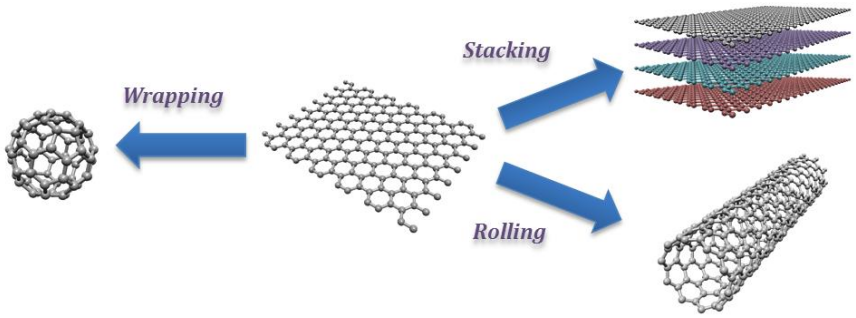


**Figure 1.1.** Graphitic forms of carbon nanomaterials. Graphene can be wrapped up into 0D buckyballs, rolled into 1D nanotube or stacked into 3D graphite.

Graphene consists of a single-atomic layer of $sp^2$ hybridized carbon atoms which form an hexagonal honeycomb structure. The hybridization between one *s* orbital and two *p* orbitals leads to a trigonal planar structure with each carbon atom linked to three equivalent atoms by $\sigma$ bonds separated by 1.42 Å. The conjugated system is produced by the formation of out of plane oriented $\pi$ bonds due to the covalent interaction of the unaffected *p* orbitals (each of them containing one single electron). The $\sigma$ band is

responsible for the robustness of the lattice structure, while the half-filled $\pi$ system, formed by the bonding ($\pi$) and anti-bonding ($\pi^*$) bands confers the electronic properties to the material.[10]

The conductive or insulator character of a material is determined by the difference of energy between the valence band and the conduction band. The band structure of graphene, calculated by Wallace in 1947, can be regarded as two cones, which represent the valence (bonding) and conduction (antibonding) bands, touching by a single point (Dirac point)and representing the Fermi surface (**Figure 1.2(a)**). Since the valence band and the conduction band touch at this point, graphene is typically labeled as a zero-gap semiconductor.[11, 12] Graphene exhibits large surface areas, up to 2600 $m^2g^{-1}$, high thermal conductivity (ca. 5000 $WmK^{-1}$), fast charged carrier mobility (ca 200000 $cm^2V^{-1}s^{-1}$) and strong Young's modulus (ca. 1 TPa). Its physical and chemical properties are associated with the unique energy-band structure and the behavior of the electrons in the lattice (Dirac fermions), which can be modified by tailoring the electronic structure.[13]

Although graphene is ideally composed by a single atomic layer, the properties of materials containing two or more layers have been extensively studied. Nowadays, three different types of graphene-based materials can be defined: single-layer, bi-layer and few-layer graphene (≤10 layers). Structures with more than 10 layers are considered as thick graphene sheets and are of less scientific interest.

Graphene can be synthesized by different routes including micromechanical exfoliation of bulk graphite, chemical vapor deposition (CVD), arc discharge method, epitaxial growth on SiC, chemical and thermal reduction of graphene oxide, as well as liquid phase exfoliation and unzipping of CNTs.[14] Micromechanical exfoliation of bulk graphite employing scotch-tape was the first successful method reported to obtain high quality single layer graphene.[5] This method allows the characterization and exploration of the properties of the material, nevertheless the number of exfoliated layers

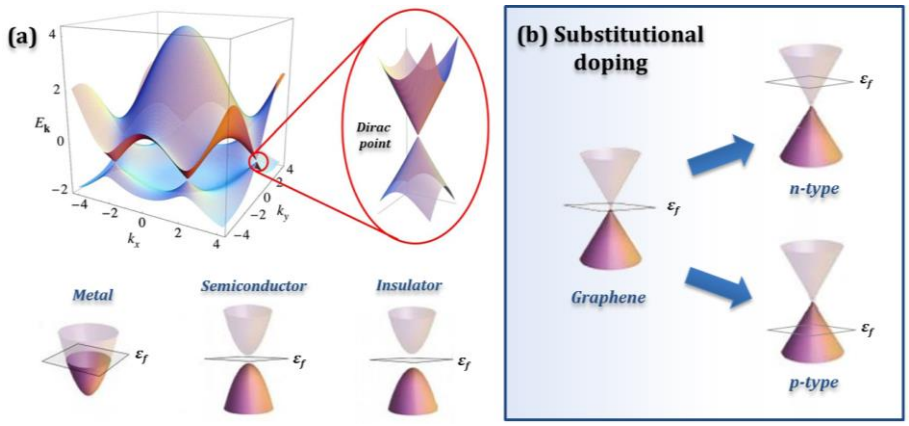


**Figure 1.2.** (a) Band structure of graphene. The energy band (zoom) of graphene is represented like an "intermediate" between the conductive character of metals and the semiconductor materials with a small difference between the valence and conductive bands. Reprinted with permission from ref. [10] (b) Substitutional doping types.

cannot be easily controlled and it does not represent an approach for large-scale production. For this purpose, both exfoliation of graphite and graphite derivatives by chemical or thermal methods and CVD-based processes have been proposed as promising approaches. Chemical exfoliation of graphite is carried out employing intercalating atomic or molecular species which break the electrostatic interactions present between the layers.[15] Liquid phase techniques include dispersion of pure graphite in organic solvents such as N-methyl-pyrrolidone,[16] aqueous solutions containing surfactants[17] or ionic solvents.[18] However, the main drawback of this approach is the presence of an important amount of defects in the structure. On the other hand, in order to obtain a successful thermal exfoliation, pre-treatments of graphite to produce expanded graphite or the use of graphite intercalation compounds are required. Various graphite derivatives, heating sources and temperatures have been employed, leading to high quality graphene samples. Finally, to overcome the Van der Waals attractions between the graphite layers additional procedures have been proposed. Microwave irradiation, electrochemical[19] or supercritical fluids exfoliation[20] are promising techniques for the large-scale synthesis of graphene.[21] High quality and large-area samples are obtained by CVD, which employs a

hydrocarbon gas (as carbon source) flowing through a system containing transition metal surfaces like Cu or Ni or metal alloys, where graphene is finally grown.[22] Several modifications have been developed to improve the production of graphene by CVD, but this method is rather costly and undesired derivatives like carbides or amorphous carbon are produced. The approach is interesting though since it allows a controlled sized growth of single or few layer graphene and the easy free of damage transfer of graphene to other substrates.[23] The arc discharge method and epitaxial growth of graphene on silicon carbide produce materials with improved quality, good crystallinity and high thermal stability. In the case of the SiC procedure the number of layers is temperature dependent; nevertheless, issues like thickness control and large-scale production have to be solved. The unzipping of CNTs involves the longitudinal opening of multiwalled carbon nanotubes (MWCNTs) followed by chemical and thermal exfoliation. It offers the possibility of large-scale production with well controlled widths.[15] Despite that many routes have been proposed for the synthesis of graphene from MWCNTs, the employed method for the production of high quality materials are either costly, with a low throughput or require harsh experimental conditions. Alternative approaches involving the preparation of size controllable polycyclic aromatic hydrocarbons (PAHs, very small two-dimensional graphene fragments) have been considered as well.[24]

Conventional processing techniques cannot be applied to tailor the physicochemical behavior of graphene based materials. Pristine graphene layers interact forming wrinkles and restacking together through $\pi$-$\pi$ bonding and Van der Waals forces. Due to the strong hydrophobic interactions between the layers, graphene is dispersible in a limited group of organic solvents and susceptible to aggregation in aqueous solvents.[16, 24] Besides, its high chemical stability as well as the zero band-gap reduce the potential applicability in electronics, optoelectronics, catalysis or sensors. Many efforts have been carried out to modify the electronic structure and intrinsic properties of the material. The main approaches include surface functionalization and doping.

## 1.1.1. Chemical Modification of graphene.

### 1.1.1.1. Functionalization of graphene.

Functionalization of pristine graphene is usually carried out to obtain a more dispersible material[7] in both aqueous and organic media, being the first step for more complex reactions. Depending on the employed approach, namely covalent or non-covalent functionalization, different strategies of synthesis can be employed.

A typical graphene sheet presents two regions of interest suitable for functionalization. The interaction of the planar structure with the reactive specie may occur either at the edges or on the surface. The covalent attachment of different moieties (Scheme 1.1) causes the transition from $sp^2$ to $sp^3$ hybridization of the atoms involved in the reaction, leading to the saturation of a double bond, which modifies the *p*-system.[25] However, atoms along the edges are considerably more reactive than those located on the basal plane due to the presence of dangling bonds, vacancies and defect sites, which usually consist of O-based functionalities. The formation of tetrahedral $sp^3$ results in a lower strain when involves external carbon atoms. The edge modification do not alters the band gap in a significant manner because the conjugated $\pi$-$\pi$ system is barely modified.

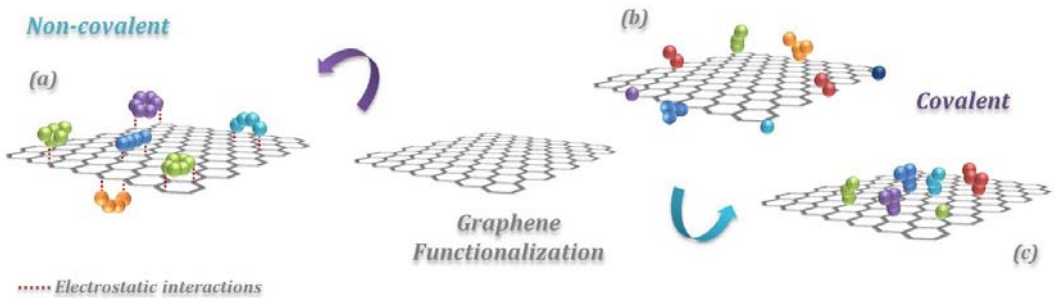


**Scheme 1.1.** Chemical functionalization of graphene. Different moieties can be linked to the sheet by (a) non-covalent interactions and covalent bonds on (b) the edges and (c) the basal plane.

Therefore, this approach is usually employed to improve the physical properties of the material, as well as a former step for further modifications. The edges enable cycloaddition, pericyclic and insertion reactions. The modification of the graphene basal plane **(c)** requires the use of stronger reactives. It allows tuning the optical, chemical and mechanical properties of the material. The absence of one or more carbon atoms (defects) along the honeycomb system enhances the reactivity of surrounding carbon atoms. Thus, the basal plane is responsible for the modification of graphene with a variety of chemical species, through *p–p* interactions or electron transfer processes.

Covalent functionalization of the basal plane of graphene involves the attachment of organic moieties, such as free radicals or dienophiles to the pristine graphene layer,[26, 27] producing different derivatives containing aliphatic and/or aromatic groups[28] which can be employed for the formation of nanocomposite graphene based materials. Hydrogenation, fluorination, free radical addition and oxidation reactions are well documented. The attachment of a wide variety of groups causes the distortion of the conjugated system modifying properties like the optical transparency. The oxidation reactions are the most usually employed.[29] Oxidized materials can be obtained by different approaches including direct oxidation of graphene, lengthwise cutting of CNTs and oxidation of graphite. Graphene oxide (GO) is one of the most investigated graphene derivatives. It has attracted a wide interest due to its high hydrophilicity and excellent water dispersability. Its ability to adsorb on interfaces and lower the surface or interfacial tension confers it surfactant properties and it can be employed for the emulsification of organic solvents in water.[30] Moreover, its preparation by chemical oxidation and exfoliation of graphite, followed by a final reduction step has been considered as one of the most promising alternatives for low-cost, large–scale production of graphene, or strictly speaking reduced graphene oxide (RGO).[31, 32]

Non-covalent functionalization of graphene is used to enhance the solubility of the material in organic solvents as well as to minimize the stacking effect produced by

interlayer attractions. These interactions are governed by electrostatic, induction and/or dispersion energies between the decorating moiety and the conjugated system which do not produce appreciable distortions in the lattice, maintaining the properties of graphene invariable.[26] Non covalent adsorption is usually employed to obtain few layered graphene by exfoliation of graphite. For this purpose, solvents with similar surface energies to the graphene sheets, surfactants in aqueous media and ball milling are useful approaches to obtain individualized sheets.

***Graphene Oxide (GO).***

Considerable efforts have been directed to stablish the chemical structure of GO. The complexity of the material, its amorphous character, nonstoichiometric atomic composition, along with the limitations in the characterization techniques, make difficult the precise assessment of the GO structure. However, many structural models have been proposed.[33] From solid state NMR studies, Lerf and Klinowski suggested a system composed by epoxy and hydroxyl groups decorating the basal plane of GO, while the edges would be functionalized mainly by carboxyl groups. Spectroscopic analyses combined with a series of chemical reactions allowed to detect the presence of at least two inequivalent alcohol species (mainly tertiary groups) and 1,2-ethers on the GO surface.[34] Carboxylic acid groups and ketone groups were present in lower quantities. The authors also studied the interactions between water and GO and determined the aromatic and/or conjugated character of the double bonds. The presence of further derivatives such as 5- and 6-membered lactols on the periphery, esters of the tertiary alcohols on the basal plane and quinones has been additionally proposed; the latter being responsible of the wrinkling of the platelets.[35] Furthermore, due to the complexity of the system, internal transformations (such as keto-enol isomerization) in the conjugated lattice might probably occur. The presence of polar functionalities increases the hydrophilicity and reactivity of the material. GO can be easily dispersed in aqueous media and further derivatized through chemical

reactions with the oxygen containing moieties. Properties of the material are closely related to the amount of oxygen present. Typically, GO is composed of about 30-40 % of oxygen-bearing functionalities, with total content depending on the synthesis procedure.

GO can be prepared by direct oxidation of graphite with strong oxidants such as concentrated $H_2SO_4$, concentrated $HNO_3$, $KMnO_4$ or mixtures of reactives like Jones' reagent ($H_2CrO_4/H_2SO_4$). Several methods, leading to similar levels of oxidation have been also explored by Brodies', Staudenmaiers', Offeman' and Hummers'. Hummers' method is the most widely used and involves the oxidation of graphite followed by exhaustive exfoliation. The combination of $KMnO_4$ and concentrated $H_2SO_4$ produces diamanganese heptoxide ($Mn_2O_7$), a strong oxidant when heated at temperatures above 55 ˚C, that is responsible of the oxidation of graphite.[33]

***Reduction of GO.***

Reduction of GO might restore the electronic properties of the sheets, which is useful for application in devices. The chemical and structural characteristics of the reduced GO are closely related to the procedure. Controlling the degree of reduction up to the total removal of the oxygen based moieties, as well as obtaining RGO free of defects still constitute a big challenge. A major obstacle is the partial cleavage of the hexagonal framework of in plane C-atoms and the high amount of defects introduced during the GO synthesis.[36-38]

Reduction of GO can be carried out through chemical,[36, 39] thermal, electrochemical, microwave and photochemical treatments.[40] The most common chemical treatments of GO employ reducing agents such as hydrazine. [32, 41, 42] Other reducing agents have been proposed to enhance the electrical properties of the material, to minimize the toxicity of the process or to produce RGO functionalized with particular groups.[43-46] Thermal reduction might be a proper approach to obtain a highly exfoliated sample

with a minimum degree of structural defects. Unfortunately, elevated temperatures typically above 900 ˚C, are usually required for treatments.[40, 47-49] Finally, electrochemical, microwave and photochemical assisted reduction of GO are emerging techniques for the removal of the oxygen based moieties from the GO sheets. Electrochemical reduction of GO produces high quality samples, it is a low time and low power consuming method and avoids the use of harmful chemical agents. However, the level of reduction is not comparable with chemical and thermal reductions and large-scale production is not possible.[50] Photochemical reductions take place by the transference of electrons from a catalyst excited by UV irradiation to the GO sheets. The interaction of GO with the electron donor improves its response to UV or Visible increasing its potential applications.[51, 52] Finally, microwave assisted reactions induce rapid and mild thermal reduction of GO. The elimination of O-bearing moieties being proportional to the time of exposure.[53]

#### 1.1.1.2. Doping of graphene.

Tailoring the electrical properties of graphene is possible by structural and/or chemical modifications of the conjugated lattice.[12] Doping has been proposed as an efficient approach of modifying the band gap, leading to a metal-semiconductor transition. Generally, graphene can be doped by changing the gate voltage (electrical doping) and by the interaction with chemical species (chemical doping). The latter tunes the bandgap by shifting the Dirac point relative to the Fermi level.

Chemical doping can be achieved either by interstitial modification, that consists on introducing atoms or molecules on the surface of graphene (surface transfer doping, STD) and substitutional modification (SUD), where the dopant species are introduced into the honeycomb lattice and chemically bonded. Depending on the electrophilic character of the dopant specie graphene sheets can suffer *n*- or *p*-type modification. In case of STD the charge transfer is determined by the relative position of the molecular orbitals in the adsorbed molecule and the Fermi level of graphene. When the highest

occupied molecular orbital (HOMO) of the dopant is located above the Fermi level the dopant will act as a donor of negative charge (*n*-type); meanwhile if the lowest unoccupied molecular orbital (LUMO) is located below the Fermi level the dopant will act as an electron acceptor (*p*-type). $NO_2$, $Br_2$, and $I_2$, can be adsorbed on graphene acting as *p*-type dopants (electron acceptors). On the other hand the interaction with ethanol, $NH_3$ or CO causes *n*-type modifications. Not only small molecules can interact with graphene; big organic molecules and metals have been extensively employed for this purpose. Otherwise, substitutional doping is governed by the presence/absence of valence electrons in the specie replacing carbon atoms from the graphene lattice. *p*-type doping drives the Dirac points of graphene above the Fermi level and it is usually obtained by the addition of atoms with few valence electrons as compared with carbon. Finally, species like nitrogen, rich in valence electrons lead to substitutional *n*-doping by the displacement of the Dirac point below the Fermi level (**Figure 1.2 (b)**).

Heteroatom-doped graphene can be prepared by both, *in situ* treatments, which include CVD, solvothermal and arc discharge reactions or via post synthesis modification, by thermal annealing or plasma, employing atmospheres with molecules containing heteroatoms. First approach leads to samples homogeneously modified, with the N-based moieties distributed along the surface of the sheet, while the latter generally produce only surface modifications.[25, 54-56]

***Nitrogen (N-) doping of graphene.***

N-doping can effectively tune the work function of graphene, creates a magnetic moment and enhances the PL emission. N-doping can be carried out by both chemical reactions with graphene (or GO) through the substitution of oxygen (in case of oxidized sheets) or carbon atoms with nitrogen during reduction or annealing reactions or *in situ* during graphene growth methods.[26] Reactions of nitrogen sources with $sp^3$ atoms from the edges lead to the formation of N-functionalized samples maintaining the $sp^2$ system unmodified. When the defect sites are located into the basal plane

nitrogen can be introduced into the graphene lattice forming three main bonding configurations: pyridinic N, pyrrolic N and quaternary N (or graphitic N).

Nitrogen creates polarization in the network due to the larger electronegativity relative to carbon. The semiconducting properties of N-doped graphene are strongly dependent on the nitrogen bonding type into the lattice. In graphitic N the nitrogen interactions through three $sp^3$ orbitals, one of the lone pair electrons contribute to a $p$-bond formation and the other is involved in the $p^*$-state. The final effect is an $n$-type doping by the contribution of electrons to the conjugated $\pi$-system. In contrast, pyridinic and pyrrolic N atoms induce $p$-doping effects by withdrawing electrons from the graphene sheet.

## 1.2. Carbon nanotubes. General aspects.

The first observation of carbon-based tubular structures was reported back in the 1950s. Nevertheless, the "official" discovery of CNTs has been attributed to Iijima, who in 1991, after analyzing the cathodic soot recovered from arc-evaporation experiments reported the presence of ''a new type of finite carbon structure consisting of needle-like tubes''.[4, 6]

A single walled carbon nanotube (SWCNT) can be visualized as a rolled-up sheet of graphene forming a seamless cylinder. Assuming that the $sp^2$ system of the graphene layer does not suffer significant modifications after rolling-up, a theoretical SWCNT should be considered as a perfectly crystalline structure (defect free). Now, if the formation of concentrically rolled-up tubular structures comes from double, triple or few layers graphene a multiwalled carbon nanotube (MWCNT) is obtained. Both, single walled and multiwalled CNTs are considered as the main 1D carbon based structures, having particular and exceptional chemical, mechanical and electrical properties.[6]

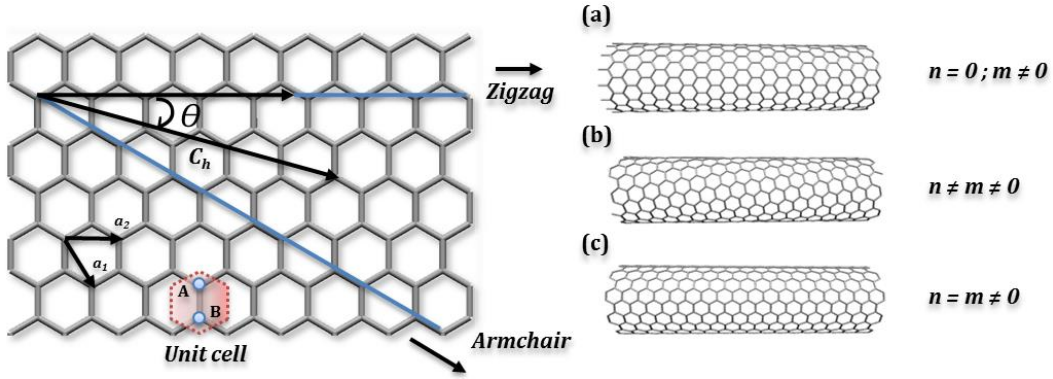


**Figure 1.3.** A 2D graphene sheet (left) showing the chiral vector $C_h$, chiral angle ($\theta$), and possible rolling directions, which origins (a) zigzag, (b) chiral and (c) armchair nanotubes (right).

SWCNTs have diameter typically between 0.4 nm and 2 nm and their electrical character can be metallic or semiconducting, depending on their chirality, which is defined by the way in which the graphene sheet is wrapped. **Figure 1.3** shows a schematic representation of the formation of the different types of SWCNTs. The chiral vector ($\boldsymbol{C_h}$) connects two crystallographically equivalent sites of the layer, and forms an angle ($\theta$) with the zigzag direction. The chiral vector is defined by two integers n and m, which represent the number of unit vectors ($\boldsymbol{a}$ and $\boldsymbol{b}$) along two directions in the honeycomb crystal lattice of graphene. Therefore, the vector $\boldsymbol{C_h}$ can be expressed as:

$$C_h = na_1 + ma_2$$

There are two highly symmetric structures, namely zig zag (n = 0; m ≠ 0) and armchair nanotubes (n = m ≠ 0). The intermediate structures, formed when $0<\theta<30$ are called chiral nanotubes. The electronic properties of CNTs are governed by its symmetry and therefore depend on the n, m values. Armchair nanotubes have metallic character; on the other hand when $n-m=3q$, with $q\neq0$, nanotubes behave like semiconductors with a small gap. Finally, all the other possible structures should be semiconductors with a band gap inversely dependent on the nanotube diameter. In conventional synthetic processes for SWCNTs, metallic nanotubes account for the 33 % of the sample, the remaining being semiconducting.[57, 58] Ideal nanotubes are ballistic conductors due

to the 1D confinement of electrons. However, the conductive character is highly influenced by the presence of structural defects or impurities.[59, 60]

MWCNTs have diameters in the 5-100 nm range and interlayer distances of approximately 0.34 nm. Both the layers separation and the ABAB… stacking being strongly dependent on the symmetry of the tubes.[6] There is a 1/3-2/3 ratio between the metallic and semiconducting SWCNTs; thus, it could be expected at least one of the walls in MWCNTs having the former character. Due to the weak interactions between the concentric nanotubes the electronic properties of an ideal MWCNT would be similar to those of perfect SWCNTs. When defects are introduced, five and seven membered rings could be present in nanotubes, which confer positive and negative curvatures to the structure respectively.

Physical properties of CNTs have been widely studied. Theoretical calculations predict high thermal conductivities (ca. 6600 W $m^{-1}.K^{-1}$) for an isolated specimen[61] as well as low thermal expansion coefficients for defect-free nanotubes.[62] Despite that the study of individual nanotubes and the determination of the experimental values is challenging, measurements have been carried out for isolated MWCNTs, obtaining values greater than 3000 W $m^{-1}.K^{-1}$. The thermoelectrical properties of CNTs are directly dependent on the temperature.[63] CNTs are physically stable and flexible, having a Young's modulus of around 1 TPa[64] and tensile strengths up to 150 GPa.[65] With respect to the optical properties, carbon-based $sp^2$ materials are able to absorbe light in a wide range of wavelengths due to the presence of the $\pi$ cloud. Furthermore, the metallic character of pure graphite confers reflective properties. Nanotubes are a low carrier density system. Since for visible light the free carrier density is inversely proportional to the penetration depth, the latter property is rather large for CNTs and very thin layers of the material can be transparent. SWCNTs present a chirality dependent fluorescence.[66]

### 1.2.1. Synthesis and purification of carbon nanotubes.

Synthesis of CNTs is usually carried out following two approaches: “grow-then–place” and “grow-in-place” techniques. The first involves the preparation of substrate-free CNTs and include arc discharge and laser ablation. Both approaches are based on energy transfer between graphite and an external radiation source. Synthesis of SWCNTs by arc discharge employs a catalyst (e.g. Fe, Ni or Co) deposited on one of two carbon-based electrodes located into a chamber filled with an inert gas (usually He or Ar). Finally, the system is subsequently heated by applying an electric current. In the case of laser ablation a pellet, containing both the carbon source and the catalyst, is heated by a laser source, vaporizing the sample (pulsed laser vaporization, PLV), which is condensed into a water–cooled copper collector. The quality, size and type of the resulting structures are directly related to the temperature and the laser operation conditions.[57, 67, 68]

Grow-in-place procedures employ thin films of catalyst for the preparation of the sample through CVD techniques. Tuning the parameters of growth of CNTs in CVD processes, namely atmosphere, carbon source, catalyst and temperature leads to the synthesis of nanotubes with different characteristics. Transition metals such as Fe, Ni or Co, either as single crystals or nanoparticles are usually employed as catalyst. Its interaction with a carbon source (small molecules, e.g. $CH_4$ or $C_2H_4$) which decomposes by applying an energy source produces the growth of both MWCNTs and SWCNTs. Liquid hydrocarbons like benzene, ethanol, etc. and solid hydrocarbons like naphthalene and camphor are used as CNT precursors in CVD. Organometallic compounds like metallocenes and nickel phtalocyanine have been used as carbon cum-catalyst sources. Among these, ferrocene is the most commonly reported.[69] The decomposition of the carbon source can be carried out by inductive heating (thermal CVD) or plasma treatment (PECVD). When selective growth of SWCNTs with a controlled diameter is desired, the high pressure CO disproportionation process

(HiPCO) is usually considered.[70] Generally, control over diameter, shell number, and growth rate of CNTs is efficiently obtained by CVD processes. Table 1.1 summarizes the operating conditions, advantages and drawbacks of the most important synthetic techniques for the production of CNTs.

Many approaches have been developed for the synthesis of both MWCNTs and SWCNTs; nevertheless none of them is able to produce pure CNTs. In case of CVD techniques, aromatic and amorphous carbons, or graphitic polyhedral carbons with enclosed metal particles as well as free metal nanoparticles are observed after synthesis. Meanwhile, for arc-discharge and laser ablation, the main by-side products include fullerenes, amorphous carbon and graphite particles. The amount of impurities typically increases with the decrease of the diameter of CNTs.[71] The properties of the resulting material are affected by the presence of impurities. Therefore, the development of efficient purification techniques has been of a wide interest.[72] The methodology employed for the elimination of by-side products depends on their chemical nature. In the case of amorphous carbonaceous impurities and fullerenes, the oxidation and washing with specific solvents can be employed. On the other hand, free

**Table 1.1.** Operational details and characteristics of the most usually employed CNTs synthetic procedures.

| Method | Operating conditions | Advantages | Disadvantages |
|---|---|---|---|
| Arc discharge [71] | 2000-6000 °C; DC 150 $A.cm^{-2}$ | Production of highly crystalline structures (SWCNTs, DWCNTs and MWCNTs). | Separation from secondary products is necessary. Low quality and purity. |
| Laser ablation [73] | Laser pulses 5-500 ns. RT to 1200 °C | High quality and controlled size SWCNTs. MWCNTs (1.5-3.5 nm diameter, 300 nm length). | Costly. Not amenable for scale-up. |
| Thermal CVD | 500-1200 °C | Control of nanotube position. Lower temperatures when compares with other tech. | Risk of damaging during synthesis. |
| PECVD [74] | 100-800 °C | Lower T than thermal CVD. | Defective sample. |
| HiPCO [75] | 30-50 atm. 900-1100 °C | Large scale production. High yield and controlled diameter of SWCNTs. | Metal-based impurities. |

metal particles can be dissolved by using acidic solutions. When metallic nanoparticles are contained inside graphitic shells, these must first be released for subsequent elimination. Since graphitic particles are highly resistant to oxidation treatments, more aggressive approaches are considered. At the same time, the purification technique might be carefully chosen to avoid damage of the structure of the nanotubes. Chemical and physical approaches have been explored for CNTs purification:

***Purification of carbon nanotubes by chemical oxidation.***

As mentioned, chemical methods are based on the difference in the stability of carbonaceous species against the treatment with an oxidant agent. Both the presence of a larger amount of functionalities in amorphous carbon and the curved shape of carbon nanoparticles (containing 5-atomic rings) make those species more sensitive to oxidation. This way, a "selective" reaction occurs in where carbon-based impurities are more preferentially oxidized than CNTs. CNTs are highly stable in presence of chemical agents, but its structure and especially the tips, which are more reactive, can be affected by oxidant treatments. After initial oxidation treatment, acid washing is usually required to remove the non-exposed metal catalyst particles. It is also possible to employ strong oxidizing acid, such as nitric acid, to simultaneously oxidize both the carbon and the metal impurities. Nevertheless the use of such aggressive treatment leads to the functionalization of the CNT structure and to an extensive disruption of the $sp^2$ conjugated system. CNTs can be purified by gas phase oxidant treatments at high temperature (200-800 ˚C) in presence of oxidant agents such air,[76] a mixture of $Cl_2$, $H_2O$ and HCl,[77] steam,[78] or $O_2$ mixed with other reactants in different ratios.[79-81] Additionally, these techniques are useful to open the caps of the nanotubes without introducing a large amount of sidewall defects. Gas phase treatments are a good choice for samples which contain no metal catalyst or as a first step to remove the graphitic particles that sheath the metal catalyst.[72]

Steam treatment of CNTs has been reported as a versatile technique for the purification of both single and multiwalled CNTs.[78, 82] As a mild oxidant, steam is able to remove the carbonaceous material, including graphitic shells that coat the metal nanoparticles without affecting the tubular structure of CNTs. The exposed metal nanoparticles can be easily removed by subsequent acid treatment. Steam reacts with the closed tips, which are the most reactive fraction of the nanotube, maintaining the integrity of the walls. In this manner, this technique allows the simultaneous purification and opening of the ends. Additionally, the length of the nanotubes can be reduced by controlling the time of the steam treatment. Both, opening and shortening of CNTs, are important for further applications in a variety of fields including biomedicine,[83, 84] and sensing.[83]

Liquid phase oxidation techniques offer different alternatives to remove both, catalyst and carbonaceous material. $H_2O_2$, as a mild, inexpensive and green oxidant is able to eliminate amorphous carbon with a low consumption of CNTs. Nevertheless, in order to remove the metal particles an additional acid treatment is required.[85, 86] Microwave-assisted treatments can produce the efficient dissolution of metals maintaining the structural integrity of the tubes with short time treatments.[87] Methods employing mixtures of acids such as $HNO_3$ and $H_2SO_4$,[88] and $KMnO_4$ enhance the elimination of side-products, taking advantage of the oxidant character of the $MnO_4^-$ ion;[89] nevertheless, the removal of the $MnO_2$ generated during the oxidation requires additional purification steps. $HNO_3$ can efficiently remove amorphous carbon and due to its low cost and oxidizing character is the most widely used agent for purification of CNTs. The conditions of reaction should be carefully chosen, because strong treatments lead to the formation of carbonaceous impurities and oxidation debris. As mentioned, liquid phase treatments with strong oxidants usually produce modifications in the surface of CNTs. The introduction of aliphatic functionalities by oxidant agents increases the chemical activity and dispersability of CNTs in water and polar solvents.

These variations could in fact be desired to extend the application of this material in areas requiring the modification of the structural or electrical properties.

***Physical purification of carbon nanotubes.***

Physical methods are based on the differences in physical size, aspect ratio, gravity, magnetic properties or solubility between the impurities and CNTs. The most commonly employed techniques include microfiltration, chromatography, electrophoresis, centrifugation and high temperature annealing or laser treatments. These procedures do not involve chemical interaction with the sample and therefore the risk of CNTs damaging the CNT structure is very low. The major drawback is that they are time–consuming and less effective than chemical approaches. Separation by filtration takes advantage of both, the difference in size and dispersability to remove the undesired species. By employing specific organic solvents, fullerenes and polyaromatic carbons can be separated from the sample. A major problem of the technique is that the pores of the filtration system can be blocked by large species. However, the efficiency of the process can be enhanced by preparing stable CNT suspensions with surfactants or by increasing the pressure of the system.[90, 91] Chromatographic techniques are useful for collecting CNTs with a given range of length which are required for some applications.

The presence of metal particles employed for the growth of CNTs (catalysts) is in general not desired. The elimination of metal nanoparticles that are encapsulated into graphitic shells is difficult. Therefore it is necessary to remove first the graphitic particles. Free metal nanoparticles can be removed by annealing the sample at very high temperature (typically above 1500 ˚C) under non-oxidant atmospheres.[92, 93] The temperature of evaporation of metals is usually below that of damaging the CNTs. In fact, annealing treatments can enhance the mechanical properties of CNTs by removing structural defects along their walls and tips.[94] Purified samples free of

catalyst and carbonaceous impurities are in general obtained by combination of chemical and physical techniques.

### 1.2.2. Modification of carbon nanotubes.

As in the case of graphene, modification of the CNT structure is usually necessary for practical applications. CNTs and in particular SWCNTs, tend to form bundles and ropes due to Van der Waals interactions. Their dispersability in aqueous/polar solvents is very poor making difficult the processability of the material. To overcome these limitations and also to increase their reactivity, chemical modification arises as an interesting approach that provides value in a wide range of areas, from the preparation of hybrids to the production of sensors.[6] CNTs can be modified by following four different approaches which involve covalent and non-covalent functionalization, endohedral filling and external decoration with inorganic materials.

#### 1.2.2.1. Functionalization of carbon nanotubes.

***Non-covalent functionalization.***

CNTs can interact with a large variety of compounds able to form $\pi$-$\pi$ interactions. The most commonly used protocols to attach the chosen molecules include agitation provided by magnetic stirring and ultrasonication, followed by addition of reactives with chemical affinity such as N-methylpyrrolidone or phenylethylalcohol, able to interact by Van der Waals forces with CNTs.[95]

The adsorption of surfactants onto the nanotubes sidewalls improves the dispersability in water. These species are relatively cheap, commercially available and prevent the CNTs aggregation. The simultaneous presence of a hydrophobic tail and a hydrophilic head makes surfactants acting like a bridge between nanotubes walls and the aqueous bulk solvent (**Figure 1.4 (a)**), which induces the formation of stable suspensions.[96-

98] Polymers **(b)** and biomolecules can also enhance CNTs dispersion in water by its reversible anchoring to the sidewalls; the interaction with molecules containing aromatic moieties being more strongly favored **(c)**. The main advantage of non-covalent functionalization is that the integrity of the material is preserved.[99]

***Covalent functionalization.***

Covalent functionalization is based on covalent linkage of functional entities onto the nanotube's carbon scaffold at the termini of the tubes or at their sidewalls. It can be carried out through two different approaches: sidewall and defect group functionalization. The first one is associated with a change in hybridization from $sp^2$ to $sp^3$ and therefore a loss of conjugation. A wide amount of synthetic routes following this methodology has been reported in the literature [100] and include halogenation,[101, 102] cycloaddition[103, 104] and radical-based reactions,[105] among many other strategies. Acid treatments (employing $HNO_3$ and $H_2SO_4$) are specially employed since they simultaneously produce the attachment of O-based functionalities to the sidewalls and cutting of the nanotubes.[100] As already mentioned, short CNTs are desired for some specific applications. Defect group functionalization takes advantage of the structural defects of CNTs such as pentagon and heptagon irregularities in the hexago-

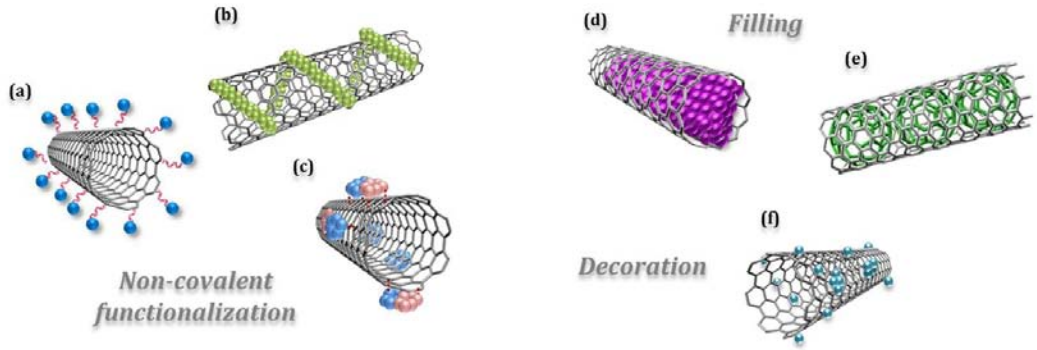


**Figure 1.4.** Representation of non–covalent interactions of CNTs with (a) surfactant species, (b) polymers and (c) aromatic moieties. Some possible strategies for covalent functionalization; [100] (d) Filled SWCNTs, (e) $C_{60}$@SWCNT ("Nanopeapod") and (f) external decoration of CNTs.

nal lattice as well as oxidized areas in the tubular structure (mainly located at the tips).[106] When defects are not intrinsically present in the sample, these are generally produced through liquid-phase, gas-phase or electrochemical oxidation methods. The generation of O-bearing functionalities (mainly carboxylic groups) serves as starting point for further derivatization. Despite covalent functionalization induces disruption of the conjugated system, the creation of chemically stable bonds is desired for some applications and opens up the possibility to modulate the physicochemical properties of the CNTs. It can also render the CNTs more reactive against particular species.[107]

#### 1.2.2.2. Endohedral functionalization: Encapsulation of materials inside CNTs.

The characteristic cylindrical structure of CNTs gives versatility to these materials for diverse functionalization approaches. Endohedral functionalization involves the encapsulation of foreign materials into the hollow cavities of CNTs and can be carried out either during the synthesis of the nanotubes themselves (*in situ*)[108] or in a post-synthesis process through the open tips (*ex situ* methods). The confinement of specific compounds into the empty area can alter the properties of CNTs and can be a useful approach to isolate functional molecules from external environments. Besides, the confinement into a small area might alter the chemical properties of the guest molecules, leading to the formation of new crystalline structures.[109] The filling of CNTs has been reported as a potential approach for applications in gas storage,[110, 111] electrochemical energy storage,[112] battery electrodes,[113] catalysis[114] or biomedicine.[84] Since the electrical properties of CNTs can be modified by the presence of a guest into the hollow cavities, their potential utility in nanoelectronic devices has been recently explored.[115]

Liquid and vapor-phase methods have been reported to encapsulate materials within CNTs; the strategy of synthesis depends on the physicochemical properties and stability of the filler.[116] Liquid phase filling can be carried out either by immersing the

nanotubes into a solution containing the selected filler or by annealing the mixture at temperatures above the melting point (molten phase capillary wetting method) of the chosen material. The latter has being widely employed.[117, 118] The exposure of SWCNTs and MWCNTs to a metallic vapor leads to the formation of metal nanowires [119]and nanoparticles[120] within the cavities of the CNTs (vapor-phase filling). This approach not only produces filled CNT, but also CNTs coated with the vaporized compound/element can be obtained.

The simultaneous growth and encapsulation of inorganic materials within CNTs (*in situ* filling) has been proposed as an alternative for the synthesis of filled CNTs. For this purpose arc discharge methods in solution employing layered graphene sheets have been reported.[121, 122]

An important factor for achieving a high filling yield is the presence of open ended nanotubes. Therefore, before the encapsulation processes the oxidation of the capped tips of CNTs is carried out, which can be accomplished by some of the methods previously detailed. The morphology, chemical and structural properties of the guests can be notably modified when introduced into the hollow cavity. Different morphologies have been reported after endohedral functionalization of CNTs. Not only 1D nanowires of a high amount of inorganic compounds with diverse crystallization patterns results from the confinement within the CNTs,[123-126] but also the preparation of metallic nanoparticles,[127] inorganic nanoribbons,[128] and recently single-layered inorganic nanotubes (SLINTs)[129] encapsulated within CNTs have been reported. The wide range of diameters in CNTs (which depends on the number of walls and method of synthesis) not only allows the encapsulation of inorganic compounds, but also a wide range of organic compounds, such as metallocenes,[130], β-carotene[131] small proteins and biomolecules,[132] as well as graphene derivatives[133] and fullerenes.[134]

Fullerenes, also called buckyballs, are composed entirely of carbon arranged in hexagonal and pentagonal rings (resembling the classic soccer balls), forming of a hollow sphere.[57] The most common $C_{60}$ molecule consists of an icosahedral structure of carbon atoms with $sp^2$ bonding each carbon (joined to three neighbours). Fullerenes can be obtained as a secondary product during the PLV synthesis of CNTs. Usually the purification processes applied for the elimination of amorphous carbon and graphitic particles also removes fullerenes. However $C_{60}$ has been found inside SWCNTs in the form of self-assembled chains[135] even after purification. Filling of SWCNTs with fullerenes has been widely explored. Smith, Monthioux and Luzzi reported first studies of fullerenes contained into the cavities of CNTs, generally called "*nanopeapods*", and how the incidence of energy produces the coalescence of the $C_{60}$ molecules leading to the formation of new inner nanostructures.[136] The distance between two $C_{60}$ encapsulated into a SWCNT is shorter than that encountered in the $C_{60}$ crystals, which favors their coalescence. This can be induced by thermal annealing or UV radiation resulting in pill-shaped, concentric, endohedral capsules.[137] If the proper amount of energy is applied to a $C_{60}$@SWCNT a double walled carbon nanotube (DWCNT) can be formed, becoming a new alternative for the selective formation of these structures.[138] In this case SWCNTs behaves like a "template" for the growth of a new nanomaterial.

#### 1.2.2.3. External decoration with inorganic materials.

The external decoration of the sidewalls of CNTs with inorganic materials, in particular metal-based and semiconductor nanoparticles (NPs), has emerged as a useful approach for the preparation of carbon nanotube-inorganic hybrids with enhanced properties combining the characteristics of both nanostructures.[139] Decorated CNTs can be obtained by either *in situ* processes or through an *ex-situ* modification. In the first approach CNTs play two simultaneous roles, acting as templates but also contributing to the formation of the NPs. The main drawback of this approach is the weak bonding

between the CNTs walls and the decorating material, as well as the low control of the morphology of the NPs. *In situ* decoration of CNTs has been carried out through electrochemical methods, which not only deposit NPs on the external walls but also introduce them into the hollow cavity of CNTs, solution,[121] sol-gel, hydrothermal and high temperature treatments through the decomposition of diverse precursors.[140-142] In the *ex-situ* preparation of nanotube-inorganic hybrids, the process requires the previous synthesis of the NPs and the subsequent decoration on the CNTs sidewalls. Despite that the latter approach involves a more complex process; it allows a better control of the size and shape of the NPs as well as the formation of stronger bonds/interactions with the CNTs. Generally, as synthesized NPs are coated with organic shells, which not only prevent the agglomeration of the NPs, but also might enhance the interaction with the CNTs surface. NPs can be attached to the CNTs through covalent or non-covalent functionalization and a wide amount of species have been linked to the sidewalls of the tubular structures.[143, 144]

Graphene and CNTs-based materials have a wide interest in materials science due to their outstanding properties. The modulating of their properties through the diverse approaches of modification enhances their potential applications in many fields. In this thesis the modification of the structure of graphitic materials is the main purpose. Solid-gas and solid-liquid reactions as well as systematic studies of the conditions of treatment and stability of the materials are required. Otherwise the use of CNTs as template could be an interesting approach for the preparation of different hybrid nanostructures, namely 1D inorganic nanotubes, nanorods and nanoparticles contained inside the host cavities or attached to the external surface of the nanotubes.

The main objectives of this thesis are recorded below.

## 1.3. General objectives.

- To develop a simple, efficient and reproducible method of synthesis of nitrogen-doped reduced graphene oxide.

- To accomplish a proper assessment of the characteristics of the synthesized materials to obtain the unambiguous structural determination of the species introduced within the GO lattice and to evaluate the physical and chemical properties.

- To develop an efficient method of synthesis of single-layered inorganic nanotubes employing MWCNTs as directing agents for the growing of the inner 1D nanostructures.

- To analyze the effects of the variation in the conditions of synthesis in the final content and nature of the encapsulated 1D nanostructures.

- To synthesize MWCNTs decorated with titanium-based nanoparticles and $TiO_2$ nanostructures.

- To explore the potential applications of the synthesized titanium-based materials in the degradation of organic compounds under UV- energy.

# Chapter 2.

# Experimental Methods.

This chapter describes the synthetic procedures and chemicals employed in the preparation of the materials which are the subject of study of this thesis. It also details the equipments used for the characterization of the samples along with the experimental conditions of the measurements and when required, the sample preparation.

# 2.1. Synthetic procedures.

## 2.1.1. Graphene-based materials.

Graphene-based materials have been prepared starting from graphite powder (<20 μm, Sigma-Aldrich) and graphite flakes (<150 μm, Sigma-Aldrich). In order to obtain a reactive precursor for the ammonolysis reactions, namely graphene oxide (GO), both powder and flakes were chemically oxidized by a modified Hummer´s method.[29] This procedure requires treatment with concentrated $H_2SO_4$ (98 %, Panreac) and $NaNO_3$ (≥99 %, Sigma-Aldrich), followed by the addition of $KMnO_4$ (99 %, Panreac) and $H_2O_2$ solutions (35 %, Acros Organics) under controlled conditions of temperature.

Nitrogen-modified materials were synthesized by annealing GO in the presence of pure $NH_3$ gas (Carburos Metálicos, 99.99 %). Additionally Ar (Carburos Metálicos, 99.99 %), $N_2$ (Carburos Metálicos, 99.99 %)) and a mixture of argon/hydrogen ($Ar/H_2$, Carburos Metálicos, 99.99 %) were employed for the reduction of graphene derivatives.

## 2.1.2. Ammonolysis and high temperature treatments under inert atmospheres.

Nitrogen-containing samples have been prepared by reactions at temperatures between 25 °C and 800 °C, variable times (10-300 min) and flow rates (100-600 $mL.min^{-1}$). Flowmeters were calibrated in normal conditions. In all cases, when one parameter was modified, the others were kept constant. **Figure 2.1 (a)** shows the employed ammonolysis system. Due to the high toxicity and reactivity of ammonia, the system must be rigorously checked for possible leaking. $NH_3$ begins to dissociate appreciably into $N_2$ and $H_2$ at temperatures higher than 500 ˚C. However the dissociation of $NH_3$ is slow and the proportion of $NH_3$, $N_2$ and $H_2$ can be controlled by the

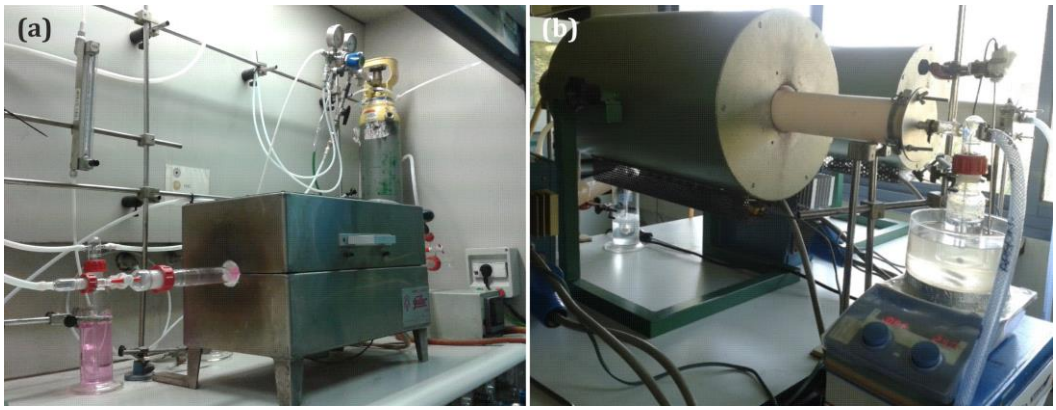


**Figure 2.1.** (a) Ammonolysis system employed for the preparation of nitrogen-modified materials. (b) Purification system employed for the elimination of amorphous carbon and graphitic particles from CNT samples.

flow rate.[145] High flow rates decrease significantly the $NH_3$ dissociation and should be used at high temperatures.

The GO samples treated in $NH_3$ were subsequently annealed at temperatures between 500 °C and 1050 °C under different atmospheres (Ar, $N_2$, and Ar/$H_2$). All reactions were carried out in tubular furnaces, which were previously purged with the corresponding gas at a flowing rate of 150 mL.min$^{-1}$, in order to eliminate the oxygen present in the system. Samples were previously dried, ground in an agate mortar and pestle, and spread into a sintered alumina boat ($Al_2O_3$, 99.7 %, ALSINT, Keratec).

### 2.1.3. Purification of multiwalled carbon nanotubes.

MWCNTs used for the synthesis of inorganic-modified nanostructures were grown by chemical vapor deposition and have been provided as a dry powder by Thomas Swan & Co. Ltd. Elicarb®. In order to remove the unwanted carbonaceous material and the remaining catalyst present in the sample, MWCNTs were previously treated during 2-5 h under steam, generated by constant heating of water. A continuous 190 mL.min$^{-1}$ Ar flow was employed to have an oxygen free system (**Figure 2.1 (b)**). The sample was

subsequently treated at 110 °C during 6 h with a 6 M acid solution prepared by diluting HCl (37 %, Panreac) in distilled water and collected by filtration over polycarbonate membranes (0.2 μm, Whatman).[146] The sample was washed with water until the pH of the filtrate was neutral and dried overnight at 60 °C.

## 2.1.4. Synthesis of carbon nanotubes-inorganic nanostructures.

### 2.1.4.1. Filling and decoration of multiwalled carbon nanotubes.

Previously purified MWCNTs have been employed for the preparation of hybrid materials with selected inorganic compounds. Samples were synthesized by high temperature solid-state reactions of CNTs with fullerenes ($C_{60}$, 99.5 %, SES research), $PbI_2$ (99.99 %, Stream Chemicals), $ZnI_2$ (99.99 %, Sigma-Aldrich), $CeI_3$ (99.99 %, Sigma-Aldrich), $CeCl_3$ (≥99.99 %, Sigma-Aldrich) and $TiCl_2$ (99.98 %, Sigma-Aldrich). As the inorganic halides employed for filling the nanotubes are highly reactive to air, handling of samples was performed under an argon-filled glove box (Labconco 50700). MWCNTs and the chosen inorganic salt were ground together with an agate mortar and pestle until the mixture showed a uniform color. The powder was then transferred into an ampoule of amorphous silica (Ø=10 mm), evacuated during 30 min and sealed under vacuum ($10^{-5}$ mbar). Afterwards, the system was placed into a furnace where it dwelled (6-48 h) at temperatures ranged between 400 °C and 1060 °C. The temperatures of treatment have been selected considering both the melting points and the decomposition temperatures of the inorganic salts.[129] In case of filling with fullerenes the treatment temperature was chosen taking into account the sublimation point of the material.[147, 148] The heating/cooling rates were also modified depending on the material, in order to obtain different crystalline structures. After the treatment was completed the resulting samples were kept in a glove box. Due to the extreme sensitivity of $TiCl_2$ in air, the silica ampoules were previously annealed at 800 °C to eliminate the presence of hydroxyl groups. Furthermore, a metallic titanium foil

(0.25 mm thickness, ca. 5 $cm^2$ area) was used to capture the excess of oxygen remaining into the silica tube.

In order to modify the oxidation state of titanium in the nanoparticles the decorated MWCNTs were subsequently annealed. For this purpose the samples were spread into sintered $Al_2O_3$ boats inside an alumina furnace tube and were treated in an oxidizing atmosphere ($O_2$, flowing at 165 $mL.min^{-1}$. Temperatures between 200 °C and 450 °C were employed for the treatment.

### 2.1.5. Washing and removal of the inorganic material after synthesis.

In order to remove the inorganic material after the annealing treatments, the samples were dispersed in different solvents by sonication, and were subsequently heated during 16-24 h. After washing, the samples were recovered by filtration under vacuum, rinsed and dried overnight at 60 °C.

### 2.1.6. Photochemical activity of titanium oxide-multiwalled carbon nanotube derivatives.

The catalytic activity of the titanium oxide-multiwalled carbon nanotube derivatives was evaluated by measuring the degradation of methyl orange (MO, 85 %, Sigma Aldrich) at room temperature. For this purpose, aqueous solutions of the organic compound (MO) were prepared in concentrations ranged between 0.5 $mg.mL^{-1}$ and 1 $mg.mL^{-1}$. Afterwards the synthesized materials were added to the solutions (0.5-1 $mg.mL^{-1}$) and the mixtures were kept in a dark box and magnetically stirred overnight to allow the adsorption-desorption equilibrium to be reached. Subsequently, the solutions were irradiated with UV light provided by a 30 W Vilbert Lourmat lamp (7 $mW.cm^{-2}$) with a light filter to cut off the light at 365 nm The lamp was located at ca. 25 cm from the sample, until the complete disappearance of the color was observed.

The evolution of the reaction was followed using UV-Vis spectroscopy, by measuring the concentration of the dye at different time points. The first aliquot was taken out at the end of the dark adsorption period (just before the UV light was turned on), in order to determine the MO concentration in solution, which was hereafter considered as the initial concentration ($C_0$). Aliquots (5 mL) were then collected regularly from the reactor and immediately centrifuged to separate any suspended solid. The clean transparent solution was analyzed.

## 2.2. Characterization techniques.

### 2.2.1. Electron microscopy.

The morphology of graphene-based materials and inorganic modified MWCNTs has been studied by transmission electron microscopy (TEM), high resolution transmission electron microscopy (HRTEM), high-angle annular dark field (HAADF) imaging, high resolution scanning transmission electron microscopy (STEM) and scanning electron microscopy (SEM). Additionally, atomic force microscopic (AFM) measurements and selected area electron diffraction (SAED) patterns have been carried out to determine the number of layers present in the graphene samples.

TEM Images and SAED Patterns were obtained using a JEOL 1210 Microscope, operating at 120 kV. HRTEM, HAADF and STEM were carried out in a FEI, TECNAI G2 F20 Microscope operated at 200 kV. AFM images were recorded using an INOVA Bruker in tapping mode and SEM imaging was acquired using a Quanta FEI 200 ESEM FEG microscope, operating at 10.0 kV.

*Preparation of the samples:* Samples for TEM, HRTEM, SEM, HAADF and STEM analyses were prepared dispersing by sonication a small amount of the powder in anhydrous hexane (95 %, Sigma-Aldrich,). Afterwards, the solution was placed dropwise onto a

lacey carbon support grid and let to dry. In some cases, due to the hydrophilicity of some of the samples, absolute ethanol (max 0.02%, water Panreac) was employed as solvent. In case of AFM studies, graphene samples were sonicated in a 1:1 ethanol:water mixture, followed by centrifugation at 5000 rpm. A highly diluted dispersion was obtained, which was subsequently dropcasted on a cleaned Silicon substrate.

### 2.2.2. Elemental analysis.

Elemental analyses (EA) were employed for the determination of carbon, nitrogen, hydrogen and sulfur contents in the N-containing materials prepared by ammonolysis treatments. The data were recorded by the combustion of ca. 1 mg of sample placed on a Thermo Scientific™ FLASH 2000 Series CHNS Analyzer using a Metler Toledo MX5 microbalance.

### 2.2.3. Thermogravimetric analysis.

Thermogravimetric analyses (TGA) were performed on a Netzsch STA 449 F1 Jupiter® instrument. An alumina crucible, containing the sample (1-5 mg), was placed into a microbalance at room temperature and the treated under flowing synthetic air or oxygen up to temperatures of 800-1400 ˚C using a heating rate of 10 °C.min$^{-1}$, until the total combustion of the sample. The variation in the weight of the sample was registered in function of the temperature. The final temperature of the heating program was selected depending on the analyzed sample. In some cases the program was stopped before the total combustion of the sample in order to analyze the intermediate species produced during the oxidation.

### 2.2.4. X-Ray Diffraction.

X-ray diffraction (XRD) was carried out in order to identify the phase composition of the nanoparticles grown on the external walls of the nanotubes, as well as to study the evolution of these nanostructures after subsequent thermal treatments.

Diffraction patterns were obtained in a Rigaku Rotaflex RU-200B diffractometer (Kα Cu, λ=1.5418 Å). *2θ* values were acquired at 0.02 ˚ intervals between 5 ˚ and 90 ˚. XRD of air sensitive samples was recorded by protecting the sample with a Kapton® film.

### 2.2.5. Contact angle measurements.

Surface wettability measurements of the graphene-based samples were carried out in a DSA100 Contact Angle Measuring System (Krüss) by the sessile drop method. Contact angle measurements (CA) were recorded after dropping 5 μL of water directly into a compact and dried film of the sample. This film was prepared by sonication of 5 mg of sample in 5 mL of water; subsequently the dispersion was deposited by vacuum filtration onto a 0.2 μm polycarbonate membrane. After drying, the membrane containing the solid sample was glued to a glass slide with double-sided tape. Measurements were carried out in at least three different areas of the film, and the final average value was provided.

### 2.2.6. Fourier transform-infrared spectroscopy.

Fourier transform infrared spectroscopy (FT-IR) spectra were recorded in transmission mode on a Perkin-Elmer Spectrum One in the rage of energies of 450 to 4000 $cm^{-1}$. The samples were prepared by dropping a dispersion of the material in 2-propanol dispersions (ca. 10 $mg.mL^{-1}$) onto a preheated ZnSe disks (2 mm thickness, 70 °C).[78]

### 2.2.7. Ultraviolet-visible spectroscopy.

For ultraviolet-visible (UV-Vis) spectroscopic measurements a Varian Cary 5 spectrophotometer with an operational range of 200 nm was employed. Samples were prepared by sonication of 1 mg of powder in 5 mL of a 1:1 ethanol-water mixture. Afterwards, the dispersions were centrifuged at 4500 rpm during 15 min. Analyses were carried out in absorbance mode using 1 cm quartz cuvettes, and dispersions were analyzed before and after centrifugation.

In case of the evaluation of the titanium oxide-multiwalled carbon nanotube derivatives the spectrum for each sample was recorded in the 200-800 nm range. The absorbance was determined at the characteristic wavelength 660 nm for each degraded MO solution. The concentration of the dye in the solution was determined employing a calibration curve previously obtained from absorbance data recorded from MO solutions with known concentration.

### 2.2.8. X-ray photoelectron spectroscopy.

X-ray photoelectron spectroscopic (XPS) analyses were recorded in a Kratos AXIS ultra DLD spectrometer using monochromatic Al Kα. All samples were introduced in the preparation chamber as a powder placed onto the same substrate (Cu) to maintain the analysis conditions invariable. The general survey scans and high resolution spectra of C1s, O1s and N1s regions were registered.

### 2.2.9. Raman spectroscopy.

Raman spectra were recorded using a Horiba Jobin Yvon operating at 532 nm and using 100× objective. Acquisition time was set to 30 s and laser power to 0.5 mW. Spectra were recorded from different spots of the samples prepared by dropping 2-propanol dispersions onto preheated microscope slides.

# Results I.

# SYNTHESIS, CHARACTERIZATION AND THERMAL PROPERTIES OF N-CONTAINING REDUCED GRAPHENE OXIDE.

# Chapter 3.

# Tuning the nature of nitrogen atoms in N-containing reduced graphene oxide.

This chapter describes the synthesis and characterization of N-containing reduced graphene oxide. In order to prepare samples with different degree of functionalization and doping and tune the nature of the nitrogen atoms, a gas phase reaction of graphene oxide and ammonia was carried out under different experimental conditions.

# 3.1. Introduction.

Graphene, the main building block of all graphitic materials (which include carbon nanotubes and fullerenes), has recently attracted a great interest due its promising applications in important fields such as batteries, sensors, and biomedicine.[149] Its structure, a monolayer of $sp^2$ hybridized carbon atoms packed into a 2-D honeycomb lattice, confers it extraordinary physical, electrical and mechanical properties, including high electrical mobility, chemical and thermal stability and high surface area.[8, 150] Many approaches have been explored to tune these properties and further expand the range of applications. Chemical functionalization and doping are an efficient way to tailor the physical and chemical behavior of materials.[13, 151] In this context, N-doping is an interesting approach since allows *n-type* doping[55] and improves its performance in electrocatalysis,[152, 153] supercapacitors,[154] sensors[155] or as magnetic material.[156, 157] Different methods have been explored to introduce nitrogen either (i) during the synthesis of the graphene sheets (*in situ* approach) via CVD[158] and arc discharge,[159] or (ii) via a post synthesis modification. The majority of post synthesis doping strategies usually employ graphene oxide (GO) as starting material. GO has been doped in the presence of ammonia at high temperature,[160] by means of plasma treatment,[161] and under hydrothermal conditions with aqueous ammonia [162] and hydrazine.[163] The latest has been extensively employed for the preparation of reduced graphene oxide (RGO), however in terms of doping the hydrazine approach does not exceeds ca. 5 % of nitrogen. The amount of nitrogen and level of reduction achieved by each particular method determines the electrical and conducting properties of the resulting material,[55] depending not only on the chosen technique but also on the experimental conditions employed.

In the continuous race to achieve the highest possible amount of N-doping,[164] the nature of the resulting nitrogen atoms is sometimes overlooked. X-ray photoelectron spectroscopy (XPS) is the most widely employed technique to characterize the resulting

materials. Despite XPS provides information on the nitrogen environment it cannot unambiguously discern between N-bearing aliphatic functionalities and N-doping.[165] Therefore there is a growing tendency to assume that all nitrogen species are incorporated within the graphene lattice (doping). To obtain a proper assessment of the type of nitrogen present in the samples, a toolbox of characterization techniques is proposed. The characterization not only includes the most commonly employed techniques for the determination of functional groups (X-ray photoelectron spectroscopy (XPS), fourier transform infrared (FT-IR) and ultraviolet-visible (UV-Vis) spectroscopies), but also benefits from other methods that are not typically used for this purpose: Thermogravimetric analysis (TGA), contact angle (CA) measurements and the degree of dispersability.

Thermally stable graphene is of interest as a reinforcing material in components exposed at elevated temperatures and friction, and to prepare catalysts with applications in fuel cells. It has been reported that N-doping reduces the presence of easily oxidizable defects, which are unstable under fuel cell operation.[166, 167] We have investigated the effect of the presence of nitrogen within the structure of graphene-based samples in the thermal stability against oxidation by air. A thermodynamic approach has been employed to compare the combustion reaction of nitrogen in different coordination environments (pyridine, pyrrole and graphitic) with a graphene fragment (undoped).

## 3.2. Objectives.

- To synthesize N-containing RGO by gas phase treatments of GO with ammonia.

- To determine the influence of the treatment conditions in the final nitrogen content.

- To assess the species present in the modified GO lattice.

- To analyze the thermal behavior of the samples against its oxidation by air, as well as the influence of the presence of N-containing functionalities in the physical and chemical properties of the material.

- To determine the thermal stabilities of the specific N-bearing moieties present in the N-containing RGO.

# 3.3. Synthesis of N-containing reduced graphene oxide.

## 3.3.1. Synthesis and Characterization of graphene oxide.

GO was synthesized by a modified Hummer's method as starting material for the preparation of RGO and N-containing RGO. Both graphite powder and graphite flakes (<20 μm and <150 μm, respectively) were employed for the synthesis. 115 mL of concentrated $H_2SO_4$, 5 g of graphite and 2.5 g of $NaNO_3$ were mixed together, maintaining the temperature under 0 °C. Afterwards 15 g of $KMnO_4$ were added slowly (in order to keep the temperature below 20 °C) and the reaction mixture was warmed up to 35 °C and stirred for 30 min. After cooling down to room temperature, 230 mL of distilled water were added maintaining the reaction temperature at 98 °C for 2 h. Then additional water (1 L) and 5 mL of 30 % $H_2O_2$ solution were added to the mixture to solubilize the manganese salts. Finally, the brownish content was air cooled and purified washing with distilled water, followed by centrifugation until the pH of the solution was neutral. **Figure 3.1** shows a schematic representation of the employed procedure.

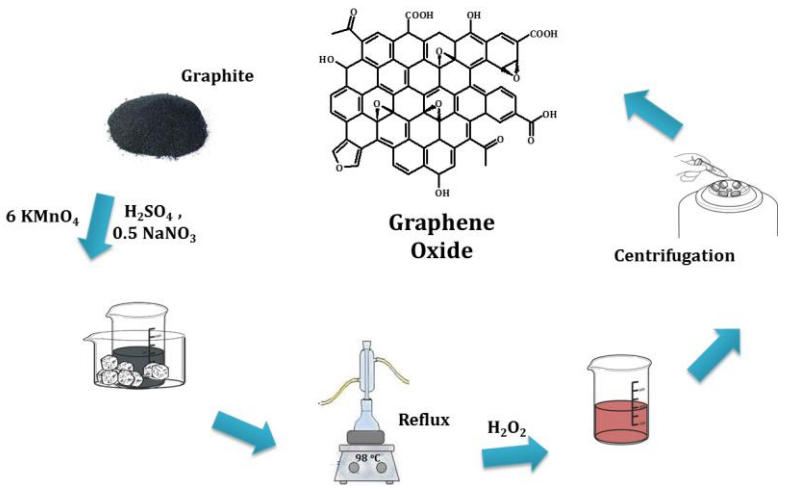


**Figure 3.1.** Synthetic procedure employed to prepare graphene oxide by chemical oxidation of graphite powder.

In order to determine the composition and morphology of the synthesized materials, the samples were characterized using TGA, TEM, SEM and XPS. **Figure 3.2** shows a comparison of TGA results of GO prepared from graphite powder (black line) and graphite flakes (red line).[1] Visual inspection of the TGA reveals an initial continuous weight before the first remarkable event at ca. 200 °C for both materials. This continuous weight loss can be attributed to absorbed atmospheric species, typically water, being already an indication of the hydrophilicity of the samples. As it has been previously reported[168] O-bearing functionalities (mainly carboxylic and lactone groups) starts decomposing at temperatures around 250 °C, which is also in agreement with the event at 220 °C (36 wt. % and 25 wt. % for graphitic powder and flakes respectively). This temperature was therefore selected for subsequent experiments un-

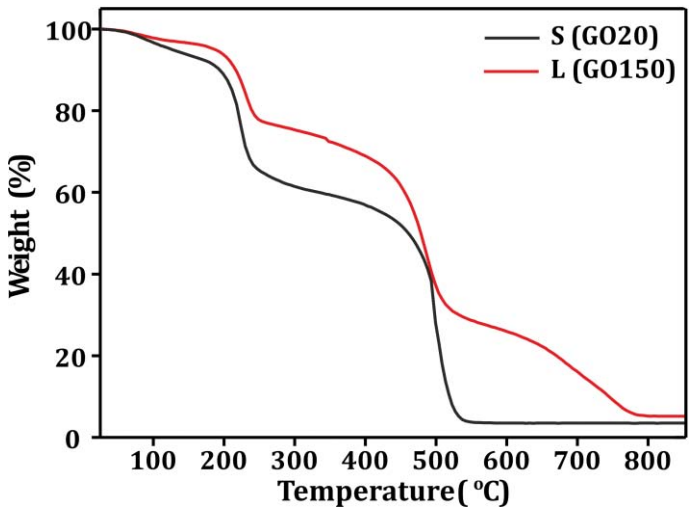


**Figure 3.2.** Thermogravimetric analysis of GO prepared from graphite powder <20 μm (S, continuous line) and GO prepared from graphite flakes <150 μm (L, dashed line). Analyses were performed under flowing air at a heating rate of 10 °C.min$^{-1}$.

[1] According to the particle size of the starting graphite, we will refer to these GO samples as S, for small (20 μm) and L, for large (150 μm) respectively.

der ammonia, rather than 200 °C, as it will be presented later (**Section 3.3.2**). The complete combustion of the sample S takes place at about 490 °C and mainly includes hydroxylic groups and carbon oxidation. TGA of the sample L shows an additional weight loss. We suggest that this additional event could arise from incompletely oxidized flakes, due to the large particle size of the starting material. This was confirmed by TEM analysis of a sample of L under air during 6 h at 550 °C.

Microscopic analysis is useful to evaluate the morphology of the samples (**Figure 3.3 (a-b)**). The dimensions of the oxidized sheets were measured from ca. 140 SEM images of GO prepared from both sources of graphite. In case of S (GO) prepared from graphite

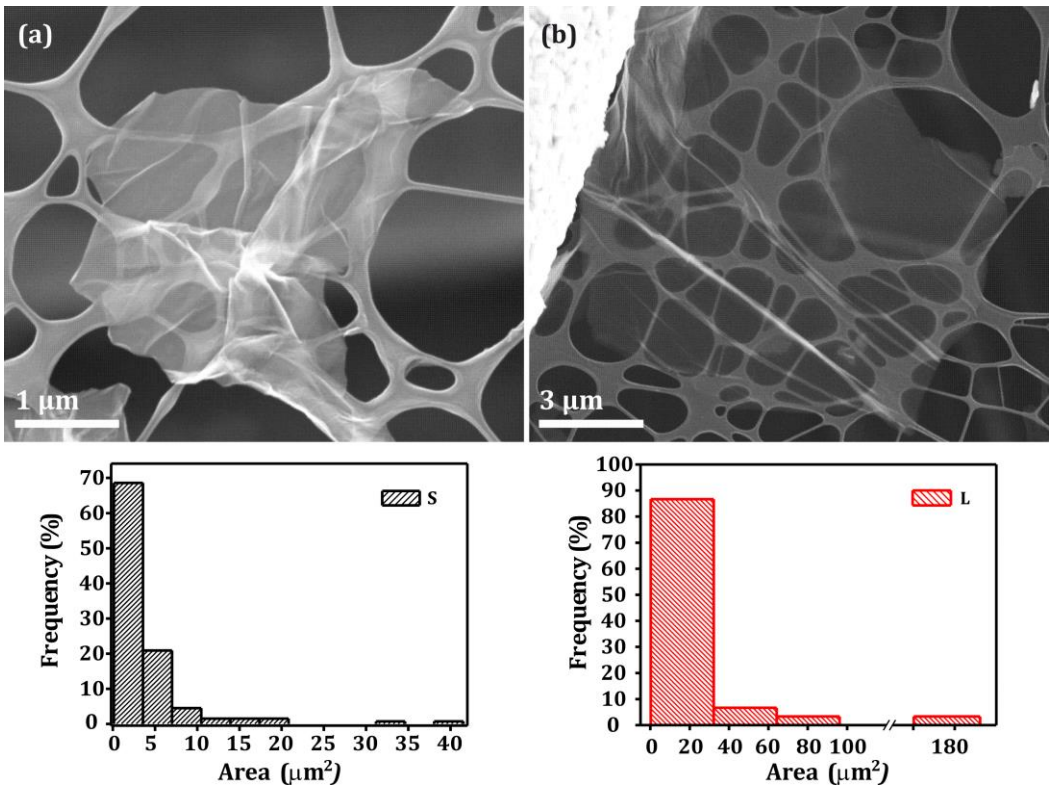


**Figure 3.3.** SEM images of GO samples prepared from (a) graphite powder (S) and (b) graphite flakes (L). The distribution of sizes of both (c) S and (d) L was determined by measuring the acquired images.

with the smaller size of particle), the oxidation of the sample led to GO sheets with a mean area of 3.6 $\mu m^2$. Meanwhile, when the material prepared from the larger graphite flakes (L) was measured, the flakes showed a mean area of 17.9 $\mu m^2$. In both cases the distribution of the size of the particles was quite homogeneous. A ca. 69 % of the evaluated specimens in S did not exceed the 3.5 $\mu m^2$ **(c)**, while the higher amount of the observed L sheets had areas between 1 $\mu m^2$ and 20 $\mu m^2$ (87 %, **(d)**). However, the larger sized (<120 $\mu m^2$) in L particles may correspond to the material whose oxidation was not complete during the synthesis.

**Figure 3.4 (a)** shows the TEM image of a specimen from the GO sample (S). The SAED pattern **(b)** shows well defined diffraction spots, confirming the graphitic crystalline structure of the synthesized material, which corresponds to the (100) and (110) planes (d-spacing = 2.12 Å and 1.23 Å) respectively.[169] The higher intensity observed for the inner diffraction spots (twice the intensity of the outer ones) is in agreement with the presence of single-layered GO.[169]

High resolution XPS were next acquired to confirm the presence and analyze the distribution of the O-bearing functionalities (structural defects) present in the samples. **Figure 3.5** shows XPS of sample S. Peaks ranged 282-292 eV and 530-536 eV correspond to the C1s and O1s binding energies (BE) respectively. Analysis of the C1s and

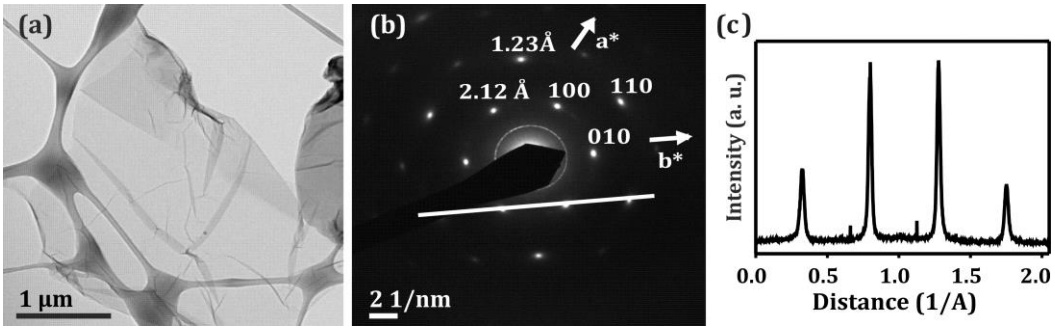


**Figure 3.4.** (a) TEM image of GO (S) with the corresponding (b) SAED pattern and (c) line profile.

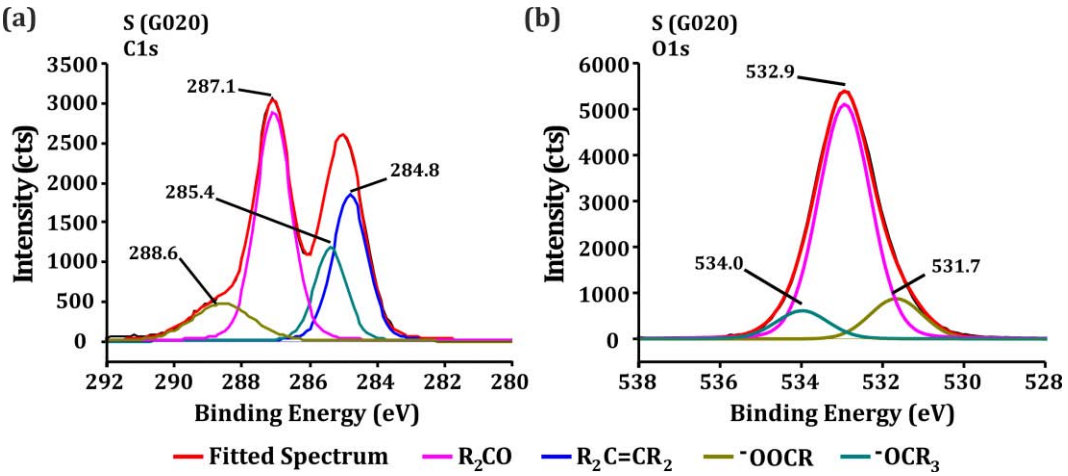


**Figure 3.5.** (a) C1s and (b) O1s high resolution XPS of GO (S) prepared by a modified Hummer's method.

O1s spectrum reveals that the synthetic procedure creates different oxidized groups (R-$O^-$, $R_2C$=O and $RCOO^-$) with a predominant presence of carbonylic groups, corresponding respectively to a 43.9 at. % and 78.0 at. % of the total area of C1s (BE=287.1-288.6 eV) and O1s (BE=532.9-534.0 eV) deconvoluted spectra.

### 3.3.2. Ammonolysis treatments. Influence of the conditions of reaction.

N-containing RGO samples[2][170] were synthesized by thermal annealing of GO under a continuous flow of pure ammonia gas. We will refer to this set of samples as SNR and LNR depending on the starting GO, S or L. Ammonolysis was performed at

[2] Following the nomenclature proposed by Bianco et al. reduced graphene oxide refers to samples of graphene oxide that have been processed to reduce its oxygen content. This definition includes both, N-doping and substitution of oxygen-moieties by nitrogen. Therefore to discern between structural nitrogen-doping and N-aliphatic groups, samples are referred as N-doped RGO and N-functionalized RGO respectively.

temperatures ranged between 25 °C and 800 °C. Taking into account that significant $NH_3$ decomposition begins at ca. 500 °C, being important at 700 °C (e.g. above 40 % for a flow rate of 60 mL $min^{-1}$),[171] higher temperatures of treatment were not considered for this study.

**Figure 3.6** summarizes the nitrogen content of the synthesized samples, as determined by elemental analyses (purple triangles). In order to determine the influence of the time of treatment and flow of ammonia in the final nitrogen content these parameters were also modified. Experiments using flow rates between 100 mL.$min^{-1}$ and 600 mL.$min^{-1}$ and times of treatments between 10 min and 300 min were carried out. Analysis of these results reveals that whereas the temperature plays a major role and allows tuning the nitrogen content between 4.8 wt. % (T = 25 °C) and 14.6 wt. % (T = 220 °C), both the time of treatment and the ammonia flow rate have a minor effect on the nitrogen content, with differences below 0.5 wt. % N between samples. These values actually lie within the range of the experimental error. After annealing the samples at different times

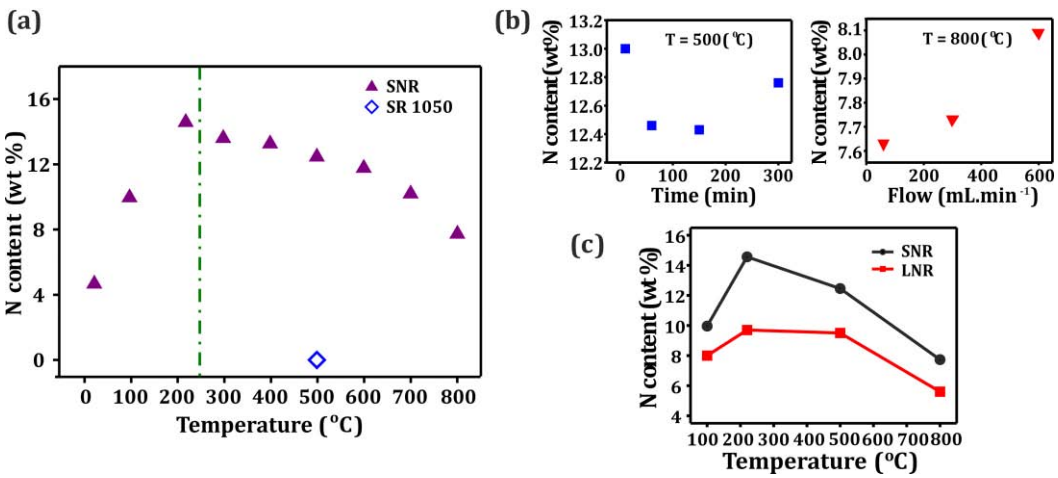


**Figure 3.6.** Nitrogen content in N-containing RGO samples prepared by annealing GO in $NH_3$ atmosphere. The rhombus corresponds to a sample of RGO-treated in $NH_3$ (sample name: SR1050). (a) Effect of temperature (flow $rate_{NH_3}$= 300 mL.$min^{-1}$; time = 60 min), (b) role of the time (T = 500 °C; $flow_{NH_3}$ = 300 mL.$min^{-1}$) and flow rate (T = 800 °C; time = 60 min). (c) Nitrogen content of the ammonia-treated GO prepared from 20 μm graphite powder (black line, SNR) and 150 μm graphite flakes (red line, LNR).

(keeping temperature (500 °C) and gas flow rate constant (300 mL.min$^{-1}$)), the highest N content 13.0 (3) wt. % was achieved after 10 min, similar to that obtained after 1 hour (12.5 wt. %); however, subsequent treatments were performed for 60 min to reach a stable equilibrium temperature.[172] Furthermore, an additional treatment was done in order to evaluate the influence that the O-bearing functionalities present in the starting sample have on the final content of nitrogen introduced after the $NH_3$ treatment. A sample, previously reduced by annealing S at 1050 °C during 2 h under $Ar/H_2$ atmosphere (RGO),[172] was treated under $NH_3$ at the same conditions (500 °C, empty rhombus). Elemental analysis confirms the absence of nitrogen in the ammonia treated RGO sample (SR1050, **Table 3.1**), stressing the importance of having O-bearing functionalities in the graphene structure for an efficient incorporation of nitrogen in the sample. There is no linear correlation between the temperature of treatment and the amount of nitrogen introduced in the samples. An initial increase in the nitrogen content is observed at low temperature treatments, reaching its maximum for the 220 °C $NH_3$ treated sample (SNR220). Afterwards, nitrogen content shows a continuous decrease when increasing the temperature of treatment up to 800 °C (7.7 wt. %). This is in agreement with the report of Dai et al. where a decrease of the nitrogen content was observed when the temperature of treatment was increased from 500 °C to 800 °C. Despite that a similar trend is observed, the use of pure $NH_3$ gas allows the introduction

**Table 3.1.** Composition of C, N and H present in GO and ammonia-treated samples determined by elemental analysis.

| Sample | C (wt. %) | N (wt. %) | H (wt. %) |
|---|---|---|---|
| Graphene Oxide (S) | 48.0 | <0.2 | 2 |
| SNR25 | 54.5 | 4.8 | 2 |
| SNR100 | 53.6 | 10 | 2.4 |
| SNR220 | 68.1 | 14.7 | 1.4 |
| SNR300 | 74.8 | 13.6 | 0.8 |
| SNR400 | 78.1 | 13.3 | 0.7 |
| SNR500 | 80.9 | 12.5 | 0.6 |
| SNR600 | 83.3 | 11.8 | 0.4 |
| SNR700 | 84.5 | 10.2 | 0.4 |
| SNR800 | 85.7 | 7.7 | 0.4 |

of a higher amount of nitrogen into the lattice at 500 °C (ca. 13 wt. %), as compared to treatments at the same temperature under mixtures $NH_3$ ($NH_3$/Ar, 10 % of $NH_3$) as per the work of Dai.[160]

The effect of the size of the starting graphite in the final content of nitrogen was next investigated by ammonolysis of L at 100 °C, 220 °C, 500 °C and 800 °C (LNR samples). **Figure 3.6 (c)** compares the N content of both SNR and LNR. Despite the fact that LNR (red line) follows a similar than the SNR samples (black line), the final nitrogen content is significantly higher when the GO employed comes from smaller particles of graphite. As shown in TGA of the GO samples, there is an important difference in the amount of defects generated after the oxidation of L and S. The presence of a higher amount of reactive sites in S produces an increase in the final nitrogen content.

**Figure 3.7 (a-b)** shows a SEM and a TEM image of the 500 °C $NH_3$ treated sample (SNR500). The area of the SNR500 sheets was measured from SEM images and the resulting distribution of sizes is presented as inset. The mean area of SNR500 (1.3 $\mu m^2$) was found to be smaller than that of S (3.6 $\mu m^2$, **Figure 3.3**) indicating the fracture of the

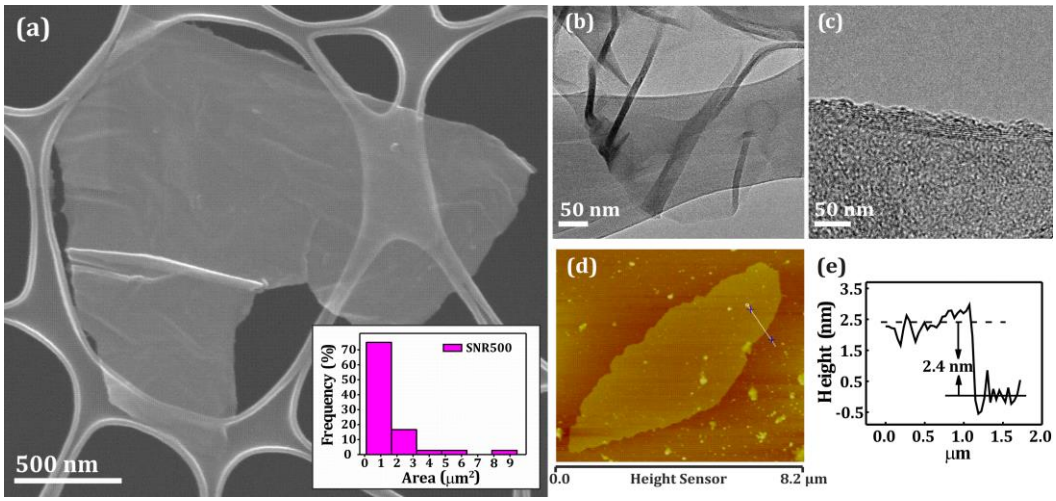


**Figure 3.7.** (a) SEM, (b), TEM, (c) HR-TEM and (d) AFM of nitrogen-containing samples prepared from S at 500 °C (SNR500). The inset in (a) shows the size distribution of the obtained sheets.

sheets through the more defective sites during the ammonolysis. When HRTEM imaging was carried out, particles containing few layers were observed (<10 layers, **Figure 3.7 (c)**). AFM also allows the determination of the number of graphene layers present in flakes of a given sample. A representative AFM image of RGO prepared at 500 °C under $NH_3$ (SNR500) is shown in **Figure 3.7 (d)**. Taking into account that single-layered graphene has been reported to have a height of 0.661 nm by AFM,[162] and that the distance between two consecutive layers in graphite is 0.34 nm, the 2.4 nm height recorded in the sample **(e)** would correspond to about 5 layers.

FT-IR spectroscopy is a useful tool to identify the nature of the different functionalities present in both, S and the ammonia treated samples. **Figure 3.8** shows the recorded spectra for the samples prepared at 100 °C, 220 °C, 600 °C and 800 °C). S spectrum (black line) shows the characteristic bands present in oxidized derivatives of graphite,[173, 174] illustrating the presence of free O-H groups ($\nu_{O-H}$ 3000-3700 $cm^{-1}$) which can arise from either absorbed water or from the stretching vibrations of phenol and hydroxyl groups when carboxylate moieties (C=O band at $\nu_{C=O}$ 1723 $cm^{-1}$) are present. Additionally, the C=C signal ($\nu_{C=C}$ 1585 $cm^{-1}$, from the conjugated structure), C-O stretching ($\nu_{C-O}$ 1220 $cm^{-1}$) and O-H bending ($\nu_{O-H}$ 1120 $cm^{-1}$) signals, originated by hydroxyl groups closely linked to the structure are also present.[175]. Significant changes in the intensity and position of the bands are evident after the ammonolysis treatment. There is a decrease in both, free and linked O-H signals, upon increasing the treatment temperature. Moreover, following the same trend, there is a decrease in the C=O/C=C intensity ratio. The elimination of C=O containing groups becomes evident with the sample treated at 600 °C implying the restoration of the conjugated structure. A new band around 1074 $cm^{-1}$ appears in the low temperature treated samples (100 °C and 220 °C) corresponding to the C-N stretching of aliphatic amines. Taking into account that the signal originated by the carbonyl groups ($\nu_{C=O}$ 1723 $cm^{-1}$) is still clearly visible in both of these samples, the presence of amide groups is also considered. The C-N band becomes weaker when increasing the treatment temperature, suggesting that the

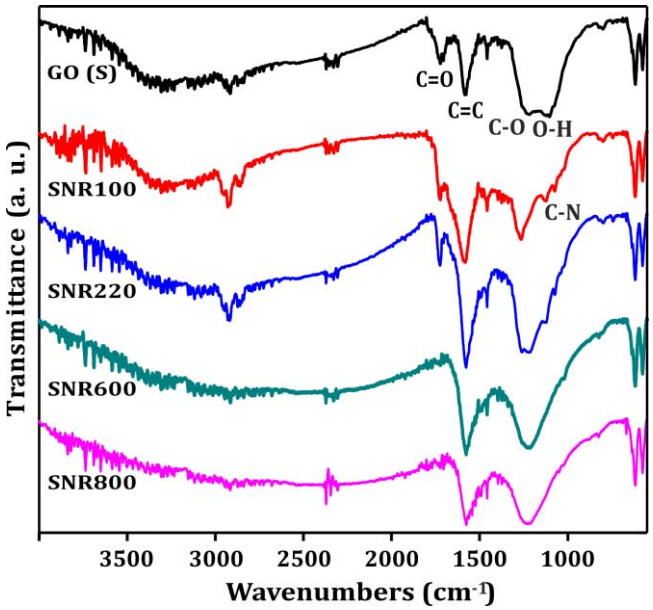


**Figure 3.8.** FT-IR of GO (S) and ammonia-treated GO (SNR samples) at temperatures ranged between 100 °C and 800 °C.

nitrogen atoms are no longer part of aliphatic functionalities, but rather incorporated within the graphene lattice. On the other hand, a triplet ca. 2900 $cm^{-1}$ is clearly visible in the FT-IR spectra of S, SNR100 and SNR220. Bands in this area can either correspond to an spectral artefact,[176] or originate from C-H stretching vibration. In this case, a decrease of intensity is observed for the samples treated at high temperature, in agreement with the hydrogen contents determined by elemental analyses (2 wt.% in S; 2.4 wt.% at 100 °C; 1.4 wt. % at 220 °C; 0.4 wt. % at 600 °C and 800 °C; see **Table 3.1**). Therefore the band at ca. 2900 $cm^{-1}$ is assigned to C-H bonds, easily correlated to the presence of oxygen and nitrogen-bearing functionalities in S and the low temperature ammonia treated samples.

Thermogravimetric analyses were carried out to assess the role of the functional groups detected by FT-IR with the thermal oxidation behavior of the samples (**Figure 3.9**). For the samples treated in ammonia at low temperature (25 °C-400 °C) the weight losses observed at temperatures below ca. 200 °C should correspond to either absorbed

water or $CO_2$ or to the oxidation of both O and N-bearing aliphatic functional groups. The initial continuous weight loss previously associated to the high hydrophilicity of the sample in the GO thermal analysis is also visible for the 100 ˚C and the samples treated in ammonia 220 ˚C (SNR100 and SNR220). A progressive decrease in the amount of aliphatic functionalities is observed when increasing the temperature of treatment, in agreement with the FT-IR analysis. Additionally, a significant increase in the onset of the complete combustion of the sample is observed until 569 °C (for the sample prepared at 400 °C). This behavior is attributed to the continuous removal of O-bearing functionalities ("defects") from the GO structure. However, despite the fact that a significant amount of aliphatic groups have been removed at 400 °C, the presence of these species cannot be discarded. Therefore, this set of samples (25 °C - 400 °C) containing different degrees of aliphatic nitrogen will be referred to as N-functionalized RGO in this study. Ammonia has been shown to be an efficient reducing agent for the synthesis of RGO, being more efficient at high temperatures. When S is treated at temperatures above 500 °C in ammonia (**Figure 3.9 (b)**) only the process leading to the complete combustion of the sample is observed by TGA in air. The initial weight loss attributed to oxygen and nitrogen-bearing aliphatic functionalities, in the samples trea-

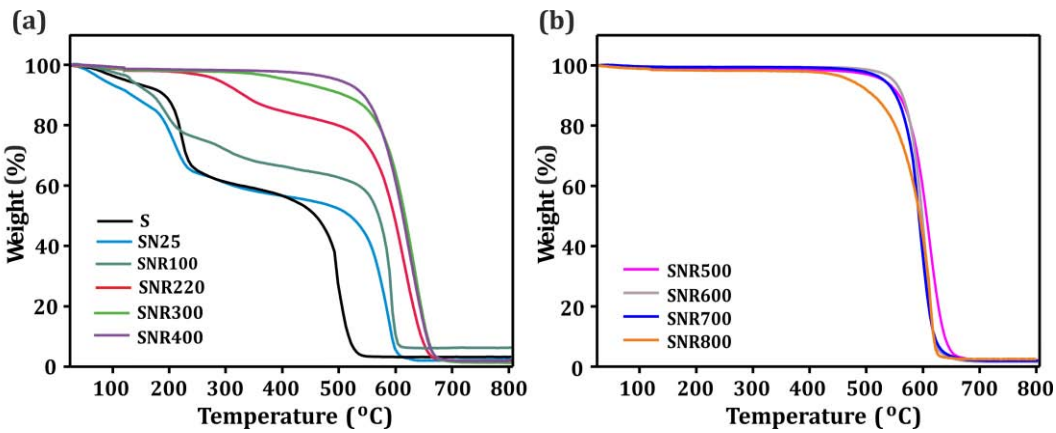


**Figure 3.9.** TG analyses of S and the N-containing RGO samples (SNR) prepared by annealing S under ammonia at temperatures ranged between (a) 25 °C- 400°C and (b) 500 °C- 800°C. Thermal analyses were performed under flowing air at a heating rate of 10 °C.min$^{-1}$.

**Table 3.2.** Onset of combustion temperature in air of S annealed in ammonia at temperatures ranged between 500 °C and 800 °C.

| Sample | N content (wt. %) | Onset of combustion |
|---|---|---|
| SNR500 | 12.5 | 579 °C |
| SNR600 | 11.8 | 577 °C |
| SNR700 | 10.2 | 571 °C |
| SNR800 | 7.7 | 520 °C |

ted in $NH_3$ at low temperatures is not observed. This suggests the incorporation of nitrogen into the planar structure (synthesis of N-doped reduced graphene oxide). Therefore, to differentiate this set of samples prepared at high temperature (500 °C-800 °C) from the low temperature treatments (100 °C-400 °C), the former will be referred as N-doped RGO and the latter, as N-functionalized RGO. The terminology N-functionalized RGO is used to stress the presence of aliphatic N-containing moieties in the samples, which tends to be neglected, but N-doping might already have taken place below 500 °C. Furthermore, the samples treated between 500 °C and 800 °C show an inverse trend in thermal stability against oxidation. The higher the nitrogen content is the higher onset of combustion temperature is observed (**Table 3.2**). For instance, whereas the sample prepared at 500 °C, with 12.5 wt. % N, presents an onset of combustion at 579 °C, the sample prepared at 800 °C, with 7.7 wt. % N, starts to oxidize at lower temperatures (520 °C). In the case of samples prepared at 300 °C and 400 °C, the decrease of O-bearing functionalities would explain the increase in stability, despite the slight decrease in the nitrogen content. As it will be discussed in **Section** ¡Error! No se encuentra el origen de la referencia., the same trend is observed in samples prepared from larger sheets in both, low and high temperature treatments.

As mentioned, the initial loss in TGA observed in S, also visible for the SNR25 and SNR100 samples, is typically assigned to desorption of physisorbed molecules. Therefore, it is an indication of the hydrophilicity of the materials, directly related to the presence of functional groups in carbon nanomaterials.[177] To take advantage of this phenomenon and quantitatively determine the wettability properties, contact angle

(of a water droplet lying on thin layers) of the samples was measured. The contact angle measurements of the N-containing RGO samples along with those of GO (S) and graphite are presented in **Figure 3.10**. As expected, graphite powder shows the lowest interaction with the droplet of water (empty blue square), i.e. the highest hydrophobicity of all the analyzed samples due to the absence of functional groups in the structure (contact angle 160.6 °) nearly followed by the N-doped RGO samples. In contrast, the N-functionalized RGO samples (25 °C-400 °C) presented a more hydrophilic character. The most hydrophilic of the studied materials is GO (75 °), followed by the sample prepared at 25 °C (120 °). The marked increase in the contact angle at this temperature suggests that, already at room temperature, structural changes have occurred after the $NH_3$ treatment. Then a continuous increase of the contact angle is observed upon increasing the temperature of treatment. The observed trend is in agreement with the gradual disappearance of functionalities observed by both FT-IR and TGA when increasing the temperature of treatment.

The higher wettability of the N-containing samples compared to that of graphite arises from electrostatic interactions of different functional groups with the droplet. In the case of the N-doped RGO samples, small differences are observed with respect to graphite that can originate from the in-plane polarization induced by the presence of N heteroatoms or from thermally stable oxygen functionalities, as reported by Romanos et al.[168] Thus, wettability measurements are a useful and simple tool to provide, in a fast and qualitative manner, information on the degree of functionalization of the samples.

The hydrophilic/hydrophobic character of the samples can also be assessed by the dispersability of the material in aqueous solvents. For this purpose, UV-Vis absorption spectra of dispersions of S and ammonia treated S samples were measured. 1 mg of the sample was initially dispersed in 5 mL of an ethanol-water (1:1) mixture (bath sonication, 30 min) and subsequently centrifuged (2 min, 2500 rpm) to precipitate the larger particles from the dispersion. **Figure 3.11 (a)** displays the UV-Vis spectra obtai-

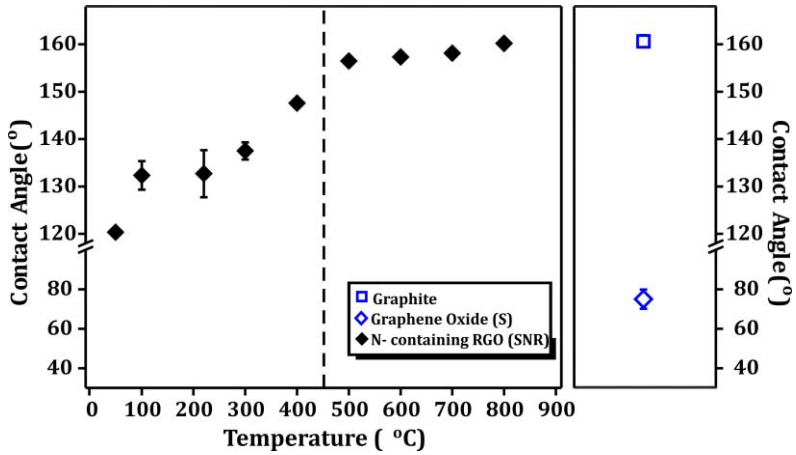


**Figure 3.10.** Effect of the temperature of treatment in the wettability of thin layers of the N-containing RGO samples (SNR, black solid rhombus), prepared after ammonolysis reactions. Both, GO (S, blue empty rhombus) and graphite (blue empty square) are include as benchmarks. The dashed line separates the N-functionalized RGO (100-400 °C) from the N-doped RGO samples (500-800 °C). Error bars are included for all the samples (some of them are almost not visible due to the low error of the measurement).

ned after sonication and partial centrifugation**.** There are two well differentiated regions of absorbance in S (continuous black line), corresponding to the $\pi$-$\pi^*$ (239 nm) and $n$-$\pi^*$ (ca. 300 nm) transitions previously assigned to C=C and C=O bonds respectively.[178] The second region of absorbance (shoulder) decreases in the ammonia treated samples until its total disappearance in N-doped reduced graphene oxide samples (see SNR500 spectra), due to the continuous elimination of O-bearing functionalities.[179] Furthermore, a marked shift is observed in the first region (239 nm) when S spectrum is compared to those of N-containing RGO samples. Despite the fact that this shift can be attributed to the gradual restoring of the electronic conjugation, the presence of N atoms in the structure might play a role. Comparison of the UV-Vis spectrum of the 600 °C $NH_3$-treated sample (continuous grey line, 10.0 at. % N as per XPS) and the 700 °C sample (blue dotted line, 7.7 at. % N) reveals a major shift to the red area of the spectrum (+7.2 nm); see the inset in **Figure 3.11 (a)**. Both samples having similar oxygen content (ca. 2 at %; Table 2), the origin of the shift must reside in the different nitrogen content of the samples. Therefore, the amount of nitrogen

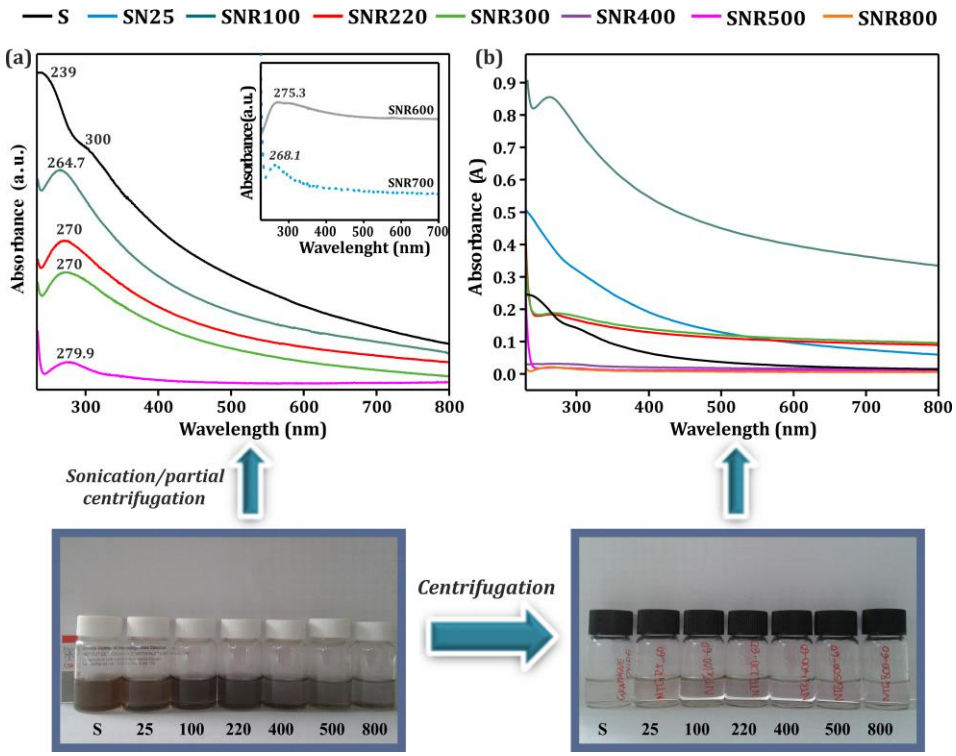


**Figure 3.11.** UV-Vis spectra of S and $NH_3$ treated S samples after (a) dispersion-partial centrifugation and (b) dispersion-exhaustive centrifugation in water:ethanol (1:1).

and its distribution into the layer has a noticeable influence in the spectroscopic properties of the material.[180] The higher the nitrogen content and the temperature of treatment is, the higher shift to the red region of the spectra is observed, once taken into account the contribution from the oxygen. **Figure 3.11 (b)** shows UV-vis spectra of the same dispersions after exhaustive centrifugation (15 min, 4500 rpm). There is a marked difference in both the shape and the absorbance between S and the samples prepared at low (25 °C-300 °C) and high temperatures (400 °C-800 °C) under $NH_3$. The higher dispersability presented by the first group of samples is mainly caused by the presence of O-bearing functionalities (in the case of S) and O/N-bearing functionalities in N-functionalized RGO samples (which agrees with the FT-IR spectra assignments). The presence of such functional groups enhances the dispersability via the formation of electrostatic interactions between the sample and the polar solvent. Despite the fact

that the solubility of S would a priory be expected to be higher than the N-containing samples, the inverse trend is observed for the samples prepared at 25 °C and 100 °C. The formation of intralayer hydrogen bonds in the sample of S might account for this. Hydroxyl and carbonyl group derivatives (such as quinones) can interact forming internal hydrogen bonds (**Scheme 3.1**).[181]

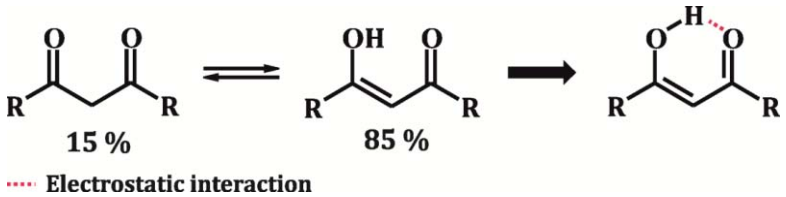


**Scheme 3.1.** Internal electrostatic interaction (H-bond) between hydroxylic and carbonylic groups present in GO sheets. The hydroxy-ketone form turns to be the most abundant resonant structure (85 %).

In agreement with previous reports[178] carbonyl functionalities are found to be the most abundant moieties present in S (24.0 at. % as determined by XPS, vs 2.9 at. % of hydroxyl groups; **Table 3.3**). The presence of carboxylic groups (3.9 at. %) might also contribute to this fact, through the formation of dimeric moieties resulting from electrostatic interactions. A marked decrease in the amount of C=O (ca. 30 %) is observed by ammonolysis of S at 25 °C. At 100 °C ca. 60 % of carbonylic groups have been already eliminated from the sample. An important decrease in water dispersability is observed at 400 °C indicating the continuous elimination of the aliphatic functionalities when increasing the temperature of the treatment. The images in **Figure 3.11** present the partially centrifuged (2 min, 2500 rpm; left) and exhaustively centrifuged (15 min, 4500 rpm; right) dispersions. S presented a similar appearance when compared with the dispersion of N-functionalized RGO sample treated at 25 °C (SNR25, brownish); nevertheless, the samples prepared at higher temperatures (100 °C and 220 °C) become darker than S. In contrast with the stable solutions obtained for the samples treated in $NH_3$ at low temperature, a clearer appearance along with the formation of a black precipitate is observed for the N-doped

**Table 3.3.** Nitrogen, oxygen and carbon content of S, $NH_3$ treated S (25 °C-800 °C) and Ar treated S (500 °C, 800 °C) determined by XPS analysis. (*) These energies could be contributed either by aliphatic functionalities ($CONH_2/CNH_2$) or by structural pyridinic ($C_5N$:) and pyrrolic ($C_4N$:) groups.

| Sample | N content (at. %) | | O content (at. %) | | C content (at. %) | |
|---|---|---|---|---|---|---|
| | $CONH_2$/ $CNH_2$ | $C_5N$:/$C_4N$:/$C_4N$+ | -OOCR/$OCR_2$/-$OCR_3$ | PhOCOOPh | C=C | C-X (X=O, N) |
| S | -- | | 3.9/24.0/2.9 | -- | 18.8 | 49.7 |
| Total | 0.7 | | 30.8 | | 68.5 | |
| SNR25 | 3.0/1.1 | -- | 4.9/16.8/4.6 | -- | 29.5 | 40.0 |
| Total | 4.1 | | 26.4 | | 69.5 | |
| SNR100 | 4.6/3.2 | -- | 8.1/9.7/1.9 | -- | 37.2 | 35.3 |
| Total | 7.8 | | 19.7 | | 72.5 | |
| SNR220 | | 3.9*/4.7*/2.4 | 4.4/2.5/2 | -- | 40.3 | 39.8 |
| Total | 11.0 | | 8.9 | | 80.1 | |
| SNR300 | | 4.4*/4.3*/2.3 | 2.3/1.6/1.8 | -- | 43.9 | 39.4 |
| Total | 11.0 | | 5.7 | | 83.3 | |
| SNR400 | | 4.3*/4.6*/2.2 | 1.8/1.3/1.6 | -- | 46.5 | 37.7 |
| Total | 11.1 | | 4.7 | | 84.2 | |
| SNR500 | -- | 4.5/3.7/2.1 | 1/1.1/1.4 | -- | 36.9 | 49.3 |
| Total | 10.3 | | 3.5 | | 86.2 | |
| SNR600 | -- | 4.0/3.6/2.4 | 0.7/0.8/0.8 | -- | 42.4 | 45.3 |
| Total | 10.0 | | 2.3 | | 87.7 | |
| SNR700 | -- | 2.9/2.6/2.2 | 0.5/0.6/0.9 | -- | 49.8 | 40.5 |
| Total | 7.7 | | 2 | | 90.3 | |
| SNR800 | -- | 2.3/1.8/1.6 | 0.5/0.7/0.9 | -- | 62.6 | 29.6 |
| Total | 5.7 | | 2.1 | | 92.2 | |
| SArR500 | -- | -- | 3.9/1.5/6.1 | 0.9 | 53.2 | 33.8 |
| Total | 0.6 | | 12.4 | | 87.0 | |
| SArR800 | -- | -- | 1.5/2.0/1.1 | 0.8 | 64.7 | 29.4 |
| Total | 0.5 | | 5.4 | | 94.1 | |

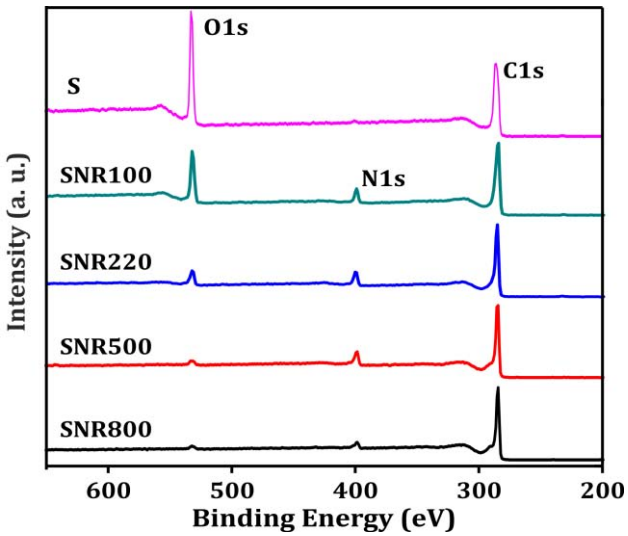


**Figure 3.12.** General survey scan of S and 100 °C, 220 °C, 500 °C and 800 °C $NH_3$ treated S samples (SNR).

RGO samples (500°C-800 °C) in agreement with the higher hydrophobicity presented by these samples. After a longer time of centrifugation (**Figure 3.11 (b)**), stable dispersions were obtained (collected supernatant) and no precipitate powder was observed.

**Figure 3.12** shows the XPS general survey scans of GO (S) before and after ammonolysis at 100 °C, 220 °C, 500 °C and 800 °C. The S spectrum presents two signals around 530 eV and 284 eV corresponding to the O1s and C1s binding energies respectively. After ammonia treatment, one additional peak, assigned to the N1s binding energy (ca. 400 eV) becomes clearly visible, confirming the presence of nitrogen in all the treated samples. For ease of comparison all the spectra are normalized to the C1s peak. A continuous decrease in intensity of the O1s signal is observed when increasing the temperature of treatment; from 30.8 at. % in S down to 2.3 at. % already at 600 °C (Table 3.3). This highlights the efficiency of $NH_3$ as reducing agent for the synthesis of RGO. After 600 °C no significant change in the at. % of oxygen is observed. In comparison with previous works the 600-800 °C treatments are the

most reduced samples of GO reported to date when temperatures under 1000 °C are employed. When RGO is prepared under an inert Ar atmosphere at 800 °C (SArR800), the level of oxygen is about 5.4 at. % (Table 3.3). Similar values are obtained under reducing atmospheres ($H_2$) even at higher temperatures (1100 °C; 2.7-9.2 at. % O)[160, 162] or in the presence of N-dopant conditions (ca. 3 at. % O)[182] [183]. This stresses the role of $NH_3$ in the removal of O-bearing functionalities.

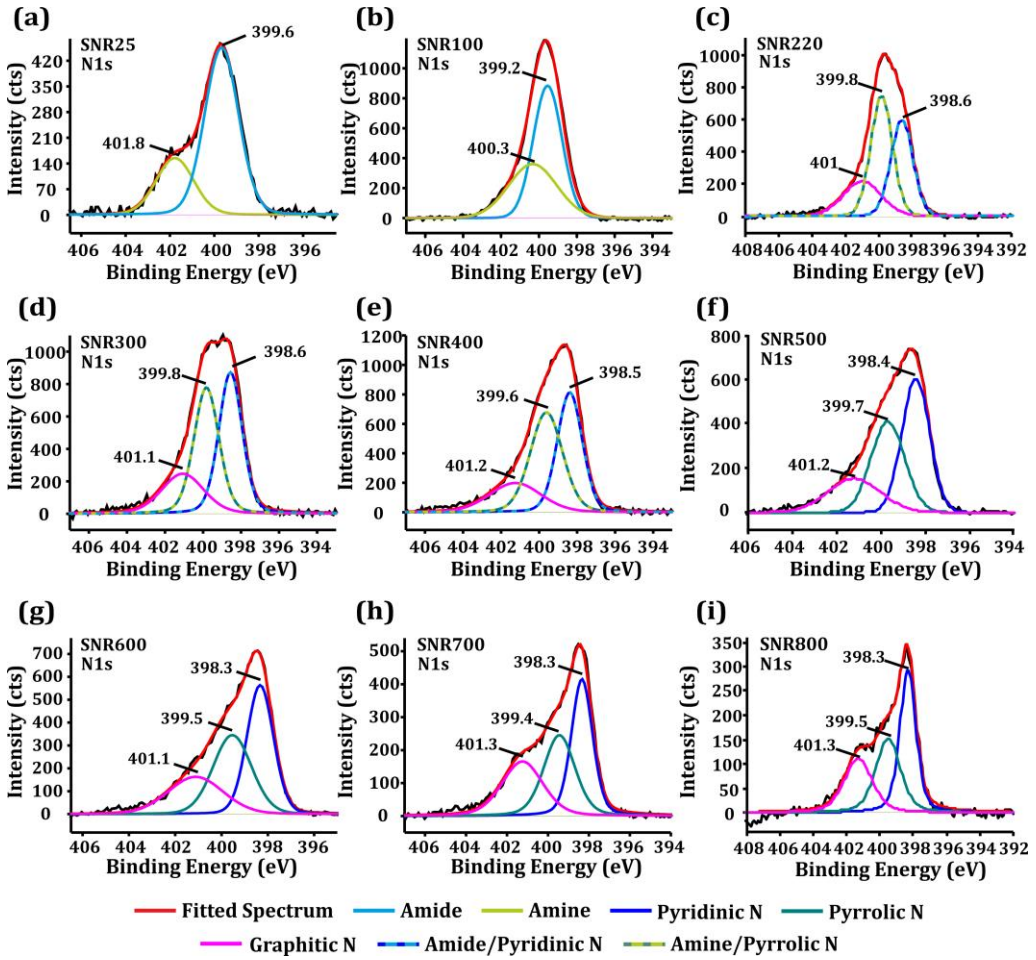


**Figure 3.13.** High resolution N1s XPS spectra of (a-e) N-functionalized RGO (25 °C- 400 °C) and (f-i) N-doped RGO (500 °C- 800 °C ) samples prepared by ammonolysis of GO (S).

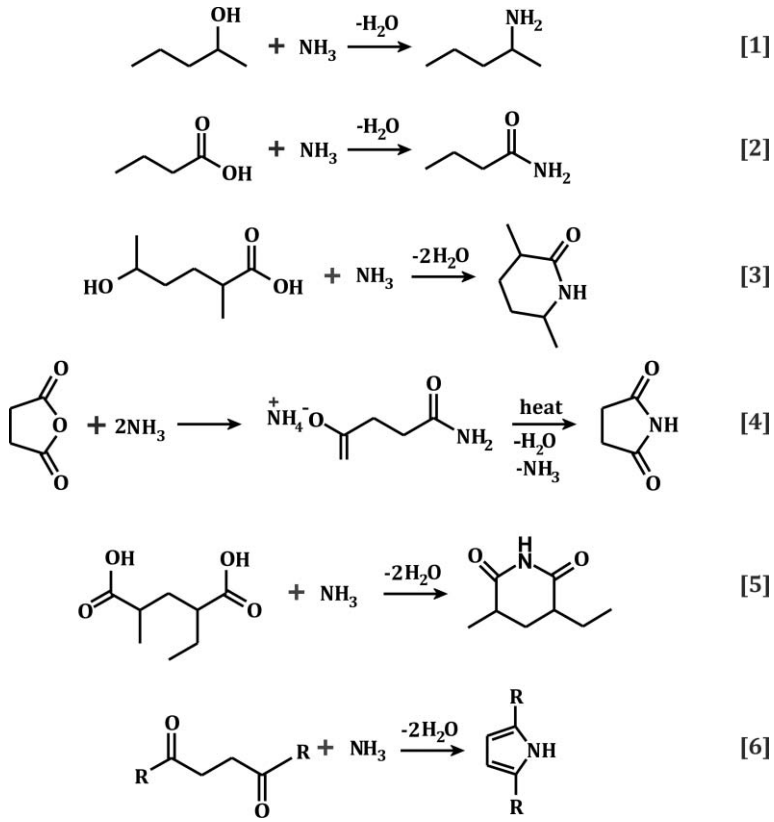


**Scheme 3.2.** Synthesis of some N-containing moieties via $NH_3$ nucleophilic addition to hydroxylic, carbonylic groups and derivatives. Higher temperature treatments favor reduction and formation of cyclic moieties.

The high-resolution N1s spectra of nitrogen-containing RGO show marked differences in the distribution of N species (**Figure 3.13**). SNR25 and SNR100 (a-b) samples present two well differentiated peaks that can be assigned to amide (ca. 399.2 eV) and amine (ca. 400 eV) functionalities. The binding energies (BE) of these peaks are in good agreement with the report of Gabriel et al., where well defined organic molecules, namely 4, 5-ethyl enedithio 4',5' di(methyl carbamoyl)-tetrathiafulvalene and 4-aminothiophenol were employed to respectively define the peak position of amide and amine groups. [184] Despite that both XPS signals could arise from the presence of mentioned structural nitrogen, all the analyses performed so far complementary confirm the presence of aliphatic nitrogenized species.

The ammonia nucleophilic addition to the oxidized graphene lattice can lead to different functionalities depending on the groups involved into the acid-base reaction. In this manner, amines and amides result from interactions of $NH_3$ with hydroxylic and carboxylic groups respectively (**Scheme 3.2 (1-2)**). Additional reactions of oxygen-bearing functionalities closely located at the GO (S) surface with ammonia produce diverse nitrogen-based functionalities, including lactams (3), five and six-membered imides (4-5) and pyridinic and pyrrolic groups; all contributing to the planar system. [185] When S sample is treated at temperatures above 200 °C (SNR220), a new peak at higher binding energy (ca. 401 eV) appears corresponding to graphitic nitrogen (quaternary N).[13] As per TGA, the elimination of oxygen-based functional groups begins to be important at this temperature. This suggests that a fraction of the nitrogen atoms are already integrated into the RGO lattice (N-doping) by substitution of the eliminated carbon atoms. The 5.2 % relative increase in the pyrrolic/amine signal (399.8 eV) and the strong decrease of O=C groups (42.3 %) in SNR220, with respect to the SNR100 sample (**Table 3.3**), might account for the formation of N-bearing 5-membered rings resulting from the reaction of ammonia with dicarbonylic species. However, the presence of both, N-functionalization and N-doping cannot be discarded. For this reason this signal is represented as a dashed line with contribution of both, aliphatic and structural groups (**Figure 3.13(c)**). The same discernment can be applied for samples treated under ammonia at 300 °C and 400 °C, even though the increase in the temperature of treatment favors the formation of cyclic structures and the elimination of oxygenized functionalities (4.7 at % for SNR400), thus suggesting the selective formation of rings free of oxygen. At 500 °C a decrease in the intensity of the peak at ca. 399.8 eV is observed and it is thought to only arise from pyrrolic nitrogen. Taking into consideration the previously performed analyses, the presence of aliphatic moieties is not expected at this temperature of synthesis. Higher temperatures of treatment (800 ° C) favor the formation of graphitic N (401.3 eV).

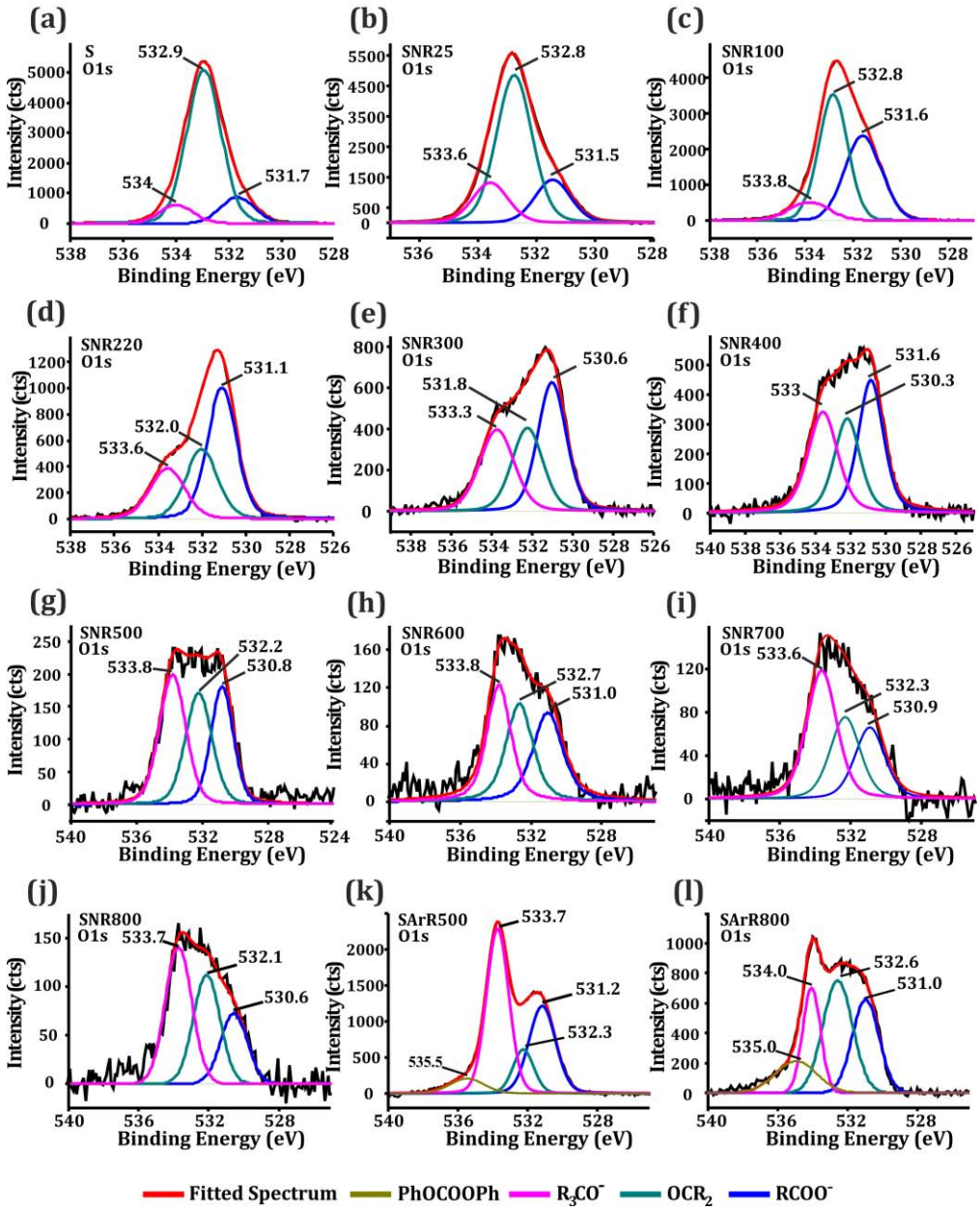


**Figure 3.14.** High-resolution O1s spectra of (a) S, (b-j) $NH_3$ treated S (100 °C to 800 °C) and (k-l) Ar treated S (500 °C and 800 °C).

The high resolution O1s XPS also shows significant differences in the distribution of the oxygen species (**Figure 3.14**). Therefore, the temperature employed for the treatments not only determines the degree of reduction (elimination of oxygen leading to RGO) but also allows tuning the nature of the O-bearing functionalities in the resulting material. Three different signals assigned to O-C=O (ca. 531 eV), O=C (ca. 532 eV) and O-C (ca.534 eV) are present in S and $NH_3$-treated samples.[161] The comparison between SNR100 and SNR500 samples reveals a significant decrease of both O=C (88.7%) and O-C=O groups (87.7 %) in the latter (**Table 3.4**). The removal of O-C groups (26.3 %) takes place in a lesser extent, since these moieties show a higher stability against thermal oxidation.[168] An additional 35.7 % loss of O-C groups is observed upon increasing the temperature of treatment to 800 °C. To get further insights on the impact that the ammonia treatment has on the distribution of the O-bearing functionalities, the O1s spectra of SArR500 and SArR800 are included in **Figure 3.14(k-l)**.

**Table 3.4.** Ratio between N, O and C species present in S, $NH_3$ treated S (100 °C-800 °C) and Ar treated S (500 °C, 800 °C) determined by XPS analysis. (*) These energies could be contributed either by aliphatic functionalities ($CONH_2/CNH_2$) or by structural pyridinic ($C_5N$:) and pyrrolic ($C_4N$:) groups.

| Sample | N content (%) | | O content (%) | C content (%) | |
|---|---|---|---|---|---|
| | $CONH_2$/ $CNH_2$ | $C_5N$:/$C_4N$:/$C_4N$+ | $^{-}O_2CR$/ $OCR_2$/$OCR_3$/PhOCOOPh | C=C | C-X (X=O, N) |
| S | -- | -- | 12.8/78.0/9.2/-- | 27.5 | 72.5 |
| SNR25 | 72.6/27.4 | -- | 18.7/63.9/17.4/-- | 42.5 | 57.5 |
| SNR100 | 59.3/40.7 | -- | 41.1/49.3/9.6/-- | 51.3 | 48.7 |
| SNR220 | | 35.2*/42.8*/22.0 | 48.9/28.4/22.7/-- | 50.3 | 49.7 |
| SNR300 | | 40.6*/38.8*/20.6 | 40.5/28.5/31.0/-- | 52.7 | 47.3 |
| SNR400 | | 38.8*/41.7*/19.5 | 37.8/28.0/34.2/-- | 55.2 | 44.8 |
| SNR500 | -- | 43.4/35.8/20.8 | 29.1/32.7/38.2/-- | 42.8 | 57.2 |
| SNR600 | -- | 40.3/35.6/24.1 | 32.8/32.6/34.6/-- | 48.3 | 51.7 |
| SNR700 | -- | 37.9/33.0/29.1 | 25.4/29.0/45.6/-- | 55.2 | 44.8 |
| SNR800 | -- | 40.8/32.3/26.9 | 22.4/34.4/43.2/-- | 62.6 | 37.4 |
| SArR500 | -- | -- | 31.3/12.3/49.5/6.9 | 61.2 | 38.8 |
| SArR800 | -- | -- | 27.7/36.9/20.8/14.6 | 68.8 | 31.2 |

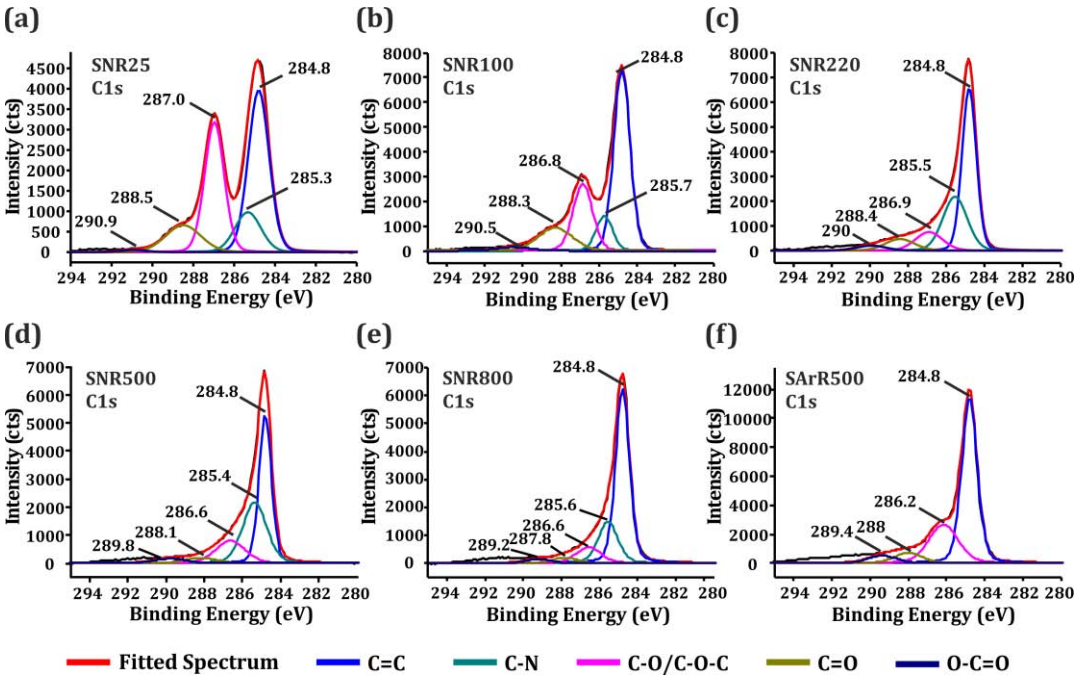


**Figure 3.15.** High-resolution C1s spectra of (a-e) N-containing RGO samples prepared by ammonolysis treatment at temperatures ranged between 25 °C and 800 °C and (f) Ar treated S at 500 °C.

Noticeably, a new peak around 535 eV appears which increases with the temperature of treatment. This new peak, not present in the ammonia treated S, can be assigned to aromatic derivatives resulting from condensation reactions of phenolic groups, previously observed in oxidized carbonaceous materials.[186] Some authors have also reported the presence of phenolic groups in S by analysis of the C1s peak, overlapping with the hydroxyl/ether signal (ca. 285.4 eV).[35, 187] In this study this band has not been employed for the quantification of the N or O-based species due to the difficulty in the separation of the components after the deconvolution of the high resolution spectra. The asymmetry of the C1s peak, the overlapping of several signals and the low concentration of the heteroatoms produce a high uncertainty in the determination of the functionalities present in the material.[188, 189] However, changes in the structure can be perceived through the visual inspection of the high resolution C1s XPS of the samples after the ammonolysis treatments (**Figure 3.15**). All the C1s spectra present

the characteristic peak from the $sp^2$ C-C bond as well as a broad band ca. 291 eV, which is commonly assigned to the $\pi$-$\pi^*$ interband.[190] Already at 25 °C, a 56.9 % increase in the main peak (C=C groups, BE=284.8 eV) is observed, suggesting the elimination of aliphatic functionalities. The same trend is observed for all the low temperature treated samples (N-functionalized RGO, **(a-c)**), obtaining the highest increase at 400 °C (46.5 at. % against the 18.8 at. % C=C observed for the S sample), being an evidence of the restoring of the conjugated system by the elimination of the O-bearing functionalities. Despite that a new signal has appeared affecting the shape and position of the deconvoluted peaks, it is difficult to assign the positions to a particular functionality, since the binding energies of the C-N and C-O are both located in the 285-287 eV range.[191] Nevertheless, the samples treated at high temperature (N-doped RGO, **(d, e)**) show a broad asymmetric signal, attributed to the presence of lattice disorders originated by N-doping.[10]

A schematic representation of the different N-functionalities that can be present in the samples is presented in **Scheme 3.3.** The scheme also illustrates that the environment of the nitrogen atoms and the level of reduction is temperature dependent.

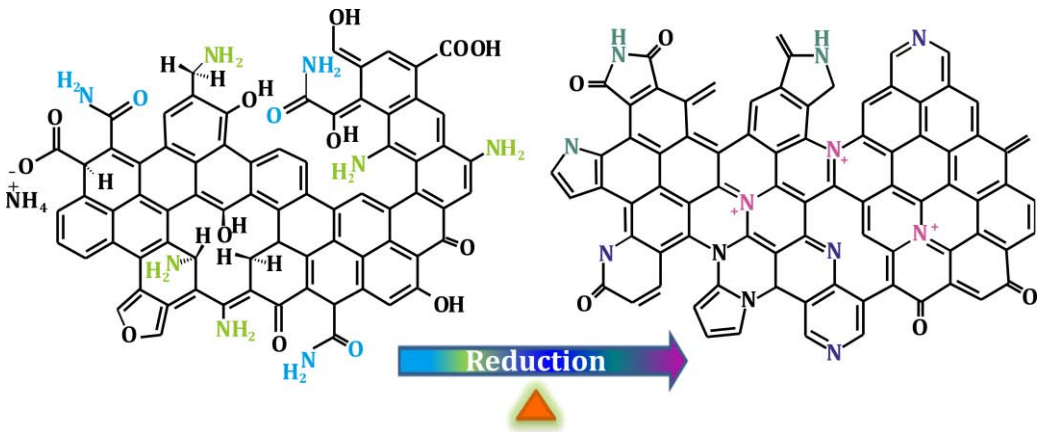


**Scheme 3.3.** Graphical representation of both, N-bearing functionalities and structural nitrogen introduced into the graphene oxide structure after ammonolysis treatments at low (left) and high (right) temperatures.

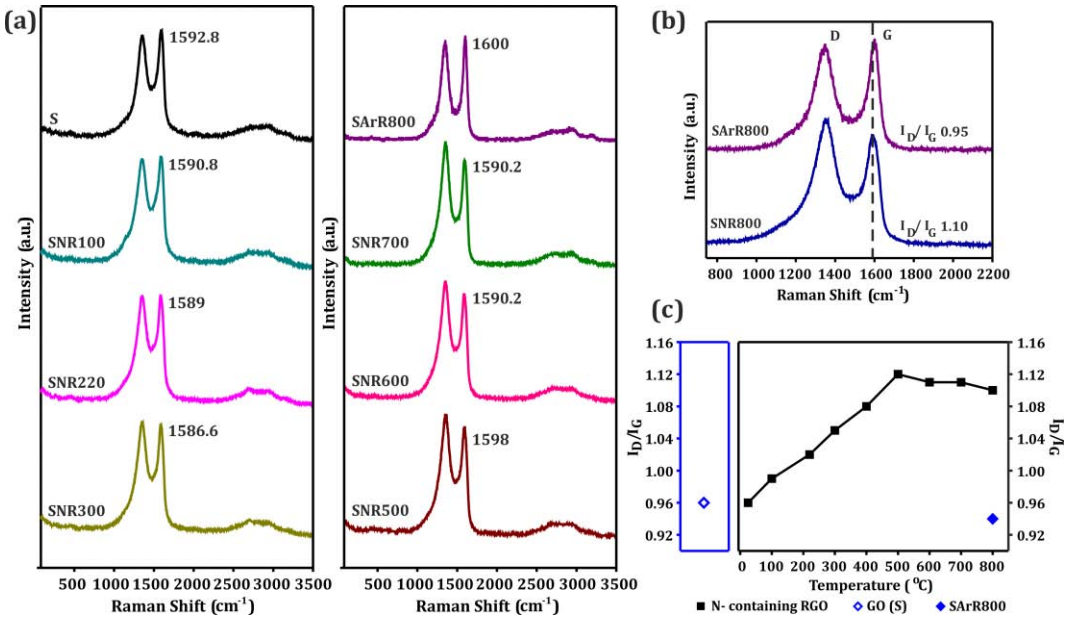


**Figure 3.16.** (a) Raman spectra of N-containing RGO (100 °C-800 °C, SNR) and RGO (800 °C, SArR800). (b) Comparison of the G-band position of two samples treated at 800 °C under Ar and $NH_3$. (c) Effect of temperature on the D-band to G-band intensity ratio ($I_D/I_G$) of N-containing RGO (black squares). A sample of GO (S) and GO reduced under Ar (SArR800, blue rhombus) are also included for comparison.

Raman spectroscopy is a useful tool frequently employed to detect variations in the honeycomb carbon lattice.[192] To complete the present study, Raman spectra of the $NH_3$-treated (100 °C-800 °C) and Ar RGO (800 °C) samples were recorded (**Figure 3.16**). As previously reported,[193] a down shift in the position of the G-band is observed by nitrogen-doping of the graphene lattice, from 1600 $cm^{-1}$ (RGO) down to 1590.8 $cm^{-1}$ (N-doped RGO) -both samples being treated at 800 °C-. Furthermore, in agreement with the report of Cho et al.[194] an increase in the relative intensity of the D-band ($I_D/I_G$) is also observed after the $NH_3$ treatment ($I_D/I_G$ = 1.10 for N-doped RGO at 800 °C; $I_D/I_G$ = 0.95 for RGO at 800 °C). The samples treated in ammonia at low temperature (100 °C-400 °C) present a continuous increase of the $I_D/I_G$ ratio when increasing the temperature of treatment (**Figure 3.16**), which levels off for the N-doped samples (500 °C-800 °C). The latest presenting similar $I_D/I_G$ ratios. From the analyses

performed in the present study it becomes patent that the employed characterization techniques provide relevant but partial information on the type of N present in N-bearing graphene samples. Taking this into account, and making profit of the physical and chemical properties of the synthesized materials, a toolbox that allows a proper assessment of the different nitrogen species that can be present in graphene-based materials is proposed (Table 3.5).

**Table 3.5.** Toolbox of characterization techniques for the assessment of N-containing species in graphene-based materials.

| Information / Technique | Aliphatic N | | N-doping | | Comments |
|---|---|---|---|---|---|
| **Elemental Analysis** | | | | | Allows N content determination. |
| **Thermogravimetric analysis** | Combustion starts well below the complete oxidation of the sample. | | Single combustion process. | | |
| **Contact angle** | Lower wettability than GO. | | Lower wettability than aliphatic N (and GO). | | Presence of N results in a higher contact angle than GO. |
| **FT-IR Spectroscopy** | ~1725 $cm^{-1}$ (C=O from amide groups). ~1074 $cm^{-1}$ (aliphatic amines) | | | | |
| **UV-Vis Spectroscopy (π- π* transition)** | Higher wavelength than GO. | | Higher wavelength than aliphatic N (and GO). | | Presence of N results in a red shift vs GO. |
| **UV-Vis Spectroscopy (dispersability)** | High dispersability. | | Low dispersability. | | |
| **XPS analysis (High resolution N1s spectrum)** | Amide | Amine | Pyridinic N | Pyrrolic N | Allows N content determination. |
| | | | Graphitic N | | |
| **RAMAN Spectroscopy** | | | Down shift and increase of the D band. | | Requires comparison with undoped sample. |
| **Combined techniques** | **Precise assessment of N containing species** | | | | |

**No info. can be obtained** | **Partial information** | **Conclusive information**

## 3.4. Thermal stability of N-doped reduced graphene oxide.

Thermal oxidation stability of samples treated at high temperatures (N-doped RGO) has been analyzed and correlated with their nitrogen content and temperature of treatment. In order to detect measurable differences between the behavior of the samples, the study has focused on the SNR samples that showed the highest (SNR500) and lowest (SNR800) nitrogen contents and compared to the samples of S annealed under flowing Ar at the same temperatures and treatment time (thereafter undoped SArR samples). TGA and DSC analyses of the four samples are shown in **Figure 3.17** and the onsets of the combustion temperature are summarized in Table 3.6**.**

As it has been previously established, annealing GO under an inert atmosphere results in the decomposition of functional groups leading to the formation of RGO. The higher the annealing temperature is, the lower the degree of O-bearing functionalities present in the reduced material,[160, 168] which in turn should confer the sample a higher stability against air oxidation. This is in agreement with XPS analyses and TGA data. As

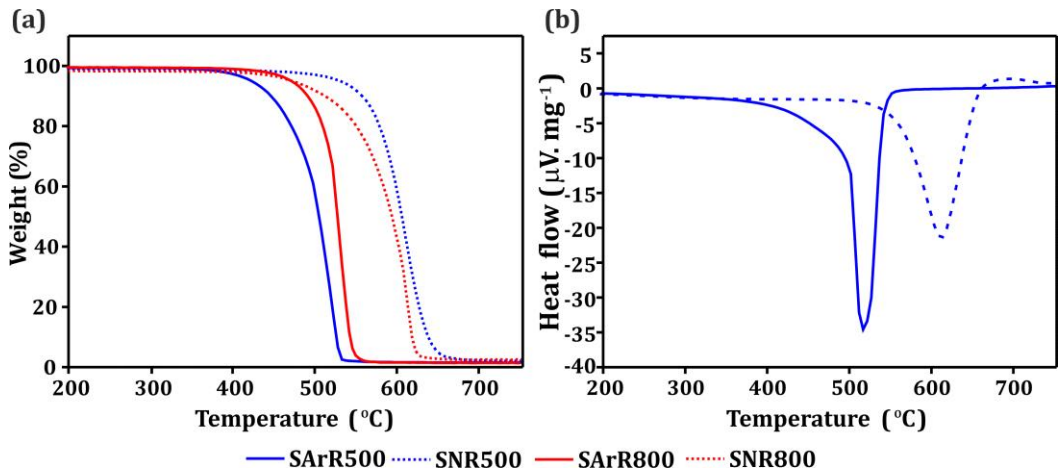


**Figure 3.17.** (a) TG analyses and (b) DSC curves of undoped RGO (SArR) and N-doped RGO ($NH_3$ treated S, SNR) prepared at 500 °C and 800 °C. TGA and DSC analyses were performed under flowing air at a heating rate of 10 °C.min$^{-1}$.

**Table 3.6.** Onset of combustion temperature in air of GO annealed in $NH_3$ (N-RGO) and Ar (RGO) at 500 °C and 800 °C.

| Temperature of treatment | Atmosphere | Onset of combustion |
|---|---|---|
| 500 °C | Argon | 417 °C |
| | Ammonia | 579 °C |
| 800 °C | Argon | 499 °C |
| | Ammonia | 520 °C |

seen in **Table 3.3** and Table 3.6, the SArR800 sample shows lower oxygen content (5.4 at. %) and higher onset of combustion temperature (red solid line, 499 °C) compared to SArR500 (blue solid line; oxygen content: 12.4 at. %; onset: 417 °C). Remarkably, the opposite trend is observed in the thermal stability of the N-doped RGO samples (dashed lines) where treatment of GO (S) in $NH_3$ at 500 °C (blue dashed line) confers a higher stability to the sample (onset: 579 °C) than after being treated at 800 °C (red dashed line; onset: 520 °C). The performed XPS analysis has revealed that $NH_3$ is more efficient than argon in reducing the oxygen present in the samples. Notably, the amount of oxygen is still higher in the SNR500 sample (3.5 at. %) compared to SNR800 (2.1 at. %). The higher stability of the SNR500 must arise from the larger amount of nitrogen (12.5 wt. %) compared to its counterpart prepared at 800 °C (7.7 wt. %). The ca. 5 wt. % difference in the nitrogen content seems to prevail over the oxygen content and be responsible for the different observed thermal oxidation stabilities.

To better appreciate the role of nitrogen on the thermal stability of RGO samples, N-doped RGO and Ar-treated S samples at the same given temperature are compared. A remarkable increase of 162 °C is observed at 500 °C (blue lines) between the undoped (blue solid line) and N-doped (blue dashed line) samples, which corresponds to about 39 % increase in thermal stability (**Figure 3.17 (a)**). The same trend, although to a lesser degree, is observed between the samples annealed at 800 °C (red lines). N-doped samples are markedly more stable against thermal oxidation in air than their non-doped counterparts. From the experimental XPS data, where N1s deconvoluted peaks (398.3-401.3 eV) have been previously assigned to pyridinic, pyrrolic and graphitic

nitrogen (**Figure 3.13**), a shoulder at higher binding energies (above 400 eV) appears in the sample prepared at 800 °C, which arises from pyrrolic and graphitic type nitrogen, the latter having a major effect. Actually a higher intensity of the fitted graphitic nitrogen peak (ca. 401.4 eV) is observed in this sample, when compared with SNR500; so the ratio of the peak intensities is clearly related with the annealing temperatures, which is in agreement with Kondo et al. reports.[195] **Table 3.7** summarizes the content of each type of nitrogen. Since the total amount of nitrogen present in SNR800 (7.7 wt. %) is much lower than SNR500 (12.5 wt. %), the total weight percent of the three types of N is also lower in SNR800. Interestingly, the weight percent of both pyridine and pyrrole decreases by about 42.5 % (40.7 % for pyridinic N, from 5.4 wt. % to 3.2 wt. %; 44.4 % for pyrrolic nitrogen, from 4.5 to 2.5 wt. %) whereas the total amount of graphitic nitrogen decreases by only 19.2 % (from 2.6 to 2.1 wt. %). Comparing the relative percentage shows the effect that temperature has on the relative fraction of each type of nitrogen. It is clear that treatment of S in $NH_3$ at higher temperatures favors the formation of graphitic nitrogen. A ca. 6 % increase in the graphitic content is observed for SNR800 with respect SNR500 (26.9 relative % graphitic nitrogen at 800 °C; 20.9 % at 500 °C). Accordingly both pyridinic and pyrrolic nitrogen suffer a ca. 3 % relative decrease. From such analyses, it is difficult to attribute the enhanced thermal stability of N-doped samples to the presence of a particular type of nitrogen.

To get further insights on the stability that N-doping confers to the samples, we looked at the thermodynamic aspects of the combustion reaction for each type of nitrogen and

**Table 3.7.** Nitrogen content determined by elemental analysis (total content) and XPS (ratio of nitrogen types) in samples of N-doped RGO prepared at 500 ˚C and 800 ˚C in $NH_3$.

| Sample | | Total N | Pyridine N | Pyrrolic N | Graphitic N |
|---|---|---|---|---|---|
| SNR500 | N (wt %) | 12.5 | 5.4 | 4.5 | 2.6 |
| | % | 100 | 43.4 | 35.7 | 20.9 |
| SNR800 | N (wt %) | 7.7 | 3.2 | 2.5 | 2.1 |
| | % | 100 | 40.8 | 32.3 | 26.9 |

carbon for undoped S, considering the fragments depicted in the reactions of **Scheme 3.4**. The enthalpy of combustion for each type of nitrogen, which can be estimated from the mean bond enthalpies (averages of bond enthalpies over a related series of compounds) for the gas-phase reaction, was first worked out.[196] The enthalpy changes accompanying the breaking of C-C(C=C), C-N(C=N) and O=O bonds in a typical reaction of combustion, and the subsequent formation of the oxidation products ($CO_2$ and $N_2$, as per Atkins and Paula[197]) must be considered (**Table 3.8**). The estimated combustion enthalpy for the NC2 (pyrrolic and pyridinic N), NC3 (graphitic N) and CC3 (graphene) fragments, depicted in **Scheme 3.4**, is -1760 kJmol$^{-1}$, -2560 kJmol$^{-1}$, and -3124 kJmol$^{-1}$, respectively. Comparison between the combustion of N-containing moieties reveals that whereas both pyrrolic and pyridinic nitrogen have the same enthalpies of combustion, the oxidation of nitrogen in a graphitic environment leads to the release of more energy. Furthermore, the combustion of a graphene fragment (with no N) is more exothermic than that of an N-doped structure. The enthalpy of a transition can be determined from differential scanning calorimetry (DSC) measurements. DSC analyses of the SArR500 and SNR500 samples are registered in **Figure 3.17 (b)**. A more exothermic process is observed for the undoped RGO combustion compared to the N-doped sample. The enthalpy of the process is proportional to the integrated area of the associated peaks, having a value of -11013 μV.s.mg$^{-1}$ for the SArR (Ar treated) and -7707 μV.s.mg$^{-1}$ for the SNR ($NH_3$ treated). This is in good agreement with the thermodynamic calculations, which predict the release of

**Table 3.8.** Mean bond enthalpies ($\Delta H$) involved in the combustion reaction of SArR and SNR samples.[196]

| Bond | $\Delta H$ (kJ.mol$^{-1}$) |
|---|---|
| C-C | 345.6 |
| C=C | 602 |
| C-N | 304.6 |
| C=N | 615 |
| O=O | 493.6 |
| C=O ($CO_2$) | 799 |
| N≡N | 941.7 |

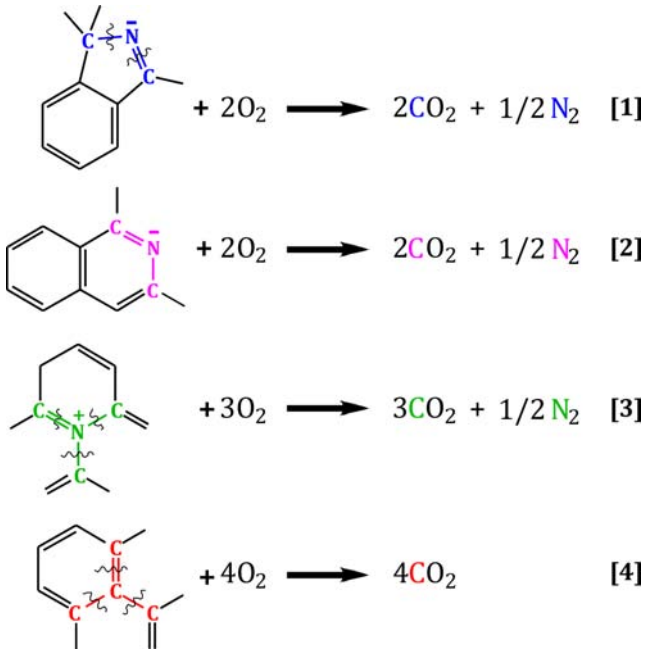


**Scheme 3.4.** Combustion reactions for the different types of nitrogen and carbon present in N-doped RGO (1-3) and RGO (4).

more energy for the combustion of undoped samples. Finally, the Gibbs energy ($\Delta G$) has been calculated to estimate the spontaneity of the combustion reaction for each of the considered fragments (reactions 1-4, **Scheme 3.4**). For ease of comparison, and taking into account that the combustion of all the samples starts to occur in the 417–579 °C range, the temperature was fixed at the mean value of 500 °C for the calculation of both $\Delta S$ and $\Delta G$. The entropy changes for the reactions of oxidation of RGO and N-doped RGO at 500 °C (773 K, $T_2$) were calculated using the tabulated data for the entropy values of the compounds involved in the combustion at 298 K ($T_1$), and the heat capacity, $\Delta C_p$ (assumed to be constant) at the initial temperature.[198] Thus,

$$\Delta S_{(T_2)} = \Delta S_{(T_1)} + \Delta C_p \ln\left(\frac{T_2}{T_1}\right)$$

Estimated values of $\Delta G_{500}$ of -1870 kJ.mol$^{-1}$, -2682 kJ.mol$^{-1}$, and -3176 kJ.mol$^{-1}$ have been obtained for $NC_2$, $NC_3$, and $CC_3$ systems, respectively (**Table 3.9**). From the obtained values, both pyridinic and pyrrolic N are expected to confer a higher thermal stability to the system than graphitic N. The calculated $\Delta G$ further supports the experimental observation because from a thermodynamic point of view the reaction of undoped samples with oxygen is more spontaneous than when nitrogen is present.

**Table 3.9.** Changes in the Gibbs Energy ($\Delta G$) for the combustion reactions of RGO and N-doped RGO.

| Reaction | $\Delta C_p$ (kJ.K$^{-1}$.mol$^{-1}$) | $\Delta S_{298}$ (kJ.K$^{-1}$.mol$^{-1}$) | $\Delta S_{773}$ (kJ.K$^{-1}$.mol$^{-1}$) | $\Delta G$ (kJ.mol$^{-1}$) |
|---|---|---|---|---|
| (1-2) | 30.1 | 113.1 | 141.8 | -1869.6 |
| (3) | 37.8 | 121.7 | 157.8 | -2681.9 |
| (4) | 31.0 | 34.6 | 66.2 | -3175.6 |

## 3.5. High temperature post-synthesis treatments.

As we have shown, N-containing RGO can be prepared by annealing GO under $NH_3$. By controlling the temperature of treatment, not only the level of reduction, but also the nature of the N-based functionalities can be easily tuned. Lower temperatures result in the introduction of N-containing aliphatic functionalities into the sample, whereas the formation of more stable nitrogen species (N-doping) requires the use of higher temperatures. N-doping confers the sample an enhanced stability against thermal oxidation.[172] In light of these results, high temperature post-synthesis treatments of the N-containing RGO samples have been carried out. The role of the annealing temperature as well as the atmosphere employed during the treatment on the thermal and structural properties of the samples was evaluated. N-containing samples, prepared at temperatures ranged between 220 ˚C and 800 ˚C, were selected to explore how the characteristics of these initial materials (nitrogen content and nature of the N-based groups) change with the annealing process. For this purpose, different sets of

samples were prepared and for ease of comparison, the influence of each parameter will be analyzed separately. In some cases the data obtained after the characterization of a given sample will be included in more than one table and/or figure to facilitate the analysis of the results.

### 3.5.1. Role of the atmosphere used in the treatments.

Initially, in order to analyze the role of the gas on the final content of nitrogen, a 500 °C N-doped RGO sample (LNR500) was annealed at 1050 °C under three non-oxidant atmospheres ($N_2$, Ar and $Ar/H_2$). As mentioned before, the 500 °C treatment leads to the highest level of doping. A small amount of oxygen groups are still present in LNR500 after the ammonolysis treatment (6 % as determined by XPS, **Table 3.10**).

A control sample was prepared by annealing L at 1050 ˚C under $N_2$ ($L1050N_2$) following the same protocol applied to the N-doped samples. This allowed us to determine any possible interaction of the oxygen-bearing functionalities with the flowing gas ($N_2$), since $N_2$ (plasma treatment) has been used for the synthesis of nitride-based compounds.[13] Thus, the samples were treated during 2 hours at 1050 ˚C under the chosen atmosphere and were cooled down to room temperature. **Table 3.10** and **Table 3.11** show the carbon, nitrogen and hydrogen composition of the annealed samples as determined by XPS and elemental analyses respectively. After treatment of GO (L) under $N_2$ no significant changes in the nitrogen content are observed. Thus, the use of $N_2$

**Table 3.10.** Nitrogen, oxygen and carbon atomic content (at. %, determined by XPS) present in LNR500 (500 °C $NH_3$ treated L sample) before and after annealing at 1050 °C under Ar, $N_2$ and $Ar/H_2$.

| Sample | C (at. %) | N (at. %) | O (at. %) |
|---|---|---|---|
| LNR500 | 85.5 | 8.5 | 6 |
| LNR500-1050$N_2$ | 92 | 3.7 | 4.3 |
| LNR500-1050Ar | 87.1 | 4.4 | 8.5 |
| LNR500-050$Ar/H_2$ | 95.8 | 1.3 | 2.9 |

gas is not expected to contribute towards the final nitrogen content in the LNR500 post-treated samples. As expected, both the N-doped RGO and L samples showed an increase in the final content of carbon by the annealing treatment, as consequence of the elimination of the remaining aliphatic functionalities present in the samples. For the high temperature treated N-doped RGO sample, some differences are observed in the final composition as a function of the employed gas. In all the cases a decrease in the nitrogen content was observed, from 9.6 wt. % in LNR500 to 4.9 wt. % when LNR500 was treated under Ar (LNR500-1050Ar) and $N_2$ (LNR500-1050$N_2$). This represents a 49 % of decrease in the nitrogen content of the samples. Even a more dramatic decrease (68.8 % N) is observed when an Ar/$H_2$ atmosphere was employed (LNR500-1050 Ar/$H_2$; 2.9 wt. % N).

**Table 3.11.** Composition of carbon, nitrogen and hydrogen (wt. % determined by elemental analysis) present in L and LNR500 (500 °C $NH_3$ treated L samples) annealed at 1050 °C under different inert atmospheres.

| Sample | C (wt. %) | N (wt. %) | H (wt. %) |
|---|---|---|---|
| L1050$N_2$ | 94.9 | 0.3 | 0.2 |
| LNR500 | 81.3 | 9.6 | 0.9 |
| LNR500-1050$N_2$ | 90.0 | 4.9 | 0.2 |
| LNR500-1050Ar | 91.0 | 4.9 | 0.3 |
| LNR500-1050Ar/$H_2$ | 91.7 | 3.0 | 0.3 |

As previously described (**Section 3.3.2**), XPS is usually employed to differentiate the functionalities present in the samples because the binding energies of the core elements in the atoms are strongly dependent on their chemical environment. After the deconvolution of the high-resolution spectra of the elements, small variations in the position of the peaks allow both the identification and the quantification of the chemical groups contained in the material. As shown in **Table 3.12** the LNR500-1050Ar and the LNR500-1050$N_2$ samples did not suffer important variations in the distribution of both the $sp^2$ band and the signal corresponding to functionalized carbon atoms. On the other hand, the XPS spectrum of the LNR500 sample treated at 1050 ˚C under Ar/$H_2$ (LNR500-1050Ar/$H_2$) did show significant changes in the amount and distribution of the

**Table 3.12**. Carbon, nitrogen and oxygen atomic content (at. %, determined by XPS) present in LNR500 (500 °C $NH_3$ treated L sample) before and after annealing at 1050 °C under Ar, $N_2$ and $Ar/H_2$. In all cases the contribution of the specific functionalities is registered.

| Specie | | Sample | | | |
|---|---|---|---|---|---|
| | | LNR500 | LNR500-1050Ar | LNR500-1050$N_2$ | LNR500-1050$Ar/H_2$ |
| C content (at. %) | RC=CR | 43.1 | 42.3 | 49.7 | 60.4 |
| | Functionalized carbon | 42.4 | 44.8 | 42.3 | 35.4 |
| | **Total** | **85.5** | **87.1** | **92** | **95.8** |
| N content (at. %) | Pyridinic N ($C_5N$:) | 3.8 | 1.8 | 1.1 | 0.3 |
| | Pyrrolic N ($C_4N$:) | 3.4 | 0.9 | 0.7 | 0.2 |
| | Graphitic N ($C_4N^+$) | 1.3 | 1.0 | 1.3 | 0.6 |
| | Pyridinic $N^+O^-$($C_4N^+$-$O^-$) | -- | 0.7 | 0.6 | 0.2 |
| | **Total** | **8.5** | **4.4** | **3.7** | **1.3** |
| O content (at. %) | $^-O_2CR$ | 2.6 | 4.9 | 1.6 | 1.3 |
| | $OCR_2$ | 2.3 | 2.6 | 2.1 | 1.6 |
| | $^-OCR_3$ | 1.1 | 1 | 0.6 | -- |
| | **Total** | **6** | **8.5** | **4.3** | **2.9** |

species. **Figure 3.18** shows the deconvoluted high resolution C1s **(c)** and O1s **(d)** spectra of the 1050 ˚C $Ar/H_2$ treated sample. The spectra of the initial material (LNR500) are included for comparison. After exposure of the N-doped RGO to the annealing treatment an increase in the signal corresponding to the $sp^2$ carbon is evident (ca. 40 %, **Table 3.12**). As a consequence, a decrease in the contribution of the functionalized carbon (oxygen and nitrogen-based species) is produced. In the case of the O1s signal, drastic changes in the shape and even number of deconvoluted peaks are observed. A significant decrease in the concentration of the carboxylic and ketone groups is produced (50 % and 30 % respectively); however, the most evident variation is the disappearance of the signal corresponding to the oxygen groups directly related to the RGO lattice.

The presence of molecular hydrogen in the flowing gas may induce a further reduction of the sample. Mikoushkin *et al.* have studied the hydrogenation of GO by thermal reduction (T > 750 ˚C) in $H_2$.[199] The elimination of the C-O groups may be induced either by the high temperature treatment (restoring the C=C conjugation) or by the introduction of hydrogen atoms (from the flowing gas) in the conjugated graphitic struc-

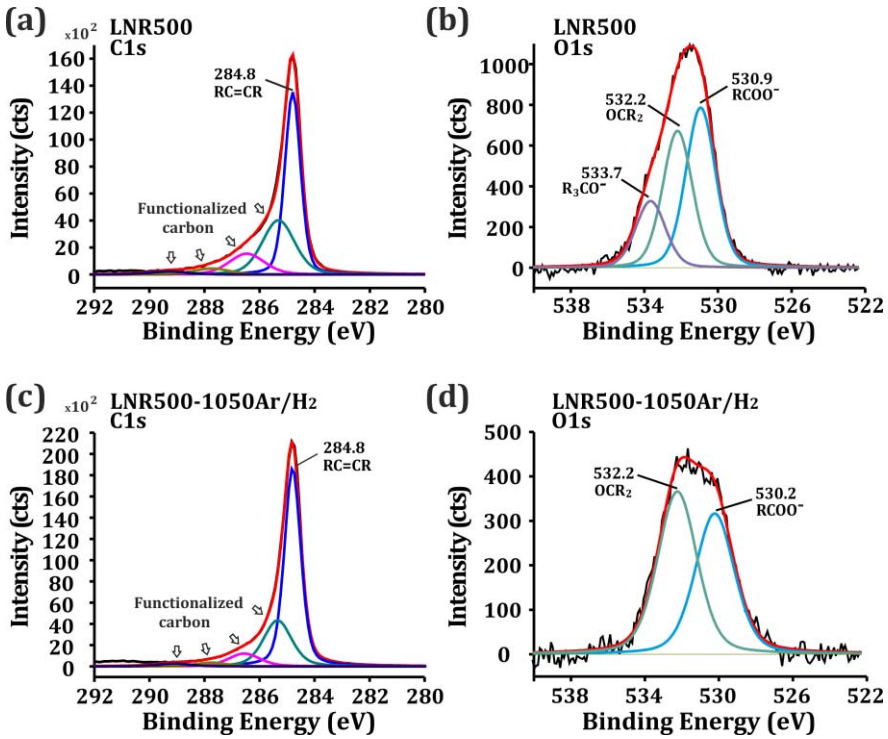


**Figure 3.18.** High resolution (a, c) C1s and (b, d) O1s spectra of LNR500 and LNR500-1050Ar/$H_2$ samples respectively.

ture. Moreover, the hydrogen atoms can act as reducing agents of the oxidized aliphatic moieties. The hydrogenation process of the RGO lattice may induce the formation of $sp^3$ defects in the surroundings of the N-containing sites. This modification can alter the reactivity of the material favoring the elimination of nitrogen from the structure; which would explain the highest decrease in the nitrogen content of the LNR500-1050Ar/$H_2$ if compared to the LNR500 when treated in presence of Ar or $N_2$.

TGA were next carried out to analyze the influence of the variations observed in the composition of the samples in their thermal stabilities (**Figure 3.19**). For the LNR500-1050Ar/$H_2$ sample (continuous green line), a 60 °C decrease in the onset of combustion (506 °C) was observed against the LNR500 sample (pink dashed line). This behavior is in agreement with the results obtained for the S-based samples (SNR), confirming the

important role of the nitrogen species in the thermal stability of reduced RGO. The combustion of the sample with the lowest nitrogen content (3 wt. %) is observed at the earliest temperature. Surprisingly, TGA data of the LNR500-1050Ar (continuous blue line) and the LNR500-1050$N_2$ (continuous orange line) samples show the inverse trend. Both post annealed samples show a slight enhanced thermal stability (**Table 3.13**), despite the marked decrease in their nitrogen content (4.9 wt. %).

One could think that the reductive character of the flowing Ar/$H_2$ should produce an enhanced thermal stability due of the highest elimination of oxygen-bearing moieties (2.9 at. % O); nevertheless, the introduction of hydrogen within the RGO lattice after the annealing treatment in presence of $H_2$ may induce the formation of defect sites ($sp^3$ hybridized sites), contributing to the decrease of the thermal stability of the sample.

As mentioned, samples treated under argon and nitrogen showed an increase in their onset of combustion. Focusing on the atomic composition of the samples slight differences can be observed. LNR500-1050Ar and LNR500-1050$N_2$ contain similar amount of nitrogen, but the oxygen composition of the argon-treated sample (8.5 at. % O)

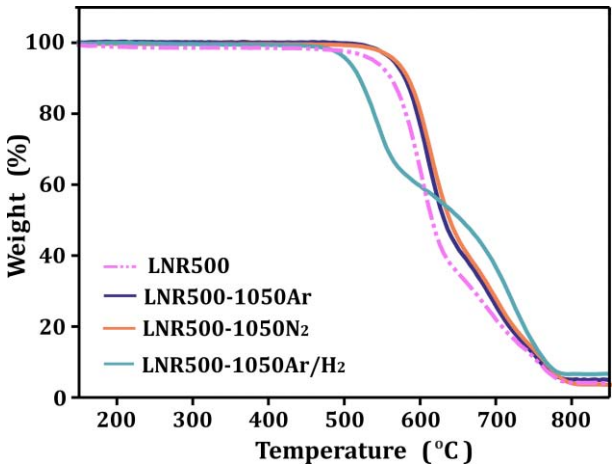


**Figure 3.19.** TGA of N-doped RGO sample prepared under $NH_3$ at 500 °C before (dashed line) and after (continuous lines) annealing treatment under $N_2$ (orange), Ar (blue) and Ar/$H_2$ (green) at 1050 °C. TGA were performed under flowing air at a heating rate of 10 °C.min$^{-1}$.

**Table 3.13.** Onset of combustion temperature in air of the 500 °C ammonia-treated L sample (LNR500) after annealing at 1050 °C under Ar (LNR500-1050Ar), $N_2$ (LNR500-1050$N_2$) and Ar/$H_2$ (LNR500-1050Ar/$H_2$ ).

| Sample | Onset of Combustion |
|---|---|
| LNR500 | 566 °C |
| LNR500-1050$N_2$ | 581 °C |
| LNR500-1050Ar | 578 °C |
| LNR500-1050Ar/$H_2$ | 506 °C |

duplicates the amount determined in the sample treated under $N_2$ (4.3 at. % O). A higher thermal stability would be expected for the LNR500-1050$N_2$ sample. Furthermore, if the same discernment is applied for all the materials, LNR500 should be more stable than its counterpart treated under argon, due to its lower oxygen content (6 at. % O). Analyzing the obtained results, the observed trend cannot be explained a priori, either in terms of the total atomic composition of the samples or by the mean bond enthalpies, as previously explained for the N-doped RGO samples. However, these results reinforce our findings which indicate that the thermal stability of the N-doped RGO (against oxidation by air) is mainly governed by the presence and nature of the N-based moieties and that in this case, the oxygen content plays a minor role.

Considering that the functionalities present in the N-containing RGOs are responsible of the physicochemical properties of the materials (including their thermal stability), and that their presence is markedly affected by the temperature of the ammonolysis treatments;[200] structural changes in the high temperature treated samples are expected. **Figure 3.20** shows the high resolution N1s XPS spectra of the N-doped sample before and after the post synthesis treatments. For the N-doped RGO, three different peaks, corresponding to pyridinic nitrogen (ca. 398.5 eV), pyrrolic nitrogen (ca. 400 eV) and graphitic nitrogen (ca. 401 eV) are frequently reported.[190] Nevertheless, after the 1050 °C annealing treatments an additional signal arising above 403 eV is observed. The position of this peak corresponds to positive charged pyridinic nitrogen, usually stabilized by negative oxygen atoms (pyridine N-oxide).[197] Beyond the appearance of a new signal, the most relevant change observed in the N1s spectra is

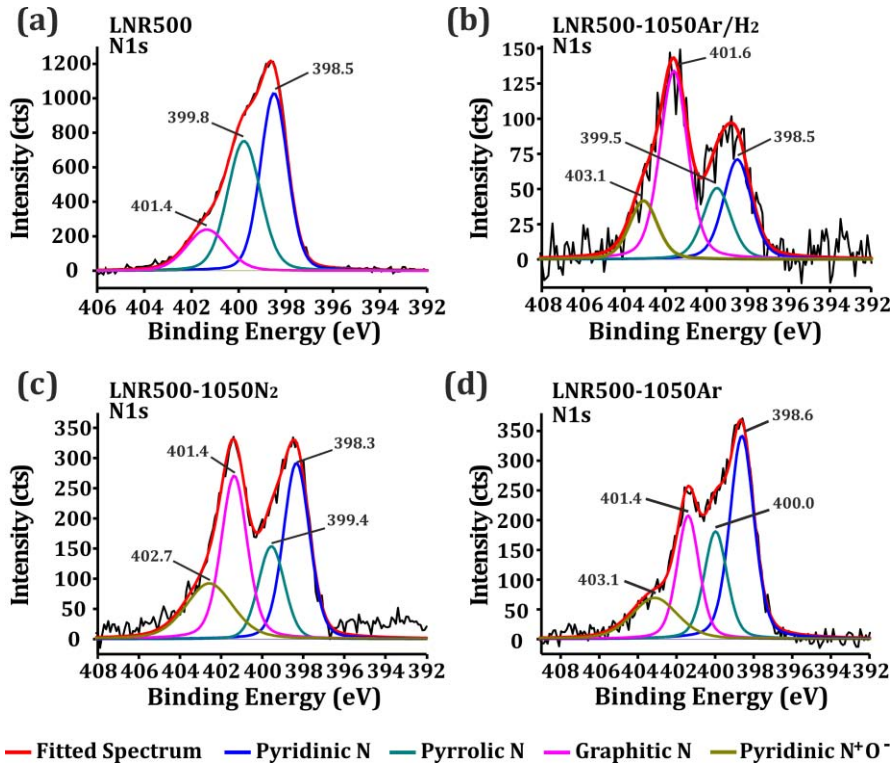


**Figure 3.20.** High-resolution N1s spectra of (a) LNR500, (b) LNR500-1050Ar/$H_2$, (c) LNR500-1050$N_2$ and (d) LNR500-1050Ar samples.

the decrease of the pyrrolic and pyridinic nitrogen contents after the high temperature treatments. The thermal stability of the Ar and $N_2$-treated samples is markedly enhanced, despite the abrupt elimination of the nitrogen present in the five and six-membered rings. The observed increase in thermal stability could arise from the decrease of the pyrrolic species, which have been reported by Kundu et al. as the less stable of the structural nitrogens. The authors have studied the thermal stabilities of N-containing carbon nanotubes,[201] finding that ca. 49 % of the pyrrolic nitrogen is already removed at 700 °C. The content of graphitic nitrogen remains almost invariable after the thermal treatment, which is in agreement with the high stability reported for these N-based moieties. The graphitic N is the most stable functionality when compared

with pyridinic and pyrrolic N.[201] On the other hand, the six-membered structure of the pyridine N-oxide could also contribute to the stability of the sample.

As discussed, LNR500-1050Ar and LNR500-1050$N_2$ present differences in the degree of oxidation (8.5 at. % O and 4.3 at. % O respectively). The similar stabilities of the samples can be explained by the slightly higher amount of nitrogen present in the LNR500-1050Ar (4.4 at. % N, **Table 3.12**) against the 3.7 at. % N determined for the sample prepared under $N_2$. Moreover, the higher amount of six-membered rings which are more stable than five-membered cyclic moieties can also contribute to the stability of the Ar-treated samples. Finally, the lower stability of the LNR500-1050Ar/$H_2$ sample can be explained in terms of the distribution of the nitrogen moieties. The significant decrease in the structural nitrogen-containing groups, and specially the elimination of a ca. 50 % of the graphitic moieties produce the earlier combustion of the material.

Pyridine N-oxide groups are probably generated by internal rearrangements or either by the interaction of unstable nitrogen, contained in six-membered rings, with oxygen from the O-bearing functionalities remaining after the 500 °C ammonolysis treatment (6 at. % O). In the LNR500-1050Ar/$H_2$ sample the formation of these species is not favored due to the highly reductive character of the Ar/$H_2$ mixture, which induces the elimination of the oxygen-based groups.

### 3.5.2. Role of the functionalities present in the starting material.

Taking into account that thermal treatments clearly induce both, the elimination of the less stable species and internal structural rearrangements, the nature of the initial functionalities could play a major role in the final structure of the samples. As previously discussed ammonia treatments at 220 °C not only produce the formation of nitrogen-based aliphatic moieties (functionalization), but also cause the incorporation of nitrogen into the graphitic lattice. When this temperature is employed for the ammonolysis, the highest content of nitrogen is achieved, whilst presenting a

significant amount of O-bearing functionalities in the sample. Otherwise, the 800 °C ammonia treated L (LNR800) has been registered as the material with the highest degree of reduction. Furthermore, the totality of the N-based groups present in the sample corresponds to structural species, namely pyridinic, pyrrolic and graphitic N. For these reasons both materials were chosen for the post-annealing studies, due to the wide difference in their structural conformation. The LNR220 and LNR800 samples were annealed at temperatures ranged between 500 °C and 1050 °C under an inert atmosphere. As we have shown in the previous section, the atmosphere employed for the annealing treatment may induce changes in the composition of the samples. For this reason, the treatments were carried out under the same inert gas. Samples were prepared by placing the N-containing RGO previously prepared by annealing GO under $NH_3$ at 220 °C (LNR220) and 800 °C (LNR800) into a tubular furnace. The system was purged with argon to eliminate any trace of oxygen and subsequently dwelled for 2 h at the chosen temperature. After cooling down, the composition of the samples was determined by elemental analysis, and XPS measurements. TG curves were recorded to evaluate the stability of the samples against its oxidation by air.

**Table 3.14.** Composition of carbon, nitrogen and hydrogen (wt. %, determined by elemental analysis) present in LNR220 and LNR800 before and after annealing at 1050 °C under Ar.

| Sample | C (wt. %) | N (wt. %) | H (wt. %) |
|---|---|---|---|
| LNR220 | 72 | 9.8 | 1.3 |
| LNR220-1050Ar | 92.4 | 4.0 | 0.2 |
| LNR800 | 90.0 | 5.6 | 0.2 |
| LNR800-1050Ar | 92.3 | 3.5 | 0.2 |

**Table 3.14** shows the composition of the samples as determined by elemental analysis before and after the 1050 ˚C treatment. After annealing both, LNR220 and LNR800 present an increase in the concentration of carbon, accompanied by the removal of nitrogen atoms from the material. In the case of the LNR220, the decrease in the N content could correspond to removal of aliphatic moieties (amine or amide groups) as well as structural nitrogen. On the other hand, LNR800 was strictly composed by

nitrogen atoms directly linked to the RGO lattice. Thus, the eliminated species correspond to pyridinic, pyrrolic and graphitic N fractions.

**Figure 3.21** shows the TGA of the prepared samples after annealing at 1050 °C under argon. Thermal analyses of the N-doped samples before treatment are included for comparison. All the high temperature treated samples showed an enhanced thermal stability, compared to the former materials. However, the highest difference was observed for the 1050 °C Ar treated LNR220 (LNR220-1050Ar, red continuous line), due to the disappearance of the continuous loss of weight (220 °C-440 °C) present in LNR220 (blue dashed line). This thermal event corresponds to the elimination of the aliphatic functionalities (oxygen and nitrogen-bearing moieties). Furthermore, the onset of combustion of the sample presented a slight increase, reaching a similar stability to the LNR500-1050Ar sample (blue continuous line, **Table 3.15**). Considering that nitrogen-aliphatic moieties (amine/amides) introduced by ammonolysis treatments were removed after the argon treatment, synthesized samples are referred hereinafter as N-doped RGO. In case of the 1050 ˚C treated LNR800 (LNR800-1050Ar, grey continuous line), although the sample was treated under the same conditions, the lo-

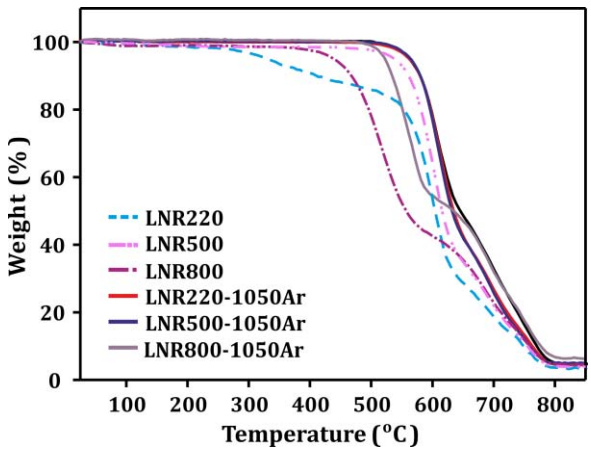


**Figure 3.21.** Thermogravimetric analyses of nitrogen containing RGO samples (220 °C, 500 °C and 800 °C) after thermal treatment at 1050 °C under Ar atmosphere. Thermal analyses of the starting materials are included for comparison. Analyses were performed under flowing air at a heating rate of 10 °C.min$^{-1}$.

**Table 3.15.** Onset of combustion temperature in air of the nitrogen containing materials (LNR) before and after treatments under argon at 1050 °C.

| Sample | Onset of Combustion |
|---|---|
| LNR220 | 549 °C (2nd weight loss) |
| LNR500 | 566 °C |
| LNR800 | 471 °C |
| LNR220-1050Ar | 578 °C |
| LNR500-1050Ar | 578 °C |
| LNR800-1050Ar | 525 °C |

west onset of combustion (525 °C) is observed. As previously reported the 800 °C ammonia treatment is the most effective temperature to eliminate oxygen-bearing aliphatic groups but also is responsible of the lowest introduction of nitrogen within the N-doped RGO lattice. The low concentration of N-based structural groups leads to a sample with relatively low thermal stability (**Section 3.3.2**), when compared with the samples treated under lower temperatures (500-700 °C $NH_3$-treated samples). Surprisingly, the same trend is observed for high temperature treatments. Despite that the onset of combustion of LNR800 (471°C) shows the highest increase (54 °C, **Table 3.15**) after the 1050 °C treatment, the final stability of the resulting material is still the lowest among this set of Ar-treated samples.

XPS was carried out to determine the distribution of the functionalities within the RGO lattice and their influence in the thermal behavior of the samples. **Figure 3.22** shows the high resolution O1s XPS of the LNR220 **(a)** and LNR800 **(b)** samples and the 1050 °C treated ones (LNR220-1050Ar **(c)** and LNR800-1050Ar **(d)**) under argon. There is no a direct trend between the distribution of the oxygen-bearing moieties and the temperature of treatment. Interestingly, a new peak (BE ca 534 eV) is observed after annealing the LNR220 sample at 1050 °C. This signal, previously observed in argon-treated GO samples (500 °C and 800 °C, **Figure 3.14**), can be assigned to aromatic derivatives (mainly PhOCOOPh groups). Taking into account that the starting sample is the most oxidized among the evaluated nitrogen-containing RGO samples; the formation of these groups could arise from the condensation reactions of phenolic func-

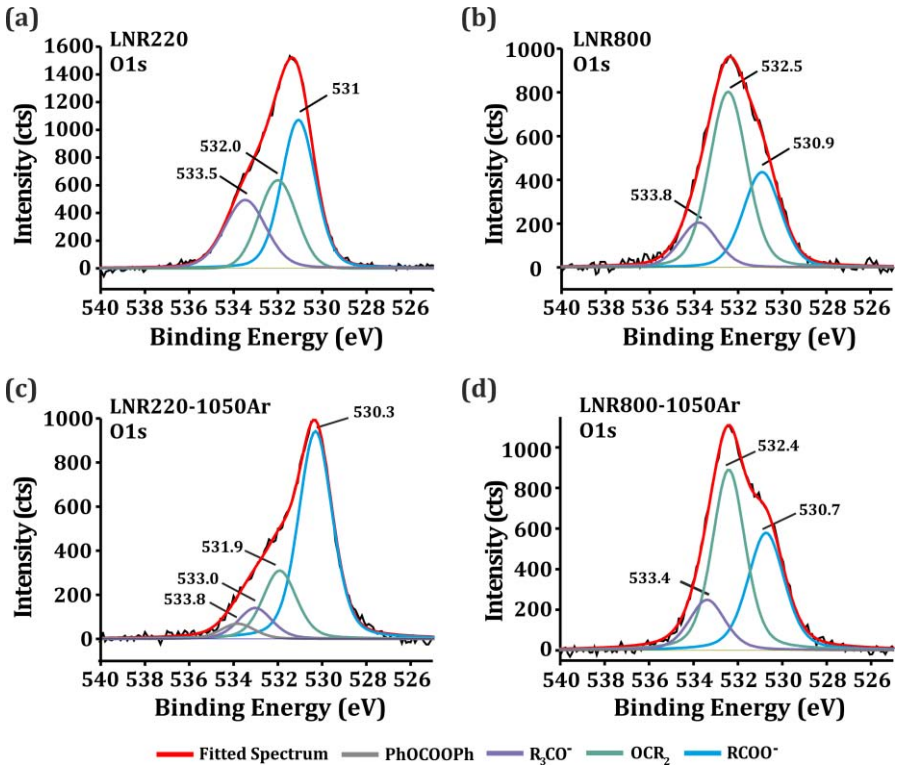


**Figure 3.22.** High Resolution O1s XPS of the 220 ˚C N-containing RGO (LNR220) and the 800 ˚C N-doped RGO (LNR800) (a-b) before and (c-d) after the 1050 ˚C treatment under Ar respectively.

tionalities still present after the initial treatment under ammonia.

The variation in the concentration of the functionalities can be also appreciated in the high resolution C1s data (**Table 3.16**). The 1050 ˚C treatments produce the increase in the C=C signal due to the elimination of nitrogen and oxygen-bearing moieties. Slight differences are observed in the N1s spectra of the Ar-treated samples. The presence of the pyridinic N-oxide groups (ca. 403 eV) is observed for both, the initially N-functionalized and N-doped samples. Considering the numerical values obtained after the analysis of the data (**Table 3.16**), similar results were observed for the total amount of nitrogen in the LNR220 and LNR500 samples after the 1050 °C treatment (4.0 at. % and 4.4 at. % N respectively). The atomic content of pyridinic, pyrrolic, graphitic N and pyridine N-oxide groups is in agreement with the overlapping observed

in the TG curves. The highest elimination of the N-containing species from the low temperature $NH_3$-treated sample (LNR220, ca. 81 % for the pyrrole/amine group) could be explained by the presence of N-aliphatic functionalities (amides/ amides) which are not present in the N-doped sample (LNR500). However, the signal corresponding to graphitic nitrogen remains almost invariable confirming that this temperature (220 °C) is already useful to introduce highly stable functionalities, which indeed contribute to the high stability of the material against its oxidation by air. For the LNR800-1050Ar the lower concentration of O-bearing functionalities produces the formation of a smaller amount of pyridine N-oxide groups (0.3 at %). The highest decrease of the total N-content would explain the lowest onset of combustion, if compared with the Ar-treated samples (525 °C, **Table 3.15**), despite that this sample presents the highest restoring of the C=C lattice (92.2 at % C).

**Table 3.16.** Carbon, oxygen and nitrogen content (at. % determined by XPS) of $NH_3$-treated L (220-800 °C) before and after 1050 °C treatment under argon, determined by XPS analysis. (*) These values could correspond to aliphatic functionalities ($CONH_2/CNH_2$) or to structural pyridinic ($C_5N$:) and pyrrolic ($C_4N$:) groups.

| Specie | | Sample | | | | |
|---|---|---|---|---|---|---|
| | | LNR220 | LNR800 | LNR220-1050Ar | LNR500-1050Ar | LNR800-1050Ar |
| C content (at. %) | RC=CR | 40.5 | 48.5 | 50.7 | 42.3 | 63.4 |
| | Functionalized carbon | 41.0 | 41.1 | 40.5 | 44.8 | 28.8 |
| | **Total** | **81.5** | **89.6** | **91.2** | **87.1** | **92.2** |
| N content (at. %) | Pyridinic N ($C_5N$:) | 2.9* | 2.2 | 1.2 | 1.8 | 0.6 |
| | Pyrrolic N ($C_4N$:) | 4.7* | 1.7 | 0.9 | 0.9 | 0.4 |
| | Graphitic N ($C_4N^+$) | 1.6 | 1.6 | 1.0 | 1.0 | 0.4 |
| | Pyridinic $N^+$-$O^-$($C_4N^+$-O) | -- | -- | 0.9 | 0.7 | 0.3 |
| | **Total** | **9.2** | **5.5** | **4.0** | **4.4** | **1.7** |
| O content (at. %) | $^-O_2CR$ | 4.3 | 1.5 | 3.1 | 4.9 | 2.2 |
| | $OCR_2$ | 2.6 | 2.7 | 1.0 | 2.6 | 3.0 |
| | $^-OCR_3$ | 2.4 | 0.7 | 0.5 | 1.0 | 0.9 |
| | PhOCOOPh | -- | -- | 0.2 | -- | -- |
| | **Total** | **9.3** | **4.9** | **4.8** | **8.5** | **6.1** |

### 3.5.3. Role of temperature.

As we have just seen, 1050 °C treatments under oxygen free atmospheres are useful for the elimination of oxygen-bearing functionalities, allowing the structural modification of the N-doped RGO lattice. The high temperature treatments induce an enhanced thermal oxidation stability against air, but at the same time, the elimination of a remarkable amount of nitrogen from the sample is observed. The synthesis of N-doped RGO at 500 °C and 800 °C under $NH_3$ induces a high thermal stability and the elimination of oxygen-based groups respectively. For these reasons, these temperatures were chosen for a new set of high temperature treatments under argon, aiming to obtain a high elimination of the less stable oxidized groups whilst minimizing the removal of the N-based functionalities. Following a protocol similar to that employed before, N-containing RGO samples (220 °C and 500 °C $NH_3$ treated samples) were annealed at 500 °C and 800 °C. When relevant, the data previously obtained with the treatments at 1050 °C are also included in the tables and figures for ease of comparison. In all the cases, the temperature employed for the Ar treatment was higher

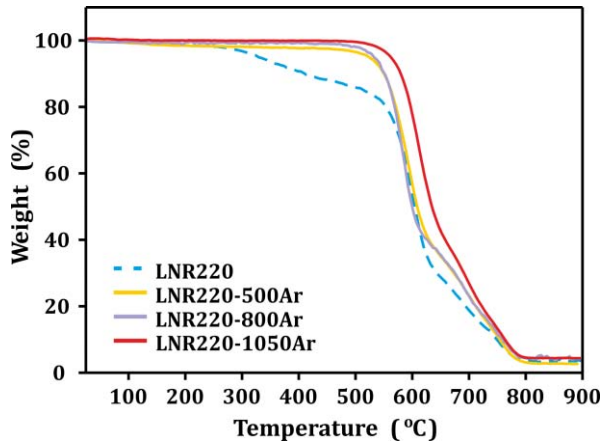


**Figure 3.23.** Thermogravimetric analyses of the 220 °C nitrogen functionalized RGO sample before (LNR220) and after thermal treatment at 500 °C (LNR220-500Ar), 800 °C (LNR220-800Ar) and 1050 °C (LNR220-1050Ar) under argon. Analyses were performed under flowing air at a heating rate of 10 °C.min$^{-1}$.

**Table 3.17.** Onset of combustion temperature in air of the nitrogen-containing materials (LNR) before and after treatments under argon at 500 °C, 800 °C and 1050 °C.

| Sample | Onset of Combustion |
|---|---|
| LNR220 | 549 °C (2nd weight loss) |
| LNR220-500Ar | 557 °C |
| LNR220-800Ar | 550 °C |
| LNR220-1050Ar | 578 °C |

than that employed for the preparation of the N-containing RGO.

**Figure 3.23 (a)** shows the TG curves of the LNR220 sample before and after annealing under argon at 500 °C, 800 °C and 1050 °C. After any of these treatments the disappearance of the weight loss corresponding to the aliphatic fraction present in the LNR220 sample (250°C -500 °C, blue dashed line) and a slight increase in the onset of complete combustion is observed (**Table 3.17**). These results are in agreement with the XPS data, where restoring of the conjugation is observed, as well as a decrease in the oxygen content when the temperature is increased (**Table 3.18**). Both, the 500 °C and the 800 °C post-annealed samples present similar thermal stabilities; meanwhile the highest onset of combustion was obtained for the LNR220-1050Ar sample (578 °C).

A priori, higher differences in the thermal behavior of the LNR220-500Ar and LNR220-800Ar samples would be expected due to the differences in their total content of nitrogen). The similar thermal stability might account for (i) the level of reduction of the samples and the higher elimination of the O-bearing functionalities on the sample treated at 800 ˚C. Thus, despite this sample has a lower concentration of nitrogen (5.4 at. %), these factors might increase the thermal stability. The sample treated at 1050 ˚C presented the highest level of reduction among the Ar-treated samples, and the lowest concentration of nitrogen (4.0 at. %). Analysis of the high resolution N1s XPS of the LNR220 Ar-treated samples reveals the presence of the pyridine-N-oxide species (BE ca. 403 eV, **Figure 3.24 (a-c)**). The concentration of these groups is directly related with the temperature of treatment. Whereas graphitic-nitrogen groups maintains its concentration unchanged (ca. 1.0 at. %), a progressive decrease of the pyrrolic/amine sig-

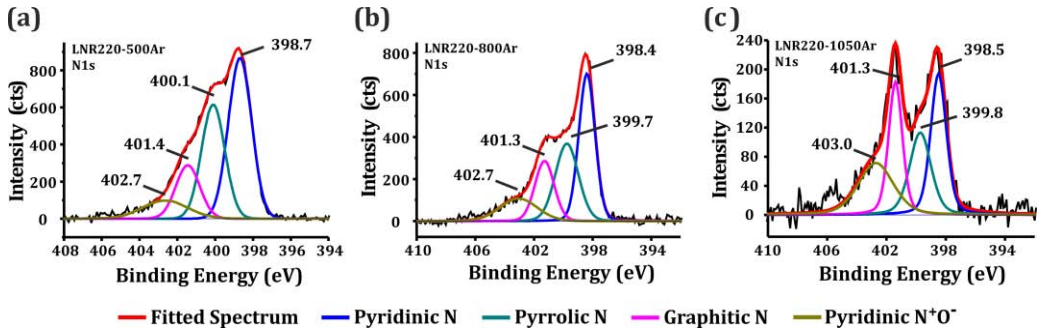


**Figure 3.24.** High- resolution N1s spectra of LNR220 after treatment at (a) 500 ˚C, (b) 800 ˚C and (c) 1050 ˚C under argon.

nal is observed. The 500 °C treatment mainly produced the removal of the aliphatic groups, but taking into account that the elimination of pyrrolic nitrogen is reported at mild conditions, [201] the loss of these functionalities at 500 °C cannot be discarded. Higher temperatures of treatment (800 ˚C and 1050 ˚C) lead to the removal of structural N groups (pyridine and pyrrolic N).

**Table 3.18.** Carbon, nitrogen and oxygen content (at. % determined by XPS) of the 220 ˚C $NH_3$-treated L (LNR220) before and after annealing at 500 ˚C, 800 ˚C, and 1050a ˚C under argon. The concentration of the species was determined by XPS analysis. (*) These energies could be contributed either by aliphatic functionalities ($CONH_2$/$CNH_2$) or by structural pyridinic ($C_5N$:) and pyrrolic ($C_4N$:) groups.

| Specie | | Sample | | | |
|---|---|---|---|---|---|
| | | LNR220 | LNR220-500Ar | LNR220-800Ar | LNR220-1050Ar |
| C content (at. %) | RC=CR | 40.5 | 46.9 | 51.1 | 50.7 |
| | Functionalized carbon | 41.0 | 38.4 | 37.3 | 40.5 |
| | **Total** | **81.5** | **85.3** | **88.4** | **91.2** |
| N content (at. %) | Pyridinic N ($C_5N$:) | 2.9* | 2.9 | 2.1 | 1.2 |
| | Pyrrolic N ($C_4N$:) | 4.7* | 2.1 | 1.6 | 0.9 |
| | Graphitic N ($C_4N^+$) | 1.6 | 1.0 | 1.0 | 1.0 |
| | Pyridinic $N^+$-$O^-$ ($C_4N^+$-O) | -- | 0.6 | 0.7 | 0.9 |
| | **Total** | **9.2** | **6.6** | **5.4** | **4.0** |
| O content (at. %) | $^-O_2CR$ | 4.3 | 4.0 | 3.2 | 3.1 |
| | $OCR_2$ | 2.6 | 3.8 | 2.0 | 1.0 |
| | $^-OCR_3$ | 2.4 | 0.3 | 0.9 | 0.5 |
| | PhOCOOPh | -- | -- | 0.1 | 0.2 |
| | **Total** | **9.3** | **8.1** | **6.2** | **4.8** |

It is worth nothing that the constant amount of the pyridinic/amide mitrogen after the 500 ˚C annealing reveals that internal rearrangements can occur when post-synthesis treatments are carried out. Thermal treatments produce the conversion of the aliphatic moieties into structural nitrogen (pyridinic N), which can be in the form of neutral species or positive fractions stabilized by oxygen atoms. When the LNR220 sample is treated at 800 °C and 1050 ˚C the same trend is observed. However, the decrease in the 298 eV signal (pyridinic N) is attributed to the formation of positive charged groups by interaction with oxygen-containing moieties (0.7 at. % N) as well as the elimination of these groups from the N-doped RGO lattice, which is favored at higher temperatures. Apparently the presence of the pyridine N-oxide groups contributes to the enhancement of the thermal stability of the materials. The higher concentration of these functionalities is observed in LNR220-1050Ar (0.9 at. % N), which in turn has the highest onset of combustion (578 ˚C, **Table 3.17**).

Treatment under argon at 800 ˚C produces samples with a high level of reduction (up to 51.1 at. % of $sp^2$ C) but with a lower decrease in the nitrogen content compared to sam-

**Table 3.19.** Composition of carbon, nitrogen and oxygen present in ammonia-treated L samples (220 ˚C and 500 ˚C) before and after annealing at 800 °C under argon. The atomic content was determined by XPS analyses. (*) These values could correspond to aliphatic functionalities ($CONH_2/CNH_2$) or by structural pyridinic ($C_5N$:) and pyrrolic ($C_4N$:) groups.

| Specie | | Sample | | | | |
|---|---|---|---|---|---|---|
| | | LNR220 | LNR500 | LNR220-500Ar | LNR220-800Ar | LNR500-800Ar |
| C content (at. %) | RC=CR | 40.5 | 43.1 | 46.9 | 51.1 | 43.6 |
| | Functionalized carbon | 41.0 | 42.4 | 38.4 | 37.3 | 43.4 |
| | **Total** | **81.5** | **85.5** | **85.3** | **88.4** | **87.0** |
| N content (at. %) | Pyridinic N ($C_5N$:) | 2.9* | 3.8 | 2.9 | 2.1 | 2.4 |
| | Pyrrolic N ($C_4N$:) | 4.7 | 3.4 | 2.1 | 1.6 | 1.8 |
| | Graphitic N ($C_4N^+$) | 1.6 | 1.3 | 1.0 | 1.0 | 1.0 |
| | Pyridinic $N^+$-$O^-$($C_4N^+$-O) | -- | -- | 0.6 | 0.7 | 0.6 |
| | **Total** | **9.2** | **8.5** | **6.6** | **5.4** | **5.8** |
| O content (at. %) | $^-O_2CR$ | 4.3 | 2.6 | 4.0 | 3.2 | 4.1 |
| | $OCR_2$ | 2.6 | 2.3 | 3.8 | 2.0 | 2.1 |
| | $^-OCR_3$ | 2.4 | 1.1 | 0.3 | 0.9 | 0.8 |
| | PhOCOOPh | -- | -- | -- | 0.1 | 0.2 |
| | **Total** | **9.3** | **6.0** | **8.1** | **6.2** | **7.2** |

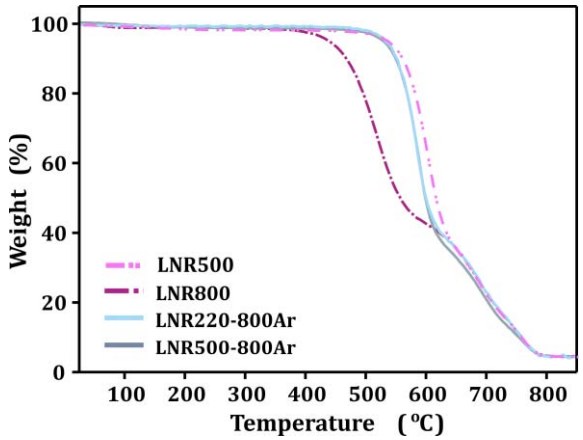


**Figure 3.25.** Thermal stabilities of the N-containing RGO materials (LNR220 and LNR500) after treatment at 800 °C under argon. The TG curves of the 500 °C and the 800 °C N-doped samples (LNR500 and LNR800 ) are included for comparison. Analyses were performed under flowing air at a heating rate of 10 °C.min$^{-1}$.

ples prepared by annealing at 1050 ˚C. In the case of the LNR220-800Ar and the LNR500-800Ar the total contribution of N-containing six-membered rings amounts to 2.8 at. % and 3.0 at %, respectively (**Table 3.19**). Again, these species contribute to the stabilization of the conjugated system, which would explain the higher thermal stability of the Ar-treated materials against their N-doped counterpart (800 ˚C $NH_3$ treated L, **Figure 3.25**).

500 °C and 800 °C argon-treated materials show similar onsets of combustion than the LNR500 sample (**Table 3.20**). Nevertheless, structural differences are clearly visible in

**Table 3.20.** Onset of combustion temperature in air of the nitrogen-containing materials (LNR220 and LNR500) before and after 500 ˚C and 800 ˚C treatments under argon. The data of the 800 ˚C N-doped RGO (LNR800) is included for comparison.

| Sample | Onset of Combustion |
|---|---|
| LNR500 | 566 °C |
| LNR220-500Ar | 557 °C |
| LNR800 | 471 °C |
| LNR220-800Ar | 550 °C |
| LNR500-800Ar | 559 °C |

the XPS analyses. The 500 °C N-doped RGO has the highest contribution of stable six-membered-containing nitrogen rings. As discussed before, the stability of the sample is not governed by a single group. In this case, despite that the pyridinic N as well as the graphitic groups (with stable concentration) should produce a later combustion of the sample, the presence of a 3.4 at. % of pyrrolic N certainly plays a negative role. However, considering the pyridinic N-oxide groups in the LNR220-500Ar, there are not significant differences in the content of six-membered species between this sample and the LNR500 (**Table 3.19**). This way, treatments at the same temperature produce similar content of a specific functionality, as long as the specie is stable at the chosen annealing temperature. The thermal stability of the samples does not show an increase when increasing the temperature until 800 °C (**Figure 3.25**) under argon. The treatment produces a slight decrease in the oxygen content and a higher restoring of the conjugation (**Table 3.19**), nevertheless the decrease in the total content of nitrogen (5.4 at. % N and 5.8 at. % N) has negative effect on the final onset of combustion of the materials.

The LNR500 sample was also treated at 800 °C under argon. The obtained material has a similar amount of nitrogen than LNR220-800Ar, resulting in a similar onset of combustion. The presence of PhOCOOPh groups is observed in the LNR500-800Ar sample (**Table 3.19**). The formation of these groups is favored in materials with higher content of oxygen, since they are not present in 800 ˚C N-doped RGO treated under Ar. Interestingly N-doping and Ar- treatments at 800 ˚C lead to similar concentrations of nitrogen within the samples (5.5 at. % N, 5.4 at. % N and 5.8 at. % N for LNR800, LNR220-800Ar and LNR500-800Ar respectively), which confirms that the final content of nitrogen within the N-doped RGO samples is governed by the temperature of treatment.

## 3.6. Conclusions.

- N-containing RGO samples with high concentrations of nitrogen (up to 14.7 wt. %) have been prepared by gas phase treatments of GO with pure ammonia gas.

- A proper assessment of the structural composition of N-containing RGO has been carried out, employing several complementary techniques which include not only XPS (being the most widely employed technique), but also FT-IR, UV-Vis, TGA and contact angle measurements. Thus, a toolbox for the identification of the N-bearing moieties present in N-based graphene materials is proposed.

- The temperature of treatment plays an important role in the formation of the N-based moieties. Low temperature treatments result in the formation of amine and amide groups (N-functionalization), while annealing at temperatures above 500 °C produce the incorporation of structural nitrogen into the RGO lattice (N-doping).

- Experimental data and thermodynamic calculations indicate that N-doping increases significantly the thermal stability against combustion of graphene-based materials.

- Ammonia is a powerful reducing agent and highly reduced samples (ca. 2 at. % O) were obtained after ammonolysis treatments, which are comparable with previous reports employing higher temperature and reducing conditions, such as $Ar/H_2$, 1050 °C.

- Graphitic nitrogen is the most stable specie among the structural N-containing moieties. $Ar/H_2$ treatment of N-containing RGO produces an

abrupt decrease of these groups (as well as the pyridinic and pyrrolic N), being responsible of the earliest combustion in air of the post-treated samples.

- Annealing of the N-containing RGO samples under argon produces internal rearrangements. Upon treatment, N-functionalized samples suffer the elimination of the aliphatic N-moieties, which in some cases can be introduced into the lattice as structural groups (mainly pyridinic N). Additionally, N-containing six-membered rings can interact with oxygen atoms, producing the formation of pyridine N-oxide species.

- Thermal stability of the samples is mainly governed by the variation in the N-species, being favored by the presence of pyridine N-oxide moieties into the lattice of the post-annealed N-containing RGO. However, the restoring of the conjugated system by the elimination of O-bearing functionalities might have a positive influence in the thermal response.

# Results II.

# SYNTHESIS OF CARBON NANOTUBE-INORGANIC NANOSTRUCTURES

# Chapter 4.

# Filling of carbon nanotubes with inorganic materials.

This chapter describes the synthesis and characterization of new inorganic nanostructures prepared by filling of multiwalled carbon nanotubes. The preparation of high quality single-layered inorganic nanotubes grown within multiwalled carbon nanotubes employing different metal halides is described. For this purpose an exhaustive study considering the influence of the treatment conditions was carried out. Finally, the use of fullerenes as versatile agents to "cork" the open tips of the carbon nanotubes or as promoting species for the release of the inorganic material contained within the cylindrical cavity of the nanotubes was studied.

# 4.1. Introduction.

The formation of low dimensional systems with quantum confinement of electrons provides a pathway for tuning the optical, electrical and thermoelectrical properties of crystalline structures.[202] As a consequence a wide variety of approaches have been explored in order to synthesize and control the characteristics of one dimensional (1D) materials, such as size and crystal structure.[203] Template-directed synthesis represents a convenient and versatile route for the growth of 1D systems and both organic and inorganic–based materials are being employed as templates.[204] For instance, Zhang et al. reported the preparation of discrete Bi nanowires from a porous alumina template[202] and Hong et al. have shown that 0.4 nm 1D silver wires can be extracted from the nanochannels of calyx-3-hydroquinone via photochemical reduction of incorporated $Ag^{+}$ ions.[205] In this sense, carbon nanotubes (CNTs) are an attractive alternative to produce discrete atomically regulated structures due to the presence of an inner cavity which is susceptible of being filled with a wide variety of materials.[126] CNTs can have diverse diameters, lengths, and conformations. Single walled carbon nanotubes (SWCNTs) have been successfully employed to grow and tune the characteristics of materials with different crystallization behavior being metal halides the most widely investigated.[206] In general, the confinement of materials within the walls of CNTs results in the formation of molecular entities, nanoclusters or nanowires which can in turn alter the physical and chemical properties of the hosting template, expanding its application from molecular magnets[207] to biomedicine.[208] The isolation of single-layers of 2D Van der Waals solids is getting an increased attention. Nanoribbons of graphene[209] and metal dichalcogenides ($MoS_2$, $WS_2$)[128, 210] have been synthesized within the cavities of single and double-walled CNTs, whereas rolled up 2D sheets of metal halides ($PbI_2$), resulting in seamless single-layered nanotubes, have been grown using multiwalled carbon nanotubes (MWCNTs) as templates.[129]

A recent theoretical study by Zhou *et al.* reveals that these confined $PbI_2$ single-layered nanotubes can substantially enhance the visible light response, suggesting potential applications in novel 2D optoelectronics and photovoltaics.[211] Despite their interest, the number of reports on single-walled inorganic nanotubes is limited due to the formation of their multi-walled counterpart is favored during the synthesis.[212] Besides, a detailed analysis taking into account the variables involved in the synthesis process is necessary. Therefore, the possibility of growing single-layered nanotubes using CNTs as directing agents opens up a new synthetic strategy for the development of advanced nanomaterials that particularly combine the characteristics of both 2D and 1D materials.[213]

The hollow cavities of CNTs are useful not only as nanoscale templates for the synthesis of nanocomposites or nanostructures. Endohedral functionalization provides an alternative toward isolating materials within the CNTs cavities, preventing any undesirable interaction with outer species which can modify the properties of the inner material or even produce the degradation of its structure. As mentioned in the introductory section, different approaches can be employed in order to fill materials within CNTs. However, a key factor to obtain a high filling yield is having CNTs with opened ends.[214] Regardless of the method used for the encapsulation of materials inside CNTs an excess of the filling agent is typically employed,[126, 215] and thus an important amount of material remains outside the nanotubes after the filling step. The filling process is usually reproducible; nevertheless, the presence of external material hinders the quantification of the filling yield. Furthermore, the removal of the non-encapsulated compounds is necessary to allow a proper characterization of the sample as well as to determine how the inner material modifies the properties of the CNTs. Otherwise, the properties of the sample cannot be exclusively attributed to the confined species but also to the presence of material external to the CNTs.[216] An area in which filled carbon nanotubes have been extensively studied is in the biomedicine field.[208] However, applications for in

vivo imaging, drug delivery or tumor targeting require the absence of species remnant from the filling process attached to the outer surface of the CNTs.[147]

The easiest procedure to clean external material from the sample involves the use of solvents which in general are also capable to dissolve the filling agent. Therefore, unless the encapsulated material has a strong interaction with the CNTs, this approach not only removes the external compounds but also washes out the confined nanostructure, since the ends of the CNTs are opened.[217] In the case of SWCNTs, it has been reported that the ends can be closed by high temperature treatments (ca. 900˚C);[218] thus allowing the removal of the external material whilst preserving the encapsulated compounds. In case of MWCNTs, closing their ends by high temperature annealing is much more difficult, due to the presence of a larger cavity. A much higher energy and hence extremely high annealing temperatures would be necessary to induce the closing, which requires the formation of C-C bonds generating high curvature strain.[219] Nevertheless, a wide range of substances can be decomposed at high temperature and an alternative strategy for sealing up the ends of the nanotubes is required. A. Capobianchi *et al*. proposed the impregnation of the open ended filled MWCNTs with a solvent unable to solubilize the filling agent when entering into the hollow cavity by capillarity. Afterwards a washing solvent could be added to the mixture without affecting the inner material (provided both liquids present a low miscibility).[220] However, the resulting filling yield is low and the elimination of the protecting solvent could be problematic.

Taking advantage of the strong affinity of fullerenes to enter into the inner cavities of SWCNTs, these molecules has also been employed as corking agents for the containment of materials previously confined within the cavities of SWCNTs.[221] The preparation of SWCNTs filled with fullerenes; usually called nanopeapods (NPPs) has been widely studied. The interaction mechanisms between the nanotubes and fullerenes involved in the filling process as well as the behavior of the $C_{60}$ upon encapsulation have attracted much interest due to the particular structures that can

be formed.[222] Theoretical studies have shown that under the appropriate energetic conditions fullerenes could be initially adsorbed onto the external walls prior to encapsulation,[223] and coalesce after confinement.[224, 225] Besides, SWCNTs with the appropriate diameter are able to perfectly accommodate a single molecule of $C_{60}$ within its two walls,[226] whose proximity allows a strong interaction between the buckyball and the nanotube. J. Sloan *et al.* showed that the presence of fullerenes within the hollow cavity of SWCNTs prevents the introduction of other foreign materials.[227]

Another important issue usually considered for some of the potential applications of filled nanotubes is the controlled release of the encapsulated material. This process requires breaking energy barriers that can be present due to attractive interactions stablished between the inner structures and the hosting CNTs after filling.[228] Releasing and transport mechanisms of liquid[229] or gaseous[230] substances, as well as the assisted removal of the filled materials have been explored.[229, 231-233] Considering the high affinity and strong intermolecular forces which can exist between fullerenes and CNTs, theoretical studies on the capability of fullerenes in displacing different species from the cavities of SWCNTs have been carried out;[234, 235] nevertheless, such studies have not been reported to date for MWCNTs.

## 4.2. Objectives.

- To use MWCNTs as directing agents for the growing of single-layered inorganic nanotubes.

- To explore the influence of the temperature of treatment in the formation of different nanostructures within MWCNTs.

- To explore the potential usefulness of fullerenes as corking agents for filled MWCNTs, avoiding the release of the inner material during the washing process.

- To explore the capacity of fullerenes to induce the release of inorganic nanostructures present within MWCNTs.

## 4.3. Purification of multiwalled carbon nanotubes.

Commercially available chemical vapor deposition (CVD) MWCNTs have been used employed for the preparation of different inorganic nanostructures. During the CVD process, besides the tubular structures, amorphous carbon and graphitic particles are also generated. Among the different techniques that have been used to remove the additional material and the remaining catalyst, steam treatment is one of the most useful approach. This procedure not only eliminates the undesired particles present into the sample, but also causes the opening of the ends of the nanotubes. Being a mild oxidant agent, annealing of the sample under steam does not produce the formation of defects by the introduction of oxygen bearing functionalities along the walls of the nanotubes, interacting selectively with the amorphous carbon and graphitic particles. Furthermore, the treatment allows the shortening of the nanotubes due to the most reactive tips are easily oxidized. This way, specimens with different length can be obtained by controlling the time of treatment.[82, 146, 236]

Since this methodology has been widely studied, MWCNTs were purified following this same protocol. 250 mg of as-received material (previously grinded with mortar and pestle) were placed in a silica tube of 25 mm diameter, and then introduced into an alumina furnace tube. Samples were annealed at 900 °C under steam, after purging the system during 2 hours with argon. Steam was introduced by bubbling the inert gas through hot water (98 °C). Argon was employed as carrier gas and to keep the system free of oxygen. After the treatment, the furnace was cooled down to room temperature. Subsequently, the sample was collected and stirred at 110 °C in 100 mL of a 6M HCl solution during 6 hours. Acid treatment allows the removal of the metallic particles exposed after the oxidation of the graphitic shells that coat them. The mixture was then filtered using a 0.2 μm polycarbonate membrane, washed until neutral pH and dried overnight.[146] The purification time was chosen according to the desired application.

## 4.4. Synthesis of single-layered inorganic nanotubes encapsulated within multiwalled carbon nanotubes.

$CeCl_3$ and $CeI_3$ single-layered inorganic nanotubes (SLINTs) encapsulated within MWCNTs were prepared by molten phase capillary wetting.[237] 5 mg of purified and open ended MWCNTs, obtained after 5 h of steam treatment,[238] were annealed during 12 h in presence of 200 mg of $CeCl_3$ at 850 °C or 100 mg of $CeI_3$ at 800 °C; ca. 30 °C above the melting points of the salts (817 °C and 766 °C respectively). Before treatments, both MWCNTs and the cerium-based compound were homogeneously mixed by grinding in an agate mortar and pestle, transferred into a silica ampoule and the system was sealed under vacuum. After cooling, the silica ampoules were opened under argon and the samples were characterized by electron microscopy analysis. A High Resolution Transmission Electron Microscopy (HRTEM) image of a $CeI_3$@MWCNT is shown in **Figure 4.1.** A single layered $CeI_3$ nanotube (pointed by a white arrow) is easily differentiated from the walls of the carbon nanotube due to the difference of contrast.

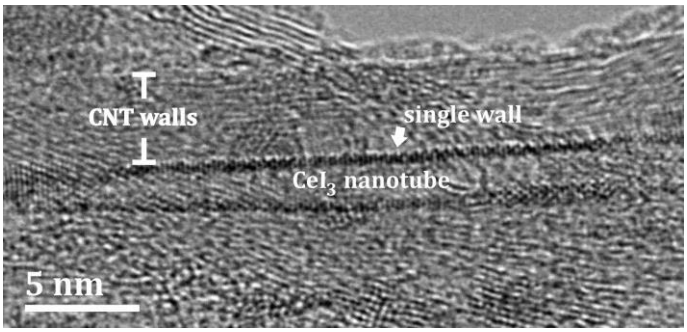


**Figure 4.1.** HRTEM image of a $CeI_3$ inorganic single-layered nanotube confined within a MWCNT.

Apart from the successful formation of inorganic nanotubes, thermal treatment also results in the formation of other nanostructures of both $CeCl_3$ and $CeI_3$ inside the CNTs (**Figure 4.2**). These other nanostructures mainly take the form of nanorods **(a-b)** but me-

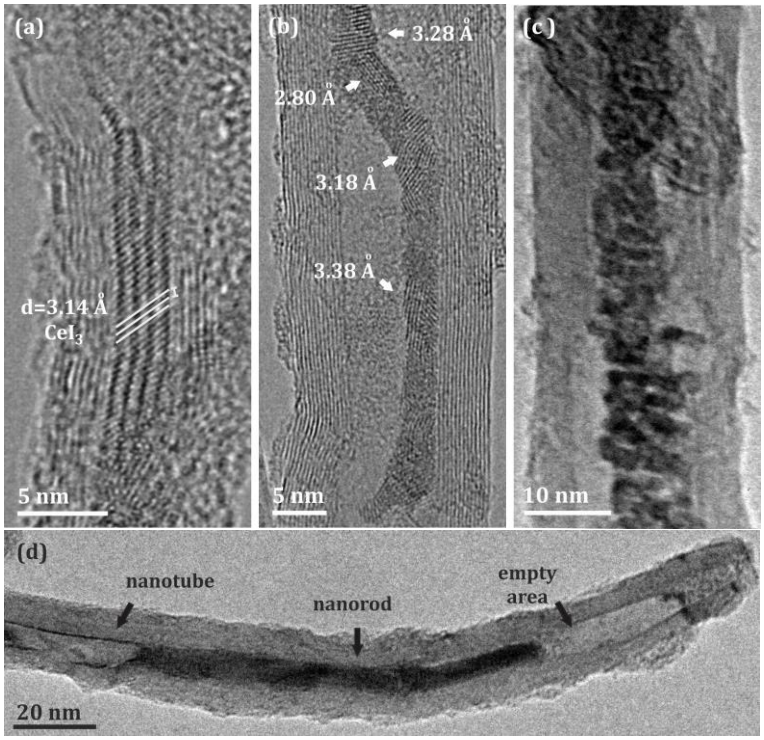


**Figure 4.2.** High-resolution transmission electron microscopy (HRTEM) images of (a) a $CeI_3$ nanorod, (b) a $CeI_3$ nanosnake and (d) $CeCl_3$ nanoparticles contained within purified multiwalled carbon nanotubes after molten phase capillary wetting. (d) The presence of different inner nanostructures can be clearly differentiated from empty areas inside the CNT.

tal halide nanoparticles have also been observed inside few CNTs **(c)**. When nanorods are present, these can either completely **(a)** or partially **(b)** fill the hollow cavity of the CNTs, the latter adopting polycrystalline snake-type morphology.[3][239] The coexistence of different types of inorganic nanostructures inside an individual CNT has also been observed. A clear differentiation between the nanotubes and nanorods can be obtained by visual inspection of TEM images **(d)**. In most cases crystalline structures

[3] To discern between both types of structures they will be referred as nanorods and nanosnakes, respectively.

are observed for the confined metal halides. The spacing of the lattice fringes can be clearly distinguished when both SLINTs and nanorods confined within carbon nanotubes are analyzed. The 3.14 Å layer separation measured in the nanorod presented in **Figure 4.2 (a)** is in good agreement with the (130) plane of bulk $CeI_3$, showing an orthorhombic structure. Otherwise, when nanosnakes contained within MWCNTs is analyzed multiple planes of crystallization are observed **(b)**.[240]

To unambiguously identify the possible presence of the inner inorganic nanotubes, High-Angle annular Dark Field (HAADF) imaging in High Resolution Scanning Transmission Electron Microscopy (STEM) was also performed. Since the constituent elements of the employed salts are heavier than carbon (from CNTs) it is possible to easily discern the filling material from the host. The contrast of HAADF-STEM images (also called *Z*-contrast imaging) scales approximately with the atomic number. Thus heavy elements, metal halides in this case, will appear brighter than light elements, such as carbon from the CNTs.[241] **Figure 4.3 (a)** shows a MWCNT containing different $CeI_3$-based nanostructures within its cavity. The inset shows a magnified image of a fraction containing a SLINT with its particular tubular appearance. The bright lines observed along the inner walls of the CNT can be attributed to $CeI_3$, the diameter and shape of the SLINT being determined by the inner cavity of the CNT. In order to confirm the presence of the inner nanostructure, the intensity profile of an empty area of a MWCNT was compared with a $CeI_3$ nanotube grown within the template (**Figure 4.3 (b)**). As shown in the obtained profiles, $CeI_3$ SLINT produces two narrows peaks (red line) with a high intensity. In contrast, the empty fraction of the CNT produces a broad and weak signal (blue line) due to the lower weight of the constituent carbon atoms. The higher intensity in the CNT walls against the central area due to the overlay of a higher number of atoms is an evidence of the presence of a hollow structure. When the same analysis is performed on a fraction of a MWCNT containing a $CeI_3$ nanorod and a SLINT, both types of structures can be easily discerned by visual inspection of the *Z*-contrast

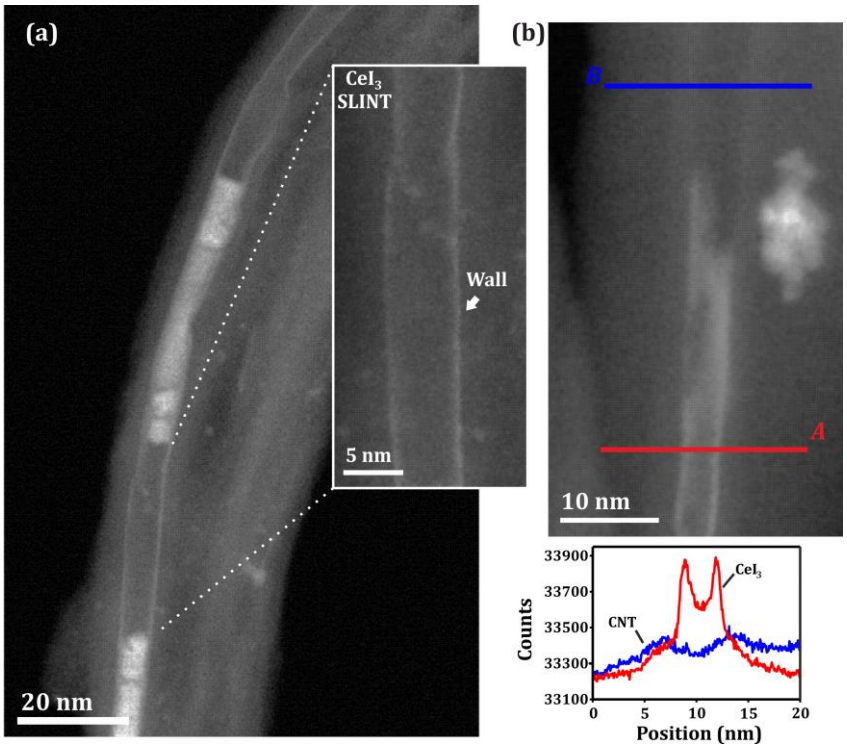


**Figure 4.3.** HAADF STEM images of (a) both $CeI_3$ tubular nanostructures and nanorods grown within a MWCNT. The inset shows a magnified area containing the $CeI_3$ SLINT. (b) Comparison of the intensity profiles of an empty and a $CeI_3$ SLINT-containing area of a MWCNT.

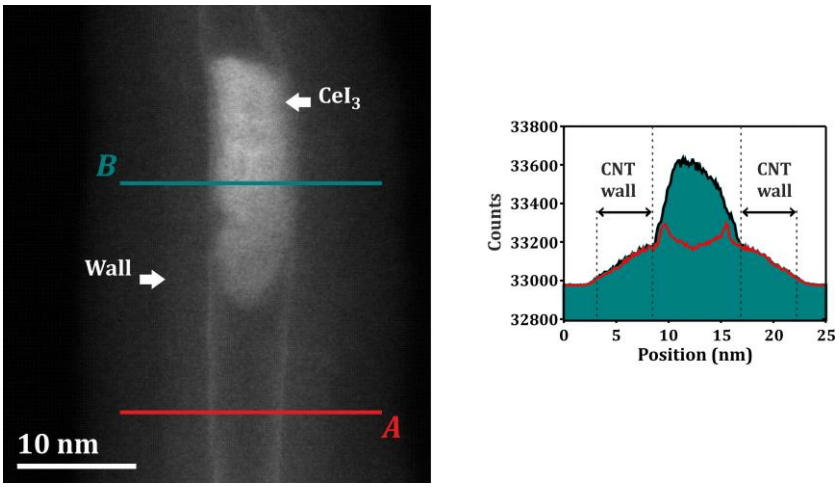


**Figure 4.4.** Intensity profiles of two segments of a MWCNT containing a nanotube (red line) and a nanorod (green line) of $CeI_3$.

**Table 4.1**. Numerical data collected after counting the number of the different types of inner nanostructures present in the samples of purified MWCNTs mixed with either $CeI_3$ or $CeCl_3$ after annealing at different temperatures.

| Sample | # of images | Nanotubes | Other nanostructures | | |
|---|---|---|---|---|---|
| | | Long /Short | Nanoparticles | Nanosnakes | Nanorods |
| $CeI_3$@MWNCTs, 800 °C | 217 | 16 /-- | 7 | 184 | 10 |
| Frequency (%) | | 7.4 /-- | 3.2 | 84.8 | 4.6 |
| $CeI_3$@MWNCTs, 900 °C | 219 | 42 /5 | -- | 153 | 19 |
| Frequency (%) | | 19.2 /2.3 | -- | 69.8 | 8.7 |
| $CeCl_3$@MWNCTs, 850 °C | 578 | 98 /9 | 6 | 441 | 24 |
| Frequency (%) | | 17 /1.6 | 1 | 76.3 | 4.1 |
| $CeCl_3$@MWNCTs, 1000 °C | 171 | 1/4 | -- | 163 | 3 |
| Frequency (%) | | 0.6 /2.3 | -- | 95.3 | 1.8 |

STEM image (**Figure 4.4**). However, further evidence can be provided by comparing the intensity profiles across the area presenting the inorganic nanotube fragment (red area, *A*) and the one containing the nanorod (green area, *B*). In case of the inner nanorod the highest intensity detected in the central space of the analyzed area confirms the complete filling of the host. In contrast, the intensity profile of the tubular fraction shows the highest intensity at the edges, which evidences the presence of a ca. 5.8 nm hollow structure. Moreover, in most of cases the inner nanorod appears to be confined within the $CeI_3$ tubular nanostructure and the carbon nanotube walls are clearly differentiated, presenting a lower detected intensity. The successful formation of single-layered $CeCl_3$ and $CeI_3$ nanotubes confirms that the use of CNTs as hosts for the formation of inorganic nanotubes is not limited to $PbI_2$ (only example available to date in the literature)[129] but is a versatile methodology where different metals (Ce instead of Pb) and anions (Cl instead of I) can be used to fill the CNTs.

The frequency (%) of the synthesized inorganic nanostructures was additionally explored. To have statistically significant data, the evaluated population comprised not less than 150 individual specimens containing inner nanostructures (from at least three different annealing treatments) and empty MWCNTs were not considered. In both $CeCl_3$@MWCNTs (850 °C) and $CeI_3$@MWCNTs (800 °C) the amount of CNTs filled with crystalline nanotubes was remarkably lower (18.6 % and 7.4 % respectively) compared

to the different structures previously mentioned (**Table 4.1**). It is also worth pointing out that when $CeCl_3$ was employed for filling the amount of inorganic nanotubes was markedly higher compared to $CeI_3$. However, a lower frequency of nanorods was observed for $CeCl_3$. As the temperature is a key factor in the molten filling process,[95] we have investigated the role of this parameter on the formation of nanotubes and other inorganic nanostructures. Therefore, the temperature employed for the encapsulation of $CeI_3$ and $CeCl_3$ was increased by annealing their mixture with CNTs at 900 °C and 1000 °C respectively. For ease of comparison, treatment time and heating rate were kept invariable.

**Figure 4.5** shows the amount of the different types of inorganic nanostructures present inside MWCNTs after the annealing treatments. In case of $CeCl_3$@MWCNTs, a 150 °C increase in the temperature of synthesis results in a lower frequency of inner nanotubes (18.6 % at 1000 °C to 2.9 % at 850 °C). In contrast, when $CeI_3$ was employed for filling the inverse trend was observed (**Figure 4.5, (a)**) and the amount of SLINTs showed a significant increase, ca. 190.5 %, compared to the samples treated at lower temperature (800 °C). A detailed analysis of the different types of nanostructures grown within the MWCNTs with respect to the temperature of treatment is presented in

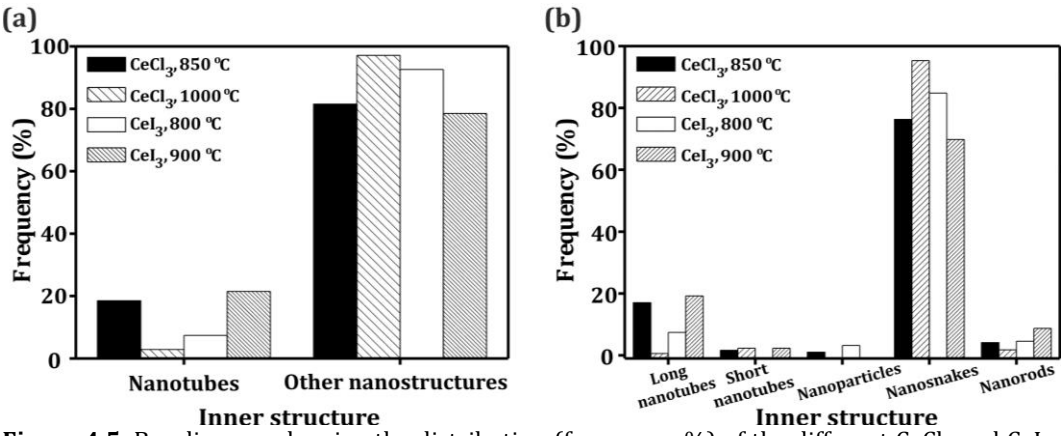


**Figure 4.5.** Bar diagram showing the distribution (frequency, %) of the different $CeCl_3$ and $CeI_3$ inner structures grown within multiwalled carbon nanotubes after annealing treatments.

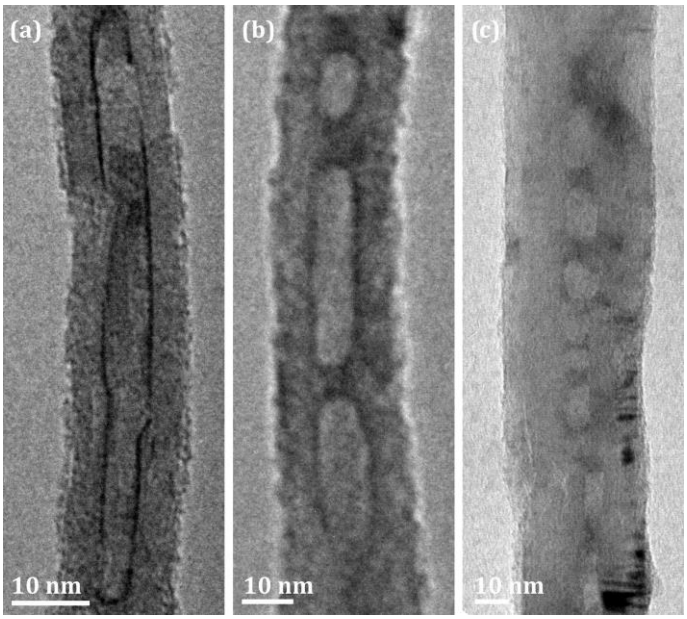


**Figure 4.6.** TEM images of (a) long $CeI_3$ single-layered nanotube, (b) short $CeCl_3$ nanotubes and (c) $ZnI_2$ short nanotubes grown within MWCNTs.

**Figure 4.5 (b)**. $CeCl_3$ and $CeI_3$ inorganic nanotubes can be present as "short" (bubble like nanostructures) or "long" nanotubes (see **Figure 4.6**), and can be distinguished in this analysis. In most cases short nanotubes were grown as at least three consecutive close-ended hollow nanostructures. As expected a lower contrast is presented by the $CeCl_3$ nanostructures compared to the iodinated salt by electron microscopy analysis. For both, $CeI_3$ and $CeCl_3$ nanostructures, the presence of long nanotubes was clearly higher than the short ones in all the prepared samples. The distribution of $CeI_3$ grown nanotubes followed the same trend when the temperature of treatment was increased. This way, the samples treated at the lowest temperature (800 °C) showed a lower frequency of both long $CeI_3$ nanotubes (7.4 %) and short nanostructures (without any observed specimen), in comparison with the 900 °C treatment (19.2 % and 2.3 % respectively). In contrast, in $CeCl_3$@MWCNTs samples the higher temperature of treatment (1000 °C) produces a negligible frequency of long inorganic nanotubes (0.6 %) against a 17 % present in the sample treated at 850 °C. Surprisingly, the inverse

trend was observed for short nanotubes, with a slight increase of these structures at 1000 °C (1.6 % at 850 °C to 2.3 % at 1000 °C). Let us now analyze the presence of nanorods and other types of structures. First of all, MWCNTs filled with nanoparticles were exclusively produced (and in a minor frequency, 1%-3.2 %) when the lower temperatures of treatment were used; at the higher temperatures of treatment these structures were not present. Interestingly, despite the formation of nanosnakes showed the same trend observed for "other nanostructures" (**Figure 4.5 (a)**), the fraction filled with nanorods showed an inverse trend for both $CeCl_3$ and $CeI_3$. $CeCl_3$ presented a less trend to crystallize filling the entire cavity of the hosting template (1.8 % of the total analyzed fraction) compare to $CeI_3$, despite that higher temperatures of treatment were employed for the former.

Taking into account that marked differences were observed with slight variations in the treatment conditions, and since the explored compounds only allow working at a limited range of temperature (as cerium halides have significant high melting points), the use of an alternative material was considered. In order to better understand the role of the temperature on the formation of the different types of inorganic nanostructures steam treated MWCNTs were filled with $ZnI_2$. This material was selected since it is also a layered Van der Waals solid,[242] it has a relatively low melting point (446 °C) and a calculated low surface tension of the melt.[243] The latter is a key parameter since liquids with low surface tensions will most readily wet the CNTs.[244] Moreover, the presence of the strongly scattering halogen (I, $Z$= 53) allows an easy differentiation of the grown structures by TEM analyses.[241] Following the same criteria employed for the cerium halides, a mixture of 10 mg of purified MWCNTs (5 h, steam) and 300 mg of $ZnI_2$ was annealed under vacuum at about 30 °C above the melting point of $ZnI_2$ (475 °C).[245] The resulting mixture was analyzed by STEM which allows confirming the successful growth of single-layered $ZnI_2$ nanotubes confined inside the carbon nanotubes. **Figure 4.7** shows HAADF images of the sample. Low magnification image **(a)** shows an overview of the inner structures formed after annea-

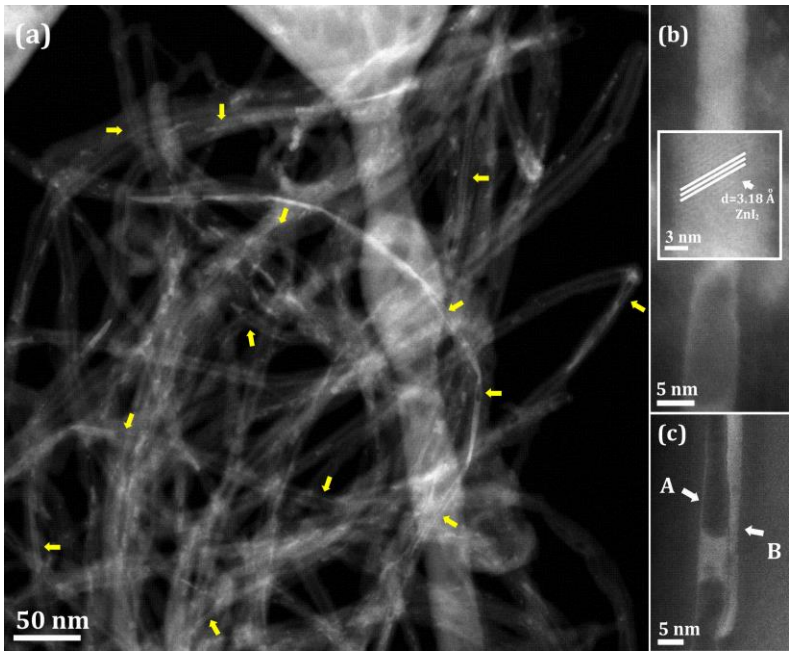


**Figure 4.7.** (a) Low magnification STEM image of $ZnI_2$@MWCNTs prepared at 475 °C, (b) crystalline patterns of $ZnI_2$ inside a MWCNT, (c) HAADF STEM images of two adjacent MWCNT containing both, an inner nanotube as well as a nanorod (A and B arrowed sections respectively).

ling the MWCNTs/$ZnI_2$ mixture at 475 °C. In case of the $ZnI_2$ nanorods **(b)**, the crystalline structure was also confirmed by measuring the lattice fringes.[246] HAADF imaging clearly distinguishes the heavy elements of the tubular structure (placed at the edges) **(c-A)**, from the inorganic nanorod **(c-B)** present into two adjacent MWCNTs. The intensity profile across an area containing a specimen of the 475 °C treated sample (red line, **Figure 4.8 (a)**) is in good agreement with the presence of a SLINT since a sharp and high intensity is observed following the inner walls of the CNT. In this case, the diameter of the $ZnI_2$ nanotube is 5.6 nm. EDX analysis confirms the presence of the constituent elements, Zn and I **(c)**. The presence of copper, aluminum and Si arises from the support and from de silica ampoule employed for the synthesis, respectively. Finally, a schematic representation of a SLINT having the same diameter that the one observed in the experimental image is included in **Figure 4.8 (d)**.

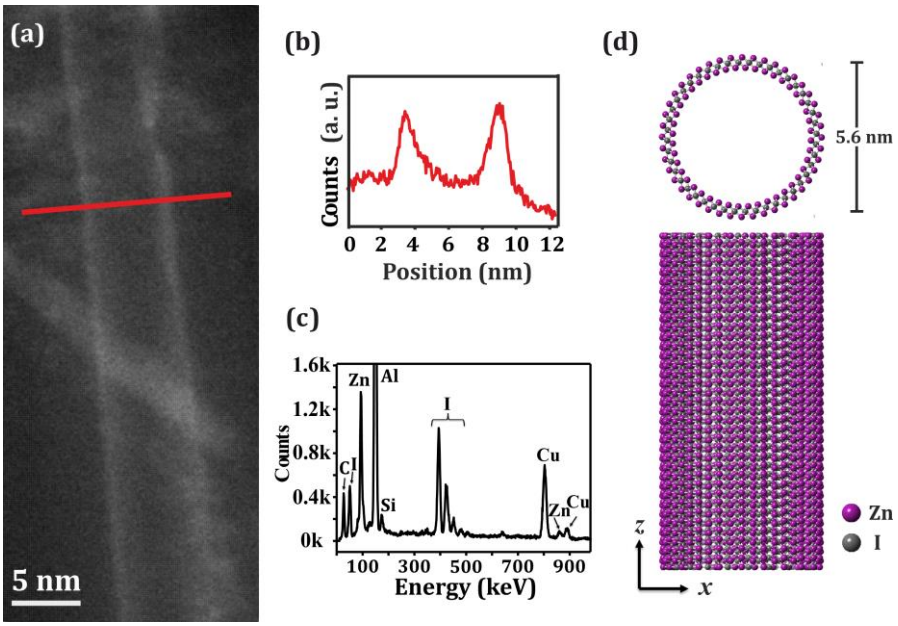


**Figure 4.8.** (a) HAADF-STEM image of $ZnI_2$@MWCNTs with its respective intensity profile along the red line (b). (c) EDX analysis confirming the presence of C, both Zn and I in the sample along with C (from the CNTs); Al and Cu signal arise from the support employed for the analysis, whereas the Si peak comes from the silica ampoule employed for the synthesis. (d) Schematic representation of a single-layered $ZnI_2$ nanotube with the diameter observed in the experimental image, projected along the main axis and cross section.

To complete the study, additional samples were prepared by annealing a mixture of $ZnI_2$ and CNTs at 575 °C, 700 °C and 1000 °C. The structure of the encapsulated compounds was determined on more than 190 filled nanotubes for each sample. **Figure 4.9 (a)** shows a low magnification TEM image of $ZnI_2$@MWCNTs prepared at 700 °C. As previously found for Ce-based materials, the formation of crystalline nanorods **(b)** as well as single-layered $ZnI_2$ nanotubes is observed. A HRTEM recorded image **(c)** shows the distinctive curvature of the inorganic nanotube grown within the MWCNT. After the annealing treatments, the distribution of the obtained structures was also analyzed. Different temperatures of treatment produce significant variations in the frequency of filled inorganic nanotubes and other types of nanostructures. As it can be seen in **Table 4.2**, an overwhelming increase on the amount of nanotubes is observed when in-

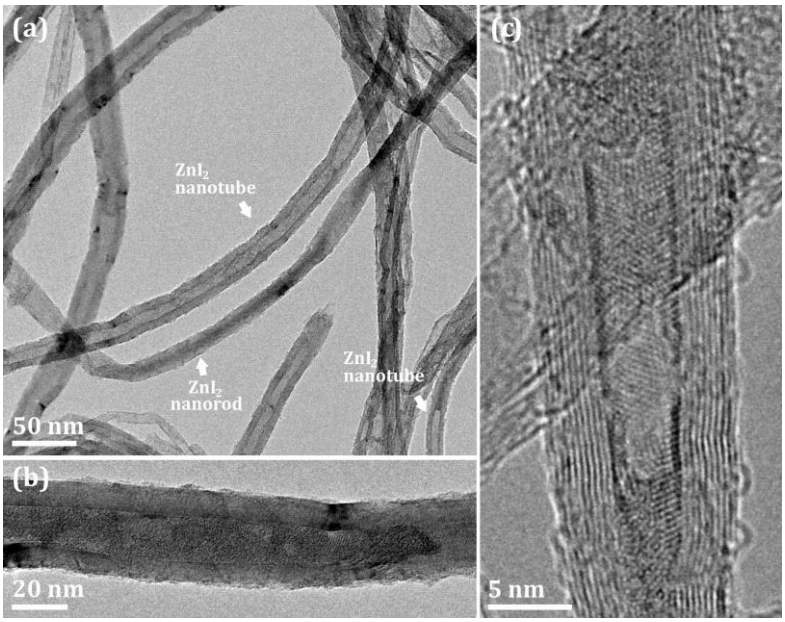


**Figure 4.9.** (a) Low magnification TEM image of $ZnI_2$@MWCNTs prepared at 700 °C. (b) TEM of a $ZnI_2$ nanorod and (c) HRTEM of an inner $ZnI_2$ nanotube inside MWCNTs. (b) and (c) have been grown at 1000 °C.

**Table 4.2.** Effect of the treatment temperature in the distribution of nanotubes and other nanostructures confined within MWCNTs.

| Temperature of filling | # of images | $ZnI_2$ nanotubes | Other nanostructures | | |
|---|---|---|---|---|---|
| | | Long /Short | Nanoparticles | Nanosnakes | Nanorods |
| 475 °C | 443 | 70/25 | -- | 324 | 24 |
| Frequency (%) | | 15.8/ 5.6 | -- | 73.2 | 5.4 |
| | | 21.4 | | 78.6 | |
| 575 °C | 426 | 72/38 | -- | 258 | 58 |
| Frequency (%) | | 16.9/8.9 | -- | 60.6 | 13.6 |
| | | 25.8 | | 74.2 | |
| 700 °C | 328 | 86/38 | -- | 94 | 110 |
| Frequency (%) | | 26.2/11.6 | -- | 28.7 | 33.5 |
| | | 37.8 | | 62.2 | |
| 1000 °C | 191 | 116/8 | 1 | 39 | 27 |
| Frequency (%) | | 60.7/4.2 | 0.5 | 20.4 | 14.2 |
| | | 64.9 | | 35.1 | |

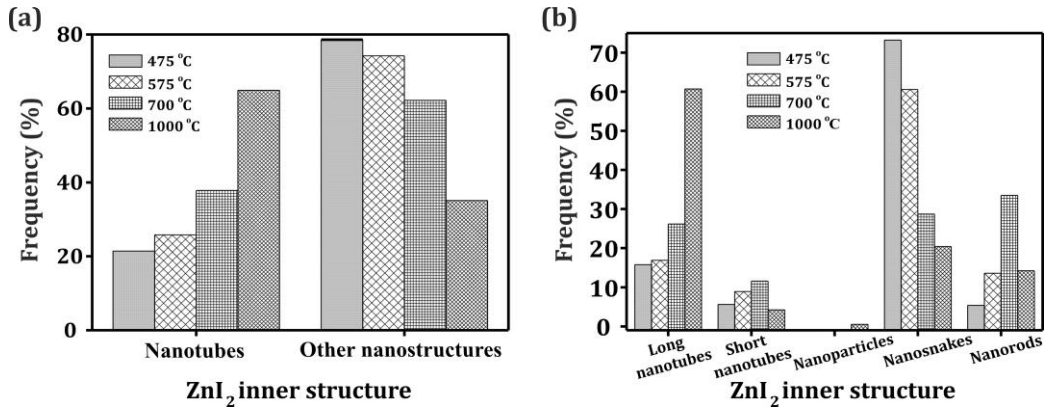


**Figure 4.10.** Bar diagram showing the distribution (frequency, %) of $ZnI_2$ inner nanostructures grown within MWCNTs after annealing treatments.

creasing the temperature of the synthesis from 21.4 % (at 475 °C) up to 64.9 % (at 1000 °C). The remnant, referred to as "other structures" includes MWCNTs filled with $ZnI_2$ forming inner nanorods and nanosnakes. Obviously, the continuous increase of the amount of $ZnI_2$ nanotubes upon increasing the temperature of synthesis, results in a proportional decrease of the amount of other nanostructures present inside CNTs (**Figure 4.10**). This is in good agreement with the trend observed for $CeI_3$ nanotubes and corresponds to a threefold enhancement of the formation of SLINTs. A detailed analysis of the grown structures reveals the presence of both long and short nanotubes, with similar characteristics to the $CeI_3$ and $CeCl_3$ samples (**Figure 4.6 (c)**). Again the amount of long nanotubes is always higher than the amount of short nanotubes for a given sample. Interestingly, a different trend is observed for the formation of short and long inorganic nanotubes upon increasing the temperature of the synthesis. In the case of long nanotubes, an increase in temperature produced a significant and continuous increase in the frequency of this type of nanostructures (from 15.8 % at 475 ˚C to 60.7 % at 1000 ˚C). In contrast, in the case of short nanotubes, although at lower temperatures there is also an increase towards the formation of this type of structures, an inflection point is clearly visible at 700 ˚C and the lowest amount of short nanotubes is recorded at 1000 ˚C (4.2 %). This implies that at 1000 ˚C not only the formation of inorganic nanotubes is favored over other nanostructures but also the $ZnI_2$ nanotubes

obtained at this temperature will be longer than 35 nm (long nanotubes). To complete the study, the distribution of the other filled nanostructures was analyzed. $ZnI_2$ inorganic nanoparticles were not observed in most of the samples, except for the sample treated at 1000 °C, where only a 0.5 % was detected (**Table 4.2**). Concerning to other nanostructures, the presence of nanosnakes was inversely proportional to the treatment temperature following the general behavior previously observed. Interestingly, again an inflection point is observed at 700 ˚C for the $ZnI_2$ nanorods which follows a similar trend than that found in short nanotubes, with a maximum at 700 ˚C (33.5 %) and showing an abrupt decrease for the sample treated at 1000 ˚C down to 14.2 % (**Figure 4.11 (b)**). The frequency of inorganic nanotubes showed a 20.6 % increase when compared to the initial treatment temperature and as a direct consequence filled host registered a 5.6 % decrease. Additionally, the 700 °C treatment (225 °C above the initial temperature of treatment) a 76.6 % increase in the frequency of $ZnI_2$ nanotubes was observed. In contrast the presence of filled hosts showed a marked decrease (78.6 % to 62.2 %). Following the same trend the sample prepared at 1000 °C presented the highest frequency of inorganic nanotubes (64.9 %) which agrees with the values shown for the $CeI_3$ nanotubes previously grown with MWCNTs (**Table 4.1**). In this manner, the higher the temperature of treatment, the higher the frequency of single layered $ZnI_2$ nanotubes and the lower the presence of other nanostructures. Now, considering the experimental data, 700 °C appears to be a critical temperature in the formation of the mentioned structures. Apparently the fact that the filling process is taking place above the boiling point of the $ZnI_2$ bulk (625 °C)[245] favors a more ordered crystallization of the material inside the hosting template. As a consequence, the highest decrease in the frequency of the partially filled MWCNTs is observed at this treatment temperature, accompanied to the important increase in both $ZnI_2$ inner nanotubes and completely filled MWCNTs (**Figure 4.11 (b)**, green line). Actually, at this temperature the frequency of the materials is quite similar, being the unique occasion where the frequency of nanorods exceeds the nanosnakes one (33.5 % and 28.7 % respectively). When the temperature increases up to 1000 °C the frequency of the nano-

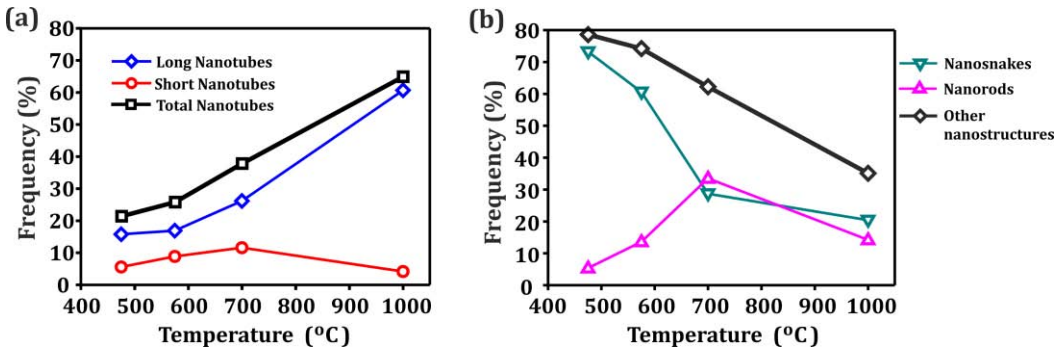


**Figure 4.11.** (a)Detailed analysis on the effect of temperature towards the formation of $ZnI_2$ nanotubes, differentiating between long and short. (b) Role of temperature in the formation of other $ZnI_2$ nanostructures, different from inorganic nanotubes, namely nanorods and "nanosnakes".

rods decreases, reversing the trend. This behavior agrees with that observed for short nanotubes as shown in **Figure 4.11 (a)**. In this case the absence of small intercalated rods contrasts with the presence of $ZnI_2$ nanotubes with a higher length.

## 4.5. Encapsulation of fullerenes: A versatile procedure for the confinement and release of materials within open-ended multiwalled carbon nanotubes.

### 4.5.1. End corking of multiwalled carbon nanotubes with fullerenes.

In this section we report the potential application of fullerenes as corking material for the confinement of inorganic nanostructures contained into MWCNTs. $PbI_2$ filled MWCNTs were employed to evaluate the capability of fullerenes of blocking the open ends of CNTs. $PbI_2$ was chosen as a model compound since both elements Pb and I present a high atomic number and thus are easily distinguishable from CNTs when these are observed by TEM. In order to prepare the sample, 6 mg of 5 h steam purified MWCNTs (see **Section 4.3**)[238] and 140 mg of $PbI_2$ were ground together with an

agate mortar and pestle, and the mixture was transferred to a silica ampoule and sealed under vacuum. Afterwards the sample was annealed at 500 ˚C during 12 h (using the molten phase capillary wetting method[237]). After cooling down, the ampoule was opened under argon atmosphere (glow box) and the encapsulation of $PbI_2$ was verified employing TEM and HRTEM analyses.

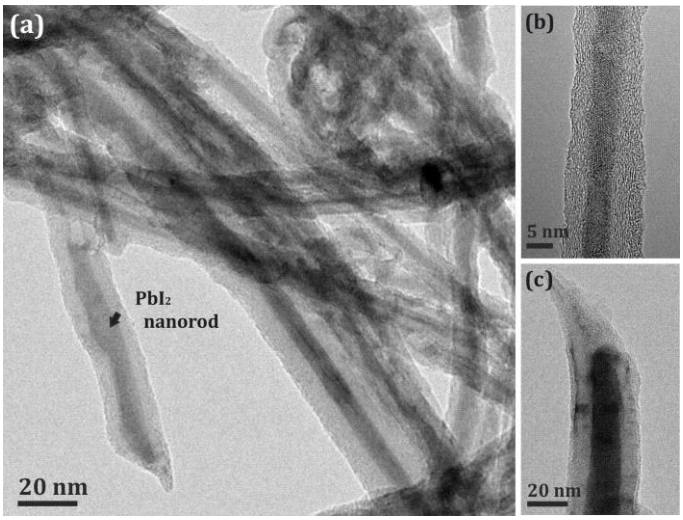


**Figure 4.12.** (a) $PbI_2$ filled MWCNTs after molten phase capillary wetting synthesis. (b) HRTEM image of a polycrystalline $PbI_2$ nanorod grown within a MWCNT. (c) Detail of an open ended $PbI_2$@MWCNT.

**Figure 4.12 (a)** shows a low magnification image of $PbI_2$@MWCNTs. As mentioned before, the contrast in TEM imaging is highly dependent on the atomic/molecular weight of the material. As $PbI_2$ contains relatively heavy atoms, the inner grown nanorods can be easily distinguished from the CNTs walls. A polycrystalline $PbI_2$ nanorod is observed in **(b)**. The spacing of the lattice fringes is in agreement with the (100) and (110) planes of bulk $PbI_2$ (**Figure 4.12 (b)**). Finally a magnification of an open ended $PbI_2$@MWCNT is observed in **(c).**

$C_{60}PbI_2$@MWCNTs were prepared from $PbI_2$@MWCNTs by a vapor-phase method.[247] Temperatures between 300 ˚C and 450 ˚C are considered to provide the energy

necessary for the formation of nanopeapods (NPPs),[225] and *in situ* studies have detected mobility of fullerenes along the CNTs walls at ca. 325 ˚C, followed by the entrance of fullerenes within the SWCNTs at 350 ˚C.[248] Furthermore, the sublimation of $C_{60}$ molecules, which is necessary for the vapor phase encapsulation,[134] has been reported to start at relatively low temperatures (ca. 375 ˚C), being favored under low pressure conditions.[249] Thus, the experimental conditions were chosen considering these factors. $PbI_2$ filled MWCNTs were homogeneously mixed with fullerenes and the mixture was subsequently annealed under vacuum at 400 ˚C during 48 h (inside a sealed silica ampoule). Taking into account that the probability of $C_{60}$ entering into the nanotubes decreases with the temperature, higher temperatures of treatment were not considered for this study.

**Figure 4.13 (a)** shows a low magnification TEM image of a $C_{60}PbI_2$@MWCNTs sample. As it can be observed, the presence of the inner nanorods within the hosting nanotubes has not been affected by the interaction of fullerenes with the sample, despite its affinity with the CNTs. The inset shows a magnification where the presence of fullerenes contained in an open-ended MWCNT is appreciated. Additionally a HRTEM image of a MWCNT containing both a $PbI_2$ nanotube and fullerenes blocking the opened tips is presented **(b)**. The presence of fullerenes on the external walls of the nanotubes (pointed by white arrow) is in agreement with theoretical calculations which suggest an “optimum” trajectory of the fullerenes when approaching to the CNTs. According to the studies of Berber *et al.*[223] fullerenes may be initially physisorbed on the outer wall of the nanotube and subsequently diffuse along the CNT surface. In this manner, the corking process involves an initial non-covalent functionalization of the CNTs walls with the fullerene molecules before the filling. Afterwards, fullerenes can displace either through the defects of the CNT walls or via the opened tips stablishing strong electrostatic interactions with the inner surface of the nanotubes.

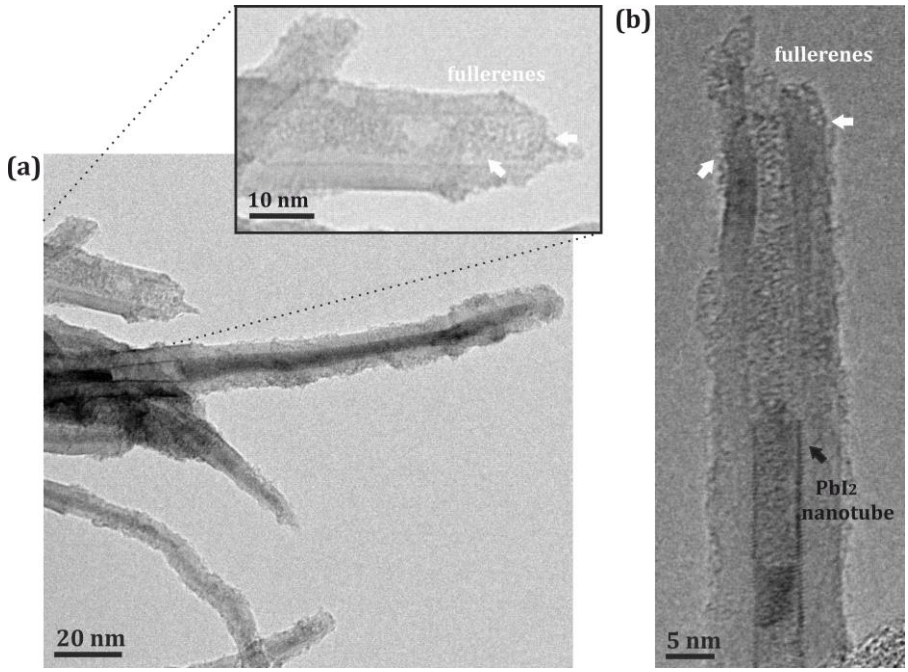


**Figure 4.13.**(a) $C_{60}PbI_2$@MWCNTs sample. The inset shows a magnified area of an open ended CNT containing fullerenes. (b)$PbI_2$ filled nanotube with fullerenes (white arrows) isolating the inorganic nanostructure.

The most common methodology for the elimination of the excess of material which has not been filled within the hosting nanotubes consists in carrying out consecutive washings with a specific solvent, capable of solubilizing the inorganic material. $PbI_2$ is barely soluble in cold water at room temperature (76 $mg.mL^{-1}$);[245] however its solubility increases when the temperature is increased. Hot water can thus be employed to remove the external material present after the synthesis of $PbI_2$@MWCNTs. Nevertheless, if the ends of the CNTs are opened, the process also washes out the material contained inside the nanotubes. Fullerenes do not present chemical affinity for water; for this reason, when these are employed to block the ends they shouldn't be easily removed, acting like "corks" and avoiding the removal of the inner nanostructures while the external material is eliminated. In order to confirm this hypothesis, 5 mg of $C_{60}PbI_2$@MWCNTs were dispersed (15 min of bath sonication) in 30 mL of distilled water and refluxed in $H_2O$ overnight. The dispersion was filtered with

a 0.2 μm polycarbonate membrane, rinsed copiously with water and dried at 60 ˚C during 12 h. As a control, $PbI_2$@MWCNTs, without $C_{60}$ corking were washed following the same procedure. After drying both, the opened and the blocked ended $PbI_2$@MWCNTs, the samples were characterized using TEM. **Figure 4.14 (a)** shows a low magnification image of the $PbI_2$@MWCNTs (open ended) sample. As it can be observed, the inorganic material was removed from the interior of the CNTs and only empty MWCNTs can be seen in the sample. In contrast, when the tips of the nanotubes were closed with the fullerene molecules, an important amount of $PbI_2$ nanorods remained into the hosting cavity of the nanotubes after washing with water. **Figure 4.14 (b)** shows a low magnification TEM image of the $C_{60}PbI_2$@MWCNTs after washing. Images of individual CNTs containing $PbI_2$ nanorods (pointed by black arrows) as well as fullerenes (white arrows) are also included (**A-C**). The presence of $PbI_2$ inside the MWCNTs confirms that fullerenes not only are useful for the isolation of inorganic materialinside SWCNTs,[147] but also can be employed for the confinement of compounds within tubular carbon nanostructures with larger diameters (MWCNTs).

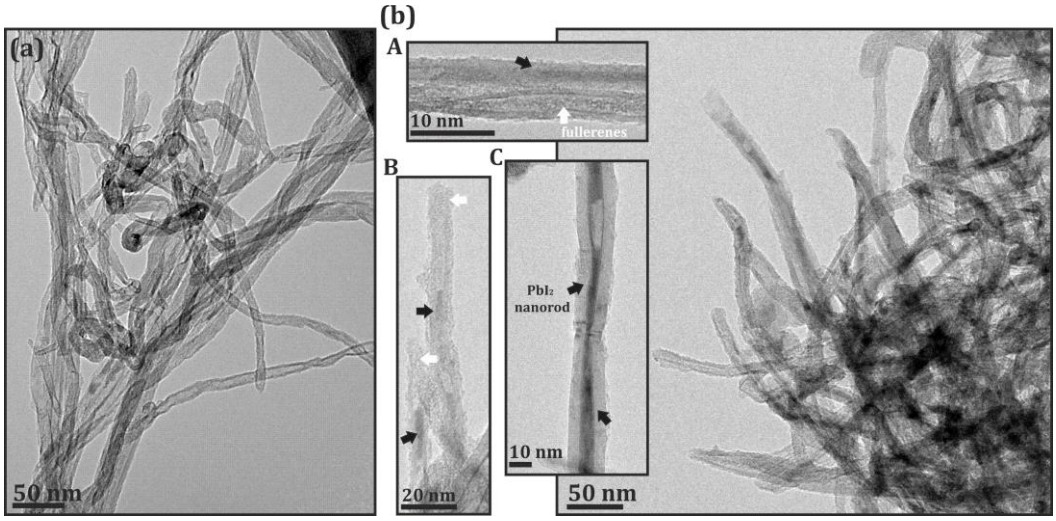


**Figure 4.14.** (a) Low magnification image of the $PbI_2$@MWCNTs after washing with water. (b) A-C show individual nanotubes containing both fullerenes (white arrows) and $PbI_2$ nanostructures (black arrows) which have not been removed after washing. A low magnification image (right) shows that most of the corked nanotubes maintained its filling after washing.

Next, the optimum amount of fullerenes necessary to cork the CNTs was explored. Since an important amount of filling agent remains outside the nanotubes, the quantification of the ratio between the CNTs and the fullerenes is not possible. However the amount of fullerenes was selected in function of the mass of CNTs which was initially mixed with the inorganic salt. In this manner, the totality of the sample after the endohedral functionalization with $PbI_2$ was mixed in 1:1, 1:2, 1:3 and 1:10 CNTs/$C_{60}$ ratios. After treatment with the lowest amount of fullerenes (1:1 ratio), and despite an important fraction of $C_{60}$ was observed along the CNTs walls and tips, the amount of filled nanotubes decreased considerably after washing with water. Meanwhile, when the samples were treated with two and three parts of fullerenes, the frequency of filled nanotubes observed after washing increased. Finally, the treatment with the highest amount of fullerenes (1:10 CNTs/$C_{60}$) did not show a significant variation in the frequency of $PbI_2$@MWCNTs, in comparison with the sample annealed in presence of three parts of fullerenes. Moreover, the washing step presented difficulties because a thick film of carbonaceous material was deposited on the surface of the washing solution. Since the use of the highest amount of fullerenes did not result in an increase of filled nanotubes after washing, a 1:3 ratio (filled sample: fullerenes) appears to be the highest suitable ratio to be employed for corking.

In order to confirm that the introduction of $C_{60}$ molecules within the filled CNTs is independent on the filling agent, MWCNTs filled with $ZnI_2$ and $CeI_3$ (**Section 4.4**) were also treated with fullerenes. $ZnI_2$@MWCNTs were prepared by annealing (475 ˚C, 12 h) 10 mg of purified MWCNTs (5 h, steam) and 300 mg of $ZnI_2$, previously ground together and transferred into a sealed silica ampoule under vacuum. Afterwards, 5 mg of $ZnI_2$ filled MWCNTs were heated during 48 h at 400 ˚C in the presence of 10 mg of fullerenes (1:2 ratio). The solubility of $ZnI_2$ in water in normal conditions is considerably high (4380 $mg.mL^{-1}$),[245] and the external material is thus easily removable by simple washings with aqueous solutions. Thus, the mixture was refluxed in distilled water (overnight) after 15 min of bath sonication. After washing the presence of both $ZnI_2$

nanorods and SLINTs encapsulated within the MWCNTs is observed (**Figure 4.15 (a)**), confirming the capability of $C_{60}$ to block the entry parts of CNTs. Following the same protocol, $CeI_3$@MWCNTs were filled employing 10 mg of MWCNTs and 200 mg of the cerium halide; the sample being annealed at 900 ˚C (temperatures selected considering the melting points of the salt). The corking procedure was performed with the same ratio between $CeI_3$@MWCNTs and $C_{60}$ (1:2, filled sample: fullerenes) and water was employed for the subsequent washings. **Figure 4.15** shows a specimen of a $CeI_3$@MWCNT present in the sample after drying at 60 ˚C **(b)**. Additionally, a MWCNT present in the $C_{60}ZnI_2$@MWCNTs sample with its external walls partially covered by fullerenes is presented in **Figure 4.15 (c)**. The presence of the $C_{60}$ molecules blocking the CNTs ends can be appreciated confirming its role as blocking agent. In this manner, the use of fullerenes is presented as a useful protocol to isolate inorganic halides grown within MWCNTs, which allows the removal of impurities remnant after the filling process.

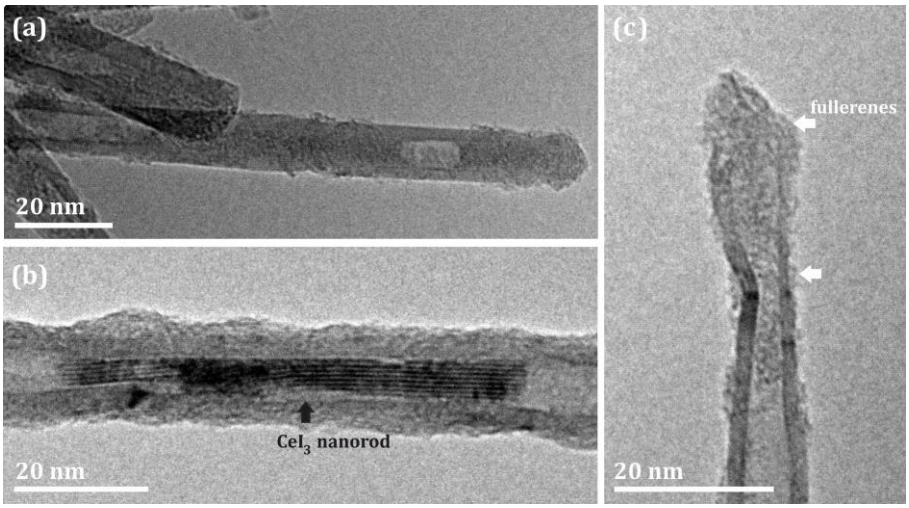


**Figure 4.15.** (a) $C_{60}ZnI_2$ @MWCNTs sample. (b) $C_{60}CeI_3$ @MWCNTs sample and (c) Open ended MWCNT covered by fullerenes after the $C_{60}$ corking of filled MWCNTs .

### 4.5.2. Release of crystalline structures from multiwalled carbon nanotubes assisted by fullerenes.

In **Section 4.5.1** the ability of fullerenes to seal inorganic material inside MWCNTs was evaluated. Following a similar approach, and taking advantage of the affinity of fullerenes towards specific solvents, the use of $C_{60}$ molecules to assist on the displacement of inorganic encapsulated nanostructures was explored.

As we have seen, washing of $C_{60}PbI_2$@MWCNTs sample with $H_2O$ maintains intact the filling while the external inorganic material is removed (**Figure 4.14 (b)**). The strong electrostatic interactions existing between the CNTs walls and the $C_{60}$ molecules, combined with the poor solubility of fullerenes in water[250] produce the corking of the opened tips of the hosting carbon nanotubes. Now, if the physicochemical properties of fullerenes are considered, employing a solvent with certain affinity with the $C_{60}$ molecules may facilitate the mobility of fullerenes inside the CNTs. Fullerenes could act as appropriate replacing agents favoring the displacement of the inorganic nanomaterial and triggering its release from the host. In order to prove this hypothesis, the corked $PbI_2$ filled sample was washed employing ethanol as promoting solvent. For this purpose, the sample was refluxed at 80 ˚C during 16 h, filtered, washed with pure ethanol and dried overnight at 60 ˚C. $PbI_2$ is not soluble in ethanol[245] and under normal conditions (in absence of fullerenes) the inorganic $PbI_2$ confined within the hosting cavitity should remain immovable from the MWCNTs. Thus, the sample without a previous $C_{60}$ corking treatment was additionally washed with ethanol as reference. In order to verify the presence (or absence) of both $PbI_2$ and fullerenes within the MWCNTs, TEM imaging was carried out.

A low magnification TEM image of the $PbI_2$@MWCNTs after washing with ethanol is presented in **Figure 4.16 (a)**. As expected, the solvent was unable to remove the crystalline nanorods grown during the molten phase treatment (due to the low solubility of the $PbI_2$ in ethanol), despite the inner material was exposed to the solvent

through the opened tips of the nanotubes (inset). In contrast, when the sample was previously annealed in presence of fullerenes and subsequently washed at the same conditions (ethanol, 80 ˚C, 16 h), the majority of the inorganic guests were washed out from the MWCNTs **(b)**.

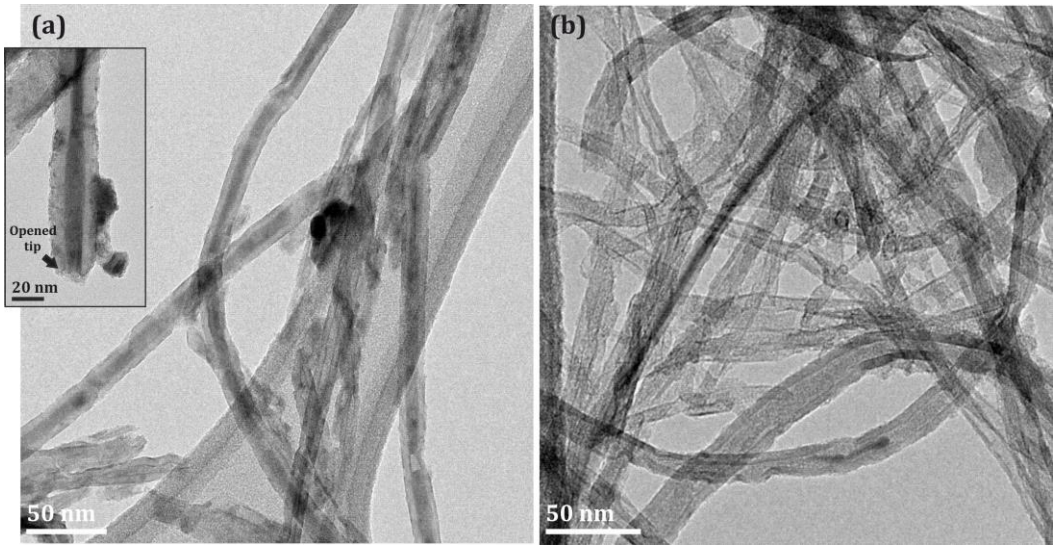


**Figure 4.16.** (a) $PbI_2$@MWCNTs and (b) $C_{60}PbI_2$@MWCNTs after washing with anhydrous ethanol at 80 ˚C during 16 h.

One could think that the strong non-covalent interactions formed between the $C_{60}$ molecules and the CNTs walls should constitute a highly energetic barrier to be overcome in order to produce the mobility of the fullerenes along the inner cavity of the nanotube. Additionally, electrostatic interactions, such as van der Waal forces, existing between the inorganic nanostructure and the CNTs may be an additional difficulty towards the displacement of the guests outside the nanotubes. The interactions between the fullerenes and the walls of SWCNTs in the system formed by $C_{60}$ encapsulated within a SWCNT (nanopeapod, NPP) have been extensively discussed.[251] Theoretical studies have described the energetic stability of the NPP, including the high binding energies present between the fullerenes and the

nanotube.[252] The strength and stability of these interactions depends on the symmetry and dimensions of the nanotube.

The entrance of the $C_{60}$ molecules into the nanotubes requires specific energies,[223] which can be provided either by high temperature treatments (see **Section 4.5.1**),[136] or by the assistance of a solvent with certain characteristics.[134] J. Yudasaka *et al.* proposed a successful methodology, which they called "nano-extraction", consisting in the incorporation of fullerenes within SWCNTs promoted by the suspension of a mixture of both materials in ethanol. This liquid phase technique, leads to the formation of NPPs and takes advantage of the solubility of the $C_{60}$ molecules in the solvent, which although poor, is strong enough to promote the interaction between the fullerenes and the CNTs, provoking the incorporation of the $C_{60}$ molecules into the nanotubes.

Fan *et al.* studied the effect of the diameter in both the incorporation and release of fullerenes into SWCNTs assisted by toluene.[253] It was found that small diameters of the host favor the encapsulation, while the removal of the encapsulated $C_{60}$ molecules presents the opposite trend. The release process requires the use of a solvent in which fullerenes are highly soluble.[254] For a system formed by MWCNTs and fullerenes, a theoretical approach would be more complex. In fact, the incorporation of fullerenes within MWCNTs has been barely reported.[255] Considering that the diameter and the contact surface between the nanotubes and the $C_{60}$ molecules may play a role in the release of the inorganic material, fullerenes incorporated within the cavities of the MWCNTs should possess weaker affinity with the inner walls if compared to the SWCNTs. Nevertheless, the established interactions appear to still be strong and the trafficking of the fullerenes along the cavities of the nanotubes may also require a driving force.

Low fullerene solubility solvents have been employed to incorporate fullerenes within the SWCNTs cavities.[134, 254] However, their potential to assist the release of the $C_{60}$ from CNTs has not been investigated.

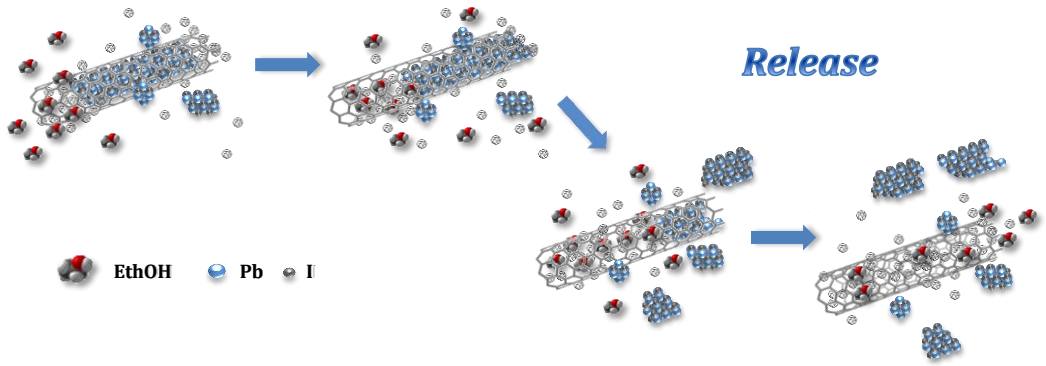


**Scheme 4.1.** Schematic representation of the fullerene assisted release of $PbI_2$ from MWCNTs employing ethanol as promoting solvent.

According to our observations, the attraction forces between the $C_{60}$ molecules and the inner walls are significantly altered when fullerenes are confined within MWCNTs. This is in agreement with theoretical studies on SWCNTs of different dimensions filled with drug molecules, where an increase in the release of the inner material is observed for nanotubes with higher diameters.[235] A graphical representation of the process of release of the inorganic salt from the CNTs cavities is presented in **Scheme 4.1**. A competitive replacement of the inorganic fraction contained within the tube is produced. The high diffusivity of the liquid solvent contributes towards the mobility of the fullerenes within the MWCNT, expelling out the inorganic salt. Additionally, the increase in the contact area between the fullerenes and the CNT wall might enhance the stability of the system by the creation of van der Waal forces between the hosting nanotubes and the $C_{60}$ molecules.[234]

In order to evaluate the protocol employed for the encapsulation of fullerenes in the efficiency of the release process an alternative strategy was employed. As mentioned before the nano-extraction technique allows the encapsulation of fullerenes within SWCNTs by suspending both materials in ethanol (liquid phase technique).[134] If this approach is applied to the removal of the inner structure assisted by fullerenes, the process would not only be reduced to a single step, but also would allow the insertion of fullerenes employing mild conditions, having potential applications to the release of

non-thermally stable guest nanostructures. For this purpose 5 mg of fullerenes were suspended in pure ethanol and dispersed by sonication during 30 min. Afterwards 5 mg of the $PbI_2$@MWCNTs were added to the dispersion and sonicated for 15 min. The mixture was refluxed (80 ˚C) during 16 h, cooled down and filtered using a 0.2 μm polycarbonate membrane. After drying overnight at 60 ˚C, the material was analyzed by TEM. A low magnification image of the $PbI_2$ filled MWCNTs after washing with the ethanolic dispersion of fullerenes is presented in **Figure 4.17 (a)**.

Microscopy analyses confirm the replacement of the encapsulated $PbI_2$ by the $C_{60}$ molecules. The small nanoparticles observed on the outer surface of the nanotubes correspond to the $PbI_2$ displaced from the cavities of CNTs. The latest protocol results in a higher amount of fullerenes present along the nanotubes. $C_{60}$ molecules were homogeneously distributed through both the external walls of the nanotubes and inside their cavities (**Figure 4.17 (b)**).

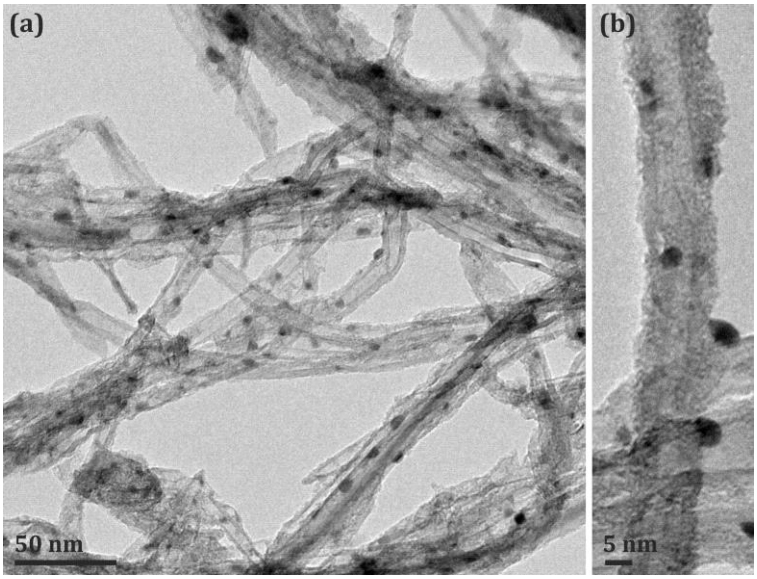


**Figure 4.17.** (a) $PbI_2$@MWCNTs after washing at 80 ˚C during 16 h with a dispersion of fullerenes in absolute ethanol.

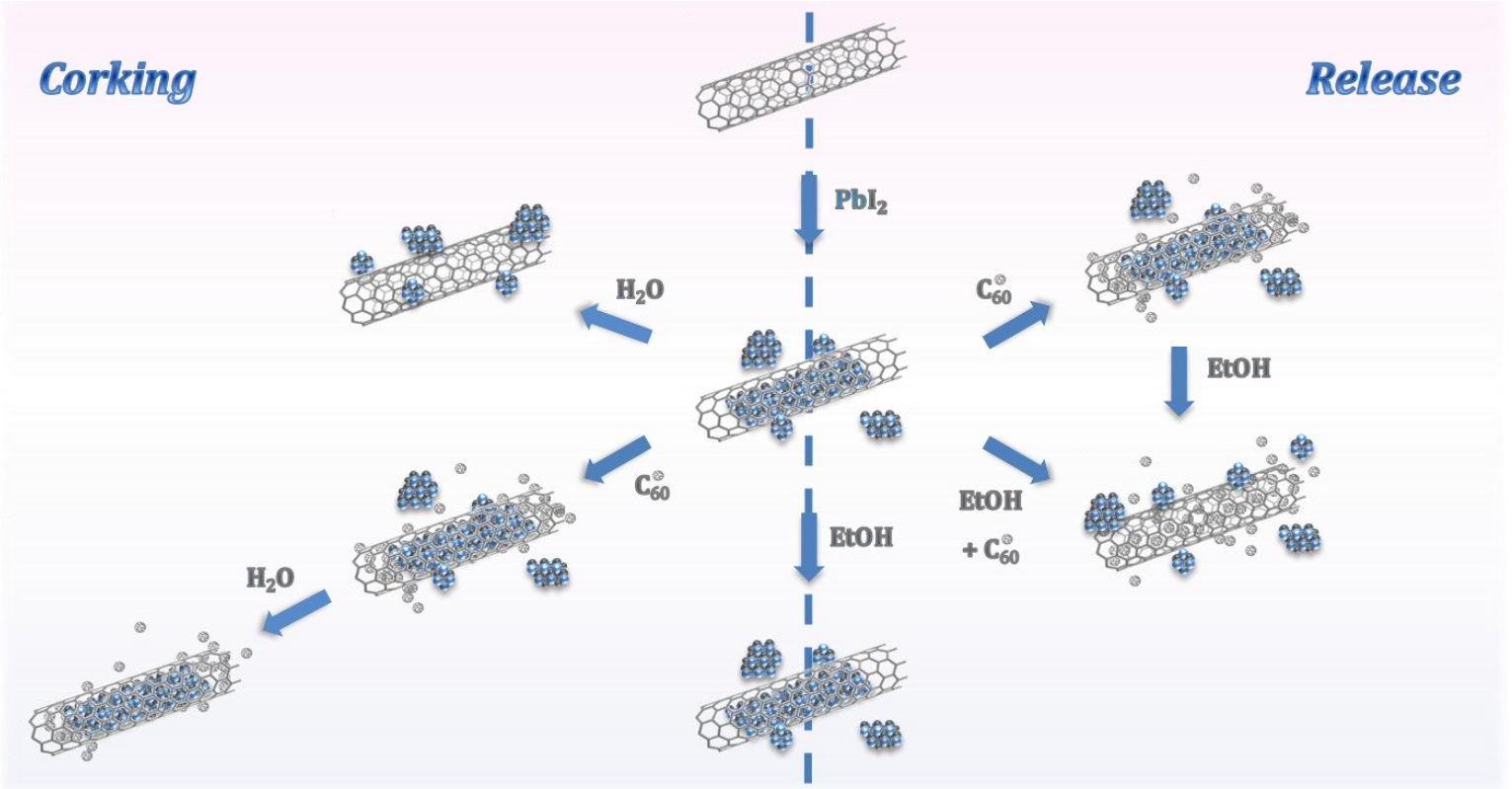


**Scheme 4.2.** Schematic representation of the mechanisms of corking of MWCNTs and release of the guest material from the hosting nanotubes promoted by fullerenes.

**Scheme 4.2.** summarizes the proposed complementary approaches: corking of MWCNTs and release of inner material confined within their cavities. On the one hand, fullerenes can be employed as efficient corking agents of open ended MWCNTs, which facilitate the removal of external material resulting from the filling process (left). This protocol is useful as long as the cleaning of the filled nanotubes is carried out employing solvents whose affinity with the $C_{60}$ molecules is extremely low. On the other hand a versatile protocol for the removal of inorganic material from the inner cavities of MWCNTs is proposed (right). The encapsulation of fullerenes by thermal treatment followed by the ethanol assisted migration of the $C_{60}$ molecules arises as a potential strategy to trigger the liberation of materials stable at elevated temperatures. Otherwise, a liquid phase methodology, involving a single step procedure and mild conditions of reaction is suggested for the simultaneous incorporation of fullerenes and release of temperature sensitive structures from the hosting CNTs.

## 4.6. Conclusions.

### Synthesis of single-layered inorganic nanotubes within MWCNTs

- MWCNTs were employed as directing templates for the growth of single-layered inorganic nanotubes.

- $CeI_3$, $CeCl_3$ and $ZnI_2$ single-layered inorganic nanotubes confined within multiwalled carbon nanotubes were successfully grown by the molten phase capillary wetting technique.

- The molten phase filling of metal halides leds to the formation of different nanostructures within the hosting MWCNTs. Apart from nanorods, inorganic nanotubes, nanoparticles and nanosnakes of the inorganic salts were also obtained.

- An increase in the temperature of treatment results in the preferential growth of $ZnI_2$ single-layered nanotubes.

- Treatments above the boiling point of the bulk $ZnI_2$ results in a higher degree of filling and in better crystallized nanostructures inside MWCNTs. Higher temperature treatments clearly favor the growth of long tubular inner structures and a decrease of other type of inorganic nanostructures.

- The employed methodology can be applied to the synthesis of 1D-layered inorganic nanotubes of different metal halides demonstrating the versatility of the proposed approach.

## Encapsulation of fullerenes within MWCNTs

- Fullerenes were employed to "cork" the ends of MWCNTs, thus allowing to isolate the inorganic materials previously filled. The presence of fullerenes avoids the release of the encapsulated payloads during the removal of the external non-filled inorganic material remnant after the filling procedure.

- Depending on the experimental conditions, fullerenes can also induce the release of inorganic nanostructures present within MWCNTs. In the present study, ethanol was employed as promoting solvent to favor the mobility of the $C_{60}$ molecules within MWCNTs, assisting the removal of inorganic nanostructures previously grown within the hosting nanotubes.

- A versatile protocol, involving high temperature treatments and liquid phase techniques has been proposed to induce the liberation of inorganic nanostructures from the cavities of MWCNTs.

# Chapter 5.

# Decoration of multiwalled carbon nanotubes with titanium oxides.

This chapter describes the synthesis and characterization of MWCNTs decorated with titanium oxides. The potential application of this family of materials in the photocatalytic degradation of organic compounds under UV irradiation is explored.

# 5.1. Introduction.

The chemistry of titanium oxides and formation of diverse polymorphs which are originated at specific conditions of pressure and temperature have been widely studied.[256, 257] The formation of $TiO_2$ is the only occurring at atmospheric pressure and it has been extensively employed due to its excellent electronic properties. $TiO_2$ is a semiconducting material with potential applications in the fields of solar cells,[258, 259] as supercapacitor[260] or field-effect transistors.[261] It has been proposed as the most promising photocatalyst for the degradation of organic pollutants in aqueous media due to its high chemical stability, abundance and low cost.[262] The $TiO_2$ photocatalytic activity has attracted interest in other important technological areas, such as air purification,[263] electrolysis of water for hydrogen generation,[264] or as self-cleaning coating.[258, 259]

$TiO_2$ exhibits three polymorphs: anatase, brookite and rutile. The latter is the most stable phase and it is generally synthesized at elevated temperatures. The synthesis of brookite is not straightforward and it has been barely studied. On the other hand the thermodynamics and kinetics of the transformation from anatase to rutile, as well as the photocatalytic properties of both polymorphs are well documented.[257] Anatase and rutile show band gaps of 3.2 eV and 3.0 eV respectively; nevertheless, the anatase phase is considered as the most active photocatalytic polymorph of $TiO_2$, due to its higher redox potential and density of surface hydroxyls, which favors the presence of reactive electron-hole pairs.[265] However, the efficiency not only depends on the conformation of the material, but also on its morphology. In fact, Degussa P25, which is usually employed as reference material for photocatalytic studies due to its high performance,[263] consists of an 80:20 mixture of anatase:rutile.

Research for the enhancement of the catalytic properties of this family of compounds has been directed to the synthesis of materials with higher surface area,[266] porosity

and crystallinity.[267] Many efforts have been triggered to the narrowing of the $TiO_2$ band gap as well as the reduction of the recombination of the photogenerated electrons and holes which are responsible of its extraordinary catalytic behavior.[268] Surface modifications to enhance the adsorption of organic pollutants, doping with metal and no-metal species to extend the range of absorbed energy to the visible light spectrum, and the stabilization of the $TiO_2$ particles employing different supports are strategies proposed to increase the efficiency of the catalyst. [269]

The potential photocatalytic applications of suboxides of titanium have also been explored. The routes of preparation of $TiO_{2-x}$ materials involve the introduction of dopant atoms,[270, 271] as well as the creation of oxygen vacancies in the $TiO_2$ structure.[272] Whereas doping with non-metal and metal ions is regarded as an efficient way for narrowing the band gap of $TiO_2$, the introduction of lattice defects, which act as carrier recombination centers, reduces the catalytic activity of the materials.[271]

In recent years the preparation of titanium monoxide (TiO) has attracted a wide interest. Its disordered structure has a cubic crystal conformation with the presence of structural vacancies, responsible of the nonstoichiometry of the system (over a range from $TiO_{0.7}$ to $TiO_{1.25}$).[273] The possibility of continuously changing the concentration of both, the anionic and cationic vacancies, confers the material diverse properties depending on the structure of the resulting phase. TiO has a great corrosion resistance, low resistance to charge transfer and high hardness,[274] which confer it versatility for a wide range of applications, such as decorative or protective coater, or as material for nanoelectronic applications.[275] Different routes have been employed to prepare TiO particles. Its synthesis usually involves the reduction of titanium dioxide in presence of metallic titanium.[276] Following this approach, different phases of TiO have been obtained by mechanochemical,[277] and high temperature treatments (1500 °C).[273] Other techniques employ laser pyrolysis of titanium isopropoxide,[270] laser ablation,[278] wet ball milling[279] and chemical and electrochemical reduction.[280]

Nevertheless, TiO is difficult to synthesize and variable phase compositions are generally obtained. However, high temperature treatments (>1500 ˚C) can promote the formation of anion vacancies ordered phases of low symmetry.[281]

The preparation of particles with small diameters is usually proposed to obtain catalysts with high surface areas. Unfortunately, these are subjected of rapid aggregation, which decrease the effective surface and hence the absorption of the target species. To overcome this problem, several supports such as carbon, clay and silica-based materials have been employed to anchor the photocatalytic nanoparticles. Depending on its nature, the supporting material can additionally enhances the catalytic performance.[268] Carbon-based nanostructures, and particularly carbon nanotubes have been documented as efficient supports due to their large surface area, high mechanical strength and adsorptive capacity.[282] Moreover the CNTs stabilize the charge separation, hindering the charge recombination and thus promoting the separation and migration of the electron-hole pair.[283]

Considering the beneficial effects reported for titanium suboxides and for CNTs in dye degradation, we have prepared MWCNTs decorated with titanium oxide nanoparticles to obtain a composite material with a high photocatalytic performance. The synthesis of a self-standing $TiO_2$-based catalyst, free of the carbon support, by oxidation of the former material was additionally explored. Preliminary photocatalytic tests to evaluate the efficiency of the synthesized materials in the degradation of an organic compound were finally carried out.

## 5.2. Objectives.

- To employ MWCNTs as template and directing agent for the preparation of TiO-decorated MWCNTs.
- To explore the influence of the morphology of the TiO nanoparticles structure in the thermal stability of the samples.
- To analyze the phase transformations occurring during the oxidation of the TiO nanoparticles at different temperatures.
- To prepare self-standing $TiO_2$-based nanostructures, free of MWCNTs, by oxidation of TiO decorated MWCNTs.
- To explore the potential use of the TiO-decorated MWCNTs before and after oxidation, as catalyst for the degradation of organic compounds.

## 5.3. Synthesis of multiwalled carbon nanotubes decorated with titanium oxide nanoparticles.

MWCNTs decorated with titanium oxide nanoparticles ($TiO_x$NPs-MWCNTs) were prepared by high temperature treatment of a $TiCl_2$/MWCNTs mixture (*in situ* modification). 12 mg of purified MWCNTs, obtained after 2 h of steam treatment (**Section 4.3**)[238] and 240 mg of $TiCl_2$ were homogeneously grinded with an agate mortar and pestle and introduced into a silica tube. Afterwards the system was sealed under vacuum and annealed at 1060 ˚C. [4][245] After the synthesis, the ampoule was opened and the product was kept under an oxygen-free atmosphere inside an Ar-filled glove box. The sample was characterized by electron microscopy analysis (TEM and SEM) and X-Ray Diffraction (XRD). **Figure 5.1 (a)** shows a low magnification TEM image of the synthesized material. Microscopic analysis confirms the formation of nanoparticles deposited on the external walls of the CNTs.

As it was described before (**Section 4.3**), the steam treatment causes the opening (oxidation) of the more reactive ends of the nanotubes, which allows the introduction of guest materials within the hosting cavities of the CNTs. The molten phase capillary wetting approach is usually employed for the filling of CNTs. After the 1060 ˚C annealing of the $TiCl_2$/MWCNTs mixture, the presence of the inorganic material inside the MWCNTs is observed. As it can be seen in the image, this approach allows the simultaneous external decoration of the MWCNTs with titanium-based nanoparticles, as well as the filling of the MWCNTs. The obtained nanocomposites can be observed in **Figure 5.1**. Besides, the presence of drop shaped particles is observed **(d)**.

[4] The sample was initially dwelled at 800 °C during 2 h and the temperature was subsequently increased up to 1060 °C (4h). Afterwards, the system was cooled down at 25 °C.min$^{-1}$.

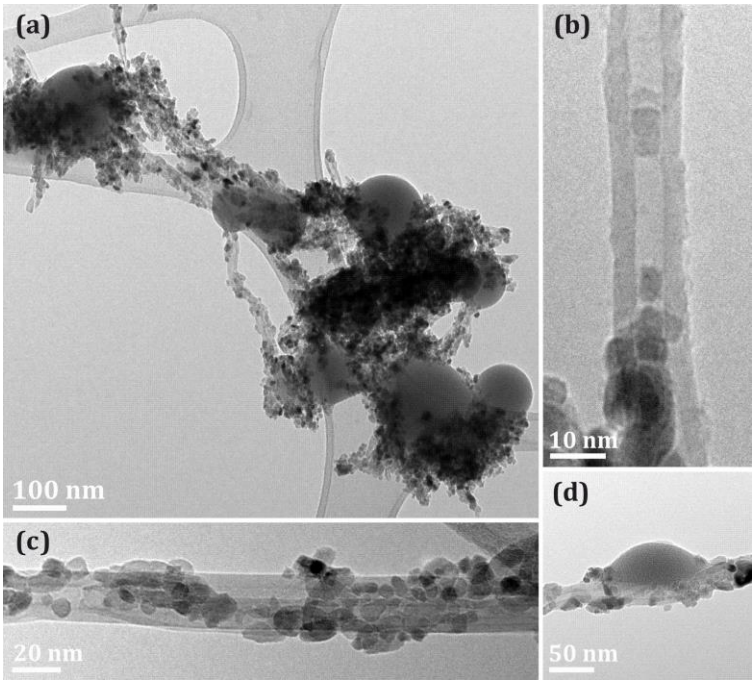


**Figure 5.1.** (a) Low magnification TEM image of the MWCNT/$TiCl_2$ mixture, after annealing at 1060 °C. (b) Nanoparticles filling a nanotube and (c-d) MWCNTs partially decorated with Ti-based nanoparticles.

After annealing the ampoule, aside from the characteristic black powder resulting from the $TiCl_2$/MWCNTs mixture, small violet drops and crystals were observed. These secondary products were also collected and analyzed by XRD. Considering that titanium derivatives with low oxidation states (II and III) are highly unstable in air the XRD measurements were carried out by protecting the sample with a Kapton® film. The XRD pattern of the analyzed crystals is presented in **Figure 5.2.** The diffraction pattern corresponds to one of the three violet modifications of the $TiCl_3$ (α structure).[284]

Titanium dichloride is a strong reducing agent. A violent reaction with evolution of hydrogen occurs in presence of water. Furthermore, it reacts easily with oxygen to form a variety of compounds with different oxidation states.[285] Considering the nature of the crystals, and the presence of the drops observed in the TEM images of the collected product (**Figure 5.1**), the particles present along the nanotubes walls may correspond to

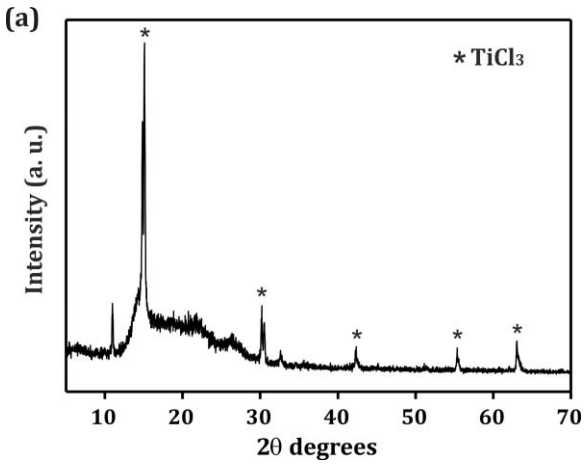


**Figure 5.2.** XRD analysis of the purple crystals obtained as secondary products in the synthesis of the MWCNTs decorated with Ti-based nanoparticles. The XRD pattern was acquired by protecting the sample with a Kapton® film (broad background within 10-30 degrees).

partially oxidized derivatives of the titanium halide ($TiCl_2$).

Energy dispersive X-ray (EDX) analysis was employed to determine the composition of the sample (**Figure 5.3**). The presence of titanium, chlorine and carbon was confirmed. It is also noticeable an intense peak of oxygen. This confirms that a series of oxidative processes may take place inside the silica ampoule. However, the ratio between the species varied drastically when different areas of the same sample were analyzed. The signals corresponding to copper, aluminum and Si arise from the support and from de silica ampoule employed for the synthesis, respectively.

Taking into account that the treatment was carried out under high vacuum conditions, the only source of oxygen in the system should come from the container. The composition and properties of crystalline and non-crystalline silica have been widely studied. It is well known that the $SiO_2$ usually possess structural defects which can affect the physical properties of the material. Several point defects are attributed to oxygen vacancies or oxygen excess which include silanol groups, peroxy linkage and peroxy radical centers (**Figure 5.4**).[286] Moreover, small quantities of water can be physically trapped in structural channels or holes, or localized along grain

boundaries.[287] Adsorbed water and oxygen from the mentioned defects can be easily removed when the temperature is increased, becoming a source of oxidative species able to provoke the formation of the oxidized derivatives of the highly sensitive $TiCl_2$. The liberation of adsorbed water and the condensation of structural species are gradually produced at different temperatures; nevertheless, the concentration of these species in the silica structure varies according to different parameters, namely the source of the employed silica, the surface area, or the environmental conditions. For this reason the transformations taking place inside the silica ampoule are hardly controllable.

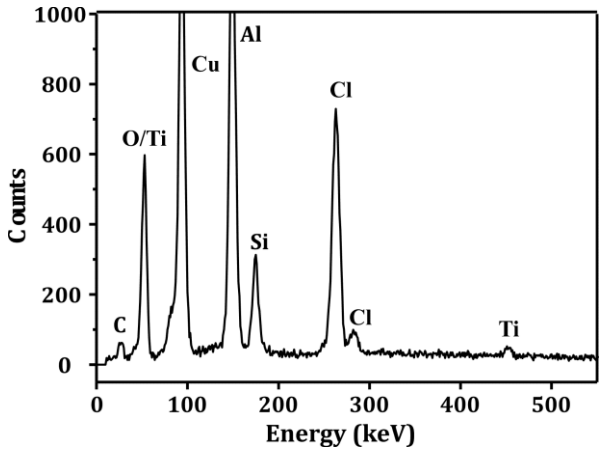


**Figure 5.3.** EDX analysis confirming the presence of Ti, Cl and C in the sample. Al and Cu signals arise from the support employed for the analysis, and the Si peak comes from the silica ampoule used for the synthesis.

The elimination of adsorbed water from the silica is well documented. Water is released discontinuously until about 600 ˚C. Higher temperatures (until ca. 1200 ˚C) may cause the removal of species coming from structural defects, for example, water coming from the condensation of silanol groups (**Figure 5.4,** dashed square). However, the release decreases significantly.

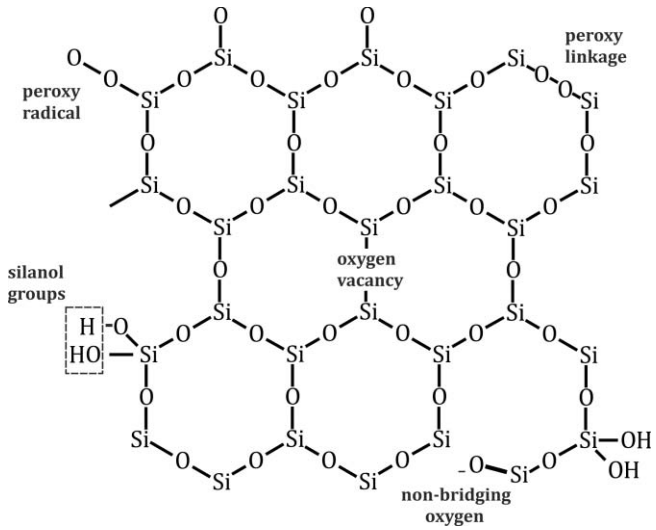


**Figure 5.4.** Scheme of oxygen point defects present in the silica structure.

In order to remove the adsorbed water present in the container, the silica tubes were subjected to an 800 ˚C preheating treatment before being used for the synthesis. In this manner, the concentration of the water molecules within the system was minimized and the formation of undesired oxidized derivatives was avoided. However, the structural defects cannot be totally removed at this temperature. The removal of these groups is produced during the annealing of the mixture of $TiCl_2$ and the MWCNTs; thus a more controlled liberation of oxidative species is expected. On the other hand, bulk TiO is manufactured by heating $TiO_2$ in presence of metallic titanium under a low pressure system (*in vacuo*).[276] To reproduce the conditions of the synthesis, the system initially employed for the decoration of MWCNTs was modified. A titanium film (5 mm x 10 mm) was introduced in the pre-heated ampoule along with the reaction mixture. The system was sealed (under vacuum) and the mixture (12 mg of MWCNTs and 240 mg of $TiCl_2$) was annealed at the same temperature (1060 ˚C). The powder obtained after cooling presented a homogeneous black color and the presence of violet crystals or drops was not observed. Electron microscopy analyses were carried out to determine the characteristics of the samples.

**Figure 5.5 (a)** shows a low magnification TEM image of the obtained powder after dispersion in hexane. In contrast to the previous sample, now the presence of drop shaped material is not observed. Titanium-based nanoparticles cover the external surface of the nanotubes forming a necklace type nanostructure, "nanonecklace" on top of the MWCNTs.

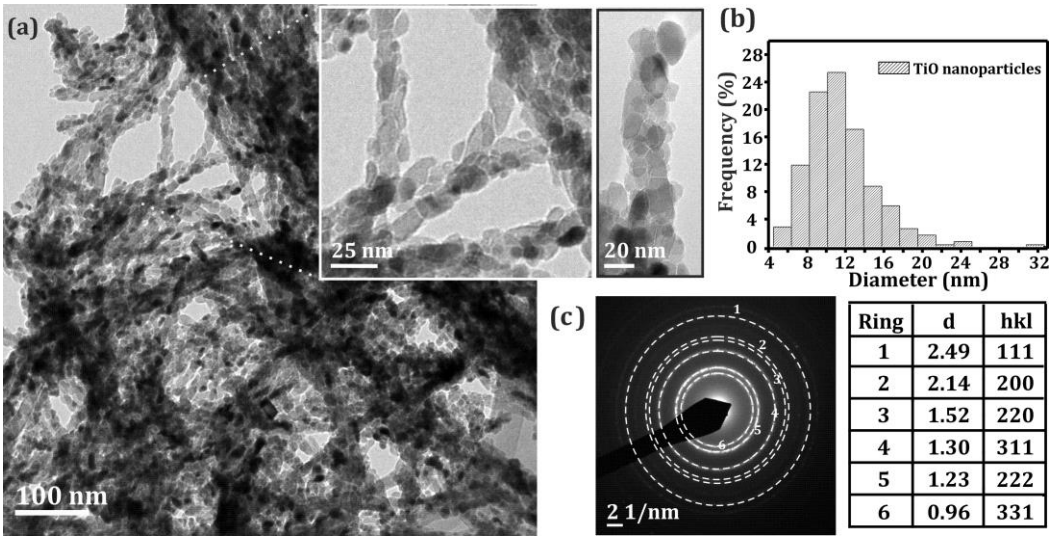


| Ring | d | hkl |
|---|---|---|
| 1 | 2.49 | 111 |
| 2 | 2.14 | 200 |
| 3 | 1.52 | 220 |
| 4 | 1.30 | 311 |
| 5 | 1.23 | 222 |
| 6 | 0.96 | 331 |

**Figure 5.5.** (a) Low magnification TEM image of the MWCNT/$TiCl_2$ mixture, after annealing at 1060 °C in presence of the titanium film. The inset shows a high magnification of a selected area of the main image. (b) Histogram showing the distribution (frequency, %) of diameters of the synthesized nanoparticles and (c) SAED pattern corresponding to the TiOx decorating nanoparticles.

The inset in **Figure 5.5 (a)** shows a high magnification TEM image of a selected area of the sample. As it can be seen, the nanoparticles cover the totality of the external walls of the nanotubes and its distribution along the sample is directed by the tubular surface of the MWCNTs. TEM images were additionally employed to determine the particle size distribution. **Figure 5.5 (b)** presents the resulting histogram. A median diameter of 11.5 nm was determined after measuring more than 400 nanoparticles decorating the MWCNTs. The nanoparticles presented diameters between 4.5 nm and 32.6 nm; however, the majority of them (65 %) were located between 8 nm and 12 nm. Finally, the

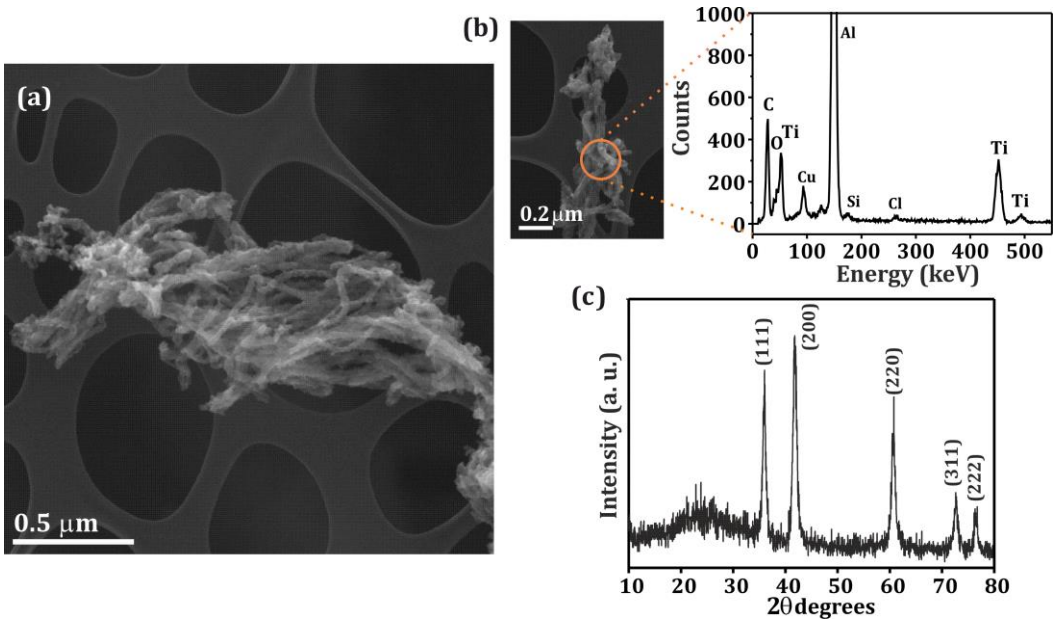


**Figure 5.6.** (a) Low magnification SEM image of MWCNTs decorated with Ti-based nanoparticles prepared by annealing a $TiCl_2$/MWCNTs mixture in presence of metallic titanium. (b) EDX analysis confirms the presence of Ti, Cl and C in the sample. (c) Powder X-ray diffraction pattern.

selected area electron diffraction (SAED pattern (**Figure 5.5 (c)**) shows the characteristic rings of a polycrystalline structure. The distance between the rings corresponds to d spacing of planes characteristics of cubic TiO.

To confirm that the nanoparticles decorating the MWCNTs correspond to TiO, EDX and XRD analyses were carried out. **Figure 5.6** shows SEM images **(a)** and the corresponding EDX spectrum of a selected area of the sample **(b)**. The presence of titanium, chlorine and carbon (the former constituent of the sample before annealing) and oxygen is observed. Again, aluminum, copper and silicon signals arise from the support and from de silica ampoule. Despite that chlorine is still present; a drastic decrease of the signal is observed when compared with the spectrum of the sample prepared in absence of the titanium film (**Figure 5.3**). EDX-SEM analyses of the samples show Ti/O atomic ratios of ca. 1 and the content of chlorine did not exceed 2 at. %. These values are in agreement with the electron diffraction pattern. Finally, the phase

composition of the titanium monoxide was confirmed by X-ray diffraction. The signals observed in the pattern of the powder **(c)** can be indexed as the cubic crystallographic phase of titanium monoxide. The presence of the highly reduced titanium oxide nanoparticles confirms that a controlled oxidative process occurs inside the system. The structural defects present in the silica container may induce the oxidation of the titanium dichloride when the oxygen-based functionalities are released from the silica at high temperatures. Nevertheless, the presence of the titanium film induces the simultaneous reduction of the oxidized species ($TiO_x$) avoiding the formation of titanium-based nanoparticles with a higher degree of oxidation. Considering that EDX, TEM and XRD analyses confirm the presence of a TiO nanostructure; we will refer to this sample as TiO nanoparticle decorated MWCNTs (TiONPs-MWCNTs).

X-photoelectron spectroscopy (XPS) allows a better understanding of the composition and chemical state of titanium in the sample. The XPS general survey scan of the TiONPs-

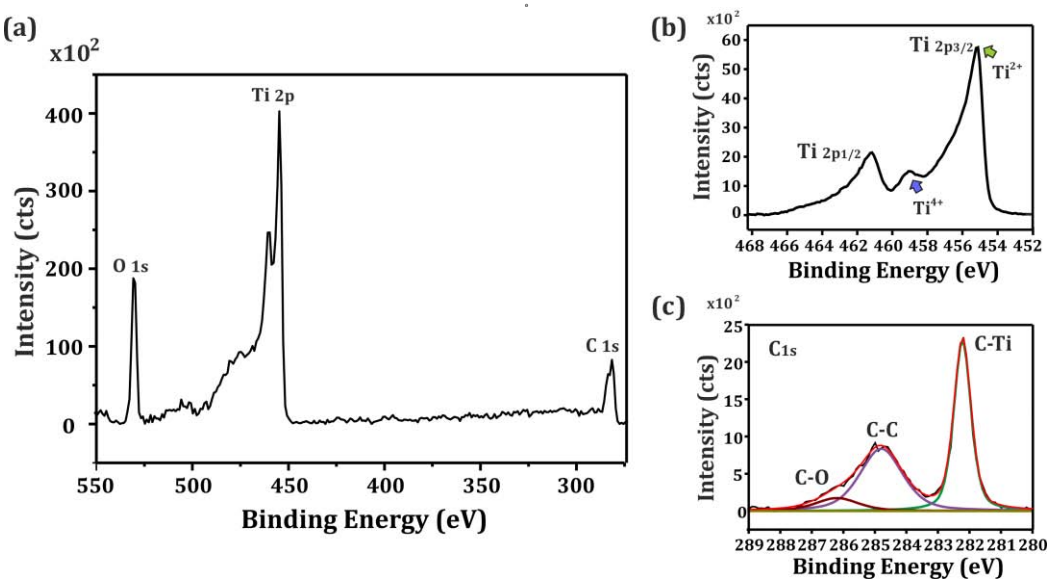


**Figure 5.7.** (a) XPS general survey scan of the TiO-decorated MWCNTs prepared after annealing a $TiCl_2$/MWCNTs mixture in presence of metallic Ti (under vacuum). High resolution spectra of the (b) Ti2p and (c) C1s regions.

MWCNTs confirms the presence of oxygen (530 eV), titanium (468-452 eV) and carbon (284.8 eV) in the material (**Figure 5.7 (a)**). The Ti2p region exhibits two main signals corresponding to the $2p_{3/2}$ (ca. 455.5 eV) and the $2p_{1/2}$ (461.5 eV). Moreover a satellite broad peak centered at ca. 475 eV is also present, which is attributed to transitions of valence electrons to states with higher energies.[288] The position and broadness of the Ti2p signals is associated to the presence of Ti atoms with different binding states.[289] According to the literature, the position of each individual peak is directly correlated with the chemical environment of the element.[290] The presence of the satellite signal in the titanium spectrum ($Ti2p_{1/2}$) is attributed to shake-up excitations or energy losses, and it is not usually considered for the quantification of the species present in the sample. **Figure 5.7 (b)** shows the high resolution XPS spectrum of the sample. Two peaks, located at 455 eV (pointed with a green arrow) and at 459 eV (pointed with a blue arrow), are assigned to titanium atoms with oxidation states of 2+ and 4+, respectively. The non-symmetric shape of the peak corresponding to $Ti^{2+}$ might arise from the presence of titanium atoms with different coordination environments. Diverse phases of titanium suboxides, forming a disordered, but thermodynamically stable state[273] are present in the Ti-O phase diagram.[291] Thus, the presence of titanium with intermediate oxidation states, cannot be discarded.[292] The peak corresponding to $Ti^{4+}$ might arise from the oxidation of a small fraction of titanium atoms located on the surface of the nanoparticles or by the interaction of titanium atoms with the walls of the MWCNTs (C-Ti bonds). The higher atomic concentration of the $Ti^{2+}$ species is in agreement with the results obtained so far by XRD and EDX analysis, indicating the formation of a titanium suboxide.

The high resolution C1s XPS allows obtaining information on the interaction of the CNTs walls and the TiO nanoparticles. The differentiation of two main peaks can be perceived after a simple visual inspection (**Figure 5.7 (c)**). Besides the characteristic peak originated from the C-C bonds of the MWCNTs (284.8 eV), a new signal located at lower binding energies (282 eV) and assigned to Ti-C,[293] confirms the existence of a

chemical bond between the CNTs walls and the TiO nanoparticles. The presence of a peak at higher binding energies (286 eV) suggests an additional binding between the carbon atoms and oxygen species forming the TiO structure. This new bond can be formed by carbon atoms occupying one of the vacancies present in the TiO structure (interstitial atoms),[278] or by substitution of the titanium atoms.[294] Finally, the concentration of the contributing species was determined from the area of the fitted peaks. The calculated area of the carbon corresponds to a 40.8 at % of the sample, whilst titanium and oxygen constitute a 31.1 at. % and a 28.1 at. % of the composite, respectively. In agreement with microscopic and DRX analyses, a ca. 1:1 Ti/O ratio was also obtained from XPS.

The thermal behavior of the TiONPs-MWCNTs sample was evaluated by TGA. The material was annealed in the presence of an oxidizing atmosphere ($O_2$) from room temperature to 1400 ˚C. Visual inspection of the TGA curve (**Figure 5.8 (a),** black line) evidences the presence of three thermal events. The first loss of weight takes place at ca. 120 ˚C and corresponds to absorbed atmospheric species, mainly water molecules. Subsequently, a significant increase in the weight of the sample is produced in the range of 200 ˚C-400 ˚C. This increase of mass can be attributed to the oxidation process of the titanium oxide, leading to the formation of titanium dioxide ($TiO_2$). The Ti:O ratio present in the sample can be determined from this event. The reaction occurring at this temperature (200 ˚C) involves a 28 % increase in the initial mass of the sample; which is close to the theoretical mass gained by the TiO during the transformation of TiO to $TiO_2$ (25 %). As seen in DSC curve (blue line) this process is highly favored by the temperature and the corresponding exothermic peak is centered at 342 ˚C. Afterwards, a drastic loss of weight (ca. 11.4 %) is observed between 400 ˚C and 470 ˚C. The exothermic process (second peak in DSC) is attributed to the combustion of the carbonaceous fraction (MWCNTs) of the sample. Purified MWCNTs shows onsets of combustion around 600 ˚C.[82] In case of the TiONPs-MWCNTs, the presence of the inorganic nanoparticles may accelerate the oxidation of the nanotubes, which explains

the earlier onset of combustion of the sample (400 ˚C). A decrease in the onset of combustion of CNTs has been previously observed when inorganic material is present.[295]

In order to identify the phase of the titanium oxide formed during the oxidation of the TiONPs, the residue recovered after the total combustion of the MWCNTs (470 ˚C) was characterized by XRD. The obtained pattern is presented in **Figure 5.8 (b)** and corresponds to the anatase phase of $TiO_2$.[296] Finally, despite no additional change of weight is appreciated in the TG curve, the DSC analysis reveals a thermal event when the sample is annealed above 600 ˚C (DSC curve, blue line). At this temperature the change of phase from anatase to rutile phase of $TiO_2$ is usually reported.[256, 257] This is in agreement with the XRD pattern[297] of the yellowish-white fraction obtained after annealing the powder at 1400 ˚C **(c)**, and with the broad exothermic process indicated by the DSC analysis.[262]

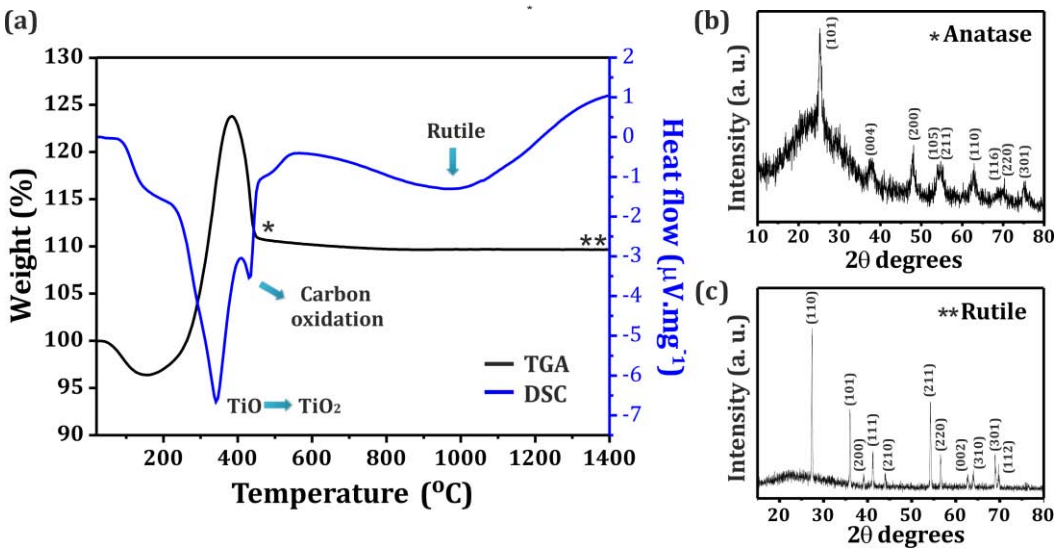


**Figure 5.8.** (a) Thermal analysis of the TiO decorated MWCNTs (TiONPs-MWCNTs) prepared by the 1060 ˚C annealing the $TiCl_2$/MWCNTs mixture in presence of metallic titanium. The analysis was performed under flowing $O_2$ at a heating rate of 10 ˚C.min$^{-1}$. XRD patterns of the residue obtained after annealing the sample at (b) 470 ˚C and (c) 1400 ˚C.

## 5.4. Post-synthesis oxidation of TiO-MWCNTs hybrids: Preparation of $TiO_2$-based catalysts.

As mentioned in the introduction, $TiO_2$ is well known by its photocatalytic applications. For this reason, the preparation of a $TiO_2$ catalyst by oxidation of the TiONPs-MWCNTs was explored. For this purpose 50 mg of the sample were spread into a sintered alumina boat and introduced inside a tubular furnace. Taking into account the results obtained after the thermal analysis of the TiONPs-MWCNTs, the sample was annealed at temperatures ranged between 250 ˚C and 450 ˚C under flowing oxygen at 165 $mL.min^{-1}$, to simultaneously oxidize the TiO nanoparticles and to eliminate the carbonaceous template (CNTs).

**Figure 5.9 (a)** shows the TG analyses of four samples resulting from annealing TiONPs-MWCNTs at 250 ˚C, 275 ˚C, 370 ˚C and 450 ˚C during 6 h in $O_2$. In all the samples a slight decrease of weight, attributed to absorbed water, is observed at temperatures below 200 ˚C. The TG curve of the sample treated at 250 ˚C presents a small increase in the initial mass (4 %) around 300 ˚C, suggesting the partial oxidation of the particles decorating the external surface of the nanotubes. Afterwards, an 8 wt. % loss between 400 ˚C and 460 ˚C, which can be attributed to the combustion of the CNTs is observed. These events appear as exothermic reactions in the DSC analysis (**Figure 5.9 (b)**). In the case of the 275 ˚C treated sample, the thermal event at ca. 300 ˚C has disappeared. Apparently, the TiONPs decorating the CNTs have already been completely oxidized by the post-annealing in $O_2$ at 275 ˚C. However, the combustion of CNTs supporting the $TiO_2$ nanoparticles is still observed at ca. 400 ˚C (ca 8 wt. % loss, violet line). Interestingly, the exothermic process corresponding to the formation of $TiO_2$ is still present in the DSC curve of the 275 ˚C annealed sample (384˚C, violet line; **Figure 5.9 (b)**), despite that the TG curve remains almost invariable at this range of temperature. This suggests that the DSC exothermic signal at ca. 370 ˚C observed in the 250 ˚C

treated sample, cannot be only attributed to the oxidation of the TiONPs but also indicates the simultaneous combustion of the CNTs. The increase of weight expected for the oxidation of the TiO nanoparticles is compensated by the loss of the carbonaceous fraction, which would explain the absence of perceptible changes in the TG curve of the 275 ˚C treated sample. This argument is in agreement with the lower weight loss of carbon observed in the TGA of the 250 ˚C and 275 ˚C (which is related to the 3rd thermal event) compared to the expected weight loss, since the calculated carbonaceous fraction from the TGA of the TiONPs-MWCNTs nanoparticles is 11.6 % (**Figure 5.8 (a)**).

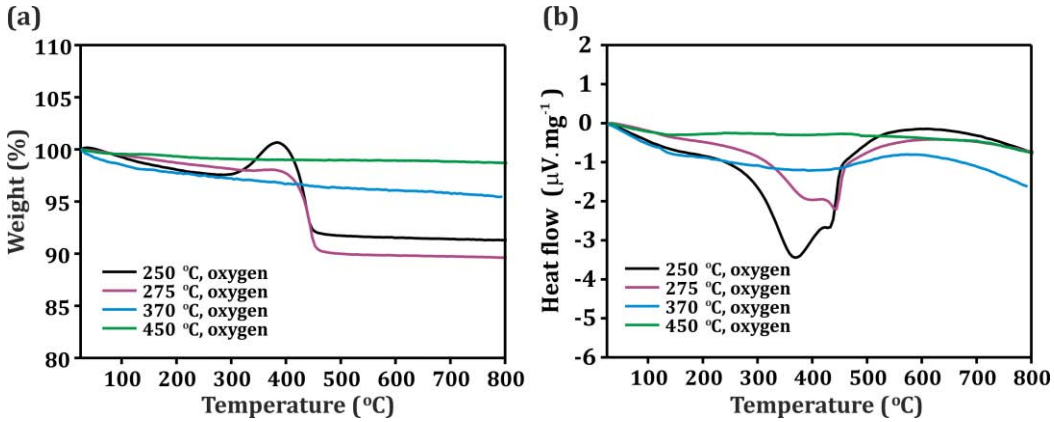


**Figure 5.9.** (a) TG and (b) DSC analyses of the TiONPs-MWCNTs sample after annealing at 250 ˚C (black line), 275 ˚C (violet line), 370 ˚C (blue line) and 450 ˚C (green line) under oxygen for 6 h. TGA and DSC analyses were performed under flowing $O_2$ at a heating rate of 10 °C.min$^{-1}$.

In order to obtain samples free of CNTs, the TiONPs-MWCNTs were annealed at temperatures ranged between 350 ˚C and 450 ˚C maintaining constant the time of treatment (6 h). At these temperatures, the total elimination of the MWCNTs was observed. In the case of the sample treated at 370 ˚C, a unique transformation (blue line, **Figure 5.9 (b)**), corresponding to the phase transition of $TiO_2$ (anatase to rutile) at high temperatures is perceived by DSC analysis. Higher treatments show similar behavior (450 ˚C, green line).

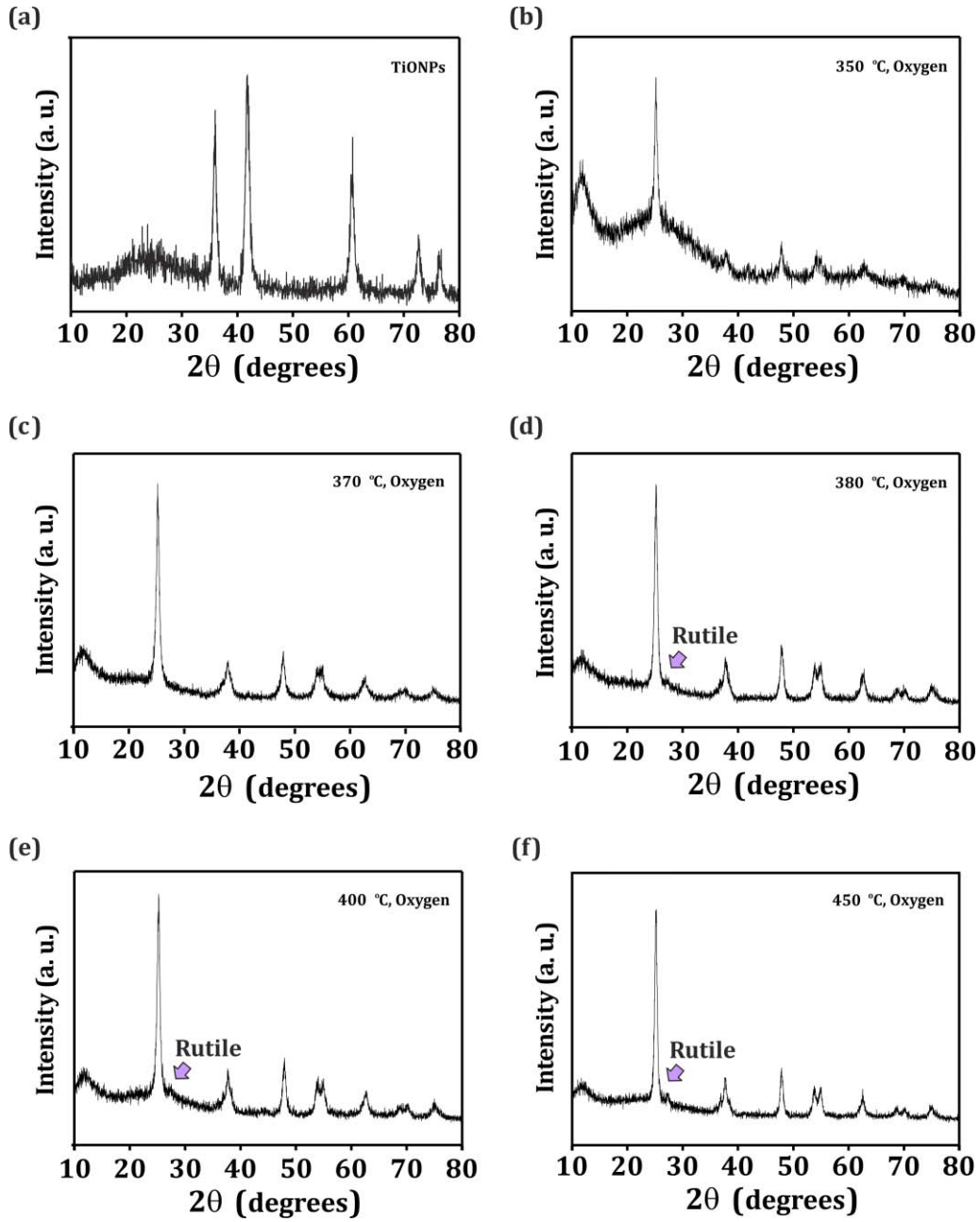


**Figure 5.10.** XRD patterns of the TiONPs-MWCNTs (a) before and after annealing at (b) 350 °C, (c) 370 °C, (d) 380 °C, (e) 400 °C and (f) 450 °C during 6h under oxygen flowing at 165 mL.min$^{-1}$.

XRD analyses were carried out to identify the phases present in the post-annealed samples. **Figure 5.10** shows the diffraction patterns of the TiONPs-MWCNTs after annealing at temperatures ranged between 350 ˚C and 450 ˚C under flowing oxygen during 6 h. The starting material is included for comparison **(a)**. As it can be appreciated, the peaks corresponding to the TiO structure are not present in the XRD patterns of the treated samples **(b-f)**. Peaks present in the patterns of the 350 ˚C **(b)** and 370 ˚C **(c)** oxidized samples indicate the presence of pure anatase. Meanwhile, when higher temperatures were employed for treatments (380 ˚C-450 ˚C) the appearance of the characteristic peak of the rutile phase (2Θ=27.4 ˚) of $TiO_2$ is observed. After treatment, all the samples showed the characteristic white color of $TiO_2$, except for the 350 ˚C annealed material. In this case, a grey colored powder was obtained, in agreement with the presence of a small unoxidized carbonaceous fraction observed by TGA.

The intensity ratio of the rutile (110) (2Θ=27.4 ˚) and the anatase (101) (2Θ=25.2 ˚) peaks is usually employed to quantify the phase proportions in a $TiO_2$ sample (Method of Spurr and Myers [298]). In our case, this value ($I_R/I_A$) presents a slight increase with the temperature of treatment, following the expected trend (**Table 5.1**). However, this approach does not consider important factors such as grain size, morphology or degree of crystallinity, which alter the ratios of the XRD peaks. It should be noted that this phase

**Table 5.1.** $TiO_2$ phase obtained after annealing the TiONPs-MWCNTs sample in $O_2$ at temperatures ranged between 350 ˚C and 450 ˚C.

| Temperature | Time | $TiO_2$ phase | $I_R/I_A$ | Color |
|---|---|---|---|---|
| 350 ˚C | 6 h | Anatase | 0 | Grey |
| 370 ˚C | 6 h | Anatase | 0 | White |
| 380 ˚C | 6 h | Anatase/rutile | 0.13 | White |
| 400 ˚C | 6 h | Anatase/rutile | 0.15 | White |
| 450 ˚C | 6 h | Anatase/rutile | 0.15 | White |
| 350 ˚C | 12 h | Anatase | 0 | White |
| 370 ˚C | 12 h | Anatase/rutile | 0.18 | White |

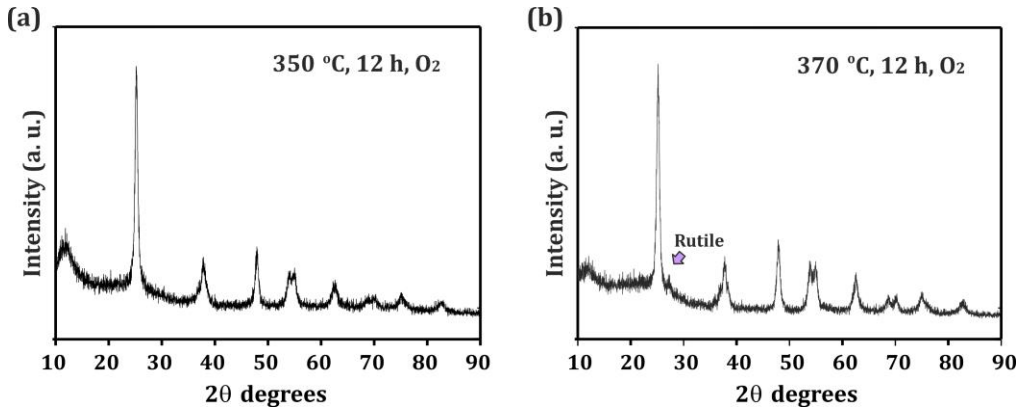


**Figure 5.11.** XRD patterns of the TiONPs-MWCNTs after annealing at (a) 350 ˚C and (b) 370 ˚C during 12 h under flowing oxygen at 165 $mL.min^{-1}$.

transition generally occurs at higher temperature and the morphological and structural characteristics of the material are strongly dependent on the conditions of preparation of the sample, including the temperature of treatment.

In order to completely remove the carbonaceous fraction of the TiONPs-MWCNTs, longer times of treatment were employed to oxidize the sample at 350 ˚C. An additional 370 ˚C oxidizing treatment during 12 h was carried out to determine how the time of treatment affects both the morphology and the structural characteristics of the $TiO_2$-based composite. A white powder was obtained after the 350 ˚C treatment (12 h) and the presence of the pure anatase phase of $TiO_2$ was determined from the XRD pattern (**Figure 5.11 (a)**). Otherwise, when the TiONPs-MWCNTs were annealed at 370 ˚C employing the same time of treatment, it was observed the appearance of the main peak corresponding to the rutile phase of $TiO_2$ (2Θ= 27.4 ˚; **(b)**).

The transformation of pure bulk anatase to rutile is an irreversible process due to its reconstructive character. The process is not instantaneous and involves the breaking and the subsequent reforming of the original bonds present in the tetragonal anatase phase to produce a more dense structure. Furthermore, the anatase-rutile transformation is highly favored by longer times of treatment. This is in agreement

with the mixture of phases observed in the sample treated at 370 ˚C during 12 h. Rutile $TiO_2$ is usually obtained when the material is annealed in air at ca. 600 ˚C.[299] Clearly, the approach employed to induce the phase transformation affects significantly the temperature at which the process occurs. The formation of rutile $TiO_2$ has been reported already at 400 ˚C.[300] The small size of the initial TiO nanoparticles also plays a positive role in the early formation of rutile.[301] Finally, the presence of defects on the oxygen sublattice is the most important factor affecting the phase transformation. The deficient amount of oxygen atoms facilitates the rearrangements due to the decrease in the structural rigidity of the material.[257] The level of oxygen vacancies is also induced by the presence of dopant atoms. In our case, carbon atoms from the MWCNTs walls may act as dopant species by their reducing character, which induce the formation of defects and hence, the transformation to the rutile phase at relatively low temperatures.

The activity of a solid catalyst is strongly dependent on parameters such as the particle size, surface area and morphology. Degussa P25 is a photocatalyst that contains a combination of the anatase and rutile and it is usually employed as reference due to its high photocatalytic performance. The presence of a small fraction of rutile (20 %) in the material reduces significantly the electron-hole recombination, improving its activity in the degradation assisted by UV irradiation. The formation of the rutile phase requires treatments at temperatures relatively high or prolonged times of synthesis. As a consequence, materials with larger grain size, which lower their adsorptive capacity, are obtained.

The morphology of the samples obtained after the subsequent oxidation of the TiONPs-MWCNTs was evaluated by TEM in order to select the most adequate conditions to obtaining well-defined nanostructures, maintaining the large surface area of the starting material. **Figure 5.12 (a)** shows a low magnification TEM image of the TiONPs-MWCNTs after treatment at 370 ˚C during 6 h. As it can be appreciated, the material maintained the necklace-like nanostructure of the parent material. However, the TiO na-

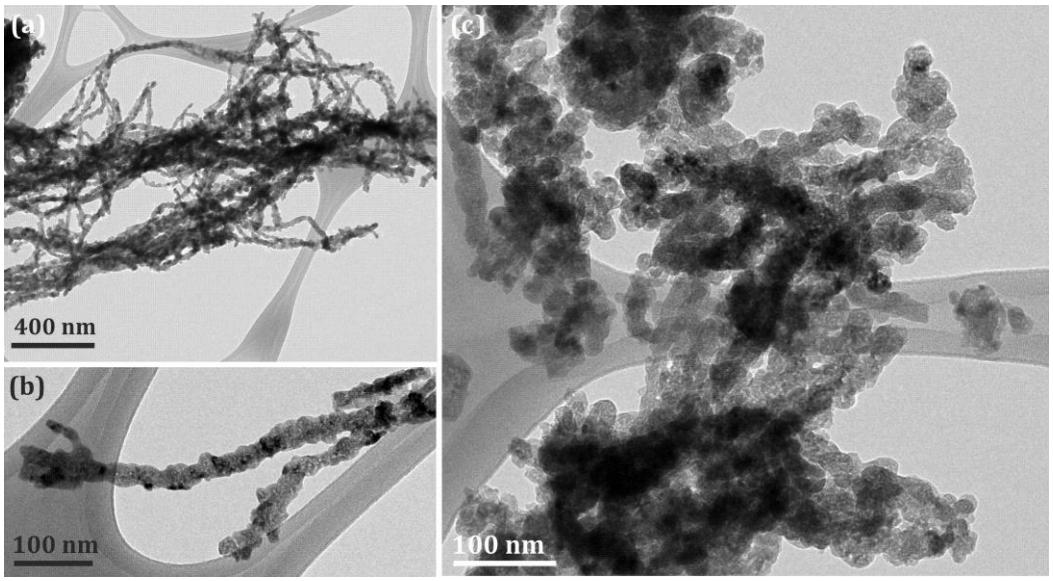


**Figure 5.12.** (a-b) TEM images of the $TiO_2$ structures obtained after annealing the TiONPs-MWCNTs at 370 ˚C, during 6 h under flowing $O_2$ (165 $mL.min^{-1}$) and (c) anatase $TiO_2$ particles resulting from the oxidizing process at 350 ˚C during 12 h.

noparticles suffered a partial sintering (**Figure 5.12 (b)**), as result of the prolonged time employed for the treatment. The 350 ˚C oxidized sample during 6 h only contained $TiO_2$ in its anatase phase but a small fraction of CNTs is still present after the oxidation of the nanoparticles. Finally, despite that a more prolonged time of treatment at 350 ˚C results in the total elimination of the carbonaceous fraction, the necklace-like structure has collapsed and the obtained material presented agglomerates of large-sized nanoparticles. Since a material with a high surface is required for an efficient catalytic performance, this sample was not considered for the photocatalytic tests.

## 5.5. Applications in UV-catalysis. Degradation of methyl orange by titanium oxide nanostructures.

The potential application of the synthesized materials as catalysts for the degradation of organic pollutants was evaluated. The catalytic activity under ultraviolet (UV) light

irradiation was tested by measuring the oxidation of methyl orange (MO). The TiONPs-MWCNTs and the $TiO_2$ necklace-like structures, prepared after annealing the TiO-decorated MWCNTs at 370 ˚C during 6 h (under flowing $O_2$), were selected for this purpose. Thus 50 mg of the sample were suspended in 50 mL of a 25 ppm MO solution and the concentration of the organic compound with time of irradiation was measured. Prior to the analysis, the suspension was stirred overnight inside a hermetically closed dark box to reach an equilibrated concentration of the components. Afterwards, a 5 mL aliquot was extracted from the solution and centrifuged at 1600 rpm to precipitate the suspended material. The supernatant was collected and the obtained MO solution (free of catalyst) was the initial point of the measurement ($C_0$). A UV lamp with a wavelength of 365 nm was located at 25 cm from the initial suspension (inside the dark box) and the lamp was immediately switched on. After 15 min, a new aliquot was collected and the centrifugation process was repeated. The same protocol was followed periodically, until a total disappearance of the color of the solution was reached. The photocatalytic activity of the materials was determined by measuring the evolution of MO from the centrifuged solution. The absorbance of the solutions was recorded at a 464 nm wavelength, employing a UV-Vis spectrometer. This wavelength corresponds to the maximum absorbance peak of a 2.5 ppm MO solution in the 800-200 nm range (**Figure 5.13 (a)**). The concentration of MO in the collected aliquots was calculated according to the calibration curve presented in **Figure 5.13 (b)**.

The degradation of MO (% D) was evaluated following the equation

$$Degradation\ (\%\ D) = \frac{C_0 - C_t}{C_0}\ x\ 100$$

where $C_0$ is the concentration of MO before irradiation and $C_t$ is the concentration of the aliquots collected at different $t$ times. Since the P25 $TiO_2$ presents an important photocatalytic performance and it is usually employed as reference, the activity of the material was also evaluated as a benchmark following the protocol previously detailed.

**Figure 5.13 (c)** shows the catalytic degradation of MO assisted by UV irradiation, employing the selected materials. The $TiO_2$ necklace-like nanostructures presented the lower degradation performance among the analyzed samples (31.6 % D, t=240 min). Since the morphology of the material plays an important role in the photocatalytic performance, the sintering of the nanoparticles due to the prolonged annealing might be responsible for the low catalytic activity. As it can be seen, the TiONPs-MWCNTs (blue line) shows the highest photocatalytic performance, followed by the P25 $TiO_2$ reference (black line). Finally, the $TiO_2$ necklace-like nanostructures (green line) presented the lowest degradation power. A photodegradation rate of 99.5 % after irradiation during 240 min was observed when the dye was exposed to UV irradiation in the presence of the TiONPs-MWCNTs. This value represents a 44 % increase in the photocatalytic activity when compared with P25 at the same time (68.9 % D, t=240 min).

Different factors may contribute to the highest photocatalytic performance of the TiO-MWCNTs hybrids. The high degradation power of titanium oxides arises from the generation of an electron-hole pair when the material is exposed to radiation. UV light is strongly enough to overcome the energy barrier between the valence band and the conducting band of the material, which causes the transition of one valence electron to the higher energy level (conducting band). It then reacts with molecules adsorbed on the surface of the catalyst leading to the formation of highly reactive radical species, responsible of the degradation of the organic compound. The presence of holes also induces the formation of radicals. While the electrons in the conduction band cause the reduction of negative-charge acceptors, the holes provoke the oxidation of electron donors, creating at the same time highly reactive species. Thus, the larger the lifetime of the electron-hole pair, the highest the photocatalytic performance of the material. The morphology of the TiO nanoparticles is likely to confer the material a higher specific surface area than P25, favoring the contact with the organic compound. Some authors have proposed a synergistic effect between the titanium oxides and the MWCNTs resul-

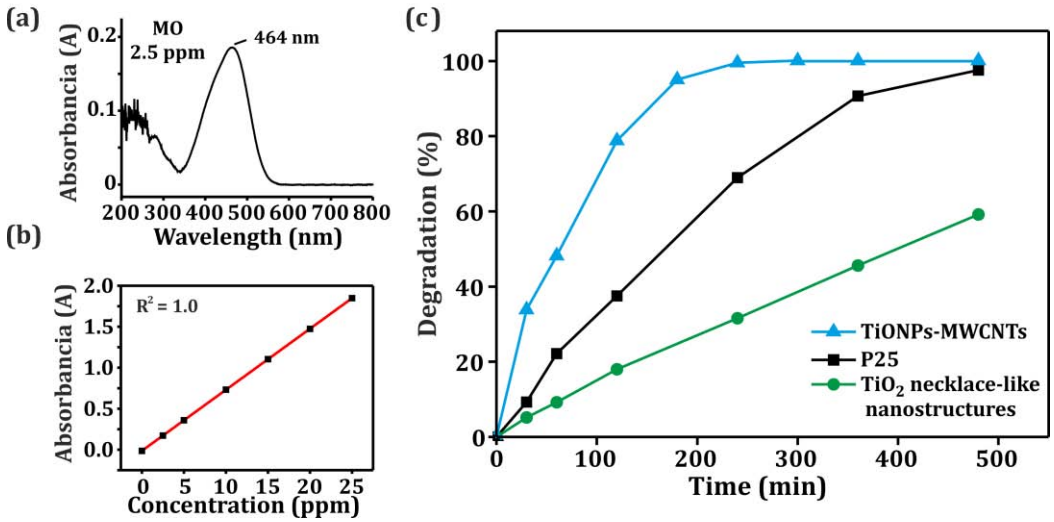


**Figure 5.13.** (a) Absorbance spectrum of a 2.5 ppm methyl orange (MO) solution, having a maximum at 464 nm, (b) calibration curve employed to calculate the MO concentration in the irradiated solutions. (c) Photodegradation rate calculated after UV irradiation of the MO solutions in the presence of TiONPs-MWCNTs prepared by annealing $TiCl_2$ and MWCNTs at 1060 ˚C (blue line), and $TiO_2$ necklace-like nanostructures prepared after oxidation of the TiONPs-MWCNTs at 370 ˚C, during 6h, under flowing $O_2$ (green line). The photocatalytic activity of the P25 $TiO_2$ (black line) is included for comparison.

ting on an enhancement of the photocatalytic activity.[302] In addition to conferring a larger specific surface area to the material, the high electrical conductivity exhibited by the CNTs favors the transfer of electrons from the titanium oxide to the CNTs surface. Thus, the CNTs act like electron transfer stations. The capture of electrons in the CNTs lowers the recombination between the photogenerated species and the holes, since it provides a larger charge separation (Schottky barrier). On the other hand, the electrons present in the surface of the nanotubes can be easily transferred to the conduction band of the titanium oxide due to the strong interaction between the surface of the CNTs and the inorganic nanoparticles. This electron transfer not only creates reducing active sites in the surface of the catalyst, but also induces the migration of electrons from its valence band to the positively charged nanotubes, forming a new positive hole. [265] The higher density of active sites in the surface of the TiO-MWCNTs hybrids

accelerates the formation of radical species, improving the degradation rate of the organic pollutant.

The intrinsic defects in the oxygen deficient structure of the TiO nanoparticles as well as the presence of titanium atoms with low oxidation states have also been reported to play a positive role in the decrease of the charge carrier recombination and the narrowing of the optical band gap of the semiconducting material.[303, 304] The carbon atoms forming the CNTs walls also act as dopant species of the titanium oxide nanoparticles. The formation of C-Ti or C-O bonds (observed by XPS (**Figure 5.7 (c)**), is produced by the substitution of an O atom from the TiO and contributes to an increase in the concentration of lattice defects.[257, 268]

## 5.6. Conclusions.

- MWCNTs were employed as templates and directing agents for the preparation of TiO-decorated MWCNTs, leading to necklace-like nanostructures.
- The phase transformations occurring during the exposure of the TiO-MWCNTs hybrids to an oxidizing atmosphere were analyzed. The TiO nanoparticles decorating the MWCNTs oxidize to $TiO_2$ at temperatures between 200 ˚C and 400 ˚C. Afterwards the combustion of the MWCNTs is observed, and overlaps with the oxidation of the TiO nanoparticles.
- Self-standing $TiO_2$-based nanostructures, free of MWCNTs, have been prepared by oxidation of the TiO-decorated MWCNTs. An early phase transition from anatase to rutile $TiO_2$ has been observed in these structures, due to the morphology of the inorganic nanoparticles and the presence of structural defects.

- The potential use of the synthesized nanostructures in the photocatalytic degradation of methyl orange was tested. A 44 % increase in the photocatalytic activity was observed for the TiONPs-MWCNTs in comparison with the P25 reference.

- The presence of structural defects in the TiO lattice, the synergistic effect between the titanium oxide nanoparticles and the CNTs and the dopant character of the carbon atoms might contribute to the enhanced photocatalytic performance of the TiO-MWCNTs hybrids.

# Chapter 6.

# General Conclusions

The general conclusions of this thesis are summarizes in this chapter.

# I. SYNTHESIS, CHARACTERIZATION AND THERMAL PROPERTIES OF N-CONTAINING REDUCED GRAPHENE OXIDE.

## Tuning the nature of nitrogen atoms in N-containing reduced graphene oxide.

- We have developed a simple, efficient and reproducible method for the synthesis of nitrogen-containing reduced graphene oxide by gas phase treatment of GO with pure ammonia. Low temperature treatments result in the formation of amine and amide groups (N-functionalization), while annealing at temperatures above 500 °C produce the incorporation of structural nitrogen into the RGO lattice (N-doping). During the treatment ammonia also plays a reducing role. Samples with ca. 2 at. % in oxygen content have been prepared at 600 ˚C. This level of reduction is comparable to that obtained when higher temperatures (110 ˚C) and reducing conditions ($Ar/H_2$) are employed.

- We have proposed an experimental toolbox for the unambiguous identification of the nitrogen species present in the RGO lattice, which includes not only XPS (commonly used), but also elemental analyses, microscopic techniques, infrared and UV-vis spectroscopies, contact angle measurements and thermogravimetric analyses.

- The presence of structural nitrogen enhances the thermal stability of the samples. Graphitic nitrogen is the most stable specie among the structural N-containing moieties, namely pyrrolic, pyridinic and graphitic N. The thermal stability of the samples can be increased by annealing the N-containing RGO samples under argon in the range of 500 ˚C-1050 ˚C. The post-synthesis treatments induce internal rearrangements leading to the

elimination of the aliphatic moieties or to the formation of structural groups, mainly N-containing six-membered rings which can interact with oxygen atoms to form pyridine N-oxide species.

## II. SYNTHESIS OF CARBON NANOTUBE-INORGANIC NANOSTRUCTURES.

### Synthesis of single-layered inorganic nanotubes within MWCNTs .

- We have employed MWCNTs as directing agents for the synthesis of $CeI_3$, $CeCl_3$ and $ZnI_2$ single-layered inorganic nanotubes. The presence of nanorods, nanoparticles and nanosnakes from the employed inorganic salts was also observed after treatments.

- The formation of the $ZnI_2$ inorganic nanostructures grown within the CNTs is governed by the temperature. An increase in the temperature of synthesis results in the preferential growth of $ZnI_2$ single-layered inorganic nanotubes. Treatments at lower temperatures lead to a higher degree of other nanostructures (nanorods, nanoparticles and nanosnakes). Furthermore, the degree of crystallinity of the host decreases when decreasing the temperature of treatment.

### Encapsulation of fullerenes within MWCNTs.

- We have studied the use of fullerenes as versatile agents, either to isolate inorganic materials present in the cavities of MWCNTs, or to promote the release of the guest structures.

- Fullerenes act as corking agents as long as the cleaning of the filled nanotubes is carried out with solvents whose affinity with the $C_{60}$ molecules is very low.

- Fullerenes are useful to trigger the liberation of guest structures from the MWCNTs cavities when solvents with high affinity to the $C_{60}$ molecules are employed to promote the release. Decoration of multiwalled carbon nanotubes with titanium oxides.

## Decoration of multiwalled carbon nanotubes with titanium oxides.

- We have employed MWCNTs as directing templates for the synthesis of MWCNTs decorated with TiO nanoparticles. A post-synthesis treatment of the samples under oxygen induces the formation of self-standing $TiO_2$ like nanostructures, free of MWCNTs.

- An early phase transformation from anatase to rutile $TiO_2$ at 370 ˚ C has been observed. It is favored by the presence of oxygen vacancies and dopant carbon atoms in the TiONPs-MWCNTs. These structural defects and a synergistic effect of both constituent materials might account for the enhanced photocatalytic performance achieved when this material was employed for the degradation of methyl orange, in comparison with the P25 reference.

# Bibliography.


[1] Acheson E, inventor Manufacture of graphite patent US568323 1896 29-09-1896.

[2] Bundy FP, Hall HT, Strong HM, Wentorf RH. Man-Made Diamonds. *Nature*. 1955, **176**, 51.

[3] Kroto HW, Heath JR, O'Brien SC, Curl RF, Smalley RE. $C_{60}$: buckminsterfullerene. *Nature*. 1985, **318**, 162.

[4] Iijima S. Helical microtubules of graphitic carbon. *Nature*. 1991, **354**, 56.

[5] Novoselov KS, Geim AK, Morozov SV, Jiang D, Zhang Y, Dubonos SV, et al. Electric Field Effect in Atomically Thin Carbon Films. *Science*. 2004, **306**, 666.

[6] Harris PJF. Carbon nanotube science synthesis, properties and applications. Cambridge [u.a.]: Cambridge Univ. Press; 2009.

[7] Pati SK, Enoki T, Rao CNR, Editors. Graphene and Its Fascinating Attributes: World Scientific Publishing Co. Pte. Ltd.; 2011.

[8] Rao CN, Sood AK, Subrahmanyam KS, Govindaraj A. Graphene: the new two-dimensional nanomaterial. *Angew. Chem. Int. Edit*. 2009, **48**, 7752.

[9] Wallace PR. The Band Theory of Graphite. *Phys. Rev*. 1947, **71**, 622.

[10] Castro Neto AH, Guinea F, Peres NMR, Novoselov KS, Geim AK. The electronic properties of graphene. *Rev. Mod. Phys*. 2009, **81**, 109.

[11] Berger C, Song Z, Li X, Wu X, Brown N, Naud C, et al. Electronic confinement and coherence in patterned epitaxial graphene. *Science*. 2006, **312**, 1191.

[12] Lu G, Yu K, Wen Z, Chen J. Semiconducting graphene: converting graphene from semimetal to semiconductor. *Nanoscale*. 2013, **5**, 1353.

[13] Wang H, Maiyalagan T, Wang X. Review on Recent Progress in Nitrogen-Doped Graphene: Synthesis, Characterization, and Its Potential Applications. *ACS Catal*. 2012, **2**, 781.

[14] Guo S, Dong S. Graphene nanosheet: synthesis, molecular engineering, thin film, hybrids, and energy and analytical applications. *Chem. Soc. Rev*. 2011, **40**, 2644.

[15] Choi W, Lahiri I, Seelaboyina R, Kang YS. Synthesis of Graphene and Its Applications: A Review. *Crit. Rev. Solid State Mater. Sci*. 2010, **35**, 52.

[16] Hernandez Y, Nicolosi V, Lotya M, Blighe FM, Sun Z, De S, et al. High-yield production of graphene by liquid-phase exfoliation of graphite. *Nat. Nanotechnol*. 2008, **3**, 563.

[17] Lotya M, Hernandez Y, King PJ, Smith RJ, Nicolosi V, Karlsson LS, et al. Liquid Phase Production of Graphene by Exfoliation of Graphite in Surfactant/Water Solutions. *J. Am. Chem. Soc*. 2009, **131**, 3611.

[18] Du W, Jiang X, Zhu L. From graphite to graphene: direct liquid-phase exfoliation of graphite to produce single- and few-layered pristine graphene. *J. Mater. Chem. A*. 2013, 1, 10592.

[19] Abdelkader AM, Cooper AJ, Dryfe RAW, Kinloch IA. How to get between the sheets: a review of recent works on the electrochemical exfoliation of graphene materials from bulk graphite. *Nanoscale*. 2015, **7**, 6944.

[20] Gao H, Hu G. Graphene production via supercritical fluids. *RSC Adv*. 2016, **6**, 10132.

[21] Cai M, Thorpe D, Adamson DH, Schniepp HC. Methods of graphite exfoliation. *J. Mater. Chem.* 2012, **22**, 24992.

[22] Muñoz R, Gómez-Aleixandre C. Review of CVD Synthesis of Graphene. *Chem. Vap. Deposition*. 2013, **19**, 297.

[23] Srivastava A, Galande C, Ci L, Song L, Rai C, Jariwala D, et al. Novel Liquid Precursor-Based Facile Synthesis of Large-Area Continuous, Single, and Few-Layer Graphene Films. *Chem. Mater*. 2010, **22**, 3457.

[24] Rodriguez-Perez L, Herranz MaA, Martin N. The chemistry of pristine graphene. *Chem. Commun*. 2013, **49**, 3721.

[25] Wang X, Shi G. An introduction to the chemistry of graphene. *Phys. Chem. Chem. Phys*. 2015, **17**, 28484.

[26] Georgakilas V, Otyepka M, Bourlinos AB, Chandra V, Kim N, Kemp KC, et al. Functionalization of Graphene: Covalent and Non-Covalent Approaches, Derivatives and Applications. *Chem. Rev*. 2012, **112**, 6156.

[27] Park J, Yan M. Covalent Functionalization of Graphene with Reactive Intermediates. *Acc. Chem. Res*. 2013, **46**, 181.

[28] Chua CK, Pumera M. Covalent chemistry on graphene. *Chem. Soc. Rev*. 2013, **42**, 3222.

[29] Marcano DC, Kosynkin DV, Berlin JM, Sinitskii A, Sun Z, Slesarev A, et al. Improved Synthesis of Graphene Oxide. *ACS Nano*. 2010, **4**, 4806.

[30] Kim J. Graphene oxide sheets at interfaces. *J. Am. Chem. Soc*. 2010, **132**, 8180.

[31] Ruoff R. Graphene: Calling all chemists. *Nat. Nanotech*. 2008, **3**, 10.

[32] Li D, Muller MB, Gilje S, Kaner RB, Wallace GG. Processable aqueous dispersions of graphene nanosheets. *Nature Nanotechnol*. 2008, **3**, 101.

[33] Dreyer DR, Park S, Bielawski CW, Ruoff RS. The chemistry of graphene oxide. *Chem. Soc. Rev*. 2010, **39**, 228.

[34] Lerf A, He H, Forster M, Klinowski J. Structure of Graphite Oxide Revisited. *J. Phys. Chem. B*. 1998, **102**, 4477.

[35] Szabó T, Berkesi O, Forgó P, Josepovits K, Sanakis Y, Petridis D, et al. Evolution of Surface Functional Groups in a Series of Progressively Oxidized Graphite Oxides. *Chem. Mater*. 2006, **18**, 2740.

[36] Stankovich S, Dikin DA, Piner RD, Kohlhaas KA, Kleinhammes A, Jia Y, et al. Synthesis of graphene-based nanosheets via chemical reduction of exfoliated graphite oxide. *Carbon*. 2007, **45**, 1558.

[37] Eda G, Fanchini G, Chhowalla M. Large-area ultrathin films of reduced graphene oxide as a transparent and flexible electronic material. *Nature Nanotechnol*. 2008, **3**, 270.

[38] Jiang D-e, Chen Z. Graphene Chemistry : Theoretical Perspectives. Somerset, NJ, USA: John Wiley & Sons; 2013.

[39] Stankovich S, Dikin DA, Dommett GHB, Kohlhaas KM, Zimney EJ, Stach EA, et al. Graphene-based composite materials. *Nature*. 2006, **442**, 282.

[40] Kuila T, Mishra AK, Khanra P, Kim NH, Lee JH. Recent advances in the efficient reduction of graphene oxide and its application as energy storage electrode materials. *Nanoscale*. 2013, **5**, 52.

[41] Gao X, Jang J, Nagase S. Hydrazine and Thermal Reduction of Graphene Oxide: Reaction Mechanisms, Product Structures, and Reaction Design. *J. Phys. Chem. C.* 2010, **114**, 832.

[42] Becerril HA, Mao J, Liu Z, Stoltenberg RM, Bao Z, Chen Y. Evaluation of Solution-Processed Reduced Graphene Oxide Films as Transparent Conductors. *ACS Nano*. 2008, **2**, 463.

[43] Zhang J, Yang H, Shen G, Cheng P, Zhang J, Guo S. Reduction of graphene oxide vial-ascorbic acid. Chemical Communications. 2010;46(7):1112-4.

[44] Wakeland S, Martinez R, Grey JK, Luhrs CC. Production of graphene from graphite oxide using urea as expansion–reduction agent. *Carbon*. 2010, **48**, 3463.

[45] Fernández-Merino MJ, Guardia L, Paredes JI, Villar-Rodil S, Solís-Fernández P, Martínez-Alonso A, et al. Vitamin C Is an Ideal Substitute for Hydrazine in the Reduction of Graphene Oxide Suspensions. *J. Phys. Chem. C*. 2010, **114**, 6426.

[46] Wang Y, Liu J, Liu L, Sun D. High-quality reduced graphene oxide-nanocrystalline platinum hybrid materials prepared by simultaneous co-reduction of graphene oxide and chloroplatinic acid. *Nanoscale Res. Lett*. 2011, **6**, 241.

[47] McAllister MJ, Li J-L, Adamson DH, Schniepp HC, Abdala AA, Liu J, et al. Single Sheet Functionalized Graphene by Oxidation and Thermal Expansion of Graphite. *Chem. Mater*. 2007, **19**, 4396.

[48] Tavakoli F, Salavati-niasari M, Mohandes F. Graphite Nanosheets: Thermal Treatment Synthesis and Characterization. Synthesis and Reactivity in Inorganic, Metal-Organic, and Nano-Metal Chemistry. 2016, **46**, 877.

[49] Schniepp HC, Li J-L, McAllister MJ, Sai H, Herrera-Alonso M, Adamson DH, et al. Functionalized Single Graphene Sheets Derived from Splitting Graphite Oxide. *J. Phys. Chem. B*. 2006, **110**, 8535.

[50] Shao Y, Wang J, Engelhard M, Wang C, Lin Y. Facile and controllable electrochemical reduction of graphene oxide and its applications. *J. Mater. Chem*. 2010, **20**, 743.

[51] Williams G, Seger B, Kamat PV. $TiO_2$-Graphene Nanocomposites. UV-Assisted Photocatalytic Reduction of Graphene Oxide. *ACS Nano*. 2008, **2**, 1487.

[52] Ng YH, Iwase A, Kudo A, Amal R. Reducing Graphene Oxide on a Visible-Light $BiVO_4$ Photocatalyst for an Enhanced Photoelectrochemical Water Splitting. *J. Phys. Chem. Lett*. 2010, **1**, 2607.

[53] Chen W, Yan L, Bangal PR. Preparation of graphene by the rapid and mild thermal reduction of graphene oxide induced by microwaves. *Carbon*. 2010, **48**, 1146.

[54] Wei D, Liu Y. Controllable Synthesis of Graphene and Its Applications. *Adv. Mater*. 2010, **22**, 3225.

[55] Liu H, Liu Y, Zhu D. Chemical doping of graphene. *J. Mater. Chem*. 2011, **21**, 3335.

[56] Pantelides ST, Puzyrev Y, Tsetseris L, Wang B. Defects and doping and their role in functionalizing graphene. *MRS Bull*. 2012, **37**, 1187.

[57] Nessim GD. Properties, synthesis, and growth mechanisms of carbon nanotubes with special focus on thermal chemical vapor deposition. *Nanoscale*. 2010, **2**, 1306.

[58] Rao CNR, Govindaraj A. Nanotubes and Nanowires. Second edition ed: RSC Publishing; 2011.

[59] Kong J, Yenilmez E, Tombler TW, Kim W, Dai H, Laughlin RB, et al. Quantum Interference and Ballistic Transmission in Nanotube Electron Waveguides. *Phys. Rev. Lett*. 2001, **87**, 106801.

[60] McEuen PL, Bockrath M, Cobden DH, Yoon Y-G, Louie SG. Disorder, Pseudospins, and Backscattering in Carbon Nanotubes. Phys. Rev. Lett. 1999, **83**, 5098.

[61] Berber S, Kwon Y-K, Tománek D. Unusually High Thermal Conductivity of Carbon Nanotubes. *Phys. Rev. Lett*. 2000, **84**, 4613.

[62] Ruoff RS, Lorents DC. Mechanical and thermal properties of carbon nanotubes. *Carbon*. 1995, **33**, 925.

[63] Kim P, Shi L, Majumdar A, McEuen PL. Thermal Transport Measurements of Individual Multiwalled Nanotubes. *Phys. Rev. Lett*. 2001, **87**, 215502.

[64] Wong EW, Sheehan PE, Lieber CM. Nanobeam Mechanics: Elasticity, Strength, and Toughness of Nanorods and Nanotubes. *Science*. 1997, **277**, 1971.

[65] Demczyk BG, Wang YM, Cumings J, Hetman M, Han W, Zettl A, et al. Direct mechanical measurement of the tensile strength and elastic modulus of multiwalled carbon nanotubes. *Mater. Sci. Eng.: A*. 2002, **334**, 173.

[66] O'Connell MJ, Bachilo SM, Huffman CB, Moore VC, Strano MS, Haroz EH, et al. Band Gap Fluorescence from Individual Single-Walled Carbon Nanotubes. *Science*. 2002, **297**, 593.

[67] Chrzanowska J, Hoffman J, Małolepszy A, Mazurkiewicz M, Kowalewski TA, Szymanski Z, et al. Synthesis of carbon nanotubes by the laser ablation method: Effect of laser wavelength. *Phys. Status Solidi B*. 2015, **252**, 1860.

[68] Rafique MMA, Iqbal J. Production of Carbon Nanotubes by Different Routes-A Review. *JEAS*. 2011, **1**, 29.

[69] Shah KA, Tali BA. Synthesis of carbon nanotubes by catalytic chemical vapour deposition: A review on carbon sources, catalysts and substrates. *Mater. Sci. Semicond. Process*. 2016, **41**, 67.

[70] Remy E, Cahen S, Malaman B, Ghanbaja J, Bellouard C, Medjahdi G, et al. Quantitative investigation of mineral impurities of HiPco SWCNT samples: Chemical mechanisms for purification and annealing treatments. *Carbon*. 2015, **93**, 933.

[71] Arora N, Sharma NN. Arc discharge synthesis of carbon nanotubes: Comprehensive review. *Diamond Relat. Mater*. 2014, **50**, 135.

[72] Hou P-X, Liu C, Cheng H-M. Purification of carbon nanotubes. *Carbon*. 2008, **46**, 2003.

[73] Dillon AC, Parilla PA, Alleman JL, Perkins JD, Heben MJ. Controlling single-wall nanotube diameters with variation in laser pulse power. *Chem. Phys. Lett*. 2000, **316**, 13.

[74] Meyyappan M, Lance D, Alan C, David H. Carbon nanotube growth by PECVD: a review. *Plasma Sources Sci. Technol*. 2003, **12**, 205.

[75] Bronikowski MJ, Willis PA, Colbert DT, Smith KA, Smalley RE. Gas-phase production of carbon single-walled nanotubes from carbon monoxide via the HiPco process: A parametric study. *J. Vac. Sci. Technol. A*. 2001, **19**, 1800.

[76] Park YS, Choi YC, Kim KS, Chung D-C, Bae DJ, An KH, et al. High yield purification of multiwalled carbon nanotubes by selective oxidation during thermal annealing. *Carbon*. 2001, **39**, 655.

[77] Zimmerman JL, Bradley RK, Huffman CB, Hauge RH, Margrave JL. Gas-Phase Purification of Single-Wall Carbon Nanotubes. *Chem. Mater*. 2000,**12**, 1361.

[78] Tobias G, Shao L, Salzmann CG, Huh Y, Green MLH. Purification and Opening of Carbon Nanotubes Using Steam. *J. Phys. Chem. B*. 2006, **110**, 22318.

[79] Jeong T, Kim W-Y, Hahn Y-B. A new purification method of single-wall carbon nanotubes using H2S and O2 mixture gas. *Chem. Phys. Lett*. 2001, **344**, 8.

[80] Xu Y-Q, Peng H, Hauge RH, Smalley RE. Controlled Multistep Purification of Single-Walled Carbon Nanotubes. *Nano Lett*. 2005, **5**, 163.

[81] Chiang IW, Brinson BE, Huang AY, Willis PA, Bronikowski MJ, Margrave JL, et al. Purification and Characterization of Single-Wall Carbon Nanotubes (SWNTs) Obtained from the Gas-Phase Decomposition of CO (HiPco Process). *J. Phys. Chem. B*. 2001, **105**, 8297.

[82] Cabana L, Ke X, Kepic D, Oro-Sole J, Tob as-Rossell E, Van Tendeloo G, et al. The role of steam treatment on the structure, purity and length distribution of multi-walled carbon nanotubes. *Carbon*. 2015, **93**, 1059.

[83] Heister E, Brunner EW, Dieckmann GR, Jurewicz I, Dalton AB. Are Carbon Nanotubes a Natural Solution? Applications in Biology and Medicine. *ACS Appl. Mater. & Interfaces*. 2013, **5**, 1870.

[84] Martincic M, Tobias G. Filled carbon nanotubes in biomedical imaging and drug delivery. *Expert Opin. Drug Deliver*. 2015, **12**, 563.

[85] Zhao X, Ohkohchi M, Inoue S, Suzuki T, Kadoya T, Ando Y. Large-scale purification of single-wall carbon nanotubes prepared by electric arc discharge. *Diamond Relat. Mater*. 2006, **15**, 1098.

[86] Wang, Shan H, Hauge RH, Pasquali M, Smalley RE. A Highly Selective, One-Pot Purification Method for Single-Walled Carbon Nanotubes. *J. Phys. Chem. B*. 2007, **111**, 1249.

[87] Chen C-M, Chen M, Leu F-C, Hsu S-Y, Wang S-C, Shi S-C, et al. Purification of multi-walled carbon nanotubes by microwave digestion method. *Diamond and Relat. Mater*. 2004, **13**, 1182.

[88] Yu L, Xiaobin Z, Junhang L, Wanzhen H, Jipeng C, Zhiqiang L, et al. Purification of CVD synthesized single-wall carbon nanotubes by different acid oxidation treatments. *Nanotechnol*. 2004, **15**, 1645.

[89] Zhang J, Zou H, Qing Q, Yang Y, Li Q, Liu Z, et al. Effect of Chemical Oxidation on the Structure of Single-Walled Carbon Nanotubes. *J. Phys. Chem. B*. 2003, **107**, 3712.

[90] Shelimov KB, Esenaliev RO, Rinzler AG, Huffman CB, Smalley RE. Purification of single-wall carbon nanotubes by ultrasonically assisted filtration. *Chem. Phys. Lett*. 1998, **282**, 429.

[91] Bandow S, Rao AM, Williams KA, Thess A, Smalley RE, Eklund PC. Purification of Single-Wall Carbon Nanotubes by Microfiltration. *J. Phys. Chem. B*. 1997, **101**, 8839.

[92] Andrews R, Jacques D, Qian D, Dickey EC. Purification and structural annealing of multiwalled carbon nanotubes at graphitization temperatures. *Carbon*. 2001, **39**, 1681.

[93] Huang W, Wang Y, Luo G, Wei F. 99.9% purity multi-walled carbon nanotubes by vacuum high-temperature annealing. *Carbon*. 2003, **41**, 2585.

[94] Kim YA, Hayashi T, Osawa K, Dresselhaus MS, Endo M. Annealing effect on disordered multi-wall carbon nanotubes. *Chem. Phys. Lett*. 2003, **380**, 319.

[95] Di Crescenzo A, Ettorre V, Fontana A. Non-covalent and reversible functionalization of carbon nanotubes. *Beilstein J. Nanotechnol*. 2014, **5**, 1675.

[96] Vaisman L, Wagner HD, Marom G. The role of surfactants in dispersion of carbon nanotubes. *Adv. Colloid Interface Sci*. 2006, **128**, 37.

[97] Rastogi R, Kaushal R, Tripathi SK, Sharma AL, Kaur I, Bharadwaj LM. Comparative study of carbon nanotube dispersion using surfactants. *J. Colloid Interface Sci*. 2008, **328**, 421.

[98] Wang H. Dispersing carbon nanotubes using surfactants. *Curr. Opin. Colloid. Interface Sci*. 2009, 14, 364.

[99] Chen L, Xie H, Yu aW. Functionalization Methods of Carbon Nanotubes and Its Applications. In: (Ed.) PJMM, ed. Carbon Nanotubes Applications on Electron Devices, 211.

[100] Wu H-C, Chang X, Liu L, Zhao F, Zhao Y. Chemistry of carbon nanotubes in biomedical applications. *J. Mater. Chem*. 2010, **20**, 1036.

[101] Kawasaki S, Komatsu K, Okino F, Touhara H, Kataura H. Fluorination of open- and closed-end single-walled carbon nanotubes. *Phys. Chem. Chem. Phys*. 2004, 6, 1769.

[102] Touhara H, Okino F. Property control of carbon materials by fluorination. *Carbon*. 2000, **38**, 241.

[103] Kamaras K, Itkis ME, Hu H, Zhao B, Haddon RC. Covalent Bond Formation to a Carbon Nanotube Metal. *Science*. 2003, **301**, 1501.

[104] Hu H, Zhao B, Hamon MA, Kamaras K, Itkis ME, Haddon RC. Sidewall Functionalization of Single-Walled Carbon Nanotubes by Addition of Dichlorocarbene. *J. Am. Chem. Soc*. 2003, **125**, 4893.

[105] Strano MS, Dyke CA, Usrey ML, Barone PW, Allen MJ, Shan H, et al. Electronic Structure Control of Single-Walled Carbon Nanotube Functionalization. *Science*. 2003, **301**, 1519.

[106] Hirsch A, Vostrowsky O. Functional Organic Materials. Syntheses, Strategies, and Applications.: WILEY-VCH Verlag GmbH & Co; 2007.

[107] Tobias G, Mendoza E, Ballesteros B. Encyclopedia of Nanotechnology. In: Bhushan PB, ed. Encyclopedia of Nanotechnology. Netherlands: Springer Netherlands 2012, p. 911-9.

[108] Seal S, Bera D, Kuiry SC, Meyyappan M, McCutchen ML. In-situ synthesis of carbon nanotubes filled with metallic nanoparticles using arc discharge in solution. Google Patents 2011.

[109] Marega R, Bonifazi D. Filling carbon nanotubes for nanobiotechnological applications. *New J. Chem*. 2014, **38**, 22.

[110] Liu C, Chen Y, Wu C-Z, Xu S-T, Cheng H-M. Hydrogen storage in carbon nanotubes revisited. *Carbon*. 2010, **48**, 452.

[111] Rashidi AM, Nouralishahi A, Khodadadi AA, Mortazavi Y, Karimi A, Kashefi K. Modification of single wall carbon nanotubes (SWNT) for hydrogen storage. *Int. J. Hydrogen Energy* 2010, **35**, 9489.

[112] Che G, Lakshmi BB, Martin CR, Fisher ER. Metal-Nanocluster-Filled Carbon Nanotubes: Catalytic Properties and Possible Applications in Electrochemical Energy Storage and Production. *Langmuir*. 1999, **15**, 750.

[113] Prem Kumar T, Ramesh R, Lin YY, Fey GT-K. Tin-filled carbon nanotubes as insertion anode materials for lithium-ion batteries. *Electrochem. Commun*. 2004, **6**, 520.

[114] Pan X, Bao X. Reactions over catalysts confined in carbon nanotubes. *Chem. Commun*. 2008, **47**, 6271.

[115] del Carmen Giménez-López M, Moro F, La Torre A, Gómez-García CJ, Brown PD, van Slageren J, et al. Encapsulation of single-molecule magnets in carbon nanotubes. *Nat. Commun*. 2011, **2**, 407.

[116] Ujjal KG, Pedro MFJC, Yoshio B, Xiaosheng F, Liang L, Masataka I, et al. Recent developments in inorganically filled carbon nanotubes: successes and challenges. Sci. Technol. *Adv. Mater.* 2010, **11**, 054501.

[117] Ajayan PM, lijima S. Capillarity-induced filling of carbon nanotubes. *Nature*. 1993, **361**, 333.

[118] Kharlamova MV, Yashina LV, Eliseev AA, Volykhov AA, Neudachina VS, Brzhezinskaya MM, et al. Single-walled carbon nanotubes filled with nickel halogenides: Atomic structure and doping effect. *Phys. Status Solidi B*. 2012, **249**, 2328.

[119] Sauer M, Shiozawa H, Ayala P, Ruiz-Soria G, Kataura H, Yanagi K, et al. In situ filling of metallic single-walled carbon nanotubes with ferrocene molecules. *Phys. Status Solidi B*. 2012, **249**, 2408.

[120] Zhang H, Pan X, Bao X. Facile filling of metal particles in small carbon nanotubes for catalysis. *J. Energy Chem*. 2013, **22**, 251.

[121] Bera D, Kuiry SC, McCutchen M, Seal S, Heinrich H, Slane GC. In situ synthesis of carbon nanotubes decorated with palladium nanoparticles using arc-discharge in solution method. *J. Appl. Phys*. 2004, **96**, 5152.

[122] Gately RD, in het Panhuis M. Filling of carbon nanotubes and nanofibres. *Beilstein J. Nanotechnol*. 2015, 6, 508.

[123] Kitaura R, Nakanishi R, Saito T, Yoshikawa H, Awaga K, Shinohara H. High-Yield Synthesis of Ultrathin Metal Nanowires in Carbon Nanotubes. *Angew. Chem. Inter. Ed*. 2009, **48**, 8298.

[124] Meyer RR, Sloan J, Dunin-Borkowski RE, Kirkland AI, Novotny MC, Bailey SR, et al. Discrete Atom Imaging of One-Dimensional Crystals Formed Within Single-Walled Carbon Nanotubes. *Science*. 2000, **289**, 1324.

[125] Philp E, Sloan J, Kirkland AI, Meyer RR, Friedrichs S, Hutchison JL, et al. An encapsulated helical one-dimensional cobalt iodide nanostructure. *Nat. Mater*. 2003, **2**, 788.

[126] Sloan J, Kirkland AI, Hutchison JL, Green MLH. Integral atomic layer architectures of 1D crystals inserted into single walled carbon nanotubes. *Chem. Commun*. 2002, **13**, 1319.

[127] Zhang J, Guo S, Wei J, Xu Q, Yan W, Fu J, et al. High-Efficiency Encapsulation of Pt Nanoparticles into the Channel of Carbon Nanotubes as an Enhanced Electrocatalyst for Methanol Oxidation. *Chem. Eur. J*. 2013, **19**, 16087.

[128] Wang Z, Li H, Liu Z, Shi Z, Lu J, Suenaga K, et al. Mixed Low-Dimensional Nanomaterial: 2D Ultranarrow $MoS_2$ Inorganic Nanoribbons Encapsulated in Quasi-1D Carbon Nanotubes. *J. Am. Chem. Soc*. 2010, **132**, 13840.

[129] Cabana L, Ballesteros B, Batista E, Magén C, Arenal R, Oró-Solé J, et al. Carbon Nanotubes: Synthesis of $PbI_2$ Single-Layered Inorganic Nanotubes Encapsulated Within Carbon Nanotubes (Adv. Mater. 13/2014). *Adv. Mater*. 2014, **26**, 2108.

[130] Li L-J, Khlobystov AN, Wiltshire JG, Briggs GAD, Nicholas RJ. Diameter-selective encapsulation of metallocenes in single-walled carbon nanotubes. *Nat. Mater.* 2005, **4**, 481.

[131] Yanagi K, Miyata Y, Kataura H. Highly Stabilized β-Carotene in Carbon Nanotubes. *Adv. Mater*. 2006, **18**, 437.

[132] Guo Z, Sadler PJ, Tsang SC. Immobilization and Visualization of DNA and Proteins on Carbon Nanotubes. *Adv. Mater*. 1998, **10**, 701.

[133] Chuvilin A, Bichoutskaia E, Gimenez-Lopez MC, Chamberlain TW, Rance GA, Kuganathan N, et al. Self-assembly of a sulphur-terminated graphene nanoribbon within a single-walled carbon nanotube. *Nat. Mater*. 2011, **10**, 687.

[134] Yudasaka M, Ajima K, Suenaga K, Ichihashi T, Hashimoto A, Iijima S. Nano-extraction and nano-condensation for $C_{60}$ incorporation into single-wall carbon nanotubes in liquid phases. *Chem. Phys. Lett*. 2003, **380**, 42.

[135] Burteaux B, Claye A, Smith BW, Monthioux M, Luzzi DE, Fischer JE. Abundance of encapsulated $C_{60}$ in single-wall carbon nanotubes. *Chem. Phys. Lett*. 1999, **310**, 21.

[136] Smith BW, Monthioux M, Luzzi DE. Encapsulated $C_{60}$ in carbon nanotubes. *Nature*. 1998, **396**, 323.

[137] Kalbac M, Kavan L, Juha L, Civis S, Zukalova M, Bittner M, et al. Transformation of fullerene peapods to double-walled carbon nanotubes induced by UV radiation. *Carbon*. 2005, **43**, 1610.

[138] Iijima S. Carbon nanotubes: past, present, and future. *Physica B*. 2002, **323**, 1.

[139] Raghu MPaGK. Chemically Modified Carbon Nanotubes: Derivatization and Their Applications. In: (Ed.) PJMM, ed. Carbon Nanotubes Applications on Electron Devices. 2011.

[140] Tannenbaum ITKaR. Magnetic Carbon Nanotubes: Synthesis, Characterization, and Anisotropic Electrical Properties. In: (Ed.) PJMM, ed. Electronic Properties of Carbon Nanotubes. 2011.

[141] Wan J, Cai W, Feng J, Meng X, Liu E. In situ decoration of carbon nanotubes with nearly monodisperse magnetite nanoparticles in liquid polyols. *J. Mater. Chem*. 2007, **17**, 1188.

[142] Ma PC, Tang BZ, Kim J-K. Effect of CNT decoration with silver nanoparticles on electrical conductivity of CNT-polymer composites. *Carbon*. 2008, **46**, 1497.

[143] Zhou H, Zhang C, Li H, Du Z. Decoration of $Fe_3O_4$ nanoparticles on the surface of poly(acrylic acid) functionalized multi-walled carbon nanotubes by covalent bonding. *J. Polym. Sci, Part A: Polym. Chem*. 2010, **48**, 4697.

[144] Deng Y, Deng C, Yang D, Wang C, Fu S, Zhang X. Preparation, characterization and application of magnetic silica nanoparticle functionalized multi-walled carbon nanotubes. *Chem. Commun*. 2005, **44**, 5548.

[145] Fuertes A. Metal oxynitrides as emerging materials with photocatalytic and electronic properties. *Mater. Horiz*. 2015, **2**, 453.

[146] Ballesteros B, Tobias G, Shao L, Pellicer E, Nogués J, Mendoza E, et al. Steam Purification for the Removal of Graphitic Shells Coating Catalytic Particles and the Shortening of Single-Walled Carbon Nanotubes. *Small*. 2008, **4**, 1501.

[147] Tobias G, Ballesteros B, Green MLH. Carbon nanocapsules: blocking materials inside carbon nanotubes. *Phys. status solidi C*. 2010, **7**, 2739.

[148] Hirahara K, Suenaga K, Bandow S, Kato H, Okazaki T, Shinohara H, et al. One-Dimensional Metallofullerene Crystal Generated Inside Single-Walled Carbon Nanotubes. *Phys. Rev. Lett*. 2000, **85**, 5384.

[149] Vashist SK, Luong JHT. Recent advances in electrochemical biosensing schemes using graphene and graphene-based nanocomposites. *Carbon*. 2015, **84**, 519.

[150] Geim AK. Graphene: status and prospects. *Science*. 2009, **324**, 1530.

[151] Tang Q, Zhou Z, Chen Z. Graphene-related nanomaterials: tuning properties by functionalization. *Nanoscale*. 2013, **5**, 4541.

[152] Park M, Lee T, Kim B-S. Covalent functionalization based heteroatom doped graphene nanosheet as a metal-free electrocatalyst for oxygen reduction reaction. *Nanoscale*. 2013, **5**, 12255.

[153] Lin Z, Waller GH, Liu Y, Liu M, Wong C-p. Simple preparation of nanoporous few-layer nitrogen-doped graphene for use as an efficient electrocatalyst for oxygen reduction and oxygen evolution reactions. *Carbon*. 2013, **53**, 130.

[154] Gopalakrishnan K, Govindaraj A, Rao CNR. Extraordinary supercapacitor performance of heavily nitrogenated graphene oxide obtained by microwave synthesis. *J. Mater. Chem. A*. 2013, **1**, 7563

[155] Li S-M, Yang S-Y, Wang Y-S, Lien C-H, Tien H-W, Hsiao S-T, et al. Controllable synthesis of nitrogen-doped graphene and its effect on the simultaneous electrochemical determination of ascorbic acid, dopamine, and uric acid. *Carbon*. 2013, **59**, 418.

[156] Liu Y, Feng Q, Tang N, Wan X, Liu F, Lv L, et al. Increased magnetization of reduced graphene oxide by nitrogen-doping. *Carbon*. 2013, **60**, 549.

[157] Purceno AD, Machado BF, Teixeira APC, Medeiros TV, Benyounes A, Beausoleil J, et al. Magnetic amphiphilic hybrid carbon nanotubes containing N-doped and undoped sections: powerful tensioactive nanostructures. *Nanoscale*. 2015, **7**, 294.

[158] Wei D, Liu Y, Wang Y, Zhang H, Huang L, Yu G. Synthesis of N-Doped Graphene by Chemical Vapor Deposition and Its Electrical Properties. *Nano Lett.* 2009, **9**, 1752.

[159] Panchakarla LS, Subrahmanyam KS, Saha SK, Govindaraj A, Krishnamurthy HR, Waghmare UV, et al. Synthesis, Structure, and Properties of Boron- and Nitrogen-Doped Graphene. *Adv. Mater*. 2009, **21**, 4726.

[160] Li X, Wang H, Robinson JT, Sanchez H, Diankov G, Dai H. Simultaneous Nitrogen Doping and Reduction of Graphene Oxide. *J. Am. Chem. Soc*. 2009, **131**, 15939.

[161] Wang Y, Shao Y, Matson DW, Li J, Lin Y. Nitrogen-Doped Graphene and Its Application in Electrochemical Biosensing. *ACS Nano*. 2010, **4**, 1790.

[162] Jiang B, Tian C, Wang L, Sun L, Chen C, Nong X, et al. Highly concentrated, stable nitrogen-doped graphene for supercapacitors: Simultaneous doping and reduction. *Appl. Surf. Sci*. 2012, **258**, 3438.

[163] Long D, Li W, Ling L, Miyawaki J, Mochida I, Yoon SH. Preparation of nitrogen-doped graphene sheets by a combined chemical and hydrothermal reduction of graphene oxide. *Langmuir*. 2010, **26**, 16096.

[164] Shi Z, Kutana A, Yakobson BI. How Much N-Doping Can Graphene Sustain? *J. Phys. Chem. Lett*. 2015, **6**, 106.

[165] Wang X, Hou Z, Ikeda T, Oshima M, Kakimoto M-a, Terakura K. Theoretical Characterization of X-ray Absorption, Emission, and Photoelectron Spectra of Nitrogen along Graphene Edges. *J. Phys. Chem. A*. 2012, **117**, 579.

[166] Xin Y, Liu J-g, Jie X, Liu W, Liu F, Yin Y, et al. Preparation and electrochemical characterization of nitrogen doped graphene by microwave as supporting materials for fuel cell catalysts. *Electrochim. Acta*. 2012, **60**, 354.

[167] Xiong B, Zhou Y, O'Hayre R, Shao Z. Facile single-step ammonia heat-treatment and quenching process for the synthesis of improved Pt/N-graphene catalysts. *Appl. Surf. Sci*. 2013, **266**, 433.

[168] Romanos GE, Likodimos V, Marques RRN, Steriotis TA, Papageorgiou SK, Faria JL, et al. Controlling and Quantifying Oxygen Functionalities on Hydrothermally and Thermally Treated Single-Wall Carbon Nanotubes. *J. Phys. Chem. C*. 2011, **115**, 8534.

[169] Meyer JC, Geim AK, Katsnelson MI, Novoselov KS, Obergfell D, Roth S, et al. On the roughness of single- and bi-layer graphene membranes. *Solid State Commun*. 2007, **143**, 101.

[170] Bianco A, Cheng H-M, Enoki T, Gogotsi Y, Hurt RH, Koratkar N, et al. All in the graphene family – A recommended nomenclature for two-dimensional carbon materials. *Carbon*. 2013, **65**, 1.

[171] White AH, Melville W. The Decomposition of Ammonia at High Temperatures. *J. Am. Chem. Soc*. 1905, **27**, 373.

[172] Sandoval S, Kumar N, Sundaresan A, Rao CNR, Fuertes A, Tobias G. Enhanced Thermal Oxidation Stability of Reduced Graphene Oxide by Nitrogen Doping. *Chem. Eur. J*. 2014, **20**, 11999.

[173] Hontoria-Lucas C, López-Peinado AJ, López-González JdD, Rojas-Cervantes ML, Martín-Aranda RM. Study of oxygen-containing groups in a series of graphite oxides: Physical and chemical characterization. *Carbon*. 1995, **33**, 1585.

[174] Shao L, Tobias G, Salzmann CG, Ballesteros B, Hong SY, Crossley A, et al. Removal of amorphous carbon for the efficient sidewall functionalisation of single-walled carbon nanotubes. *Chem. Commun*. 2007, **47**, 5090.

[175] Dyer J. Applications of Absortion Spectroscopy of Organic Compounds. New Jersey: Prentice Hall; 1965.

[176] Kim UJ, Furtado CA, Liu X, Chen G, Eklund PC. Raman and IR Spectroscopy of Chemically Processed Single-Walled Carbon Nanotubes. *J. Am. Chem. Soc*. 2005, **127**, 15437.

[177] Pérez del Pino Á, György E, Cabana L, Ballesteros B, Tobias G. Deposition of functionalized single wall carbon nanotubes through matrix assisted pulsed laser evaporation. *Carbon*. 2012, **50**, 4450.

[178] Eda G, Chhowalla M. Chemically Derived Graphene Oxide: Towards Large-Area Thin-Film Electronics and Optoelectronics. *Adv. Mater*. 2010, **22**, 2392.

[179] Zhou X, Shi T, Wu J, Zhou H. Facet-exposed anatase-phase $TiO_2$ nanotube hybrid reduced graphene oxide composite: Synthesis, characterization and application in photocatalytic degradation. *Appl. Surf. Sci*. 2013, **287**, 359.

[180] Hassan FM, Chabot V, Li J, Kim BK, Ricardez-Sandoval L, Yu A. Pyrrolic-structure enriched nitrogen doped graphene for highly efficient next generation supercapacitors. *J. Mater. Chem. A*. 2013, **1**, 2904.

[181] Roberts J. Basic Principles of Organic Chemistry. New York: W. A. Benjamin, Inc.; 1965.

[182] Jin J, Fu X, Liu Q, Liu Y, Wei Z, Niu K, et al. Identifying the Active Site in Nitrogen-Doped Graphene for the $VO^{2+}/VO^{2+}$ Redox Reaction. *ACS Nano*. 2013, **7**, 4764.

[183] Kumar NA, Nolan H, McEvoy N, Rezvani E, Doyle RL, Lyons MEG, et al. Plasma-assisted simultaneous reduction and nitrogen doping of graphene oxide nanosheets. *J. Mater. Chem. A*. 2013, **1**, 4431.

[184] Gabriel G, Sauthier G, Fraxedas J, Moreno-Mañas M, Martínez MT, Miravitlles C, et al. Preparation and characterisation of single-walled carbon nanotubes functionalised with amines. *Carbon*. 2006, **44**, 1891.

[185] Hulicova-Jurcakova D, Kodama M, Shiraishi S, Hatori H, Zhu ZH, Lu GQ. Nitrogen-Enriched Nonporous Carbon Electrodes with Extraordinary Supercapacitance. *Adv. Funct. Mater*. 2009, **19**, 1800.

[186] Cha C, Shin SR, Annabi N, Dokmeci MR, Khademhosseini A. Carbon-Based Nanomaterials: Multifunctional Materials for Biomedical Engineering. *ACS Nano*. 2013, **7**, 2891.

[187] Desimoni E, Casella GI, Salvi AM. XPS/XAES study of carbon fibres during thermal annealing under UHV conditions. *Carbon*. 1992, **30**, 521.

[188] Shao Y, Zhang S, Engelhard MH, Li G, Shao G, Wang Y, et al. Nitrogen-doped graphene and its electrochemical applications. *J. Mater. Chem*. 2010, **20**, 7491.

[189] Maldonado S, Morin S, Stevenson KJ. Structure, composition, and chemical reactivity of carbon nanotubes by selective nitrogen doping. *Carbon*. 2006, **44**, 1429.

[190] Jiménez Mateos JM, Fierro JLG. X-ray Photoelectron Spectroscopic Study of Petroleum Fuel Cokes. *Surf. Interf. Anal*. 1996, **24**, 223.

[191] Balandin AA. Thermal properties of graphene and nanostructured carbon materials. *Nature Mater*. 2011, **10**, 569.

[192] Zhao L, He R, Rim KT, Schiros T, Kim KS, Zhou H, et al. Visualizing Individual Nitrogen Dopants in Monolayer Graphene. *Science*. 2011, **333**, 999.

[193] Lv R, Li Q, Botello-Méndez AR, Hayashi T, Wang B, Berkdemir A, et al. Nitrogen-doped graphene: beyond single substitution and enhanced molecular sensing. *Sci. Rep*. 2012, **2**, 1.

[194] Park SH, Chae J, Cho M-H, Kim JH, Yoo K-H, Cho SW, et al. High concentration of nitrogen doped into graphene using $N_2$ plasma with an aluminum oxide buffer layer. *J. Mater. Chem. C*. 2014, **2**, 933.

[195] Takahiro Kondo SC, Tetsuya Suzuki, Taishi Shikano, Masataka Sakurai, Yoshihisa Harada,, Makoto Saito MO, Mario Italo Trioni, Gian Franco Tantardini, and Junji Nakamura,. Atomic-scale characterization of nitrogen-doped graphite: Effects of dopant nitrogen on the local electronic structure of the surrounding carbon atoms. *Phys. Rev. B*. 2012, **86**, 0354361.

[196] Huheey JE, Keiter RL, Keiter EA. Inorganic Chemistry, Principles of Structure and Reactivity. Fourth Edition. ed. New York; 1993.

[197] Atkins P, De Paula J. Physical Chemistry for the Life Sciences. Second ed. Oxford, U. K.: Oxford University Press.; 2009.

[198] Mortimer RG. Physical Chemistry. Third ed. Canada: Elsevier Academic Press; 2008.

[199] Mikoushkin VM, Nikonov SY, Dideykin AT, Vul, apos, AY, et al. Graphene hydrogenation by molecular hydrogen in the process of graphene oxide thermal reduction. *Appl. Phys. Lett*. 2013, **102**, 071910.

[200] Sandoval S, Kumar N, Oro-Solé J, Sundaresan A, Rao CNR, Fuertes A, et al. Tuning the nature of nitrogen atoms in N-containing reduced graphene oxide. *Carbon*. 2016, **96**, 594.

[201] Kundu S, Nagaiah TC, Xia W, Wang Y, Dommele SV, Bitter JH, et al. Electrocatalytic Activity and Stability of Nitrogen-Containing Carbon Nanotubes in the Oxygen Reduction Reaction. *J. Phys. Chem. C*. 2009, **113**, 14302.

[202] Zhang Z, Gekhtman D, Dresselhaus MS, Ying JY. Processing and Characterization of Single-Crystalline Ultrafine Bismuth Nanowires. *Chem. Mater*. 1999, **11**, 1659.

[203] Rao CNR, Deepak FL, Gundiah G, Govindaraj A. Inorganic nanowires. *Prog. Solid State Chem*. 2003, **31**, 5.

[204] Rao CNR, Satishkumar BC, Govindaraj A, Nath M. Nanotubes. *Chem. Phys. Chem*. 2001, **2**, 78.

[205] Hong BH, Bae SC, Lee C-W, Jeong S, Kim KS. Ultrathin Single-Crystalline Silver Nanowire Arrays Formed in an Ambient Solution Phase. *Science*. 2001, **294**, 348.

[206] Sloan J, Friedrichs S, Meyer RR, Kirkland AI, Hutchison JL, Green MLH. Structural changes induced in nanocrystals of binary compounds confined within single walled carbon nanotubes: a brief review. *Inorg. Chim. Acta*. 2002, **330**, 1.

[207] del Carmen Giménez-López M, Moro F, La Torre A, Gómez-García CJ, Brown PD, van Slageren J, et al. Encapsulation of single-molecule magnets in carbon nanotubes. *Nat. Commun*. 2011, **2,** 407.

[208] Martincic M, Tobias G. Filled carbon nanotubes in biomedical imaging and drug delivery. *Expert Opin. Drug Deliver*. 2015, **12**, 563.

[209] Chuvilin A, Bichoutskaia E, Gimenez-Lopez MC, Chamberlain TW, Rance GA, Kuganathan N, et al. Self-assembly of a sulphur-terminated graphene nanoribbon within a single-walled carbon nanotube. *Nat. Mater*. 2011, **10**, 687.

[210] Wang Z, Zhao K, Li H, Liu Z, Shi Z, Lu J, et al. Ultra-narrow $WS_2$ nanoribbons encapsulated in carbon nanotubes. *J. Mater. Chem*. 2011, **21**, 171.

[211] Zhou M, Duan W, Chen Y, Du A. Single layer lead iodide: computational exploration of structural, electronic and optical properties, strain induced band modulation and the role of spin-orbital-coupling. *Nanoscale*. 2015, **7**, 15168.

[212] Rao CNR, Govindaraj A. Synthesis of Inorganic Nanotubes. *Adv. Mater*. 2009, **21**, 4208.

[213] Goldberger J, Fan R, Yang P. Inorganic Nanotubes: A Novel Platform for Nanofluidics. *Acc. Chem. Res*. 2006, **39**, 239.

[214] Babaa MR, Stepanek I, Masenelli-Varlot K, Dupont-Pavlovsky N, McRae E, Bernier P. Opening of single-walled carbon nanotubes: evidence given by krypton and xenon adsorption. *Surf. Sci*. 2003, **531**, 86.

[215] Dujardin E, Ebbesen TW, Krishnan A, Treacy MMJ. Wetting of Single Shell Carbon Nanotubes. *Adv. Mater*. 1998, **10**, 1472.

[216] Brown G, Bailey SR, Novotny M, Carter R, Flahaut E, Coleman KS, et al. High yield incorporation and washing properties of halides incorporated into single walled carbon nanotubes. *Appl. Phys. A*. 2003, **76**, 457.

[217] Shao L, Tobias G, Huh Y, Green MLH. Reversible filling of single walled carbon nanotubes opened by alkali hydroxides. *Carbon*. 2006, **44**, 2855.

[218] Geng HZ, Zhang XB, Mao SH, Kleinhammes A, Shimoda H, Wu Y, et al. Opening and closing of single-wall carbon nanotubes. *Chem. Phys. Lett*. 2004, **399**, 109.

[219] Mazzoni MSC, Chacham H, Ordejón P, Sánchez-Portal D, Soler JM, Artacho E. Energetics of the oxidation and opening of a carbon nanotube. *Phys. Rev. B*. 1999, **60**, R2208.

[220] Capobianchi A, Foglia S, Imperatori P, Notargiacomo A, Giammatteo M, Buono TD, et al. Controlled filling and external cleaning of multi-wall carbon nanotubes using a wet chemical method. *Carbon*. 2007, **45**, 2205.

[221] Shao L, Lin T-W, Tobias G, Green MLH. A simple method for the containment and purification of filled open-ended single wall carbon nanotubes using $C_{60}$ molecules. *Chem. Commun*. 2008, **18**, 2164.

[222] Warner JH, Ito Y, Zaka M, Ge L, Akachi T, Okimoto H, et al. Rotating Fullerene Chains in Carbon Nanopeapods. *Nano Lett*. 2008, **8**, 2328.

[223] Berber S, Kwon Y-K, Tománek D. Microscopic Formation Mechanism of Nanotube Peapods. *Phys. Rev. Lett*. 2002, **88**, 185502.

[224] Tang Z-c, Cai X-w, Gao J-s, Mao B-w, Tian Z-q, Huang R-b, et al. In-situ characterization of $C_{60}$ coalescence reaction. *Chem. Phys. Lett*. 1999, **306**, 345.

[225] Hernández E, Meunier V, Smith BW, Rurali R, Terrones H, Buongiorno Nardelli M, et al. Fullerene Coalescence in Nanopeapods: A Path to Novel Tubular Carbon. *Nano Lett*. 2003, **3**, 1037.

[226] Nikolaev P, Thess A, Rinzler AG, Colbert DT, Smalley RE. Diameter doubling of single-wall nanotubes. *Chem. Phys. Lett*. 1997, **266**, 422.

[227] Sloan J, Dunin-Borkowski RE, Hutchison JL, Coleman KS, Clifford Williams V, Claridge JB, et al. The size distribution, imaging and obstructing properties of $C_{60}$ and higher fullerenes formed within arc-grown single walled carbon nanotubes. *Chem. Phys. Lett*. 2000, **316**, 191.

[228] Gao H, Kong Y, Cui D, Ozkan CS. Spontaneous Insertion of DNA Oligonucleotides into Carbon Nanotubes. *Nano Lett*. 2003, **3**, 471.

[229] Longhurst MJ, Quirke N. Temperature-Driven Pumping of Fluid through Single-Walled Carbon Nanotubes. *Nano Lett*. 2007, **7**, 3324.

[230] Wang Q. Atomic Transportation via Carbon Nanotubes. *Nano Lett*. 2009, **9**, 245.

[231] Panczyk T, Jagusiak A, Pastorin G, Ang WH, Narkiewicz-Michalek J. Molecular Dynamics Study of Cisplatin Release from Carbon Nanotubes Capped by Magnetic Nanoparticles. *J. Phys. Chem. C*. 2013, **117**, 17327.

[232] Král P, Tománek D. Laser-Driven Atomic Pump. *Phys. Rev. Lett*. 1999, **82**, 5373.

[233] Insepov Z, Wolf D, Hassanein A. Nanopumping Using Carbon Nanotubes. *Nano Lett*. 2006, **6**, 1893.

[234] Xue Q, Jing N, Chu L, Ling C, Zhang H. Release of encapsulated molecules from carbon nanotubes using a displacing method: a MD simulation study. *RSC Adv*. 2012, **2**, 6913.

[235] Saikia N, Jha AN, Deka RC. Dynamics of Fullerene-Mediated Heat-Driven Release of Drug Molecules from Carbon Nanotubes. *J. Phys. Chem. Lett*. 2013, **4**, 4126.

[236] Kierkowicz M, Pach E, Santidrian A, Tobías-Rossell E, Kalbac M, Ballesteros B, et al. Effect of Steam-Treatment Time on the Length and Structure of Single-Walled and Double-Walled Carbon Nanotubes. *Chem. Nano. Mat*. 2016, **2**, 108.

[237] JuL, Velasco Jr J, Huang E, Kahn S, Nosiglia C, Tsai H-Z, et al. Photoinduced doping in heterostructures of graphene and boron nitride. *Nat. Nanotechnol*. 2014, **9**, 348.

[238] Tobias G, Shao L, Salzmann CG, Huh Y, Green MLH. Purification and Opening of Carbon Nanotubes Using Steam. *J. Phys. Chem. B*. 2006, **110**, 22318.

[239] Muñoz-Rojas D, Oró-Solé J, Ayyad O, Gómez-Romero P. Facile One-Pot Synthesis of Self-Assembled Silver@Polypyrrole Core/Shell Nanosnakes. *Small*. 2008, **4**, 1301.

[240] Asprey LB, Keenan TK, Kruse FH. Preparation and Crystal Data for Lanthanide and Actinide Triiodides. *Inorg. Chem*. 1964, **3**, 1137.

[241] Sloan J, Kirkland AI, Hutchison JL, Green MLH. Structural Characterization of Atomically Regulated Nanocrystals Formed within Single-Walled Carbon Nanotubes Using Electron Microscopy. *Acc. Chem. Res*. 2002, **35**, 1054.

[242] Pinsker ZG, Tatarinova LI, Novikova VA. Electronographic determination of the structure of zinc iodide. *Zh. Fiz. Khim*. 1946, **20**, 1401.

[243] Aqra F. Surface tension of molten metal halide salts. *J. Mol. Liq*. 2014, **200**, Part B, 120.

[244] de Jongh PE, Eggenhuisen TM. Melt Infiltration: an Emerging Technique for the Preparation of Novel Functional Nanostructured Materials. *Adv. Mater*. 2013, **25**, 6672.

[245] Handbook of Chemistry and Physics. 84th ed: CRC Press; 2003-2004.

[246] Fourcroy PH, Carré D, Rivet J. Structure cristalline de l'iodure de zinc $ZnI_2$. *Acta Crystallographica Section B*. 1978, **34**, 3160.

[247] Simon F, Monthioux M. Fullerenes inside Carbon Nanotubes: The Peapods Carbon Meta-Nanotubes : Synthesis, Properties and Applications. Carbon Meta-Nanotubes. 2011, 273.

[248] Smith BW, Luzzi DE. Formation mechanism of fullerene peapods and coaxial tubes: a path to large scale synthesis. *Chem. Phys. Lett.* 2000, **321**, 169.

[249] Milliken J, Keller TM, Baronavski AP, McElvany SW, Callahan JH, Nelson HH. Thermal and oxidative analyses of buckminsterfullerene, $C_{60}$. *Chem. Mater*. 1991, **3**, 386.

[250] Heymann D. Solubility of Fullerenes $C_{60}$ and $C_{70}$ in Water. Lunar Planet. Sci. 1996, **27**, 543.

[251] Okada S, Saito S, Oshiyama A. Energetics and Electronic Structures of Encapsulated $C_{60}$ in a Carbon Nanotube. *Phys. Rev. Lett*. 2001, **86**, 3835.

[252] Dubay O, Kresse G. Density functional calculations for $C_{60}$ peapods. *Phys. Rev. B*. 2004, **70**, 165424.

[253] Fan J, Yudasaka M, Yuge R, Futaba DN, Hata K, Iijima S. Efficiency of $C_{60}$ incorporation in and release from single-wall carbon nanotubes depending on their diameters. *Carbon*. 2007, **45**, 722.

[254] Simon F, Peterlik H, Pfeiffer R, Bernardi J, Kuzmany H. Fullerene release from the inside of carbon nanotubes: A possible route toward drug delivery. *Chem. Phys. Lett*. 2007, **445**, 288.

[255] Kondo D, Kawabata A, Horibe M, Nihei M, Awano Y. Vertically aligned peapod formation of position-controlled multi-walled carbon nanotubes (MWNTs). *Superlattices Microstruct*. 2003, **34**, 389.

[256] Poland DE, Kuriakose AK, Margrave JL. The Oxidation of Titanium Monoxide at High Temperatures. *J. Phys. Chem*. 1965, **69**, 158.

[257] Hanaor DAH, Sorrell CC. Review of the anatase to rutile phase transformation. *J. Mater. Sci*. 2011, **46**, 855.

[258] He Z, Guai G, Liu J, Guo C, Chye Loo JS, Li CM, et al. Nanostructure control of graphene-composited $TiO_2$ by a one-step solvothermal approach for high performance dye-sensitized solar cells. *Nanoscale*. 2011, **3**, 4613.

[259] O'Regan B, Gratzel M. A low-cost, high-efficiency solar cell based on dye-sensitized colloidal $TiO_2$ films. *Nature*. 1991, **353**, 737.

[260] Wang D, Choi D, Li J, Yang Z, Nie Z, Kou R, et al. Self-Assembled $TiO_2$–Graphene Hybrid Nanostructures for Enhanced Li-Ion Insertion. *ACS Nano*. 2009, **3**, 907.

[261] Yoo H, Kim Y, Lee J, Lee H, Yoon Y, Kim G, et al. n-Type Reduced Graphene Oxide Field-Effect Transistors (FETs) from Photoactive Metal Oxides. *Chem. Eur. J.* 2012, **18**, 4923.

[262] Yu JC, Yu, Ho, Jiang, Zhang. Effects of F- Doping on the Photocatalytic Activity and Microstructures of Nanocrystalline $TiO_2$ Powders. *Chem. Mater*. 2002, **14**, 3808.

[263] Muggli DS, Ding L. Photocatalytic performance of sulfated $TiO_2$ and Degussa P-25 $TiO_2$ during oxidation of organics. *Appl. Catal. B*. 2001, **32**, 181.

[264] Fujishima A, Honda K. Electrochemical Photolysis of Water at a Semiconductor Electrode. *Nature*. 1972, **238**, 37.

[265] Woan K, Pyrgiotakis G, Sigmund W. Photocatalytic Carbon-Nanotube–$TiO_2$ Composites. *Adv. Mater*. 2009, **21**, 2233.

[266] Jiang T, Zhang L, Ji M, Wang Q, Zhao Q, Fu X, et al. Carbon nanotubes/$TiO_2$ nanotubes composite photocatalysts for efficient degradation of methyl orange dye. *Particuology*. 2013, **11**, 737.

[267] Djokic. VR, Marinkovic AD, Mitric M, Uskokovic PS, Petrovic RD, Radmilovic VR, et al. Preparation of $TiO_2$/carbon nanotubes photocatalysts: The influence of the method of oxidation of the carbon nanotubes on the photocatalytic activity of the nanocomposites. *Ceram Int*. 2012, **38**, 6123.

[268] Chen J, Qiu F, Xu W, Cao S, Zhu H. Recent progress in enhancing photocatalytic efficiency of $TiO_2$-based materials. *Appl. Catal. A*. 2015, **495**, 131.

[269] Dong H, Zeng G, Tang L, Fan C, Zhang C, He X, et al. An overview on limitations of $TiO_2$-based particles for photocatalytic degradation of organic pollutants and the corresponding countermeasures. *Water Res*. 2015, **79**, 128.

[270] Simon P, Pignon B, Miao B, Coste-Leconte S, Leconte Y, Marguet S, et al. N-Doped Titanium Monoxide Nanoparticles with TiO Rock-Salt Structure, Low Energy Band Gap, and Visible Light Activity. *Chem. Mater*. 2010, **22**, 3704.

[271] Choudhury B, Bayan S, Choudhury A, Chakraborty P. Narrowing of band gap and effective charge carrier separation in oxygen deficient $TiO_2$ nanotubes with improved visible light photocatalytic activity. *J. Colloid Interface Sci*. 2016, **465**, 1.

[272] Ma J, Wu H, Liu Y, He H. Photocatalytic Removal of $NO_x$ over Visible Light Responsive Oxygen-Deficient $TiO_2$. *J. Phys. Chem. C*. 2014, **118**, 7434.

[273] Gusev AI, Valeeva AA. The influence of imperfection of the crystal lattice on the electrokinetic and magnetic properties of disordered titanium monoxide. *Phys. Solid State*. 2003, **45**, 1242.

[274] Banakh O, Schmid PE, Sanjinés R, Lévy F. Electrical and optical properties of $TiO_x$ thin films deposited by reactive magnetron sputtering. *Surf. Coat Technol*. 2002, **151**, 72.

[275] Bally AR, Hones P, Sanjinés R, Schmid PE, Lévy F. Mechanical and electrical properties of fcc $TiO_{1+x}$ thin films prepared by r.f. reactive sputtering. *Surf. Coat Technol*. 1998, **108**, 166.

[276] Housecroft C. E., E. SA. Inorganic Chemistry: Pearson Prentice Hall; 2005.

[277] Veljkovic I, Poleti D, Zdujic M, Karanovic L, Jovalekic Č. Mechanochemical synthesis of nanocrystalline titanium monoxide. *Mater. Lett*. 2008, **62**, 2769.

[278] Blazevska-Gilev J, Jandová V, Kupčík J, Bastl Z, Šubrt J, Bezdička P, et al. Laser hydrothermal reductive ablation of titanium monoxide: Hydrated TiO particles with modified Ti/O surface. *J. Solid State Chem*. 2013, **197**, 337.

[279] Nguyen T-T-N, He J-L. Preparation of titanium monoxide nanopowder by low-energy wet ball-milling. *Adv Powder Technol*. doi:10.1016/j.apt.2016.04.022

[280] Tominaka S, Tsujimoto Y, Matsushita Y, Yamaura K. Synthesis of Nanostructured Reduced Titanium Oxide: Crystal Structure Transformation Maintaining Nanomorphology. *Angew. Chem. Int.* Ed. 2011, **50**, 7418.

[281] Banus MD, Reed TB, Strauss AJ. Electrical and Magnetic Properties of TiO and VO. *Phys. Rev. B*. 1972, **5**, 2775.

[282] Lam S-M, Sin J-C, Abdullah AZ, Mohamed AR. Photocatalytic TiO2/Carbon Nanotube Nanocomposites for Environmental Applications: An Overview and Recent Developments. *Fullerenes, Nanotubes and Carbon Nanostructures*. 2014, **22**, 471.

[283] Zhao D, Yang X, Chen C, Wang X. Enhanced photocatalytic degradation of methylene blue on multiwalled carbon nanotubes–$TiO_2$. *J. Colloid Interface Sci*. 2013, **398**, 234.

[284] Allegra G. Il calcolo dell'intensità di diffrazione dei raggi X da parte di strutture denotanti disordine monodimensionale. Il Nuovo Cimento (1955-1965). 1962, **23**, 502-15.

[285] Greenwood N. N., A. E. 21 - Titanium, Zirconium and Hafnium In: Earnshaw A, ed. Chemistry of the Elements (Second Edition). Oxford: Butterworth-Heinemann 1997, p. 954-75.

[286] Götze J, Möckel R. Quartz: Deposits, Mineralogy and Analytics: Springer Berlin Heidelberg; 2012.

[287] Barker C, Robinson SJ. Thermal release of water from natural quartz. *Am. Mineral.* 1984, **69**, 1078.

[288] Barone P, Barberio M, Oliva A, Bonanno A. Synthesis and Characterization of Carbon Nanotubes Wrapped on Anatase Microparticles. *Part. Part. Syst. Charact*. 2011, **28**, 64.

[289] Bartkowski S, Neumann M, Kurmaev EZ, Fedorenko VV, Shamin SN, Cherkashenko VM, et al. Electronic structure of titanium monoxide. *Phys. Rev. B*. 1997, **56**, 10656.

[290] C. D. Wagner WMR, L. E. Davis, J. F. Moulder. Handbook of X-ray Photoelectron Spectroscopy: Perkin Elmer Corporation.

[291] Wahlbeck PG, Gilles PW. Reinvestigation of the Phase Diagram for the System Titanium–Oxygen. *J. Am. Ceram. Soc*. 1966, **49**, 180.

[292] Mayer JT, Diebold U, Madey TE, Garfunkel E. Titanium and reduced titania overlayers on titanium dioxide(110). *J. Electron Spectrosc. Relat. Phenom*. 1995;**73**, 1.

[293] Shin SE, Choi HJ, Hwang JY, Bae DH. Strengthening behavior of carbon/metal nanocomposites. *Sci. Rep*. 2015, **5**, 16114.

[294] Guanglong L, Changseok H, Miguel P, Duanwei Z, Shuijiao L, Vlassis L, et al. Synthesis, characterization and photocatalytic evaluation of visible light activated C-doped $TiO_2$ nanoparticles. *Nanotechnol*. 2012, **23**, 294003.

[295] Ballesteros B, Tobias G, Ward MAH, Green MLH. Quantitative Assessment of the Amount of Material Encapsulated in Filled Carbon Nanotubes. *J. Physical Chem. C*. 2009, **113**, 2653.

[296] Howard CJ, Sabine TM, Dickson F. Structural and thermal parameters for rutile and anatase. *Acta Crystallogr. B*. 1991, **47**, 462.

[297] Restori R, Schwarzenbach D, Schneider JR. Charge density in rutile, $TiO_2$. *Acta Crystallogr. B*. 1987, **43**, 251.

[298] Spurr RA, Myers H. Quantitative Analysis of Anatase-Rutile Mixtures with an X-Ray Diffractometer. *Anal. Chem*. 1957, **29**, 760.

[299] Ghosh TB, Dhabal S, Datta AK. On crystallite size dependence of phase stability of nanocrystalline $TiO_2$. *J. Appl. Phys*. 2003, **94**, 4577.

[300] Li H, Duan X, Liu G, Jia X, Liu X. Morphology controllable synthesis of $TiO_2$ by a facile hydrothermal process. *Mater. Lett*. 2008, **62**, 4035.

[301] Sabyrov K, Burrows ND, Penn RL. Size-Dependent Anatase to Rutile Phase Transformation and Particle Growth. *Chem. Mater*. 2013, **25**, 1408.

[302] Cong Y, Li X, Qin Y, Dong Z, Yuan G, Cui Z, et al. Carbon-doped $TiO_2$ coating on multiwalled carbon nanotubes with higher visible light photocatalytic activity. *Appl. Catal. B*. 2011, **107**, 128.

[303] Wang Y, Qin Y, Li G, Cui Z, Zhang Z. One-step synthesis and optical properties of blue titanium suboxide nanoparticles. *J. Cryst. Growth*. 2005, **282**, 402.

[304] Zuo F, Wang L, Wu T, Zhang Z, Borchardt D, Feng P. Self-Doped $Ti^{3+}$ Enhanced Photocatalyst for Hydrogen Production under Visible Light. J. Am. Chem. Soc. 2010, 132, 11856.